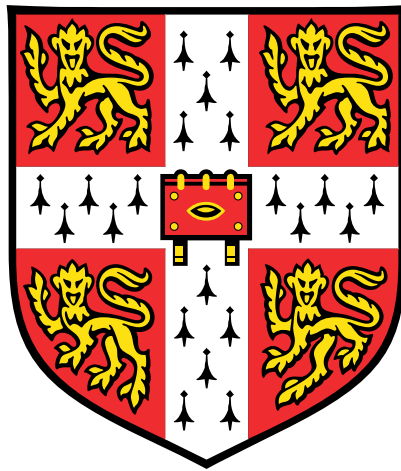# Polluted White Dwarfs:
Insights into Ancient
Extrasolar Planetary Systems

John Henry David Harrison

Institute of Astronomy

Robinson College

University of Cambridge

This dissertation is submitted for the degree of
Doctor of Philosophy

August 2020

Declaration

I hereby declare that my thesis titled **Polluted White Dwarfs: Insights into Ancient Extrasolar Planetary Systems** is original and has not been submitted in whole or in part for consideration for any other degree or qualification in this, or any other University. I further state that except where specific reference is made in the text to the work of others (including any collaborators), the contents of this dissertation are the result of my own work. This dissertation contains less than 60,000 words including appendices, footnotes, tables and equations and has less than 150 figures. The following parts of the thesis have been published or submitted to be published in academic journals:

Chapter 2 was adapted from the work done in: *Polluted White Dwarfs: Constraints on the Origin and Geology of Exoplanetary Material.* MNRAS, 479:3814-3841 (2018) and *Bayesian constraints on the origin and geology of exo-planetary material using a population of externally polluted white dwarfs.* MNRAS, submitted.

Chapter 3 was adapted from the work done in: *Polluted White Dwarfs: Constraints on the Origin and Geology of Exoplanetary Material.* MNRAS, 479:3814-3841 (2018).

Chapter 4 was adapted from the work done in: *Bayesian constraints on the origin and geology of exo-planetary material using a population of externally polluted white dwarfs.* MNRAS, submitted.

Chapter 5 was adapted from the work done in: *Evidence for post-nebula volatilisation in an exo-planetary body.* Earth and Planetary Sciences Letters, submitted.

Chapter 6 was adapted from the work done in: *A new class of Super-Earths formed from high-temperature condensates: HD219134 b, 55 Cnc e, WASP-47 e.* MNRAS, 484(1):712-727 (2018).

<div style="text-align: right">

John Henry David Harrison

August 2020

</div>

Acknowledgements

Firstly, I would like to thank my supervisor Amy Bonsor, this thesis would not be possible without her hard work, dedication, and support over the last 4 years. I would also like to thank Mihkel Kama for supporting me during Amy's maternity leave, and whose guidance allowed me to further develop my research skills. Additionally, I thank my main collaborators Oliver Shorttle and Caroline Dorn, whose expertise on the fields of geology and exo-planets allowed me to pursue interesting and insightful projects.

I thank Bill Nolan whose belief in my ability allowed me to reach this stage and who gave me the opportunity to supervise undergraduate students, something that has provided a constant source of enjoyment throughout my PhD. I must also thank Mrs Stephanie Monk whose hard work and passion for teaching allowed a young boy to pursue his dreams.

I would also like to thank the many friends who have made the last 4 years of my life so enjoyable. I thank Hugh and Roge for helping me relax, cheering me up, and keeping the spirit of Robinson 2012 going. Alex, Chris, James, and Chris for the countless good times especially on our road trips and birthday meet ups. And the whole IoA student body for making me feel at home at the institute throughout my studies.

I would also like to thank the countless members of Cambridge University Association Football Club who I have had the pleasure to grace the field with over my 8 years in Cambridge. Especially the double winning Falcons team of 16/17, the league winning Blues team of 17/18, and the varsity winning Falcons team of 19/20. Many of my fondest memories of Cambridge were made on rainy Wednesday afternoons with you boys.

My acknowledgments would not be complete without thanking my parents Kathryn and David, and my brother William, for their unwavering support throughout my life. Finally, I must thank Aislinn, for not only keeping me nourished and sane but for her love, kindness, and selflessness which have all been crucial in allowing me to complete this PhD. The countless magical moments I have spent with Aislinn over the past 7 years have made my time in Cambridge the most enjoyable of my life.

Abstract

As the study of rocky exo-planets enters an era of characterisation, the ability to determine how similar a planet is to the Earth, and thus if it is potentially habitable, is fast approaching. An understanding of the geological processes which determine a rocky world's bulk composition, geodynamics, and subsequent climate is of vital importance to this pursuit.

In this thesis, I demonstrate how the pollution of white dwarf stars by rocky exo-planetary material offers an insight into the bulk composition of rocky exo-planets, and thus, the geological processes which occur on them. I present a model which reproduces the atmospheric metal abundances present in polluted white dwarf stars and generates constraints on the origin of the polluting material. Using this model I find that for the majority of white dwarf systems the polluting material is primitive, and thus has a composition consistent with incomplete nebula condensation from a protoplanetary disc. However, this is not the case for all systems as I also find strong evidence for the accretion of core-rich, mantle-rich, crust-rich, and crust-stripped material, supporting the idea that differentiation and collisions are common processes in exo-planetary systems, and crucially, that differentiation processes and geological processes occur in a similar fashion in exo-planetary systems as they do in the Solar System. I also present evidence that white dwarf pollutants have similar masses to large Solar System asteroids and display a diversity in their formation temperatures, ranging from water ice rich comet analogues which formed below $200\,\mathrm{K}$ to refractory dominated bodies formed at above $1{,}400\,\mathrm{K}$. Additionally, I show how ancient post-nebula volatilisation processes likely occurred on the pollutant of GD362, that the average accretion event lifetimes are of the order of a few million years, and that thermohaline instabilities likely do not develop in some white dwarf atmospheres.

On the whole these results suggest that the rocky worlds which orbit other stars have compositions and geologies that are not dissimilar from the worlds which orbit the Sun. However, in the coming years more observations of polluted white dwarf systems will be required to further test this hypothesis.

Table of contents

List of figures

List of tables

Chapter 1

Introduction

The study of astronomy has always aimed to ascertain the place of the Earth in the cosmos. The uniqueness of the Earth and the uniqueness of life have always been questions which have intrigued mankind and driven scientific research.

The consensus for the majority of human history was that the Earth was the centre of the universe, and therefore was unique. Aristarchus of Samos was one of the first astronomers to argue against this when he presented a heliocentric model for the Solar System in the 3rd century BC. However, it was not until the 16th century AD that Nicolaus Copernicus outlined a viable mathematical model for heliocentrism. Over a century later, mainly due to the work of Johannes Kepler, Galileo Galilei, and Isaac Newton, the heliocentric model became the accepted view of the Solar System, causing the first significant dent in the Earth's uniqueness. The Earth was now just one of many bodies which orbited the Sun, and as observational techniques improved it became clear that in terms of size and density the Earth was very similar to Mercury, Venus, and Mars. The discovery of Mars' large southern polar ice cap by Giovanni Cassini in 1666 and the discovery of Venus' atmosphere in 1761 by Mikhail Lomonosov fueled the hypothesis that Venus and Mars were not significantly dissimilar to Earth. If this were the case, complex life may be present on our nearest neighbours potentially removing one of the Earth's most unique features. However, as mankind entered the space age, the speculation of complex life inhabiting the surface of Venus and Mars ended due to the realisation that Venus has an extremely high surface temperature and pressure, while Mars has a freezing surface temperature and lacks a substantial atmosphere. Unlike the other inner planets, the Earth possesses liquid water on its surface, a substantial atmosphere, and an active interior, all of which are thought to have played a part in the evolution of complex life. At least in the Solar System, the Earth remains unique. As the 21st century approached, the discovery of

an extrasolar planet around a main sequence star (Mayor and Queloz (1995)) restarted the quest to answer whether there were more Earth-like planets in the cosmos. The subsequent decades would yield the discovery of many more extrasolar planets around main sequence stars, making it clear that planetary systems are commonplace in the local region of the galaxy. Currently over 4,000 extrasolar planets have been discovered, and of these over 1,000 have radii between 0.5 and 2 Earth radii (NASA Exo-planet Archive). However, only a handful of these planets reside in a region around their host star where they could maintain liquid water on their surface (NASA Exo-planet Archive). In the coming decade many more potentially 'Earth-like' planets will be discovered; however Earth-like radii and 'habitable' orbital distances are only some of the features a planet must have to be considered genuinely Earth-like, and therefore potentially inhabited or inhabitable. A key component which determines whether a planet is truly similar to Earth is the planet's bulk chemical composition and internal structure. Knowing whether it is common for Earth-sized planets to have Earth-like compositions and Earth-like interiors is vital if we want to determine the number of truly Earth-like planets in the galaxy.

In my thesis, I concentrate on how observations of polluted white dwarf stars can improve our understanding of the composition and geology of rocky extrasolar worlds. I demonstrate how observing the atmospheres of polluted white dwarfs can determine the bulk composition of extrasolar rocky bodies as well as probing whether rocky extrasolar worlds experience similar geological processes to those seen on the Earth and on the other Solar System terrestrial bodies.

In this chapter, I outline the current theory and supporting data concerning the compositions of rocky worlds (Section 1.1). In Section 1.2, I summarise our current understanding of the formation, evolution, and physics of white dwarf stars and in Section 1.3, I present the current state of observations and theory concerning metal polluted white dwarfs.

1.1 The composition of rocky worlds

1.1.1 The composition of the Earth

Our understanding of the composition of the Earth, and the Earth's internal structure, has been forged by combining information from 6 main independent sources: the propagation of seismic waves through the Earth; the Earth's bulk parameters (mass, radius, moment of inertia etc.); the composition of meteorite samples which fall to the
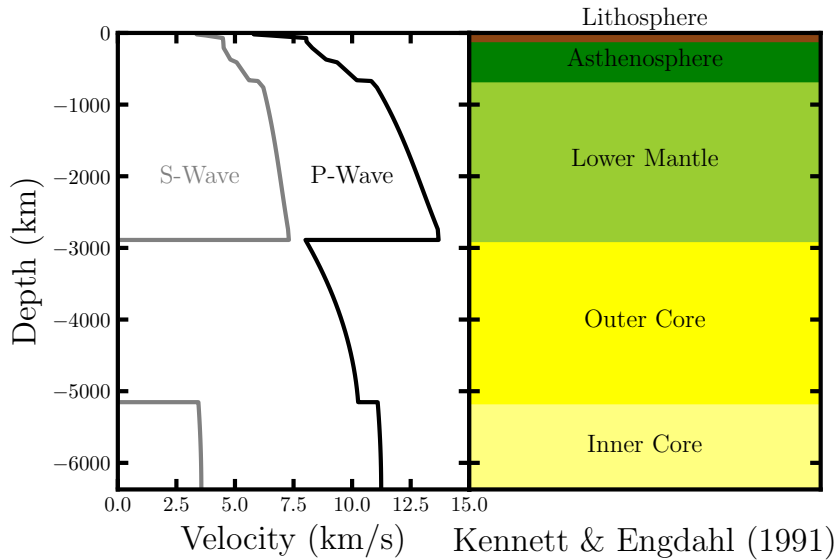
Fig. 1.1 The propagation of seismic waves through the Earth's interior allow the layered structure of the Earth and its density profile to be derived (data from Kennett and Engdahl (1991)).

Earth; the composition of rock samples from the Earth; the properties of the Earth's magnetic field; and the behavior of materials as a function of pressure and temperature in the laboratory.

Constraints from seismology

Measurements of the velocity of seismic compression waves (also called primary or P-waves) and seismic shear waves (also called secondary or S-waves) as they travel through the Earth can be used to reveal both the Earth's layered structure and its density profile (Oldham (1906); Guntenburg (1914); Kennett and Engdahl (1991)). Figure 1.1 shows the velocity of P-waves and S-waves as a function of depth inside the Earth found by Kennett and Engdahl (1991). The velocity of P-waves (V_p) and S-waves (V_s) are both functions of density: $V_p = \sqrt{\frac{\kappa + \frac{4}{3}\mu}{\rho}}$ and $V_s = \sqrt{\frac{\mu}{\rho}}$ where κ is the bulk modulus of the material, μ is the shear modulus of the material, and ρ is the density of the material. S-waves cannot travel through liquids as the shear modulus of a liquid is zero, therefore, the results plotted in Figure 1.1 highlight that the Earth is composed of five main layers, four of which are solid and one of which (the outer core) is liquid. Assuming that the Earth is spherical, in hydrostatic equilibrium, and that any compression is adiabatic, the density profile of the Earth can then be derived
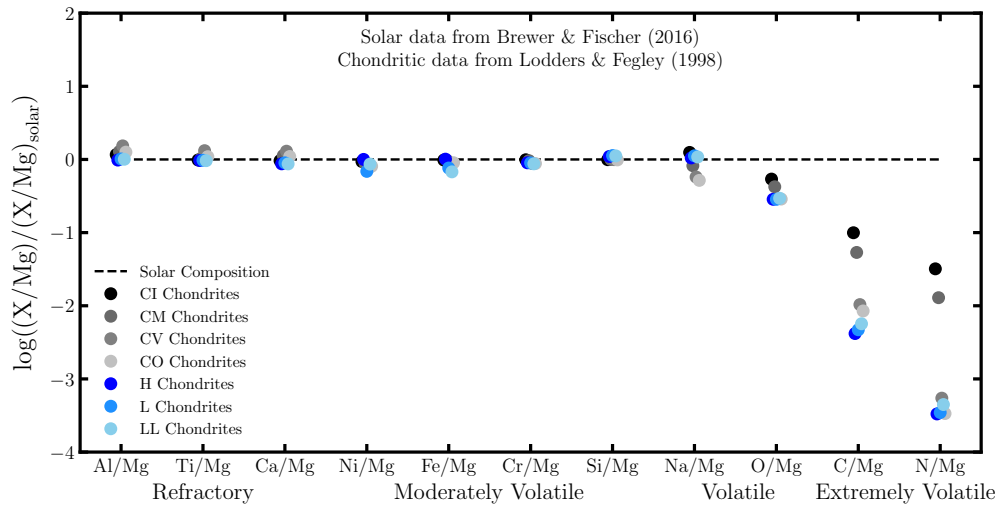
Fig. 1.2 The composition of various primitive meteorites match that of the solar photosphere in combination with a volatility dependent depletion trend (data from Lodders and Fegley (1998) and Brewer et al. (2016)).

(Williamson and Adams (1923)). The density profile derived in this way is consistent with the density profile found from the Earth's free oscillation frequencies (Dziewonski and Anderson (1981)). The density derived for the Earth's core cannot be explained by the compression of surface rocks alone (Williamson and Adams (1923)), which suggests that the core must be composed of intrinsically heavier material.

Constraints from bulk parameters

The Earth's bulk parameters can provide constraints on its interior structure and composition. The bulk mass and radius of the Earth are important parameters in constraining the Earth's interior composition as they act as boundary conditions on the density profile derived from seismic data. However, the Earth's moment of inertia is its most useful bulk parameter as it offers an independent probe of the Earth's interior structure. If the Earth's mass distribution was homogeneous throughout its interior the Earth would have a moment of inertia of $0.40MR^2$. However, from the Earth's axial precession rate, the Earth's equatorial buldge, and the nodal precession of the Earth's satellites, the moment of inertia of the Earth has been calculated to be $0.33MR^2$ (Williams (1994)). This result provides evidence that the Earth has a large fraction of its mass concentrated at the centre, reinforcing the conclusions arrived at by examining the Earth's density profile.

Constraints from primitive meteorites

The composition of meteorites which fall to the Earth from space offer valuable insights into both the composition of the Earth and the composition of rocky planetary bodies in general. The majority (86.2%) of meteorites which fall to the Earth are classified as chondrites (National History Museum Catalogue of Meteorites). Figure 1.2 highlights how the elemental abundances of various chondrites are in agreement with those of the solar photosphere, except the volatile elements which are depleted relative to the solar photosphere (Lodders and Fegley (1998); Brewer et al. (2016)). The depletion of the volatile elements in the chondrites relative to the solar photosphere is well explained by the condensation temperatures of the various volatile elements (Lodders (2003); Lodders (2010)).

Due to their composition chondrites are thought to be primitive planetesimals which are unprocessed and unaltered post formation (Lodders and Fegley (1998); Sears (2005)). The chondrites are therefore valuable probes of the early Solar System (Sears (2005)). The composition of Calcium-Aluminium rich inclusions (CAIs), found in the majority of chondrites, suggests that CAIs formed at extremely high temperatures in an extremely reducing environment, thus can be readily explained by nebula condensation processes (Yoneda and Grossman (1995); MacPherson et al. (2004)). CAIs are thought to be the first planetesimals to form in the Solar System, and the dating of their formation, and thus the age of the Solar System, can be performed by examining the abundances of various radioactive isotopes they contain (Bouvier and Wadhwa (2010)). The chondrites and CAIs provide evidence that suggests that primitive rocky planetary bodies inherit their bulk composition when they condense out of the hot circumstellar gas and into solid matter at the midplane of the protoplanetary disc (McDonough and Sun (1995); Palme and O'Neill (2003); Chambers (2004); Chambers (2009); Williams and Cieza (2011)). This suggests that the bulk composition of primitive rocky bodies is dependent mainly on the composition of the stellar nebula they form from and the temperature and pressure at which they form.

The C-type chondrites contain a higher fraction of volatile elements in comparison with the ordinary chondrites (H, L, LL type), suggesting that they formed further from the Sun (Lodders and Fegley (1998); Sears (2005)). The chondrites are believed to be fragments of bodies which originated in the asteroid belt (Sears (2005); Michel et al. (2015)). Based on their spectral features and albedo, the majority of asteroids in the asteroid belt can be classified as either C-type (carbonaceous) or S-type (siliceous) (Michel et al. (2015)). C-type asteroids are the most common (75% of all known asteroids), they are characterised by their extremely low albedos (typically less 0.10),
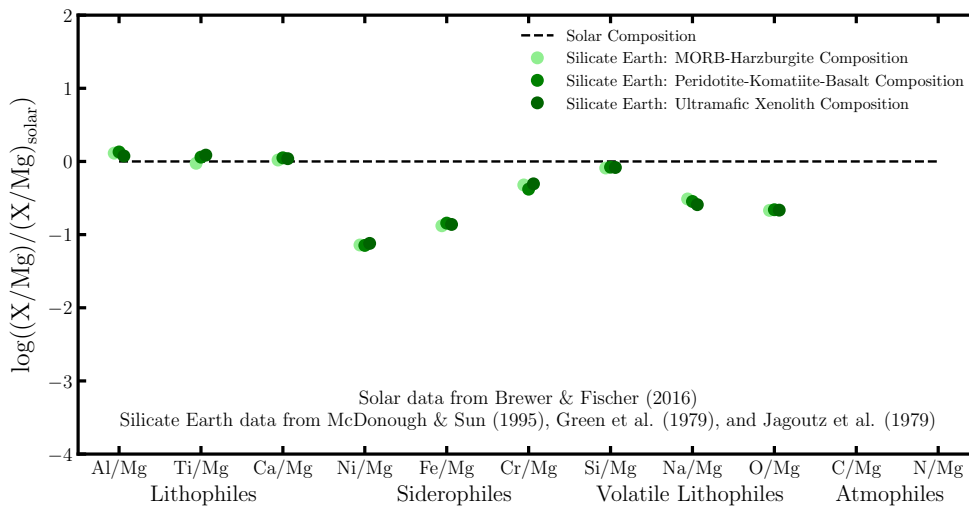
Fig. 1.3 The expected composition of the silicate Earth found by combining data from various ophiolite rock samples and laboratory experimental data (data from McDonough and Sun (1995)).

and are thought to be the parent bodies of the C-type chondrites (Michel et al. (2015)). S-type asteroids make up 17% of all known asteroids, they have much higher albedos (typically around 0.20), their spectra contain silicate absorption features, and they are thought to be the parent bodies of the ordinary chondrites (Michel et al. (2015)). If it is assumed that the formation of terrestrial planets mainly involves the aggregation of planetesimals which condense out of the stellar nebula (in a similar manner to the chondrites), then the bulk composition of the chondrites should be similar to the bulk composition of the Earth. This assumption is known as the chondritic reference model and its validity is debated; however, to first order it is expected to hold (McDonough and Sun (1995); Palme and O'Neill (2003); Campbell and O'Neill (2012)).

Constraints from rock samples

The composition of rock samples can be used to directly probe the composition of the Earth's upper layers. This composition can then be compared with the chondritic reference model. The composition of ophiolites (sections of the Earth's upper mantle which have been uplifted and are exposed above sea-level) and laboratory experimental data on the behavior of basaltic melts can be combined to produce pyrolite models for the composition of the Earth (McDonough and Sun (1995)). Figure 1.3 shows the composition predicted by three such pyrolite models, which use different reference rocks

and combine them in different ratios, for the composition of the Earth. When compared with the composition of the chondrites and the solar photosphere, there is a clear under-abundance of Ni, Fe, and Cr in the Earth. When this information is combined with the Earth's density profile and moment of inertia, it becomes clear that the Earth's core must be extremely rich, relative to Earth's rocky portion, in Fe, Ni, and Cr, all of which are heavy transition metal elements. Elements that are depleted in the silicate Earth, and therefore abundant in the core, are classified as siderophiles (iron-loving) while elements that are not depleted in the silicate Earth are classified as lithophiles (rock-loving) (Goldschmidt (1937)). The presence of the Earth's strong magnetic field, both currently and throughout geological time, further supports the conclusion that the Earth has an Fe rich core. The generation of such a strong magnetic field can only be explained by a self-exciting dynamo, which would be naturally produced if the Earth had a significant volume of convecting iron at its centre (Buffett (2000)). The Hf-W isotope system, which can be examined by comparing Earth rock samples to chondrites, also provides strong evidence for the formation of the Earth's metallic core and can be used to constrain the time of the core's formation to less than 100 million years after Ca-Al inclusion formation (Jacobsen (2005)). The precise composition of Earth's core can be estimated by laboratory experiments. Current models predict that the composition is likely an Fe-Ni mixture only containing between 5% and 10% other elements (Birch (1964); Boehler (2000); Anderson and Isaak (2002); Zhang et al. (2016)). The exact fraction of light elements sequestered in the core is heavily debated but to first order the Earth's core is an Fe-Ni mixture with a non-negligible light element component (McDonough (2003)).

Constraints from non-primitive meteorites

Not all meteorites which fall to Earth are chondritic; 8.2% of all falls are classified as achondritic meteorites, 4.6% of all falls are classed as iron meteorites, and 1.0% of all falls are classified as stony iron meteorites (National History Museum Catalogue of Meteorites). Unlike the chondrites, these meteorites are not primitive and have undergone geological and collisional processing since their parent bodies formed from material which condensed from the stellar nebula. The non-primitive meteorites provide additional support to the conclusion that the Earth's interior is chemically differentiated and that its core is composed of predominantly Fe and Ni. The iron meteorites, whose mass is dominated by Fe and Ni ($\sim$98% by mass), are thought to be fragments of the cores of disrupted protoplanets (Lodders and Fegley (1998); Scott (2013)). The iron meteorites are also thought to be linked to the 8% of known asteroids which are
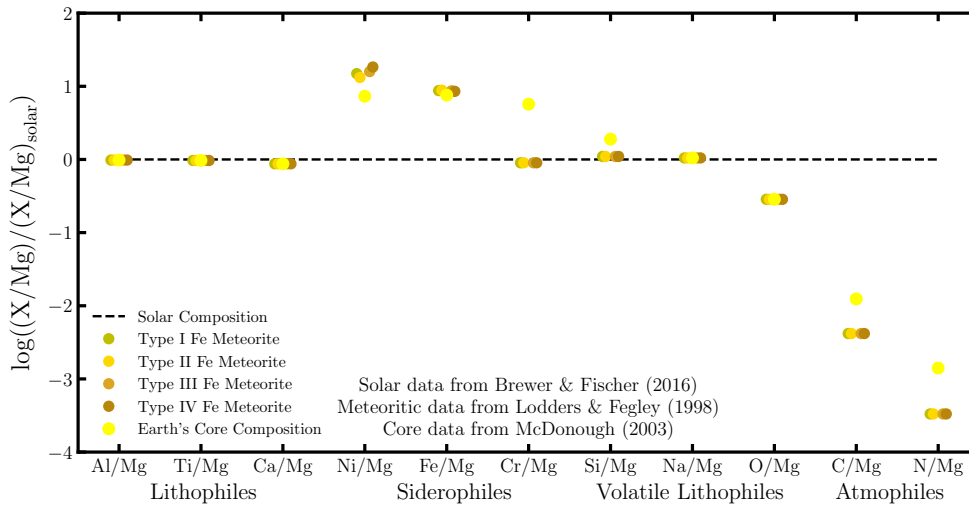
Fig. 1.4 The composition of the Earth's core can be found by combining the information on the Earth's density profile with laboratory experiments and cosmochemical data (data from McDonough (2003)). The data plotted is for hypothetical bodies composed of 50% H chondrite material and 50% either iron meteorite material or Earth's core material by number (data from Lodders and Fegley (1998)).

classified as M-type (metallic) (Michel et al. (2015)). M-type asteroids are classified as such because their spectra are devoid of any features while their surface albedos are much higher than that of C-type asteroids (Michel et al. (2015)). Figure 1.4 shows the core composition derived by McDonough (2003) compared with that of the various classes of iron meteorite. As the Earth's core and iron meteorites contain very little Mg the abundances plotted are that for material composed of 50% H chondrite material and 50% Earth's core or iron meteorite material by number fraction. The compositions of the iron meteorites are a good first order match to that predicted for the Earth's core with the notable exceptions of the relative siderophilicities (the tendency of an element to preferentially move into the core of a body) of Ni and Cr. Ni appears to be more siderophilic in the iron meteorites and Cr appears to be less siderophilic in the iron meteorites. This is well explained by laboratory experiments which show that Ni behaves in a more siderophilic fashion at lower pressures while Cr behaves in a less siderophilic fashion at lower pressures (Bouhifd and Jephcoat (2011); Siebert et al. (2012); Fischer et al. (2015)). Therefore, if the iron meteorites are fragments of differentiated asteroids this is the exact behavior one would expect as their cores would have formed at lower pressures than the Earth's. The iron meteorites also lack the light elements which are required in the Earth's core to fully explain the density deficit
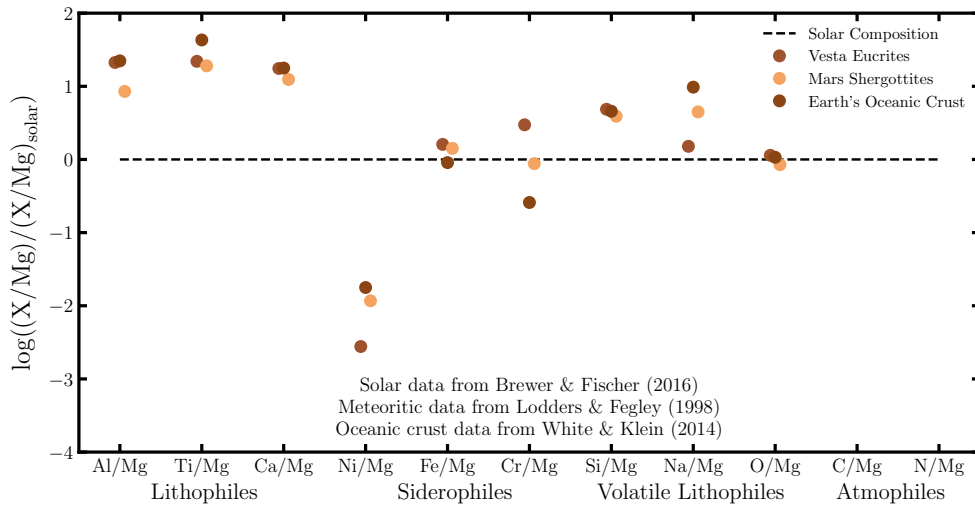
Fig. 1.5 The composition of the Earth's oceanic crust as found by White and Klein (2014) in comparison with the composition of eucrites (Vesta) and shergottites (Mars) (data from Lodders and Fegley (1998)).

(Zhang et al. (2016)), this is again thought to be due to the parent bodies of the iron meteorites differentiating under lower pressure conditions (Scott (2013); Fischer et al. (2015)). The achondrites offer further evidence for planetary chemical differentiation as they are thought to be fragments of the crusts of differentiated bodies; specifically, the SNC meteorites and HED meteorites are thought to be pieces of the crusts of Mars and Vesta respectively (Treiman et al. (2000); Mittlefehldt (2015)). Figure 1.5 shows how the compositions of these meteorites are similar to the composition of the Earth's oceanic crust. This similarity means it is thought that it is common for rocky planetary bodies to produce outflows of basaltic melts at their surface (Embey-Isztin (2007)). There is a disparity between the siderophile elemental abundances (Fe, Ni, Cr) of the Earth's oceanic crust and the achondrites, however, this is again explained by variability in the mantle compositions of the parent bodies due to core formation under different pressure conditions (Fischer et al. (2015)). The stony iron meteorites provide further evidence for differentiation into iron-nickel cores and magnesium-silicate mantles on rocky worlds, as their abundances suggest that they were produced when differentiated bodies collided and merged (Yang et al. (2010)).
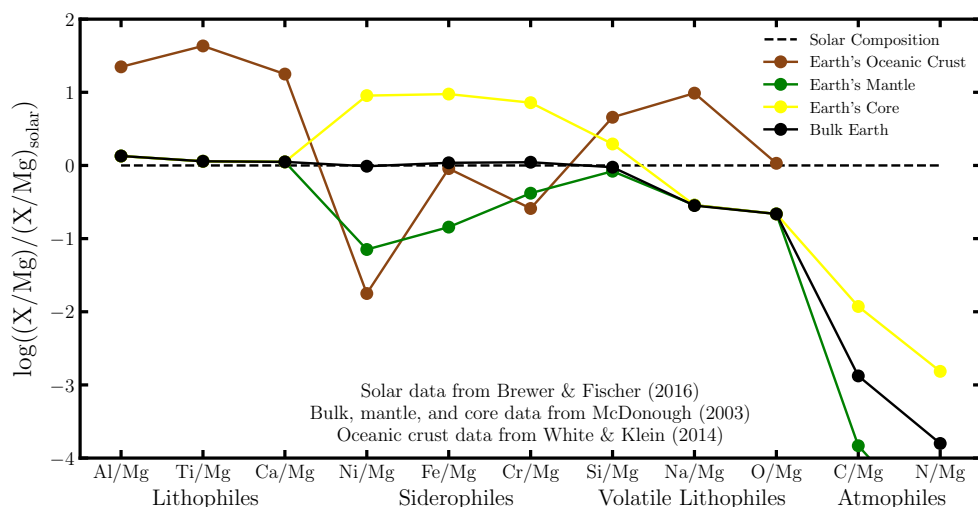
Fig. 1.6 Bulk Earth is consistent with the solar photosphere in combination with an elemental volatility dependent trend. The Earth's core is enhanced in siderophiles, the Earth's mantle is depleted in siderophiles, and the Earth's oceanic crust is enhanced in lithophiles and depleted in siderophiles. The core data plotted is composed of two thirds core material and one third mantle material by number (data from McDonough (2003), White and Klein (2014), and Brewer et al. (2016)).

Combined constraints and the importance of interior composition

The bulk composition of the Earth and the composition of its various layers have been constrained by combining data from various independent sources and producing compositions which are mutually compatible (McDonough (2003)). Figure 1.6 displays how, to first order, the composition of bulk Earth predicted by the combination of the independent sources is consistent with the Earth forming via the aggregation of planetesimals which condensed out of the stellar nebula in a similar manner to the chondrites (McDonough and Sun (1995); McDonough (2003)). Figure 1.6 also shows how the core of the Earth is enhanced in the siderophilic elements, the mantle of the Earth is depleted in the siderophilic elements, and the oceanic crust of Earth is enhanced in the lithophiles while being depleted in the siderophiles relative to bulk Earth.

Having a bulk composition similar to the Earth and being chemically differentiated in a similar manner to the Earth may be vital for life as we know it to evolve and thrive (Lammer et al. (2009)). Plate tectonics, a property which is dependent on the Earth's interior, allow for the regulation of the Earth's climate (Walker et al. (1981)),
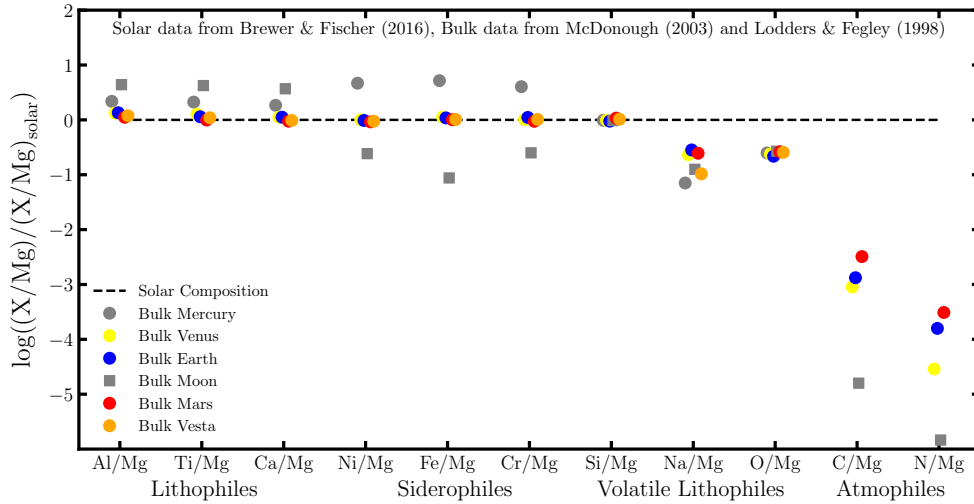
Fig. 1.7 The bulk composition of the rocky worlds in the solar system taken from Lodders and Fegley (1998) and references therein, and McDonough (2003). The available data for Venus, Earth, Mars, and Vesta suggest that their compositions are consistent with that of the solar photosphere in combination with nebula condensation and post-nebula volatilisation based trends. However, data from the Moon and Mercury suggest that they have compositions which have been altered due to the bodies experiencing planetary scale collisions post-differentiation.

while the initial composition of the Earth's secondary atmosphere is heavily dependent on the composition of the gases expelled by volcanic eruptions (Yung et al. (2015)). Chemical differentiation also leads to the production of the Earth's magnetic field which may be vital for stabilising a planet's atmosphere (Strangeway et al. (2017)). Therefore, the composition of a planet's interior is expected to be a vital parameter when determining if the planet is potentially habitable (Lammer et al. (2009)).

1.1.2   The composition of rocky Solar System bodies

The composition of the other rocky worlds which reside in the Solar System are more difficult to precisely constrain than the composition of the Earth. This is because for worlds other than the Earth there are limited rock samples, limited information on magnetic field properties, and limited data on seismic activity. However, for certain Solar System bodies bulk compositions can be ascertained by examining their bulk parameters and the composition of meteorites which are thought to originate from them. This data can then be reconciled with the models and understanding established when studying the Earth's composition in order to paint a coherent picture.

As the understanding of the Earth's internal composition and structure progressed, it became accepted that the major factors which seem to influence the bulk composition of a rocky world and the composition of its layers are: the composition of the stellar nebula from which the planetary system formed; the conditions at which the material which formed the body condensed out of the protoplanetary disc; whether the body has undergone differentiation into a siderophile rich core and a lithophile rich crust; and the conditions at which this differentiation occurred at. Studying the composition of meteorites from other worlds and the bulk parameters of other worlds can help to test whether these are indeed key factors which to first order determine a rocky worlds composition.

The Solar System worlds with compositional data

The Solar System bodies which have the most substantial meteorite suites are the Moon, Mars, and Vesta. For Mars and the Moon, direct surface rock samples mean that meteorites can be linked to the parent bodies by comparing various relevant isotopic ratios (McSween (1987); McCoy et al. (2011)). By contrast, Vesta has been linked to the HED suite of meteorites due to the similarities between the composition of the meteorites and the inferred surface composition of Vesta from reflection spectra (McSween Jr. et al. (2013)). The bulk compositions of the Moon, Mars, and Vesta can therefore be estimated by combining the relevant meteoritic data with the bulk parameters of the bodies (Morgan and Anders (1980); Lodders and Fegley (1998)).

For the other two terrestrial planets there is surface imaging data but no direct rock samples, so in order to estimate the composition of Venus and Mercury multiple assumptions must be made. Estimates for the compositions of Mercury and Venus can be made by first assuming that the planets are composed of material which condensed out of the solar nebula, and then assuming the planets differentiated such that a metallic core formed. This allows the bulk composition to be determined as the planetary bulk parameters can constrain the core mass fraction and the condensation model can determine the available reservoir of elements (Morgan and Anders (1980)). There are many other worlds in the Solar System whose bulk composition would be of interest when probing the mechanisms of planet formation and geological activity, most notably the compositions of many of the Solar Systems asteroids, comets, icy moons, and Kuiper belt objects. However, due to the lack of available data on such bodies their potential compositions shall not be discussed here. Figure 1.7 displays the estimated bulk compositions for the Solar System bodies which have the best constrained compositions, the four telluric planets, the Moon and Vesta.

The composition of Earth and Venus

As discussed in Section 1.1.1, the constraints we can place on the Earth's composition suggest that it is consistent with forming from material which condensed out of the solar nebula. Venus' bulk parameters are consistent with a model where it has lower volatile abundances than Earth but similarly formed from material which condensed out of the stellar nebula (Morgan and Anders (1980)). The bulk parameters of Venus are very similar to the Earth (Lodders and Fegley (1998)), and given the surface of Venus appears to be consistent with basaltic melts (Basilevsky and Head (2003)), the hypothesis that its interior is not too dissimilar to Earth's in terms of bulk composition seems reasonable. This similarity between the planets adds weight to the conclusions arrived at for the Earth. Figure 1.7 displays how the bulk compositions of Earth and Venus are consistent with the solar photosphere in the refractory elements, while being depleted in the volatile elements in a manner well explained by nebula condensation.

The composition of Mars and Vesta

Rock samples from Mars and Martian meteorites suggest that Mars has substantially more volatile species than Earth (Dreibus and Wanke (1985); Brückner et al. (2008)), reinforcing the conclusion that rocky worlds inherit their composition from material which condenses out of the stellar nebula; as Mars formed further from the Sun, it formed from more volatile rich material. However, not all elements have abundances which follow simple condensation sequences. Unlike the Earth and Venus, Vesta and Mars cannot be solely explained by nebula condensation processes as their expected abundances of volatile species (particularly Mn and Na) do not follow a simple condensation based trend (Siebert et al. (2018)). From meteoritic data it is known that nebula condensation is not the sole volatilisation process which determines the composition of rocky planetary material, and the composition of bodies can be significantly altered post formation (O'Neill and Palme (2008)). Significant melting and the formation of a global magma ocean can occur on rocky planetary bodies due to high energy planetary impacts and the decay of short lived radioactive isotopes (Keil (2000); Chambers (2004); Day and Moynier (2014); Pringle et al. (2014); Wang and Jacobsen (2016); Hin et al. (2017); Siebert et al. (2018)). The formation of such a magma ocean causes the preferential loss of volatile elements (post-nebula volatilisation), particularly on less massive bodies like Mars, Vesta, and the Moon, which unlike the Earth do not have sufficient surface gravity to prevent the thermal escape of the vapour during the relevant timescales (O'Neill and Palme (2008); Pringle et al. (2014)). Post-nebula

volatilisation occurs at higher pressures and in more oxidising conditions than solar nebula condensation (O'Neill and Palme (2008); Visscher and Fegley (2013)). Thus, individual elemental behaviours and volatilities may be significantly different and the abundance signatures created often do not match those expected from nebula condensation (Sossi and Fegley (2018)). The abundances of Mn and Na are a good example of elements whose behaviour is different during nebula condensation and post nebula volatilisation; Na is a volatile in both nebula and post nebula conditions, while Mn is only a volatile in nebula conditions (O'Neill and Palme (2008); Sossi and Fegley (2018); Siebert et al. (2018)). The predicted Mn/Na ratio of Vesta and Mars implies that their composition was not only determined by nebula condensation but a combination of nebula condensation and post nebula volatilisation.

The composition of Mercury and the Moon

Figure 1.7 shows how the composition of the Moon and Mercury cannot be explained by either condensation from the solar nebula nor post-nebula volatilisation, as the refractory species do not agree with the solar photosphere abundances. The Moon is expected to be enhanced in the lithophiles while being depleted in the siderophiles relative to the solar abundances, while Mercury is expected to be enhanced in the siderophiles. Such abundance patterns are typical of fragments of differentiated bodies which have uneven proportions of mantle-rich or core-rich material (Section 1.1.1).

From seismic data, rock samples, and planetary bulk parameters it is known that all the terrestrial planets, along with many of the Solar System's asteroids and moons, are internally differentiated (Lodders and Fegley (1998); Mocquet et al. (2011); Thomas et al. (2005); Russell et al. (2012)). This internal differentiation is thought to be driven by heating from two major sources: the heat created during planetary accretion and planetary impacts; and the decay of short lived radioactive nucleotides (SLRs) such as ^{26}Al and ^{60}Fe (Rubin (2005); Ghosh et al. (2006); Moskovitz and Gaidos (2011)).

For small bodies the heat generated from planetary accretion and impacts dissipates too quickly to be an important factor, however, collisional heating does provide substantial heating for bodies with diameters larger than 1000 km (Moskovitz (2009); Moskovitz and Gaidos (2011)). For smaller bodies whose mass is not substantial enough to produce or retain the interior heat required for core formation, the isotopes ^{26}Al and ^{60}Fe are therefore key in driving the differentiation process, as their decay produces the heat required to allow the onset of core formation (Ghosh et al. (2006)). Depending on the exact formation time of the planetesimal it is possible for heating from SLRs

to cause differentiation on planetesimals as small as 20 km, assuming Solar System abundances of the SLRs (Moskovitz and Gaidos (2011)).

The seismic data and bulk parameters of the Moon suggest that it has an unusually small Fe core (Viswanathan et al. (2019)) while rock samples suggest a lunar composition similar to that of the Earth's mantle (Ringwood (1986)). This information combined with isotopic data suggests that the unusual composition of the Moon when compared with the solar photosphere is due to it being formed when a planet sized body impacted the Earth after the formation of the Earth's core (Hartmann (2014)). The Moon can therefore be thought of as a mantle-rich collisional fragment. The bulk parameters of Mercury on the other hand suggest that it has an unusually large Fe core (Genova et al. (2019)). Although many hypotheses have been suggested to explain Mercury's density, the prevailing explanation, which is compatible with the all of the observations, is that Mercury has experienced a mantle stripping collision (Benz et al. (1988); Asphaug and Reufer (2014); Bhatia and Sahijpal (2017)).

Lessons from the composition of Solar System rocky bodies

Two important factors which affect the bulk composition of rocky worlds, that were not initially uncovered by the study of the Earth's composition, were found when studying the composition of rocky bodies in our own Solar System. Firstly, post-nebula volatilisation during the magma ocean phase can alter the abundances of the volatile elements in a body, if the body is heated sufficiently and the mass of the body is insufficient to keep vapour from escaping. Secondly, collisional processes can redistribute siderophile rich core material and lithophile rich mantle material post differentiation unevenly between the surviving bodies. These two factors are important in explaining the compositions of Mars, Vesta, Mercury, and the Moon.

1.1.3 The composition of rocky exo-planets

Protoplanetary discs and their composition

It is widely accepted that rocky planets form in protoplanetary discs, however, the exact mechanisms which govern their formation are not well understood (Williams and Cieza (2011); Morbidelli et al. (2012); Blum (2018)). Observations using Atacama large millimeter array (ALMA) of gaps and cavities in massive dust and gas discs around young stars allow astronomers to glimpse into the planet formation process (Andrews (2020)). The nature and composition of the protoplanetary disc is expected to play a vital role in determining the characteristics of the planets which form from it

(Williams and Cieza (2011); Moriarty et al. (2014)). The majority of protoplanetary discs survive for ~3 Myrs before accretion ceases and photoevaporation effects dominate causing the disc to dissipate (Haisch et al. (2001); Alexander et al. (2006a); Alexander et al. (2006b); Mamajek et al. (2009); Ribas et al. (2015)). The bulk composition of a protoplanetary disc is expected to be inherited from the stellar nebula from which it forms. For discs without large cavities the compositions of the accreted material are, as expected, similar to that of main sequence stellar photosphere's (Kama et al. (2015)). However, for discs with large cavities the accreted compositions are severely depleted in the refractory elements, suggesting that the dusty component, which has condensed out of the gas disc, has become trapped and can no longer accrete onto the star (Kama et al. (2015); Kama et al. (2019)). When compared with the photospheric compositions of nearby main sequence stars, the solar photosphere is compositionally average (Brewer et al. (2016)), therefore, naively it may be expected that the bulk composition of rocky exo-planets may not be too dissimilar from that of the Solar System's rocky planets. The recent discovery and characterisation of many terrestrial mass exo-planets potentially allows this hypothesis to be tested.

Exo-planet detection and bulk parameter constraints

Planets orbiting other stars are discovered by four main methods: transit photometry (77.1%), Doppler spectroscopy (19.2%), gravitational microlensing (2.1%), and direct imaging (1.2%) (NASA Exo-planet Archive (May 2020)). Transit photometry provides a constraint on the radius of the exo-planet via the following equation: $R_p = \sqrt{\frac{\Delta F}{F}} R_*$ where R_p is the radius of the exo-planet, ΔF is the change in flux of the star when the transit occurs, F is the baseline flux of the star, and R_* is the radius of the star. This equation is derived assuming that the host star is of uniform brightness (i.e. no stellar spots) and that the planet emits no flux of its own. Doppler spectroscopy provides a constraint on the mass of an exo-planet via a rearranged version of Kepler's 3rd law for a circular orbit: $M_p = \left(\frac{M_*^2 P}{2\pi G}\right)^{\frac{1}{3}} \frac{v_{obs}}{\sin(i)}$ where M_p is the mass of the exo-planet, M_* is the mass of the star, P is the period of the orbit, G is Newton's gravitational constant, i is the inclination of the orbital plane relative to the line of sight of the observer, and v_{obs} is the observed radial velocity of the star. The inclination of the orbit can only be estimated if transit photometry is available for the system which is not always possible given the requirement for the system to be aligned correctly relative to the Earth. Therefore, the mass constraint is often a lower limit. The planetary mass equation assumes the mass of the exo-planet is negligible in comparison to the host star. As transit photometry provides an estimate for a planet's radius and Doppler spectroscopy
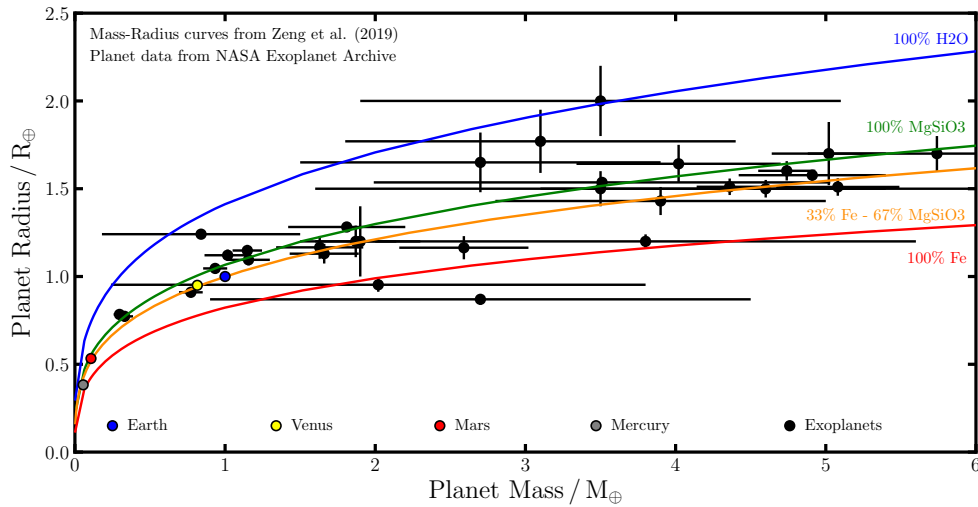
Fig. 1.8 A mass-radius plot with all confirmed exo-planets with both mass and radius constraints, where the expected mass is less than 6 Earth masses (data from NASA Exo-planet Archive). The solar system planets have also been included for reference. The mass-radius curves for a pure H_2O planet (blue), pure $MgSiO_3$ planet (green), pure Fe planet (red), and a planet composed of an Fe core and $MgSiO_3$ mantle (orange) are also plotted (mass-radius curves calculated in Zeng et al. (2019)).

provides an estimate for a planets mass, if both observations are obtained the bulk density of an exo-planet can be calculated. The bulk density of an exo-planet can then be used to constrain its interior composition and structure.

Exo-planet mass-radius distribution and degeneracy problem

Figure 1.8 displays the data for all confirmed planets with both mass and radius constraints which are less massive than 6 Earth masses (NASA Exo-planet Archive). The mass-radius curves plotted were calculated in Zeng et al. (2019) and show the expected radius as a function of mass assuming a planet is composed of H_2O (blue), $MgSiO_3$ (green), a Fe core and $MgSiO_3$ mantle (orange), or Fe (red). The Solar System planets all lie close to the orange curve (Fe core containing one third the mass of the planet and MgSiO3 mantle containing the remaining mass) with the exception of Mercury, which as discussed in Section 1.1.2, has a much larger Fe core potentially due to the collisional stripping of its mantle post-differentiation. The small exo-planets which currently have mass and radius constraints do not appear to be as confined to the orange curve as the worlds of the Solar System, even when the large uncertainties on the mass measurements are taken into account. This could potentially suggest that

giant planetary scale impacts are common place in exo-planetary systems and the planets plotted in Figure 1.8 can be explained by being either mantle-rich or core-rich. However, a far simpler solution is that many of these planets contain water-rich layers unlike the terrestrial planets in the Solar System. Different combinations of layers of rock, iron, and water can produce the same overall bulk density, therefore for a given planet mass and radius many different interior compositions can reproduce the observations (Seager et al. (2007)). This is known as the exo-planet mass-radius degeneracy problem. Additionally, exotic compositions such as carbon cores and silicon carbide mantles also cannot be ruled out using knowledge of a planets mass and radius alone (Seager et al. (2007); Madhusudhan et al. (2012)). A further degeneracy is due to the potential for the planet to possess a thick hydrogen or helium atmosphere, which would greatly affect its position in mass-radius space. For transiting planets the presence of thick atmospheres can be ruled out by monitoring the predicted radius as a function of wavelength or by examining the thermal phase curves of the planet (Sing (2018); Madhusudhan (2019)). Kreidberg et al. (2019) used the phase curve of LHS 3844b to rule out the presence of a thick atmosphere and conclude that the surface was most likely bare rock, however, even with this additional knowledge the composition of the interior still remains degenerate. In summary, concluding anything about the properties of a planet's interior from direct observations remains difficult (Seager et al. (2007)). Extrasolar planetary rock sample data, magnetic field data, and seismic data will likely not be possible, therefore, in order to break the compositional degeneracy another method for probing the interior composition will be required. From the study of exo-planet bulk properties alone it will not be possible to answer whether most terrestrial mass exo-planets are similar to the terrestrial planets of the Solar System either geologically or compositionally.

1.2 White dwarf stars

The history of white dwarf observations

The first white dwarf to be discovered was 40 Eridani B which was detected by Sir William Herschel in 1783 when he began cataloging visual binary stars (Herschel (1785)). 40 Eridani B was found to have a spectra similar to an A-type star but unlike most A-type stars it was extremely dim with an absolute magnitude of only +10.3 (Adams (1914); Lindblad (1922)). The Stefan-Boltzmann law can be used to calculate the radius of a star given its temperature and luminosity (Boltzmann (1884)). Due to its low brightness and high surface temperature, 40 Eridani B must therefore have had an
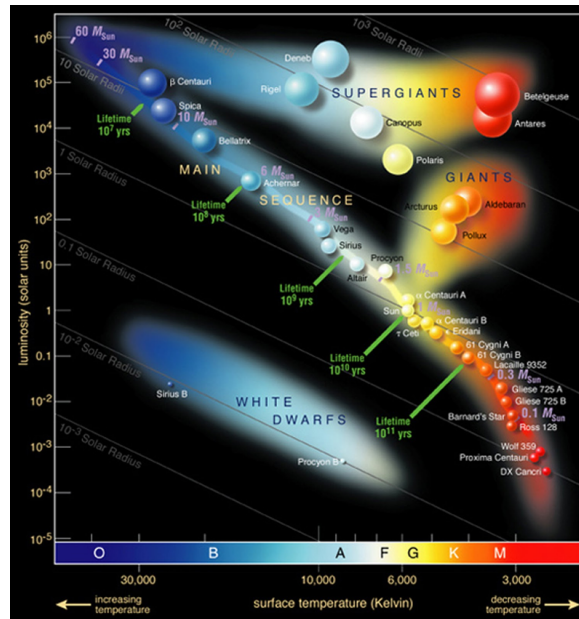
Fig. 1.9 An example Hertzsprung-Russell diagram obtained from the ESO website showing the positions of various famous stars in temperature-luminosity space, including Sirius B and Procyon B. The positions of stars such as Sirius B and Procyon B on the HR diagram were sufficiently far from the main sequence that they became classified as non-main sequence stars called white dwarfs.

extremely small radius of 0.037 solar radii (modern day measurements produce a value of 0.014 solar radii (Provencal et al. (1998))). The mass of 40 Eridani B was calculated by van den Bos (1926) to be 0.44 solar masses by observing the orbital properties of the binary system (modern day measurements produce a value of 0.573 solar masses (Bond et al. (2017))). The inferred density of 40 Eridani B was therefore extraordinarily large and not comparable to any material known at the time. The stars Sirius and Procyon were also found to have companion stars whose luminosity was extremely low given their temperature, and thus, resided in a similar area of the Hertzsprung-Russell (HR) diagram (Bond (1862); Schaeberle (1896); Adams (1915); Hertzsprung (1915)). Astrometrically derived masses also predicted that both companions were extremely dense and by 1922 Willem Luyten had suggested classifying 40 Eridani B, Sirius B, and Procyon B together as a new type of star called a 'white dwarf' (Luyten (1922); Holberg (2005)). Until the mid 1920's an explanation for the incredible densities of white dwarfs remained elusive (Eddington (1926)). Figure 1.9 highlights the positions of Sirius B and Procyon B in temperature-luminosity space and how white dwarfs in general appear distinct from main sequence stars on the HR diagram due to their high temperatures and low luminosities.

Understanding the properties of white dwarfs

Until the advent of quantum mechanics the predicted properties of white dwarfs were impossible to explain (Eddington (1926)). However, once Sir Ralph Fowler used Fermi-Dirac statistics (Dirac and Fowler (1926); Fermi (1926)) to model the electrons in white dwarfs, rather than assuming the material behaved as a classical ideal gas, the high density of white dwarf material was shown to be theoretically plausible (Fowler (1926)). Intriguingly, white dwarfs are therefore supported against gravitational collapse by electron degeneracy pressure, and thus, the more massive a white dwarf, and hence the stronger the force of gravity acting on it, the smaller the star must be in order to remain in hydrostatic equilibrium. Therefore, unlike regular matter, the index of the radius-mass relationship for a white dwarf is negative (Hamada and Salpeter (1961)). Another coincidence of this property is that white dwarfs have a critical maximum mass which they cannot exceed because their radius cannot shrink indefinitely. This mass was derived to be $\frac{5.728}{\mu^2} M_\odot$ by Subrahmanyan Chandrasekhar in 1935 (Chandrasekhar (1935a); Chandrasekhar (1935b)), where μ is the mean molecular weight per electron for the star. If a stellar core formed above this mass, electron degeneracy pressure would not be able to support it and it would therefore collapse further into either a neutron star (if neutron degeneracy pressure was substantial enough to support it) or a black hole.

The formation and evolution of white dwarfs

A solid understanding of stellar evolution began to develop in the 1950's based on the hypothesis that stellar radiation was produced when stars fused light elements together deep inside their interiors (Sandage and Schwarzschild (1952); Hoyle and Schwarzschild (1955); etc.). This theory improved the understating of the evolution of stars. It implied that stars originate on the Hertzsprung-Russell diagram defined main sequence, then evolve onto the red giant branch, before subsequently evolving onto the asymptotic giant branch, before ultimately becoming white dwarfs. White dwarfs were now understood to be the final stages of stellar evolution for many stars, and their immense densities, high temperatures, and small radii were due to the fact that they are the remnants of stellar cores (Deutsch (1956)). Unlike regular stars, white dwarfs do not fuse material deep inside their interiors in order to generate their luminosity. In fact, white dwarfs have no means of energy production, and therefore, they cool over time and migrate across the HR diagram, thus allowing their cooling age, the length of time the star has been a white dwarf, to be approximated directly
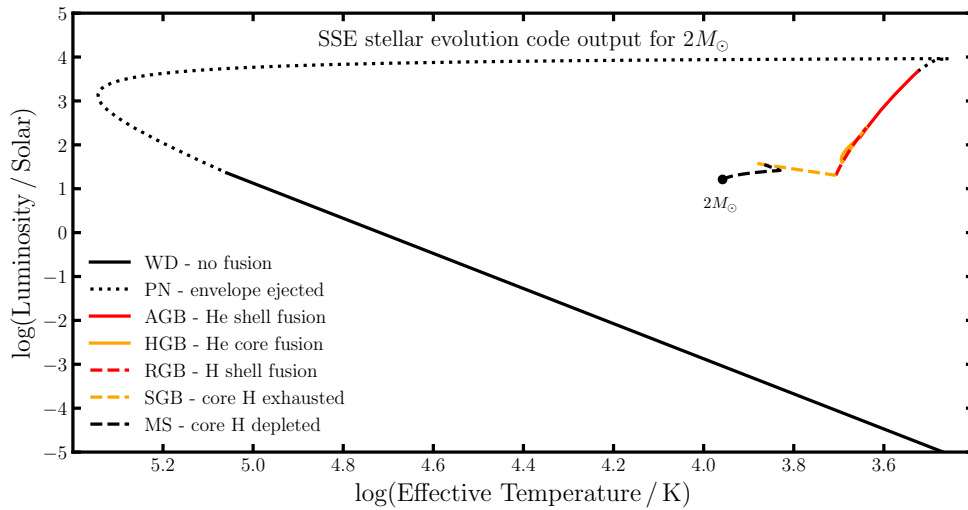
Fig. 1.10 A Hertzsprung-Russell diagram displaying the evolutionary track of a two solar mass solar metallicity star as calculated by the SSE code (Hurley et al. (2013)). White dwarfs are the final stage of stellar evolution and as they age they migrate across the Hertzsprung-Russell diagram.

from their luminosity (Mestel (1952)). Knowing the cooling age of a white dwarf star is extremely useful in multiple fields of astronomy; however, it is particularly useful when attempting to understand metal polluted white dwarfs (see Section 1.3). Figure 1.10 shows the evolutionary track of a two solar mass solar metallicity star as predicted by the single star evolution (SSE) stellar evolution code (Hurley et al. (2000); Hurley et al. (2013)). The evolutionary track of the star moves from the main sequence through the giant branches and eventually to the white dwarf phase, where it then simply cools over time.

The structure and interior of white dwarfs

It is now recognised that the majority of stars in the Milky Way galaxy will end their lives as white dwarfs (Koester (2013); Veras et al. (2016)). Stellar evolution codes predict that all stars below 8-11 solar masses will become white dwarfs (Siess (2007)). The range in maximum initial masses is because the final outcome is dependent on the initial metallicity of the star (Siess (2007)). Stars which will become white dwarfs and are more massive than 6-9 solar masses are predominantly composed of O, Mg, and Ne as their progenitors were massive enough to produce core temperatures high enough to fuse carbon (Siess (2007)). However, the majority of white dwarfs, which
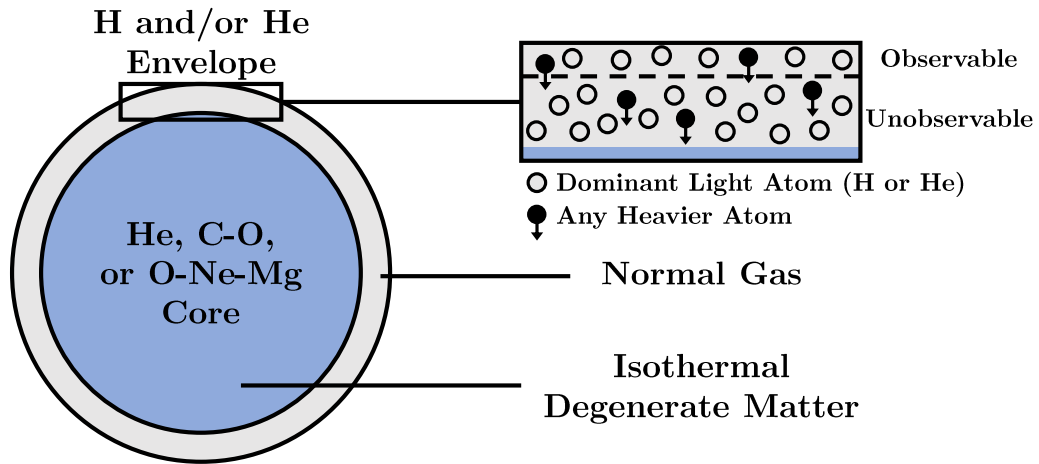
Fig. 1.11 A schematic diagram of a white dwarf highlighting possible interior compositions and how white dwarfs are expected to have observable envelopes which are either purely H or purely He due to their strong gravitational fields causing elemental stratification. Additionally, the majority of a white dwarf's interior is expected to be at the same temperature (Marshak (1940))
.

form from less massive progenitors, are predominantly composed of C and O (Siess (2007)). It is possible for white dwarfs to form which are predominantly composed of He, however, their progenitors must have had masses less than 0.65 solar masses in order for their central temperatures to be insufficient for the onset of He burning (Althaus et al. (2017)). Any He white dwarfs present in the galaxy today must have been part of binary systems, as due to their low masses no such single stars could have exhausted their fuel and reached the post-main sequence given the current age of the universe (Althaus et al. (2017)). Figure 1.11 is a schematic diagram of the interior of a white dwarf highlighting the potential core and envelope compositions expected.

The envelope and spectra of white dwarfs

White dwarfs produce strong gravitational fields which lead to gravitational stratification and therefore the envelope, for the majority of white dwarfs, is composed of a layer of He overlaid by a thin layer of H (Althaus et al. (2010)). However, as some stars undergo late thermal flashes during their post-asymptotic giant branch evolution and burn their remaining H, it is possible for some white dwarfs to form with an envelope composed entirely of He ((Althaus et al. (2010); Koester (2013)). As

well as causing gravitational stratification, the strong gravitational fields also cause any spectral lines present to become pressure broadened. Although it is not always possible, the composition of the upper part of a white dwarf's envelope may be probed by examining the white dwarf's spectra.

White dwarfs are classified into 6 main spectroscopic categories: DA, DB, DO, DC, DQ, and DZ. The spectra of DA white dwarfs are the most common (83% of all spectrally classifed white dwarfs (Montreal White Dwarf Database)) and contain only pressure broadened hydrogen absorption lines; they are therefore thought to correspond to white dwarfs with envelopes composed of a layer of H atop a layer of He (Koester (2013)).

DB white dwarfs are the next most common classification, and their spectra contain only pressure broadened He absorption lines; they are therefore thought to correspond to white dwarfs with purely He envelopes who fused all their remaining H during the post-asymptotic giant branch phase (Koester (2013)).

The spectra of DO white dwarfs contain only pressure broadened ionized He absorption lines, therefore it is expected that they are the progenitors of DB white dwarfs, and transition into such when their surface temperatures drop below 45,000 K (Althaus et al. (2010); Koester (2013)). DO white dwarfs are therefore also expected to have purely He envelopes.

DC white dwarfs have spectra with no absorption features, therefore, it is more difficult to estimate the composition of their upper envelopes. It is expected that when DA white dwarfs cool below 6,000 K or when DB white dwarfs cool below 11,000 K their spectra will become featureless, and therefore they will transition into DC white dwarfs (Koester (2013)). Hence, DC white dwarfs below 11,000 K but above 6,000 K are thought to have helium dominated atmospheres whereas DC white dwarfs below 6,000 K could have either H or He dominated atmospheres.

DQ white dwarfs have spectra dominated by broad carbon absorption features. Cool DQ white dwarfs are thought to be He dominated white dwarfs whose temperature is sufficiently low such that firstly, He absorption lines do not appear, and secondly, their convective envelopes are deep enough to cause the onset of C dredge up, which pulls C into the observable atmosphere. Hot DQ white dwarfs are more difficult to explain, however, it is thought that merger events or unusually thin He envelopes could explain their spectra (Dufour et al. (2008); Althaus et al. (2010)).

DZ white dwarfs (as well as DAZ and DBZ white dwarfs) have spectra which are characterised by strong metal absorption lines, most often Ca, Mg, Fe, and Si. Figure 1.11 highlights that due to the strong gravitational fields generated by white dwarfs

any heavy elements present in the envelope of a white dwarf, regardless of whether the envelope is H or He dominated, will diffuse through the upper envelope due to gravitational settling and become unobservable on timescales much shorter than the white dwarf's cooling age (Fontaine and Michaud (1979); Althaus et al. (2010); Koester (2013)). Gravitational settling readily explains the high frequency of white dwarfs with monoelemental envelopes, however the existence of DZ, DAZ, and DBZ white dwarfs become more difficult to reconcile (Fontaine and Michaud (1979)). A convincing explanation for the existence of white dwarfs with metal absorption lines remained elusive until the early 21st century. In the next section I introduce metal polluted white dwarfs and their study in more detail (Section 1.3).

1.3   Metal polluted white dwarf stars

The history and spectra of polluted white dwarfs

A white dwarf star which is classified spectrally as either DZ, DBZ, or DAZ, and therefore has strong metal absorption lines, is often referred to as a metal polluted white dwarf. The first metal polluted white dwarf was discovered in 1919 when van Maanen's star was shown to have strong Fe and Ca features in its spectra (van Maanen (1919)). In the century since, strong metal absorption lines have been detected in more than one thousand white dwarfs (Weidemann (1960); Zuckerman and Reid (1998); Kepler et al. (2016); Hollands et al. (2017); Coutu et al. (2019)). Figure 1.12 displays the spectra of a DA, DAZ, DB, and DBZ white dwarf. The DA and DAZ spectra are immediately recognisable due to their pressure broadened Balmer lines whose presence indicates that they have H dominated atmospheres. The DAZ star additionally has absorption features caused by ionized Mg, Fe, and Ca. The DB and DBZ spectra are recognisable due to their deep broadened He absorption lines. As well as He lines, the DBZ spectra has a plethora of metal absorption features including strong Ca, Mg, Si, and Fe lines.

Understanding the origin of white dwarf pollution

Due to the strong surface gravity of white dwarfs, metals in their atmospheres should sink and become unobservable on timescales of hundreds to millions of years for He dominated white dwarfs, and on timescales of days to thousands of years for H dominated white dwarfs (Koester (2009)). Therefore, due to the considerable cooling ages of these white dwarfs (of the order millions to billions of years), the metals
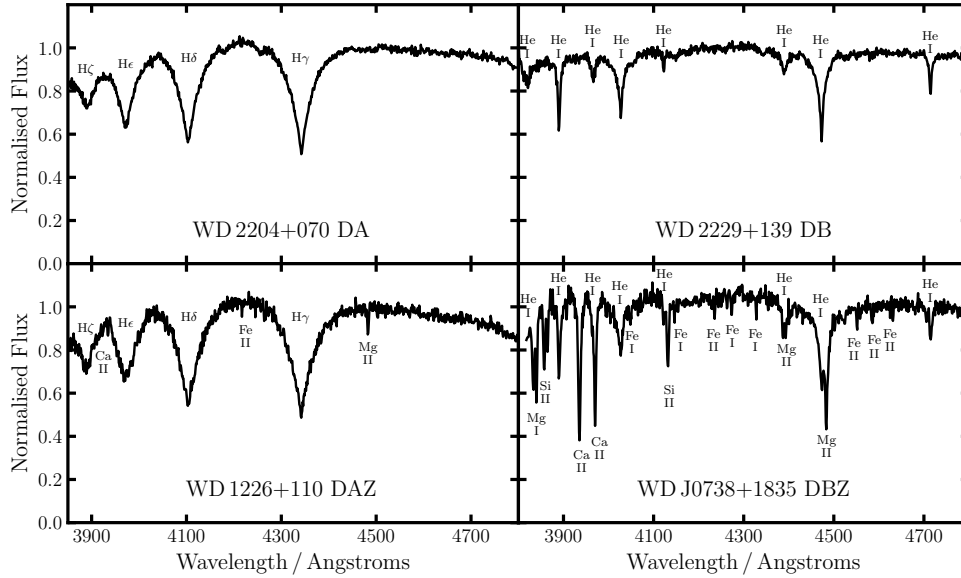
Fig. 1.12 The optical spectra of a DA, DAZ, DB, and DBZ white dwarf. Polluted white dwarfs are easily identified by the strong Ca (and other metal) absorption features in their optical spectra (Spectra from the Montreal White Dwarf Database).

producing the absorption features must have been accumulated in the white dwarf's atmosphere relatively recently and cannot be primordial. Figure 1.13 shows how the sinking timescales of metals in the atmospheres of white dwarfs compare to their cooling ages. For DAZ white dwarfs hotter than 13,000 K the sinking timescales are of the order days therefore the accumulation of metals is not just recent but must in fact be on going, as the probability of catching a white dwarf during this time is negligible.

Initially, the origin of white dwarf pollution was debated, and many theories were proposed in order to explain the metal spectral features. It was originally thought that the features could be produced by the radiative levitation of primordial metals from deeper within the white dwarf, however, although this process was viable for hot white dwarfs it was shown to be impossible for most elements in cool white dwarfs (temperatures lower than $\sim$20,000 K) (Jura and Young (2014); Preval et al. (2019)). Radiative levitation can, however, potentially explain the abundances of Al, C, and Si detected in certain lightly polluted DA white dwarfs down to temperatures as cool as 17,000 K (Chayer and Dupuis (2010); Chayer (2013); Koester et al. (2014)).

The accretion of material from a companion star was ruled out as a mechanism for producing the features, as not only were the abundances shown to be inconsistent with
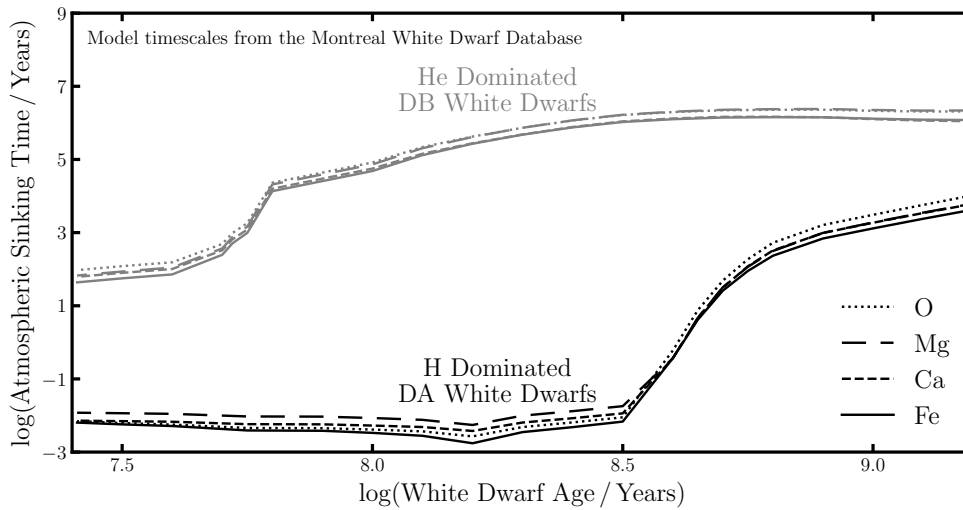
Fig. 1.13 The diffusion timescales for O, Mg, Ca, and Fe plotted as a function of cooling ages for hydrogen dominated white dwarfs and helium dominated white dwarfs. The timescales on which metals diffuse out of white dwarf atmospheres are always orders of magnitude less than the cooling ages of the white dwarf. Therefore, metal polluted white dwarfs must have recently accumulated the metals in their atmospheres' (Model timescales from the Montreal White Dwarf Database).

the accretion of material from a companion star, but the majority of the white dwarf systems which showed pollution were not in close binaries (Jura and Young (2014); Farihi (2016); Veras et al. (2017)). The accretion of the star's own asymptotic giant branch winds due to fallback has been ruled out because any circumstellar gas or grains within a few AU of the star would be removed from the system due to engulfment, radiation pressure, sublimation, or drag forces on a timescale much shorter than the cooling age of the white dwarf (Farihi (2016); Veras (2016)).

Another popular hypothesis to explain the metal features was that the white dwarfs were accreting material from the interstellar medium. A mismatch between the composition of the metals in the white dwarf atmospheres and the interstellar medium (mainly due to the frequency of DBZ white dwarfs with no polluting H), as well as a lack of correlation between the locations and velocities of polluted and non-polluted white dwarfs, ruled out the accretion of interstellar grains (Farihi et al. (2010a)).

It was not just the presence of metals in white dwarf photosphere's which needed an explanation; multiple polluted white dwarfs were also observed to have infrared excesses, and more recently, metal emission features, and time varying brightnesses. The first white dwarf discovered to have an infrared excess was G29-38 (Zuckerman

and Becklin (1987); Graham et al. (1990)). The infrared radiation observed was far above what would be expected to be emitted by the white dwarf; this excess radiation was attributed to the presence of circumstellar dust which absorbed starlight and reemitted in the infrared (Jura (2003); Reach et al. (2005)). Farihi et al. (2009) showed that many of the infrared excesses could be explained by the presence of optically thick narrow black body dust discs around the white dwarfs. Currently nearly 40 polluted white dwarfs have been observed to have confirmed infrared excesses with an additional 30 objects listed as infrared excess candidates (Farihi (2016); Veras (2016); Rebassa-Mansergas et al. (2019); Manser et al. (2020)). Not all polluted white dwarfs have observable circumstellar dust, and the fraction of polluted white dwarfs with dust is of the order of a few percent (e.g. Rebassa-Mansergas et al. (2019)). This is not unexpected as Bonsor et al. (2017) showed that multiple scenarios can cause dust which is present to not be detected.

The first metal emission features were detected by Gänsicke et al. (2006) at the polluted white dwarf WD J1228+1040. The double peaked Ca triplet emission feature is symptomatic of a gaseous disc on a Keplerian orbit and the structure of the feature can be used to calculate the inner radius of the disc (Horne and Marsh (1986)). Manser et al. (2019) used the ∼2 hour variation in the calcium triplet at WD J1228+1040 to infer the presence of a planetesimal orbiting WD J1228+1040. Currently there are seven polluted white dwarfs which are confirmed to have gaseous discs (Gänsicke et al. (2006); Gänsicke et al. (2007); Gänsicke et al. (2008); Gänsicke (2011); Farihi et al. (2012); Melis et al. (2012); Wilson et al. (2014)). The rarity of detectable gaseous discs is not unexpected, as it is thought that the origin of such discs may require the presence of an orbiting planetesimal (Manser et al. (2020)).

Vanderburg et al. (2015) discovered the first transiting material around a polluted white dwarf. The relative brightness of the polluted white dwarf WD 1145+017 was shown to drop by up to 40% and transits were found to occur on a roughly 4.5 hour period (Vanderburg et al. (2015)). The transit profiles, while highly variable, were often found to have a short ingress and a long egress, which is expected if the orbiting material was a dusty disintegrating body (Vanderburg et al. (2015)). More recently a second white dwarf, ZTF J0139+5245, was found to also experience transits (Vanderbosch et al. (2020)). The orbital period of the transiting material around ZTF J0139+5245 was found to be roughly 100 days, thus the material orbiting ZTF J0139+5245 is much further from the host star than the material orbiting WD 1145+017. Figure 1.14 shows the four observed features of polluted white dwarfs introduced here which any
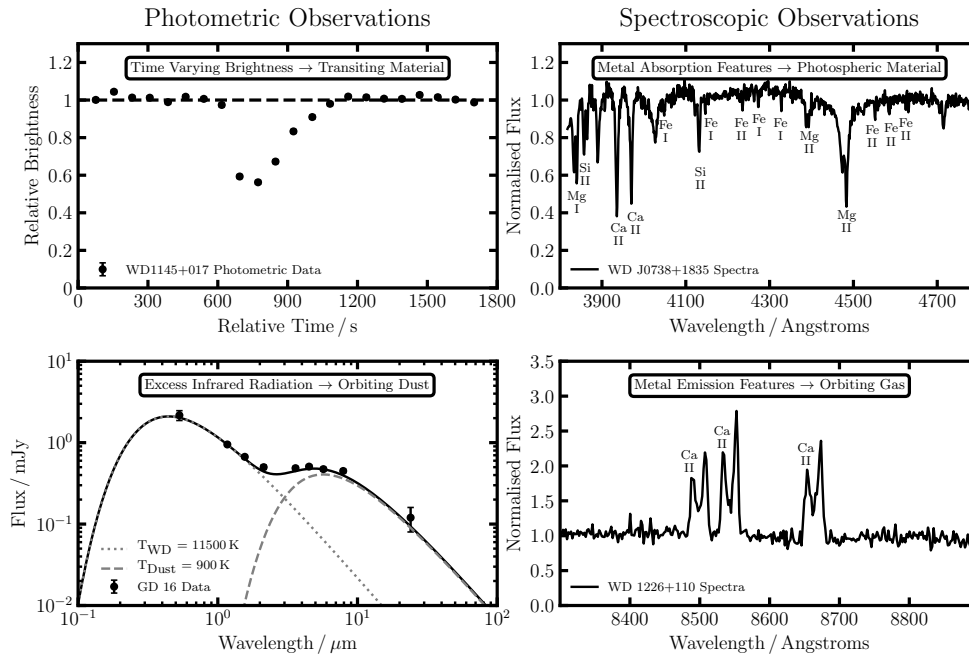
Fig. 1.14 The four main observational methods for observing white dwarf planetary systems. Photometric observations of polluted white dwarfs reveal both transiting material and orbiting dust. Spectroscopic observations show the presence of photospheric metals in white dwarfs and gaseous discs orbiting polluted white dwarfs.

hypothesis for the origin of pollution must explain (data is from Vanderburg et al. (2015), Farihi et al. (2009), and the Montreal White Dwarf Database).

The planetary body accretion hypothesis

The prevailing explanation for white dwarf pollution was first proposed by Debes and Sigurdsson (2002) and Jura (2003). They proposed that white dwarfs were able to maintain metal features in their spectra because they were actively accreting tidally disrupted asteroidal bodies which originated from the remnant planetary systems which orbited them (Jura (2003)). This hypothesis also simultaneously explains the presence of circumstellar dust, gaseous discs, and transiting material around polluted white dwarf stars.

The accretion of planetary material by white dwarf stars is currently thought to be a natural consequence of stellar and planetary evolution. During the post-main sequence evolution of a star, due to the onset of shell burning, the radius of the star can increase until it becomes of the order of astronomical units. Therefore, although

the star will engulf and vaporise any close-in planetary material, any outer planets or outer planetary material present in the system will survive (Vassiliadis and Wood (1993); Veras (2016)). There are currently no confirmed directly detected planets orbiting white dwarfs, however, the presence of an ice giant in a white dwarf system has been implied by the accretion of material rich in H, S, and O onto the star (Gansicke et al. (2019)). Adiabatic stellar mass loss and the shedding of the star's envelope on the giant branch leads to the expansion of planetary orbital radii, and eventually the production of a planetary nebula and a white dwarf (Veras (2016)). Dynamical instabilities and planetesimal scattering caused by surviving planets during the white dwarf phase can lead to planetary bodies being perturbed onto star-grazing orbits (Debes and Sigurdsson (2002); Bonsor et al. (2011); Debes et al. (2012); Veras et al. (2013); Mustill et al. (2018)), where they are likely to become tidally disrupted, form an accretion disc, and be accreted onto the white dwarf (Jura (2008); Veras et al. (2014b); Veras et al. (2015); Malamud and Perets (2020b); Malamud and Perets (2020a)). Outer planetesimal belts are therefore thought to be present in all polluted white dwarf systems, although, none have been directly observed to date (Farihi et al. (2014)).

Figure 1.15 outlines how the tidally disrupted asteroid model broadly explains the current polluted white dwarf observations. Once the minor body is scattered onto a highly eccentric orbit which intercepts the Roche radius of the white dwarf, tidal disruption causes the minor body to be ripped apart (e.g. Veras et al. (2014b)). The fragments of the minor body then collisionally evolve creating a dust disc (e.g. Jura (2008)). Poynting-Robertson drag then causes the dusty material to migrate to inside of the sublimation radius and sublimate (Rafikov (2011a)). The metallic gas produced then, due to its inherent viscosity, loses angular momentum and accretes onto the white dwarf (Rafikov (2011a)). Although the metals will eventually sink out of the white dwarf's observable atmosphere while the accretion event is ongoing the absorption features will remain in the spectra. The lower panel of Figure 1.15 also highlights the predicted architecture of white dwarf planetary systems.

Although it is now accepted that the material accreting onto polluted white dwarfs has a planetary origin, multiple additional mechanisms dissimilar to the scattering by surviving exo-planet mechanism previously outlined have been proposed in order to transport material onto the white dwarf. Wide binary companions (Bonsor and Veras (2015); Hamers and Portegies Zwart (2016); Petrovich and Munoz (2017); Stephan et al. (2017)), the liberation of exo-moons (Payne et al. (2017)), the ohmic heating of asteroids (Bromley and Kenyon (2019)), and the production of planetary impact ejecta (Veras and Kurosawa (2020)) have also been suggested as potential explanations for
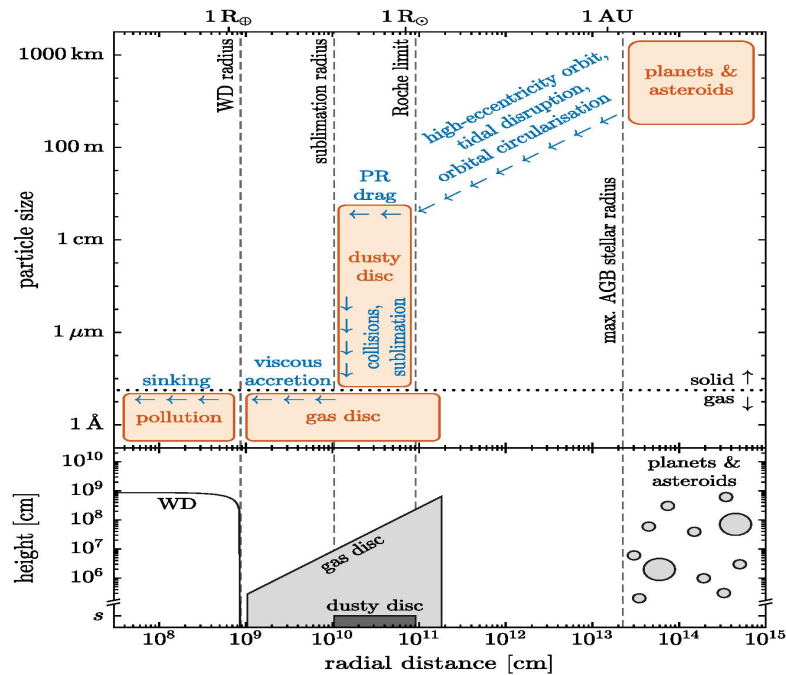
Fig. 1.15 A figure taken directly from van Lieshout et al. (2018) highlighting the current model for white dwarf pollution which can explain the observations of photospheric metals, transits, orbital dust, and gaseous discs in white dwarf systems.

the pollution of white dwarfs. The exact mechanism which dominates the transport of planetary material onto white dwarfs is still debated. However, even without a strong understanding of the exact transport mechanism polluted white dwarfs offer a valuable insight into the composition of exo-planetary material. At present, polluted white dwarfs offer the most direct way to observe the bulk composition of exo-planetary material. Therefore, measuring the chemical abundances of the rocky bodies which accrete onto white dwarfs and pollute their atmospheres presents a method for probing the formation processes and geological processes which occur in exo-planetary systems. Knowledge of the bulk composition of exo-planetary material and the geological processes which occur in exo-planetary bodies is crucial if we hope to understand the interiors of rocky exo-planets, as well as their structure, and eventually their potential to be habitable.

Insights from polluted white dwarfs into exo-planetary systems

Since the acceptance that metal polluted white dwarfs are polluted due to the accretion of exo-planetary material, research has aimed to use polluted white dwarfs to understand

the similarities and differences between exo-planetary material and the planetary material present in the Solar System.

Polluted white dwarf spectral features, when combined with white dwarf atmosphere models, can be used to constrain the abundances of the most important rock-forming elements of the material which has accreted onto the white dwarf (Koester (2009); Koester (2010)). Currently over 200 polluted white dwarf systems have abundance measurements of at least Ca, Fe, and Mg (Jura and Young (2014); Hollands et al. (2017)) and so far a total of 20 different metal elements have been detected in the atmospheres of polluted white dwarfs: C, N, O, Na, Mg, Al, Si, P, S, Ca, Sc, Ti, V, Cr, Mn, Fe, Co, Ni, Cu, and Sr (Jura et al. (2012); Xu et al. (2013); Xu et al. (2017)). As with all the rocky bodies in the Solar System, the accreted planetary material observed thus far have abundances dominated by Mg, Fe, Si, and O, possibly hinting that Solar System-like geologies are common in the galaxy and exotic geologies such as those suggested in Section 1.1.3 may be rare (Jura and Young (2014)).

The relationship between the atmospheric metal abundances and the metal abundances of the accreted material depends on the phase of accretion the white dwarf is in and is vitally important when using polluted white dwarfs to probe the composition of exo-planetary material (Koester (2009)). Initially, as the material accumulates in the white dwarf's atmosphere, the abundances of the atmosphere resemble the abundances of the polluting material (build-up phase). However, as time passes material begins to sink out of the upper convective zone and becomes unobservable. Eventually, accretion onto the white dwarf and diffusion from the upper convective zone reaches a steady state, and the abundances of the atmosphere are related to the abundances of the accreting material in a manner dependent on the individual element's diffusion timescale (steady state phase). Finally, once accretion has ceased the white dwarf enters a declining phase where material simply sinks out of the upper convective zone, and the abundances of the atmosphere are related to the abundances of the accreting material by a different expression, which is again dependent on the individual element's diffusion timescale. A full mathematical description of the Koester (2009) diffusive model will be described in Chapter 2. Arguments against the validity of such a diffusion model have been proposed by Deal et al. (2012) and Bauer and Bildsten (2018), who suggest thermohaline mixing could potentially stop a white dwarf from ever reaching a steady state of accretion and that the atmospheric abundances are identical to that of the accreting material unless accretion has finished. Koester (2014) argued against this suggesting that diffusive equilibrium would be reached before the thermohaline mixing could develop.

Evidence for the accretion of fragments of differentiated bodies onto white dwarfs has emerged due to the detection of pollutant bodies with high abundances in either the siderophilic elements or the lithophilic elements relative to the Solar System (Zuckerman et al. (2011); Xu et al. (2013); Farihi et al. (2013); Wilson et al. (2015)). Hollands et al. (2018) also found evidence for white dwarfs accreting fragments of differentiated planetesimals when they examined the abundances of 230 DZ white dwarfs and found that some of the systems presented in Hollands et al. (2017) had extreme Fe abundances. The accretion of differentiated fragments is expected, as not only do we find such bodies in the Solar System's meteorite suites (Wiik (1956); Scott and Wasson (1975); Section 1.1.1), but models of the collisional evolution of protoplanets predict a population of such fragments (Marcus et al. (2009); Carter et al. (2015); Carter et al. (2018)).

Evidence for the accretion of water ice in four systems has been based on an excess abundance of observed oxygen compared with that which could be sequestered in the form of metal oxides using the observed metal abundances (Dufour et al. (2012); Farihi et al. (2013); Raddi et al. (2015); Xu et al. (2017)). However, the majority of systems have been found to have pollutants whose abundances are dry and volatile-poor (Jura et al. (2012); Xu et al. (2013)). The accretion of water ice is not surprising though, as ice species are expected to survive the post-main sequence evolution of the host star (Jura and Xu (2010b); Malamud and Perets (2016)).

The masses of the bodies which pollute white dwarfs are difficult to constrain. The mass of metals in the convective zone can be found using the spectral features and white dwarf atmospheric models (Koester (2009); Koester (2010)). Farihi et al. (2010a) and Girven et al. (2012) found that the mass of metals in cool white dwarf convective zones ranges from 10^{16} to 10^{22} kg (using the Ca abundance and assuming a bulk Earth composition for the pollutants). However, the mass of metals in the convective zone is not equivalent to the mass of the polluting body or bodies, as some of the mass may still be in the accretion disc and, depending on the length of time that the body has been accreting onto the white dwarf, some of the mass may have sunk out of the upper convective zone and no longer be observable. Under the assumption that the pollutants are a single body, the range of masses derived by Farihi et al. (2010a) and Girven et al. (2012) can be taken as lower limits to the mass of the planetary bodies accreted. Thus, it is currently hypothesised that the pollutants have masses similar to large Solar System asteroids. The extremely depleted, relative to stellar, carbon abundances of polluted white dwarfs have also been used to conclude that the pollutant bodies are asteroidal in nature (Jura (2006)) and constraints for the diameters of the planetesimals in orbit around WD J1228+1040 and WD 1145+017, of $\sim$300 km and

$\sim$400 km respectively add further weight to this conclusion (Vanderburg et al. (2015); Gurri et al. (2017); Veras et al. (2017); Manser et al. (2019)).

The exact nature of the 'discs' around white dwarfs is not yet understood, particularly the lifetimes of such discs (Farihi (2016)). The disc lifetimes have been estimated observationally using the mass currently in DBZ white dwarf atmospheres and the mass accretion rates of DAZ white dwarfs. Using this method Girven et al. (2012) found the disc lifetimes to be of the order of 10^4 to 10^6 years which is consistent with theoretical estimates of white dwarf accretion discs (Rafikov (2011a); Rafikov (2011b)). However, Wyatt et al. (2014) used the variance of observed accretion rates for both hot and cool DAZs to estimate that the disc lifetimes must be shorter than $\sim 10^3$ years, as otherwise no variation would be seen. Constraining the lifetimes of white dwarf discs more precisely is vital if we want to understand not only the nature of the discs but the relationship between the composition of the polluted white dwarf atmospheres and the exo-planetary bodies they have accreted. Other than the disc lifetimes and pollutant body masses, other areas of study which would be valuable to better understand are the frequency of pollutant bodies which are expected to be fragments of differentiated bodies and the frequency of bodies which pollute white dwarfs as a function of radial distance from the star. Evaluating the statistical significance of the conclusions regarding the origin and geology of the exo-planetary material which pollutes white dwarfs is also an area of the field which requires further research.

1.4 Thesis layout

In this thesis I present the research I have carried out regarding the constraints polluted white dwarfs can place on the composition and origin of exo-planetary bodies. In Chapter 2, I outline the model I have created and the statistical framework I have utilised in order to constrain the origin and geology of exo-planetary material using polluted white dwarfs. The most heavily polluted white dwarf systems are individually analysed using the model in Chapter 3. In Chapter 4, I outline and discuss the results of the model when applied to the population of 230 white dwarfs whose abundances were found in Hollands et al. (2017). The specific use of the Mn/Na abundance ratio of pollutant material and the constraints it can offer on post-nebula volatilisation is presented in Chapter 5. Chapter 6 explores the potential for planetesimal formation temperature to have an effect on the exo-planet mass radius relation. In Chapter 7, I conclude the results of my thesis and highlight the areas of future study which I believe to be vital to the future of polluted white dwarf research.

Chapter 2

Modelling the metal abundances present in polluted white dwarf atmospheres

2.1 Introduction

If one wishes to understand the similarities between the Earth and the host of recently discovered rocky exo-planets, understanding the bulk composition and internal structure of rocky exo-planetary bodies is crucial. As introduced in Section 1.1.3, for rocky exo-planets, the bulk parameters which astronomers are currently able to constrain are not sufficient to robustly deduce the interior compositions or structures of the bodies. The composition of the atmospheres of polluted white dwarfs offer a unique insight into the composition of exo-planetary bodies. As introduced in Section 1.3, metal polluted white dwarfs become polluted when they accrete rocky planetary material and therefore their spectral features can be used to derive the bulk composition of extrasolar planetary material. The composition of this material can then be used to provide insights into the composition and structure of exo-planetary bodies in an analogous manner to how the Solar System meteorite suites furthered the understanding of the composition and structure of the Earth. In this chapter I outline the model I have created in order to reproduce and fit the derived polluted white dwarf atmospheric abundances. Modelling and fitting the atmospheric abundances will enhance both our understanding of how planetary bodies inherit their bulk compositions as well as granting insights into the similarities between Solar System bodies and exo-planetary

bodies, while also placing constraints on the temperatures experienced by the bodies, the geological and collisional histories of the bodies, and the mass of the bodies.

In Section 2.2, I outline the model which calculates the composition of extrasolar planetesimals. The model is dependent on the initial composition of the protoplanetary disc in which the planetesimals formed, the thermodynamic conditions at which they formed, and their geological and collisional history. In Section 2.3, I outline how these planetesimal compositions must be adjusted in order to compare them with the compositions derived for polluted white dwarf atmospheres. In Section 2.4, I discuss the various statistical techniques which can be used in order to constrain model parameters, compare models, and assess the quality of the model fits. In Section 2.5, I test the model by attempting to reproduce the compositions of various Solar System bodies in order to substantiate the validity of the assumptions made. A full discussion of the assumptions and outcomes of the model is presented in Section 2.6 and the conclusions of this chapter are summarised in Section 2.7.

2.2 Modelling planetesimal abundances

2.2.1 The initial composition of the planetesimal forming disc

As outlined in Section 1.1, the composition of the stellar nebula in which planetesimals, and eventually planets, form in plays a vital role in determining the bulk composition of the planetary bodies. Therefore, if one wishes to understand the expected composition of extrasolar planetesimals it is vital to understand the frequency and magnitude of the compositional variation expected in planet forming stellar nebulae. Theoretically the compositional variation in stellar nebulae and protoplanetary systems are difficult to model as the composition of a star's environment is dictated by many, potentially stochastic, factors including the proximity and frequency of supernovae, Wolf-Rayet stars, and giant branch stars (Brennecka et al. (2013)). For certain spectral types, and stars of a certain age range, there is a strong negative correlation between formation age and metallicity, however, at ages below 10 Gyrs there is often no strong correlation (Feltzing et al. (2001); Rebassa-Mansergas et al. (2016); Lin et al. (2018)). In order to model the possible compositional variation in stellar nebula, rather than attempt to model complex galactic chemical evolution, I simply consider that the composition of nearby stars is representative of the potential chemical diversity expected. Nearby FGK stars were chosen for the model because it allows us to maintain the same approximate formation age as the polluted white dwarf progenitors (which were most
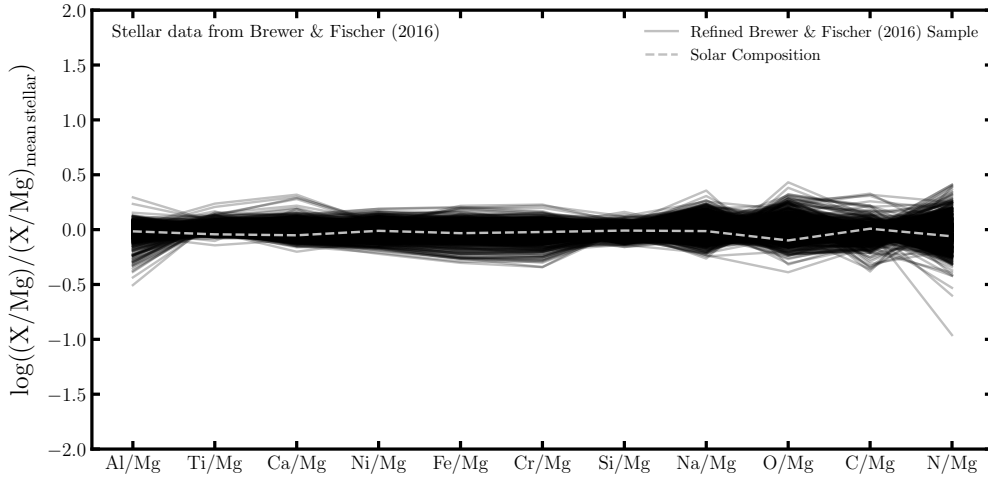
Fig. 2.1 The abundances of the refined sample of stars from Brewer et al. (2016). Compositionally the Sun appears to be an average star, however, there is variation in the stellar photospheric abundances derived by Brewer et al. (2016) of approximately 0.2 dex in most elements, which is significant given the abundances are measured to an uncertainty of ∼0.02 dex.

likely earlier spectral types), thus, if there is any potential correlation between age and metallicity it will be accounted for. The chosen catalogue is that of Brewer et al. (2016), who observed the abundances of 1617 nearby FGK type stars. The 1617 stars in the catalogue were reduced to 958 by removing any known giant branch stars, any stars with spurious spectra, any stars with $\log(g)$ less than 3.5, and any stars whose signal to noise ratio was less than 100. This reduction was performed in order to avoid contamination by unreliable data and stars which have potentially evolved atmospheric abundances, and are thus not representative of the initial stellar nebula conditions. I chose to remove stars with $\log(g)$ less than 3.5 because stars with a $\log(g)$ value below this cut off are likely to be evolved and potentially on the giant branches, therefore the dredging up of the products of nuclear fusion may be occurring and their atmospheric abundances may be dissimilar to the original stellar nebula abundances.

Figure 2.1 compares the range of abundances in the Brewer et al. (2016) sample to the solar photosphere abundances. The x axis is displayed in volatility order, increasing from left to right. The y axis is normalised to the mean value of each elemental abundance in the Brewer et al. (2016) sample. The catalogue includes abundances of Al, Ti, Ca, Ni, Mg, Fe, Si, Cr, Na, O, C, N, Mn, V, and Y, however, Mn, V, and Y will not be used in the model outlined in this chapter as not only do very

few white dwarf atmospheres have constraints on those elements but the equilbiurm chemistry model outlined in the next section (Section 2.2.2) does not include all of their major species. Figure 2.1 shows that on average the majority of stars in the Brewer et al. (2016) catalogue are compositionally similar to the Sun. However, the abundances of most elements can vary from approximately 1.5 times solar to 0.5 times solar. The abundances plotted in Figure 2.1 will be used as initial conditions for the model and will be taken as the range of possible initial nebula compositions for the progenitors of observed polluted white dwarfs. In this thesis I choose to model the complex compositional variation only using one parameter, the stellar metallicity index ($[Fe/H]_{index}$), which is defined as the rank of the metallicity in the sample from 0 (the lowest metallicity) to 957 (the highest metallicity)).

2.2.2   The condensation of planetesimals from a protoplanetary disc

In order to calculate the compositional variation expected in exo-planetary material I assume that exo-planetary bodies form via the aggregation of smaller bodies which condense directly out of the protoplanetary disc in chemical equilibrium. This is an extremely simplistic assumption as it ignores the complex processes involved in planet formation as well as planetary migration and vertical mixing in the disc. However, such models have been shown to reproduce the compositions of Solar System bodies to first order (Moriarty et al. (2014)). To calculate the compositions of exo-planetesimals I take the stellar nebula compositions outlined in Section 2.2.1 and employ a Gibbs free energy minimisation model (HSC Chemistry v.8.) which yields the abundances expected for the solids which condense from the protoplanetary disc as a function of temperature and pressure. Utilising the Chambers (2009) protoplanetary disc model not only allows the relevant temperatures and pressures to be estimated but also links these temperatures and pressures to formation locations and formation times in the disc. In the following sections I first outline the protoplanetary disc model, then the Gibbs free energy minimisation model, before finally outlining the planetesimal formation model.

Viscous Irradiated Protoplanetary Disc Model

The pressure-temperature space in which to perform the equilibrium chemistry calculations was determined by using the theoretical model derived in Chambers (2009), which models the pressure-temperature space in an evolving, viscous, irradiated disc.

This model has been previously used in the literature for the modelling of planetesimal formation in protoplanetary discs (Moriarty et al. (2014)). The Chambers model is a disc model with an alpha parameterisation which divides the disc into three sections; an inner viscous evaporating region, an intermediate viscous region, and an outer irradiated region. In Chambers (2009) the model parameters were set up to correspond to the second example in Stepinski (1998), which is consistent with a planetesimal forming disc around a solar mass star. In this work, as the aim is to model the progenitors of polluted white dwarfs, the parameters were modified from the solar values to that of an A0 type star. A0 type parameters were chosen because the progenitors of stars which are currently white dwarfs were most likely A type main sequence stars (Veras et al. (2016)). The parameters were modified using the stellar evolution curves in Siess et al. (2000) and the stellar mass protoplanetary disc mass relation given in Andrews et al. (2013). For all calculations in this work, unless noted otherwise, I use $M_0 = 0.1 M_*$, $s_0 = 33\,\mathrm{au}$, $R_{*,0} = 4.4 R_\odot$, $T_{*,0} = 4745\,K$, $\kappa_0 = 0.3\,m^2 kg^{-1}$, $\alpha = 0.01$, $\gamma = 1.7$, $\mu = 2.4$, and $M_* = 2.34 M_\odot$. Where M_0 is the initial mass of the disc, s_0 is the initial radius of the disc, $R_{*,0}$ is the initial radius of the star, $T_{*,0}$ is the initial temperature of the star, κ_0 is the opacity in the irradiated portion of the disc, α is the alpha viscosity parameter of the disc, γ is the adiabatic index of the disc, μ is the mean molecular weight of the disc, and M_* is the mass of the star.

The inner viscous evaporating region

The inner viscous evaporating region has a surface density given by

$$\Sigma(t_{\text{formation}}, d_{\text{formation}}) = \Sigma_{evap} \left(\frac{d_{\text{formation}}}{s_0} \right)^{-\frac{24}{19}} \left(1 + \frac{t_{\text{formation}}}{\tau_{vis}} \right)^{-\frac{17}{16}} \qquad (2.1)$$

where

$$\Sigma_{evap} = \Sigma_{vis} \left(\frac{T_{vis}}{T_e} \right)^{\frac{14}{19}} \qquad (2.2)$$

$d_{\text{formation}}$ is the radial location in the disc, $t_{\text{formation}}$ is the length of time the disc has been evolving and $T_e = 1380\,K$. The opacity in the inner viscous evaporating region follows the power law described in Stepinski (1998).

The temperature in the viscous evaporating inner region is given by

$$T(t_{\text{formation}}, d_{\text{formation}}) = T_{vis}^{\frac{5}{19}} T_e^{\frac{14}{19}} \left(\frac{d_{\text{formation}}}{s_0} \right)^{-\frac{9}{38}} \left(1 + \frac{t_{\text{formation}}}{\tau_{vis}} \right)^{-\frac{1}{8}} \qquad (2.3)$$

and the transition radius to the intermediate viscous region is

$$r_e(t) = s_0 \left(\frac{\Sigma_{evap}}{\Sigma_{vis}} \right)^{\frac{95}{63}} \left(1 + \frac{t_{\text{formation}}}{\tau_{vis}} \right)^{-\frac{19}{36}}. \tag{2.4}$$

The intermediate viscous region

The surface density in the intermediate viscous region is

$$\Sigma(t_{\text{formation}}, d_{\text{formation}}) = \Sigma_{vis} \left(\frac{d_{\text{formation}}}{s_0} \right)^{-\frac{3}{5}} \left(1 + \frac{t_{\text{formation}}}{\tau_{vis}} \right)^{-\frac{57}{80}} \tag{2.5}$$

where

$$\Sigma_{vis} = \frac{7 M_0}{10 \pi s_0^2} \tag{2.6}$$

and the temperature in the intermediate viscous region is

$$T(t_{\text{formation}}, d_{\text{formation}}) = T_{vis} \left(\frac{d_{\text{formation}}}{s_0} \right)^{-\frac{9}{10}} \left(1 + \frac{t_{\text{formation}}}{\tau_{vis}} \right)^{-\frac{19}{40}} \tag{2.7}$$

where

$$T_{vis} = \left(\frac{27 \kappa_0}{64 \sigma} \right)^{\frac{1}{3}} \left(\frac{\alpha \gamma k}{\mu m_H} \right)^{\frac{1}{3}} \left(\frac{7 M_0}{10 \pi s_0^2} \right)^{\frac{2}{3}} \left(\frac{G M_*}{s_0^3} \right)^{\frac{1}{6}} \tag{2.8}$$

and

$$\tau_{vis} = \frac{1}{16 \pi} \frac{\mu m_H \Omega_0 M_0}{\alpha \gamma k \Sigma_{vis} T_{vis}} \tag{2.9}$$

and the transition radius between the intermediate viscous region and the outer irradiated region is

$$r_t(t) = s_0 \left(\frac{\Sigma_{rad}}{\Sigma_{vis}} \right)^{\frac{70}{33}} \left(1 + \frac{t_{\text{formation}}}{\tau_{vis}} \right)^{-\frac{133}{132}}. \tag{2.10}$$

The outer irradiated region

The surface density in the outer irradiated region is

$$\Sigma(t_{\text{formation}}, d_{\text{formation}}) = \Sigma_{rad} \left(\frac{d_{\text{formation}}}{s_0} \right)^{-\frac{15}{14}} \left(1 + \frac{t_{\text{formation}}}{\tau_{vis}} \right)^{-\frac{19}{16}} \tag{2.11}$$

where

$$\Sigma_{rad} = \Sigma_{vis} \frac{T_{vis}}{T_{rad}} \tag{2.12}$$

and

$$T_{rad} = \left(\frac{4}{7}\right)^{\frac{1}{4}} \left(\frac{T_{*,0}R_{*,0}k}{GM_*\mu m_H}\right)^{\frac{1}{7}} \left(\frac{R_{*,0}}{s_0}\right)^{\frac{3}{7}} T_{*,0} \tag{2.13}$$

and the temperature in the outer irradiated region is

$$T(t_{\text{formation}}, d_{\text{formation}}) = T_{rad} \left(\frac{d_{\text{formation}}}{s_0}\right)^{-\frac{3}{7}}. \tag{2.14}$$

To convert the surface density profile into a pressure profile I have assumed the disc is an ideal gas with a Gaussian density profile. The surface density is converted into a pressure as follows: as

$$P = \frac{k\rho T}{\mu m_H} \tag{2.15}$$

and

$$\int \rho \, dz = \Sigma \tag{2.16}$$

and I assume that

$$\rho = \rho_0 e^{-\frac{z^2}{2H^2}} \tag{2.17}$$

I therefore find that

$$\Sigma = \rho_0 H \sqrt{2\pi} \tag{2.18}$$

hence the pressure at the midplane is

$$P = \frac{k\Sigma T}{\mu m_H H \sqrt{2\pi}}. \tag{2.19}$$

Using the standard formulae

$$c_s^2 = \frac{kT}{\mu m_H} \tag{2.20}$$

$$H = \frac{c_s}{\Omega} \tag{2.21}$$

$$\Omega = \sqrt{\frac{GM_*}{d_{\text{formation}}^3}} \tag{2.22}$$

I find that the relationship between the pressure profile and the surface density profile is

$$P = \sqrt{\frac{GM_*k\Sigma^2 T}{2\pi\mu m_H d_{\text{formation}}^3}}. \tag{2.23}$$
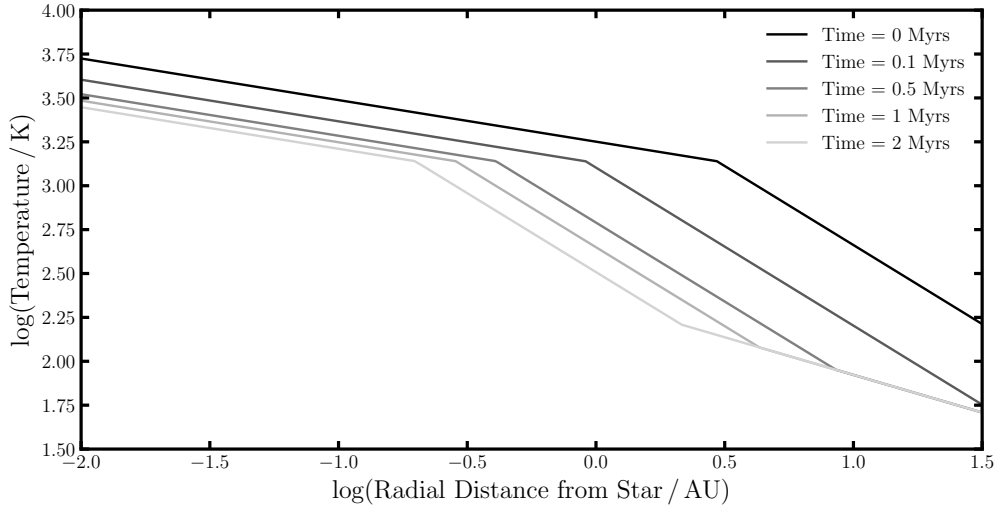
Fig. 2.2 Midplane temperature as a function of radial distance in a protoplanetary disc around an A0 type star as derived by the Chambers (2009) analytical model.

The Pressure-Temperature space mapped out by this evolving disc is displayed in Figure 2.2, Figure 2.3, and Figure 2.4.

Equilibrium chemistry condensation model

To recreate the expected abundances present in extrasolar planetesimals I employ a Gibbs free energy minimisation model at the pressures and temperatures expected to be present in a protoplanetary disc (calculated as presented previously). I assume that the composition of the solid bodies that condensed out of the disc, at various times and at various locations according to the equilibrium chemistry model, have abundances which when combined together produce the abundances expected for extrasolar planetesimals. Other processes involved in the formation of planetesimals during grain growth, like migration and mixing, are ignored as it is not expected that they will drastically change the bulk chemistry of the planetesimal. The caveats of this assumption are discussed in Section 2.6. The assumptions are validated by the fact that this method has been shown to reproduce the bulk composition of the terrestrial planets in the Solar System and the abundances of Solar System primitive meteorites (Moriarty et al. (2014)). Additionally in Section 2.5 I will again provide evidence that such a model can reproduce the abundances of the rocky worlds in the Solar System.

The equilibrium chemistry model used to find the composition of the material that condenses out of a protoplanetary disc was HSC chemistry version 8. It was set up in
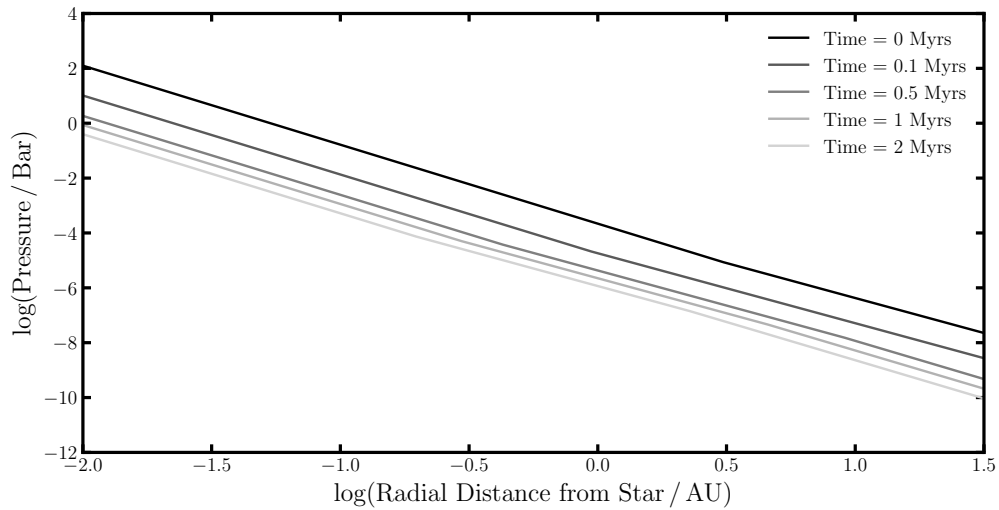
Fig. 2.3 Midplane pressure as a function of radial distance in a protoplanetary disc around an A0 type star as derived by the Chambers (2009) analytical model.
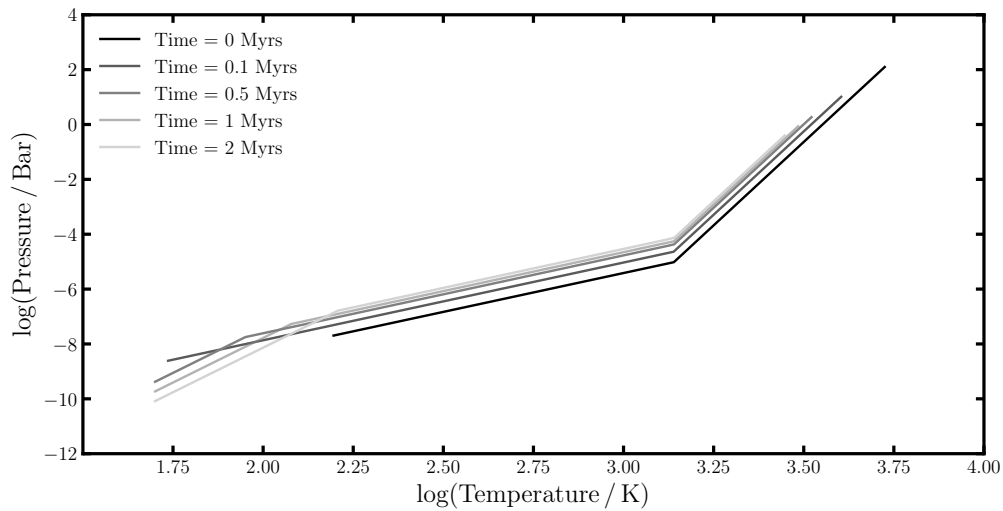
Fig. 2.4 The Temperature-Pressure space possible in the midplane of an evolving protoplanetary disc around an A0 type star as derived by the Chambers (2009) analytical model.

the same way as Moriarty et al. (2014) and Bond et al. (2010), which both used the software to model planetesimal compositions. The gaseous elements inputted, the list of gaseous species included in the model, and the list of solid species included in the model are displayed in Table 2.1, Table 2.2, and Table 2.3 respectively. The stellar abundances referenced to in Section 2.2.1 are used as inputs and represent the initial gaseous abundances.

The species included are the same as those considered in Bond et al. (2010). All solids are in pure form and no solid solutions were included. The elements modelled in this study include the 14 most abundant elements in the rocky debris in the Solar System and include the elements which are expected to be the most abundant in the galaxy. Therefore, I assume that these elements will also be the most important when forming extrasolar rocky bodies. This assumption is validated by the findings of Section 2.2.1, which showed the variation in initial stellar nebula compositions to be small, but non-negligible, and centered on solar abundances. The list of compounds included was selected by Bond et al. (2010) after the included species were found to be the most commonly occurring and important over the pressure-temperature space expected in protoplanetary discs. The list is limited by HSC chemistry's database. There are two categories of major species which are not included in HSC Chemistry's database whose inclusion would possibly alter the results. The first category of major species missing are common ice species such as: NH_3, N_2, CO, CO_2, CH_3OH, and CH_4. However, as the formation of C and N ices occurs at lower temperatures than the formation of water ice (even if clathrate species of those ices are included) in protoplanetary disc conditions (Marboeuf et al. (2014)) HSC Chemistry should predict the elemental abundances of condensed solids accurately, unless the bodies formed well beyond the water ice line such that C and N ices could start condensing from the disc. In order to mitigate this issue, I model the formation of bodies in the outer disc by additionally implementing the formation of C and N ice species using the condensation curves derived in Marboeuf et al. (2014). The second category of major species missing are the complex carbon macromolecules which are found in many asteroids and meteorites (Pizzarello et al. (2006)). This is a more difficult problem to overcome as the formation mechanism of carbonaceous matter in asteroids, especially complex macromolecules, is not yet understood. Organic material identified in meteorites suggest they were formed in radiation shielded environments and in the presence of liquid water (Glavin and Dworkin (2009)). Taking this into account one must be careful when predicting abundances of solid state C as it may be present in solid species when the model suggests it would not be. However, once conditions are cold enough for the formation

Table 2.1 The gaseous elements which were included in the equilibrium chemistry code, HSC chemistry v. 8.

Gaseous Elements Included							
H	He	C	N	O	Na	Mg	Al
Si	P	S	Ca	Ti	Cr	Fe	Ni

Table 2.2 The list of possible gaseous species which could form in the equilibrium chemistry code, HSC chemistry v. 8.

Gaseous Species Included							
Al	CrO	MgOH	PN	AlH	CrOH	MgS	PO
NS	SO	CH_4	FeS	Na	SO2	CN	HC
Ca	HPO	NiH	SiP	CaH	HS	Cr	MgH
P	TiO_2	CrN	MgO	CaS	Mg	O	TiN
CrS	C	FeOH	H_2O	Ni	SiO	TiO	CrH
N_2	Al_2O	AlOH	FeH	NH_3	S_2	Na_2	Si
CO_2	HCN	NaO	SiH	NiO	SiP_2	CaO	H_2S
NiS	Ti	PH	TiS	AlS	FeO	NO	SN
PS	Fe	S	H_2	NaH	SiC	SiS	CaOH
HCO	NaOH	SiN	AlO	S	O_2	N	MgN
CO	NiOH	CP	He				

of all the major C ice species the modelled C abundances would be valid. With this in mind I do not use the abundance of C when fitting the modelled chemical abundances to the data, unless the planetesimal C abundance is similar to that of stellar C abundances and can therefore be used to constrain the formation to being beyond the C ice line.

Figure 2.5, Figure 2.6, and Figure 2.7 show how the fraction of each element in solid state relative to gaseous state changes as a function of temperature in the protoplanetary disc at various formation times when a solar nebula gas initial composition is inputted into the equilibrium chemistry model. The figures illustrate how the model can reproduce the expected condensation series found in much more advanced simulations (Lodders (2003); Lodders (2010)). I find that in accordance with Lodders (2003) the elements condense out of the disc into solid species at roughly the temperatures expected and in the correct order. The refractory elements Al, Ca, and Ti condense out of the disc at temperatures in excess of 1,400 K while the moderately volatile elements Ni, Mg, Fe, Si, and Cr all condense out of the disc at ~1,300 K. Na is a volatile element and condenses out at ~1,000 K. C and N are extremely volatile species and only condense out of the disc at temperatures below 125 K, however, I again note that the trend for C has many caveats and is only used as a guide for a limit on

Table 2.3 The list of possible solid species which could form in the equilibrium chemistry code, HSC chemistry v. 8.

Solid Species Included			
Al_2O_3	$FeSiO_3$	$CaAl_2Si_2O_8$	C
SiC	Ti_2O_3	Fe_3C	Cr_2FeO_4
$Ca_3(PO_4)_2$	TiN	$Ca_2Al_2SiO_7$	Ni
P	Fe_3O_4	CaS	Si
$MgSiO_3$	Cr	H_2O	$CaMgSi_2O_6$
Fe_3P	$CaTiO_3$	Fe	AlN
$MgAl_2O_4$	$Mg_3Si_2O_5(OH)_4$	MgS	$CaAl_{12}O_{19}$
TiC	FeS	Mg_2SiO_4	Fe_2SiO_4
$NaAlSi_3O_8$			

formation conditions. O is a difficult element to classify as it initially condenses out of the disc with the refractories, as they condense out in their oxide form, it then condenses out further with the emergence of the moderate volatiles, however, it does not fully condense out of the disc until the temperatures drop below 200 K and water ice forms. Therefore, although O makes up a large fraction of all solid species which condense out of protoplantary discs when its overall abundance in solid material is compared with stellar abundances O still behaves like an extreme volatile.

Figure 2.8 highlights the condensation sequence derived and the relevant groupings of elements in condensation temperature space. The physical reason the elements condense out in this order is due to the compounds that most readily form at the pressures and temperatures seen in a protoplanetary disc, and the readiness of those compounds to be in the gaseous or solid phase under those conditions. The condensation series presented here, for solar elemental abundances, holds over the stellar compositional range outlined in Section 2.2.1.

Planetesimal formation model

If one simply used the results from the equilibrium condensation model as a proxy for the composition of exo-plantesimals it would be equivalent to assuming that the body formed at a single pressure and temperature, corresponding to a single radial location and single time in the protoplanetary disc. In reality a large planetesimal or minor planet will incorporate material from a range of formation locations therefore using the condensation results directly may not be valid. In order to account for this I instead assume that the material that forms a given planetesimal originates at a single time but from a range of formation locations described by a Gaussian distribution. The mean
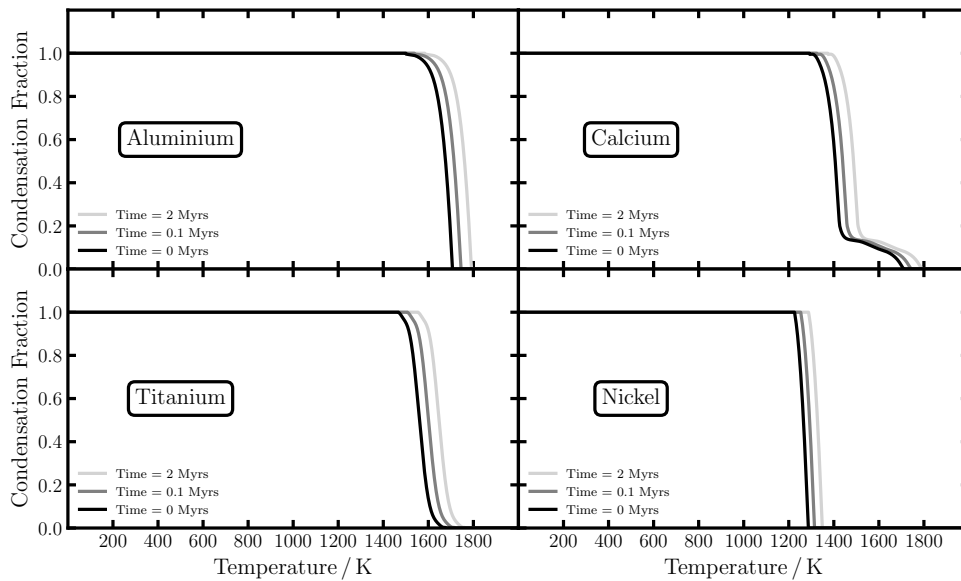
Fig. 2.5 The fraction of Al, Ti, Ca, and Ni which are in solid species rather than gaseous species as a function of formation temperature for various formation times as calculated by HSC Chemistry when an initially solar composition gas was inputted.
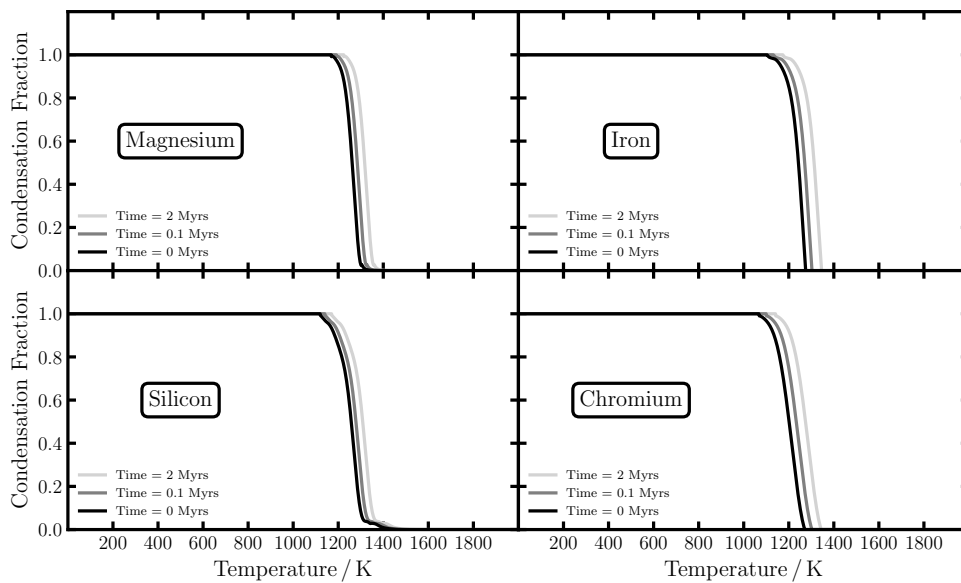
Fig. 2.6 The fraction of Mg, Fe, Si, and Cr which are in solid species rather than gaseous species as a function of formation temperature for various formation times as calculated by HSC Chemistry when an initially solar composition gas was inputted.
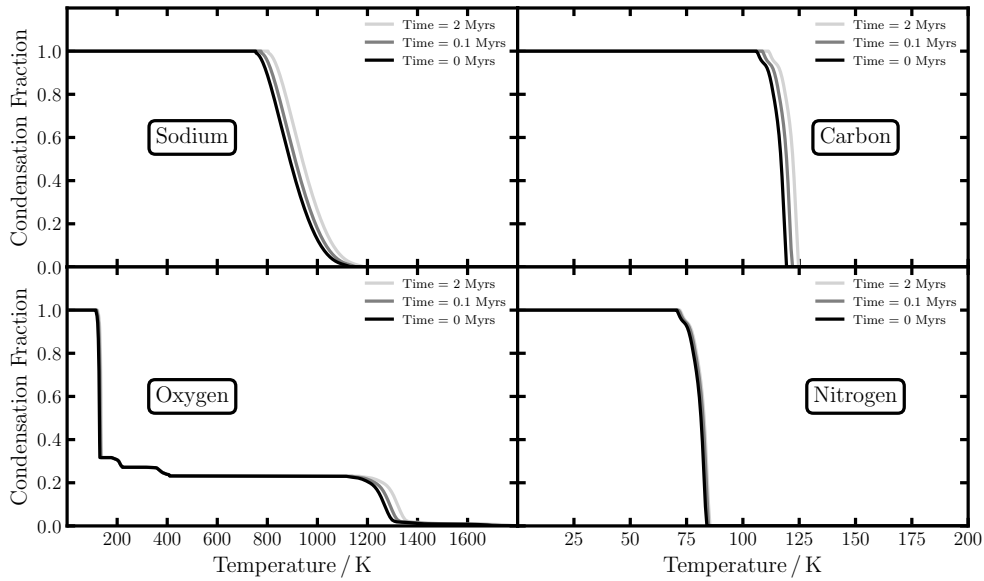
Fig. 2.7 The fraction of Na, C, O, and N which are in solid species rather than gaseous species as a function of formation temperature for various formation times when an initially solar composition gas was inputted. The curves for Na and O were calculated using HSC Chemistry while the curves for C and N were calculated using the model outlined in Marboeuf et al. (2014).
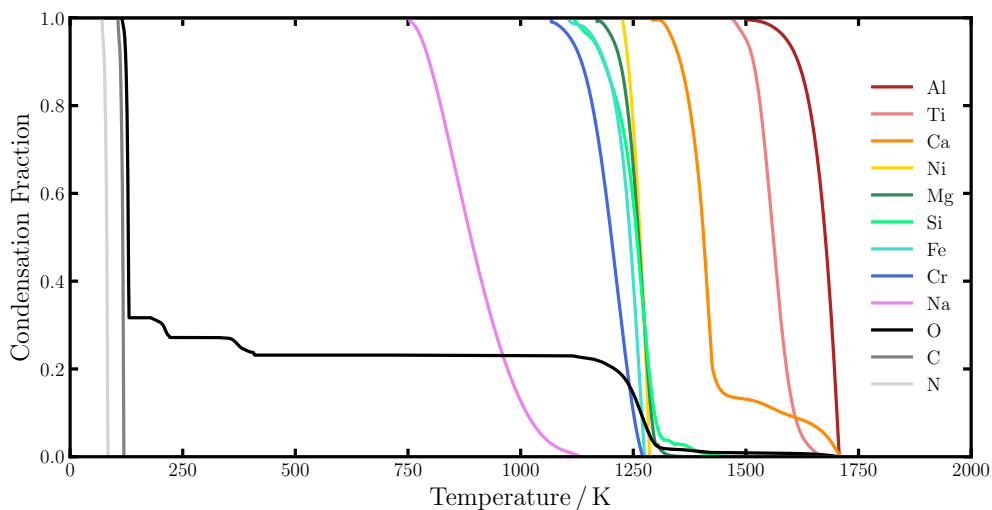
Fig. 2.8 The fraction of all modelled elements which are in solid species rather than gaseous species as a function of formation temperature for an initially solar composition gas at time equals 0 Myrs.
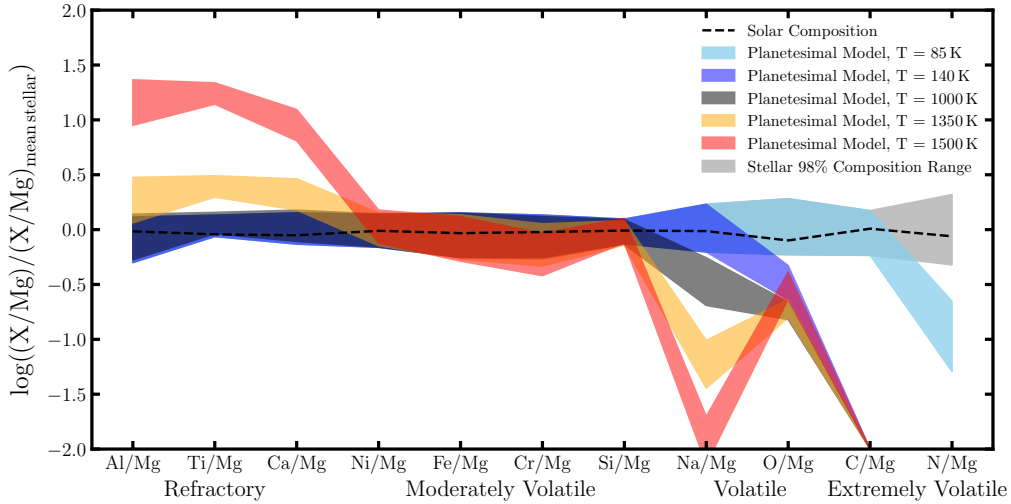
Fig. 2.9 The modelled abundances of exo-planetesimals plotted as ratios to Mg and compared with the stellar compositions from Brewer et al. (2016). The planetesimals all form at t = 1.5 Myrs and have feeding zone sizes of z = 0.05 au. The temperatures at which planetesimals form produce a clear signature in their composition which is related to elemental volatility.

of the distribution is the formation distance from the host star and is modelled as a free parameter ($d_{\text{formation}}$). While the standard deviation is a measure of the 'width' of the feeding zone and is modelled as another free parameter ($z_{\text{formation}}$). The formation time is modelled as a further free parameter ($t_{\text{formation}}$).

Figure 2.9 displays the modelled planetesimal abundances for the range of initial compositions given by Brewer et al. (2016) as a function of formation temperature (formation distance) with formation time fixed at 1.5 Myrs and feeding zone size fixed at 0.05 au. The signatures of volatile depletion due to incomplete condensation are easy to spot in Figure 2.9. If the temperature was sufficiently low such that Mg fully condensed out of the disc depletion of the volatile elements can be found by observing the sub stellar abundance ratios of Na, O, C, and N to Mg. While if temperatures were sufficiently high that Mg only partially condensed out of the disc super stellar abundance ratios of Al, Ti, and Ca to Mg would be indicative of such volatilisation processes.

2.2.3   The effect of differentiation, collisions, and fragmentation

As introduced in Section 1.1 the composition of rocky worlds can be modified from their primitive composition if they geochemically differentiate before experiencing energetic collisions. Sufficiently energetic collisions can cause the fragmentation of inhomogeneous bodies and crust-rich, mantle-rich, and core-rich material can become unevenly distributed between the collisional fragments, therefore, producing bodies with modified compositions relative to the parent body.

To model this effect I use a simple model which is based on the differentiation which occurred inside of the Earth. The model takes planetesimals (which have compositions as derived in Section 2.2.2) and allows a core, with an identical composition to the Earth's core, of some given number fraction, N_c, to form at the centre of the body. The model then allows the planetesimals to form a crust of some given number fraction, N_o, with a composition identical to the Earth's oceanic crust. The formation of these two reservoirs of elements depletes the mantle of the elements which were required to create the core and the crust. Therefore, depending on the size of the core and crust formed the mantle composition of the parent body will vary. The compositions expected in planetesimals which are fragments of larger differentiated bodies can then be obtained by linearly combining various amounts of core, mantle and crust material. Equation 2.24 outlines how enhanced an individual element, X, becomes in the collisional fragment relative to a original parent planetesimal.

$$E_{\mathrm{x}} = \frac{f_{\mathrm{o}} X_{\mathrm{o}\oplus} + \left(\frac{f_{\mathrm{m}}}{N_{\mathrm{m}}}\right)(X_\oplus - N_{\mathrm{o}} X_{\mathrm{o}\oplus} - N_{\mathrm{c}} X_{\mathrm{c}\oplus}) + f_{\mathrm{c}} X_{\mathrm{c}\oplus}}{X_\oplus} \qquad (2.24)$$

where E_{x} is the enhancement factor of element X, $X_\oplus$ is the abundance of element X in bulk Earth, $X_{\mathrm{o}\oplus}$ is the abundance of element X in the Earth's oceanic crust, $X_{\mathrm{c}\oplus}$ is the abundance of element X in the Earth's core, f_{o} is the fraction of the fragment which is made up of oceanic crust-like material, f_{m} is the fraction of the fragment which is made up of mantle-like material, f_{c} is the fraction of the fragment which is made up of core-like material, N_{o} is the fraction of the parent body which is made up of oceanic crust-like material, N_{m} is the fraction of the parent body which is made up of mantle-like material, and N_{c} is the fraction of the parent body which is made up of core-like material.
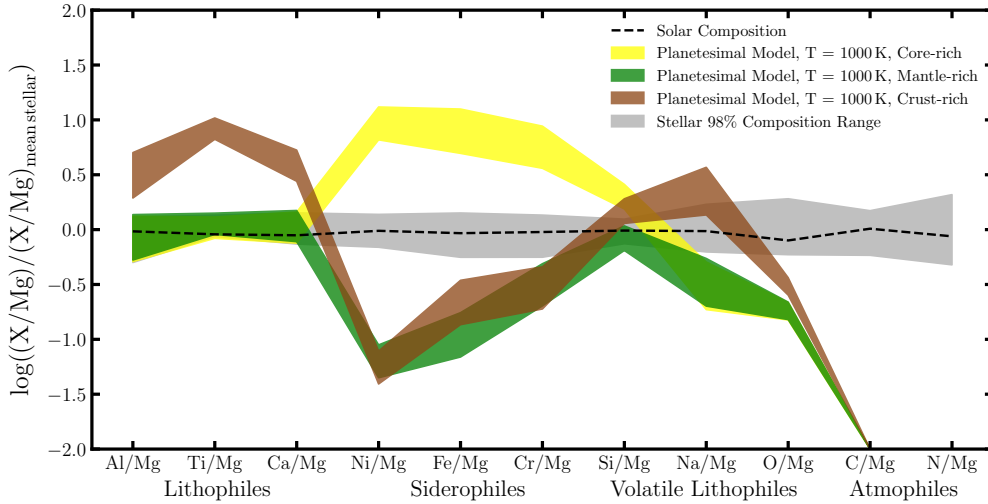
Fig. 2.10 The modelled abundances of exo-planetesimals which are fragments of differentiated bodies. The parent bodies for all the models displayed have formation times of 1.5 Myrs, formation temperatures of 1,000 K, and feeding zone sizes of 0.05 au. The core sizes and crust sizes of the parent bodies for all the models displayed are equivalent to that of the Earth. The core-rich model has had 90% of its outer layers stripped, the mantle-rich model is 100% mantle material, while the crust-rich model is 50% crust material and 50% mantle material.

Figure 2.10 displays the composition outputted by the model for crust-rich, mantle-rich, and core-rich fragments assuming the parent body had a core number fraction and crust number fraction identical to the Earth's (core number fraction 0.17 and crust number fraction 0.001). As expected planetesimals which are rich in core material are enhanced in the siderophiles, while planetesimals which are rich in mantle material are depleted in the siderophiles. Again as expected crust-rich material is enhanced in the lithophiles and depleted in the siderophiles. The core-rich model plotted is that of a fragment which had 90% of its outer layers stripped off. The mantle-rich fragment is 100% mantle material while the crust-rich fragment plotted is 50% crust material and 50% mantle material.

Figure 2.11 illustrates how tweaking the parent body core number fraction (N_c) and crust number fraction (N_o) alters the composition of the mantle and can therefore produce patterns which are different to those formed when assuming the parent body has a core number fraction and crust number fraction similar to Earth. This is a potentially important parameter to model when it comes to modelling the material which pollutes white dwarfs as various differentiated asteroids are thought to have
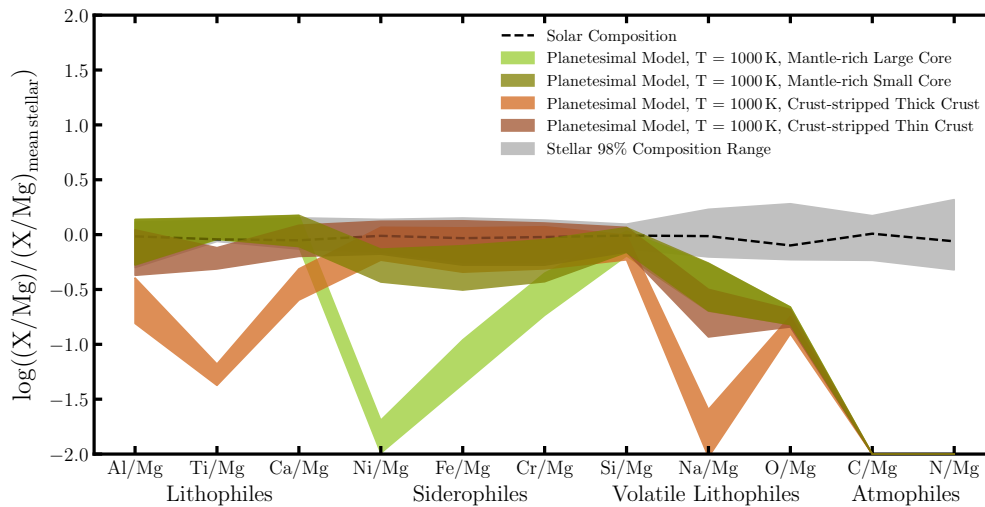
Fig. 2.11 The parent bodies for all the models displayed have formation times of 1.5 Myrs, formation temperatures of 1,000 K, and feeding zone sizes of 0.05 au. The mantle-rich models are fragments composed of 100% mantle material, while the crust-stripped models are fragments which have had their entire crusts removed. The core number fraction for the parent body of the large core model is 5% larger than Earth's and the core number fraction of the small core model is 25% less than Earth's. The thin crust model has a parent body whose crust makes up 7.5% of the parent body's total atoms while the thick crust model has a parent body whose crust makes up 15% of the parent body's total atoms.

crusts which are relatively much thicker than the Earth's and cores which are relatively much smaller (Thomas et al. (2005); Clenet et al. (2014)). Therefore, the mantles of white dwarf pollutants potentially are less depleted in the siderophiles and more depleted in the lithophiles.

The differentiation model outlined thus far is heavily based on the Earth as it assumes that all planetary crusts have a composition similar to that of the Earth's oceanic crust and that all planetary cores have a composition similar to the Earth's core. From Solar System data and laboratory experiments it is understood that the pressure at which a planetary body differentiates influences the composition of the core and mantle which subsequently form. Therefore, a valuable upgrade to the model would be to include internal formation pressure as a free parameter which would calculate the initial core composition rather than assuming the formation of a core with a composition similar to the Earth's core. Such an addition is beyond the scope of this thesis as it would require intensive geological modelling. However, in order to
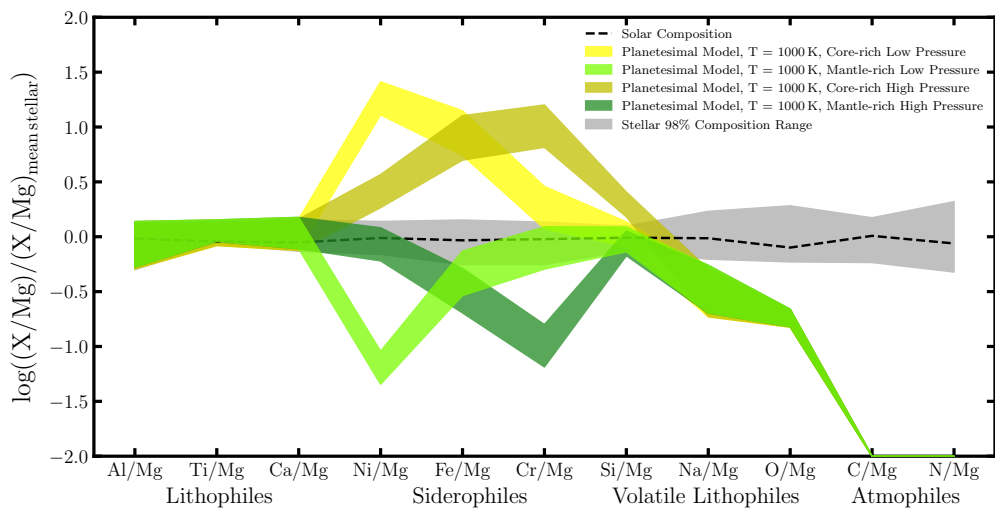
Fig. 2.12 The relative siderophilicities of Ni and Cr have been artificially adjusted to gain an understanding of how the pressure at the core-mantle boundary during formation can effect the composition of the fragments. The models are identical to those in Figure 2.10 however the high pressure model has a parent body with two times the amount of Cr, one fifth the amount of Ni, and the same fraction of light elements in comparison to the Earth's core in the while the low pressure case the core contains two times the amount of Ni, one fifth the amount of Cr, and one tenth the fraction of light elements.

estimate the effect of variable core-mantle boundary pressures on the composition of exo-planetesimals without constructing a full geological differentiation model I simply manually change the siderophilicity of each element present in the Earth's core. Using the general behaviours outlined in Fischer et al. (2015) higher pressures increase the siderophilicity of Cr, while lower pressures increase the siderophilicity of Ni. In Figure 2.12 I have modified the initial parent core composition such that in the high-pressure case the core contains two times the amount of Cr and one fifth the amount of Ni in comparison to the Earth's core, while keeping the fraction of light elements the same as the Earth. In the low pressure case the core contains two times the amount of Ni, one fifth the amount of Cr, and one tenth the fraction of light elements in comparison to the Earth's core. The mantle-rich models are 100% mantle material while the core-rich models have had 90% of their outer layers removed. Figure 2.12 shows that while the general trend in the siderophilic and lithophilic elements remains the same allowing the siderophilicity of Ni and Cr to change creates different abundance patterns within the siderophiles. The potential for variable parent core compositions will not be included in the main model presented in this thesis, however, it will occasionally be used to fit systems which cannot be reproduced by the main model in order to highlight potential systems for which the inclusion of variable differentiation conditions in the model would be a useful upgrade.

The composition of planetesimals in this thesis are modelled to be functions of the parent core fraction (N_c), the parent crust fraction (N_o), the fragment core fraction (f_c), and the fragment crust fraction (f_o) as well as metallicity of the host star ($\mathrm{[Fe/H]}_\mathrm{index}$), the formation time ($t_\mathrm{formation}$), the formation distance from the host star ($d_\mathrm{formation}$), and the feeding zone size ($z_\mathrm{formation}$).

2.3   Modelling white dwarf pollution

To produce the expected atmospheric compositions observed in polluted white dwarfs one must not only model the abundances of extrasolar planetesimals but also model how the composition of the material accreted is modified by the accretion process and atmospheric diffusion. Heavy elements present in the atmospheres of white dwarfs are expected to sink from the thin upper convective zone, due to the strong gravitational field of the white dwarf, and become unobservable. Different chemical elements sink at different rates. Thus, the observed relative elemental abundances may not match those of the accreted material. In the model I assume that each polluted white dwarf has accreted a single planetary body and that the observed compositions reflect the

composition of this planetary body prior to accretion, modified only by the fact that different elements sink out of the observable atmosphere at different rates. These assumptions are expected to hold as firstly, even if multiple bodies were accreted simultaneously the metal abundances observed would be dominated by the largest body (Wyatt et al. (2014)). Secondly, the timescale on which the accretion process occurs is thought to be far longer than the potential time differences between the sublimation of different elements and therefore, the gas accreted is expected to have a composition representative of the bulk composition of the planetary material (Jura and Young (2014)).

The modification of the pollutant abundances due to the differential sinking of heavy elements is modelled using the equations outlined in Koester (2009). The accretion is parameterised in terms of two free parameters, the time since the current accretion episode started (t) and the total length of time for which the given accretion episode can last (t_{event}), in order to take into account the possibility that accretion has now finished. While accretion is occurring the elemental abundance ratio between two elements, A and B, in the atmosphere of the white dwarf are related to the elemental abundance ratio between the two elements in the pollutant by Equation 2.25 (Koester (2009)).

$$\left(\frac{A}{B}\right)_{\text{Atmosphere, accretion on}} = \left(\frac{A}{B}\right)_{\text{Pollutant}} \left(\frac{t_{\text{sink, A}}}{t_{\text{sink, B}}}\right) \left(\frac{1 - e^{-t/t_{\text{sink, A}}}}{1 - e^{-t/t_{\text{sink, B}}}}\right) \qquad (2.25)$$

where $t_{\text{sink, A}}$ and $t_{\text{sink, B}}$ are the sinking timescales through the atmosphere of the white dwarf of elements A and B respectively and t is the time passed since accretion started. From Equation 2.25 one can see that initially the atmospheric abundances match those of the accreted material (the build-up phase) but as time passes diffusion through the atmosphere of the white dwarf and accretion onto the white dwarf equilibriate and the relationship between the atmospheric abundances and the abundances of the pollutant body tend towards a constant value (the steady state phase).

After accretion ceases the pollutant material will begin diffusing out of the upper convective zone of the white dwarf's atmosphere in a manner dependent on the individual elemental sinking timescales (the declining phase). The elemental abundance ratio between two elements, A and B, in the atmosphere of the white dwarf are now related to the elemental abundance ratio between the two elements in the pollutant by Equation 2.26 (Koester (2009)).

$$\left(\frac{A}{B}\right)_{\text{Atmosphere, accretion off}} = \left(\frac{A}{B}\right)_{\text{Pollutant}} \left(\frac{t_{\text{sink, A}}}{t_{\text{sink, B}}}\right) \left(\frac{1 - e^{-t_{\text{event}}/t_{\text{sink, A}}}}{1 - e^{-t_{\text{event}}/t_{\text{sink, B}}}}\right) e^{-(t - t_{\text{event}})\left(\frac{t_{\text{sink, B}} - t_{\text{sink, A}}}{t_{\text{sink, A}} \, t_{\text{sink, B}}}\right)} \qquad (2.26)$$

where $t_{\text{sink, A}}$ and $t_{\text{sink, B}}$ are the sinking timescales through the atmosphere of the white dwarf of elements A and B respectively, t is the total time passed since accretion started, and t_{event} is the lifetime of the accretion event.

Figure 2.13 illustrates how the equations previously outlined cause the relationship between the atmospheric composition and original pollutant composition to vary with time and additionally highlights why the effect of differential elemental sinking timescales must be taken into account when modelling polluted white dwarf atmospheres. The sinking timescales of the white dwarf affects whether, for a given accretion event duration, the system will enter a steady state phase. Sinking timescales generally increase as the white dwarf cools and are much longer for He dominated white dwarfs than for H dominated white dwarfs (as highlighted in Figure 1.13). Therefore, cool He dominated white dwarfs often remain in build-up phase until accretion switches off, whereas, hot H dominated white dwarfs almost instantly enter the steady state phase and remain in such a phase until the accretion event finishes.

Figure 2.14 shows how the abundances observed in the atmosphere of a white dwarf evolve over time due to differential sinking. The models shown are for a DB white dwarf which has a surface temperature of 10,000 K and for an accreting planetesimal which has not experienced collisional processing, has a formation temperature of 1,000 K, a feeding zone width of 0.05 au, and a formation time of 1.5 Myrs. As Mg has a comparable sinking timescale to Al, Si, Na, O, C, and N the abundances ratios of these elements do not change excessively with time, however, the abundance ratios of Ti, Ca, Ni, Fe, and Cr drop dramatically. This signature means that any systems which have finished actively accreting material can potentially be revealed by the model because if enough elemental abundances are observed the signature will not be degenerate with any of the processes previously outlined in this chapter.

To compare the modelled planetesimal abundances with the observed white dwarf atmospheric abundances the fraction of the convective zone which is composed of pollutant material must be known. I avoid any assumptions by introducing the pollutant to convective zone number fraction to be the final free parameter of the model (P_{fraction}). In conjunction with the observed convective zone mass of the white dwarf this free parameter can be manipulated to provide constraints on the total mass of the pollutant material. If the system is in either the build-up or steady state phase a lower limit on the mass of the original pollutant body may be found, however, if the system is in the declining phase a full constraint on the original pollutant mass can be derived as declining phase accretion suggests that there is no material left to accrete residing in a circumstellar orbit.
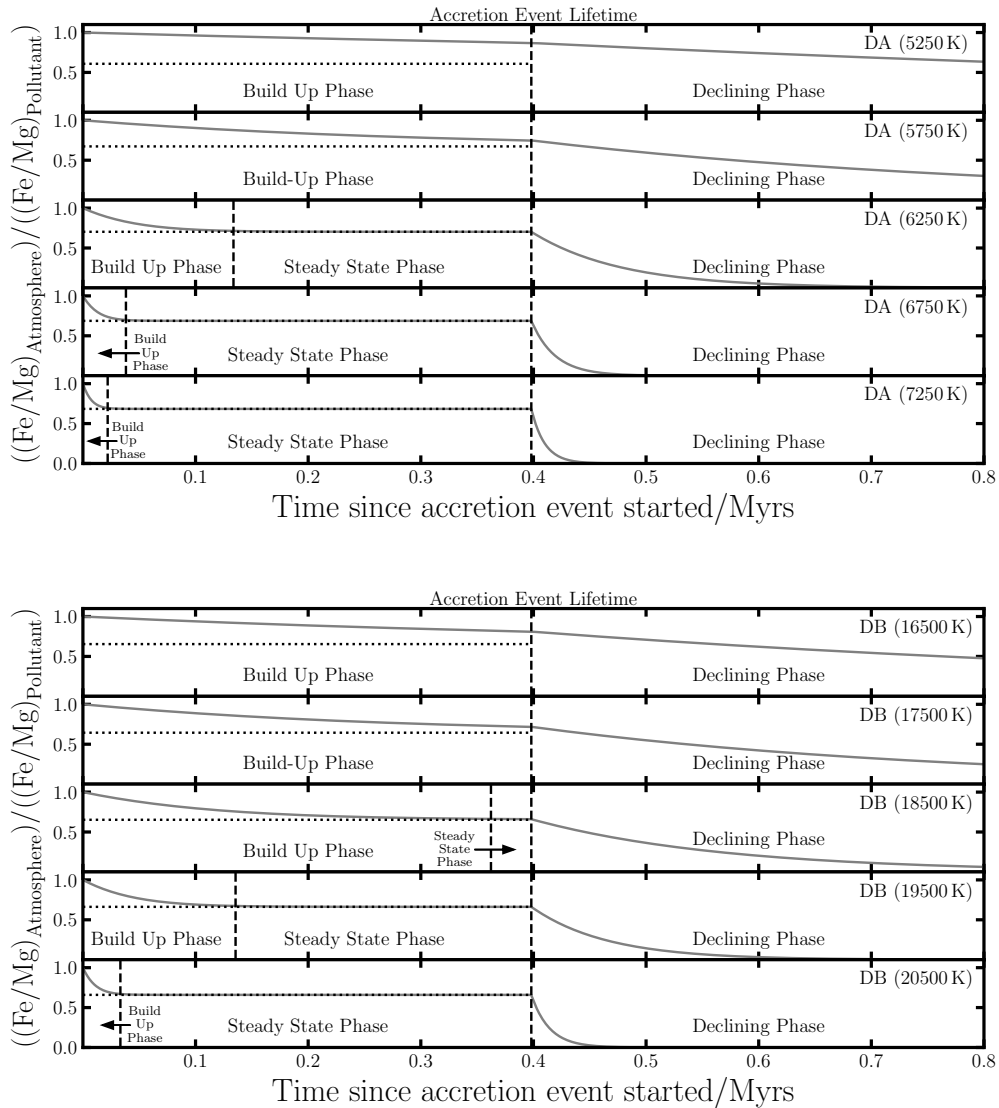
Fig. 2.13 The phases of accretion possible in polluted white dwarf systems and their affect on the observed atmospheric abundances. The upper 5 panels are for H dominated atmospheres and the lower 5 panels are for He dominated atmospheres. The dotted lines represent the steady state abundance value which the atmospheres will tend to assuming the accretion event is sufficiently long. The dashed line represents the accretion event lifetime which is chosen to be $0.398\,\mathrm{Myrs}$ in accordance with the mean value derived in Girven et al. (2012).
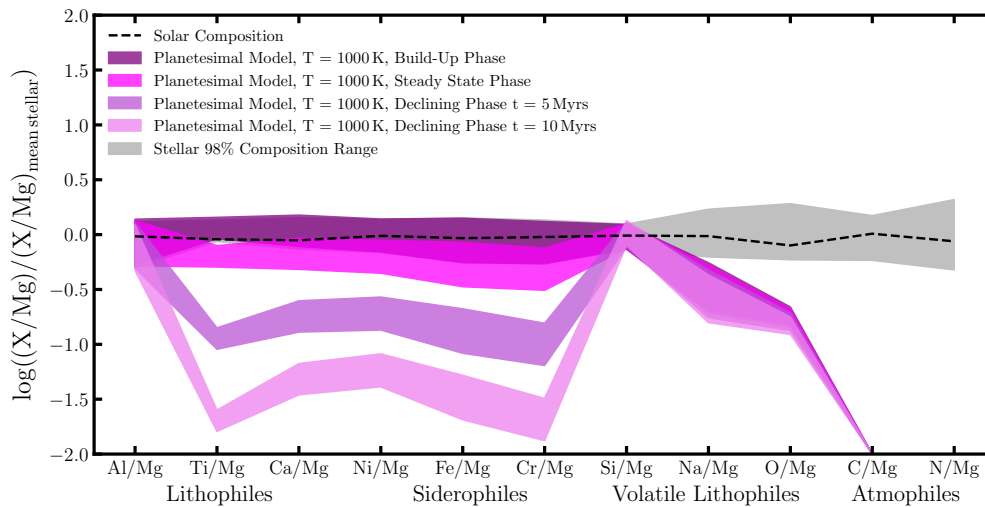
Fig. 2.14 The composition of modelled exo-planetesimals including differential sinking.

Figure 2.15 outlines the full model presented in this chapter along with a schematic diagram highlighting the processes modelled. The full model has 11 free parameters: the initial composition of the stellar nebula ($[Fe/H]_{index}$), the formation distance ($d_{formation}$), the formation time ($t_{formation}$), the feeding zone size ($z_{formation}$), the parent core fraction (f_c), the parent crust fraction (f_o), the fragment core fraction (N_c), the fragment crust fraction (N_o), the time since the accretion event started (t), the accretion event lifetime (t_{event}), and the pollution fraction ($P_{fraction}$). Recreating the observed abundances in polluted white dwarf atmospheres by modelling the accretion of exo-planetesimals not only is required in order to reaffirm the literature-accepted model of white dwarf pollution but also allows the planet formation processes and geological processes which occur in exo-planetary systems to be probed. Statistically constraining the parameters of the model and assessing the model's quality of fit to the observations is therefore vital if one wishes to use polluted white dwarf abundances to gain an insight into exo-planetary systems.
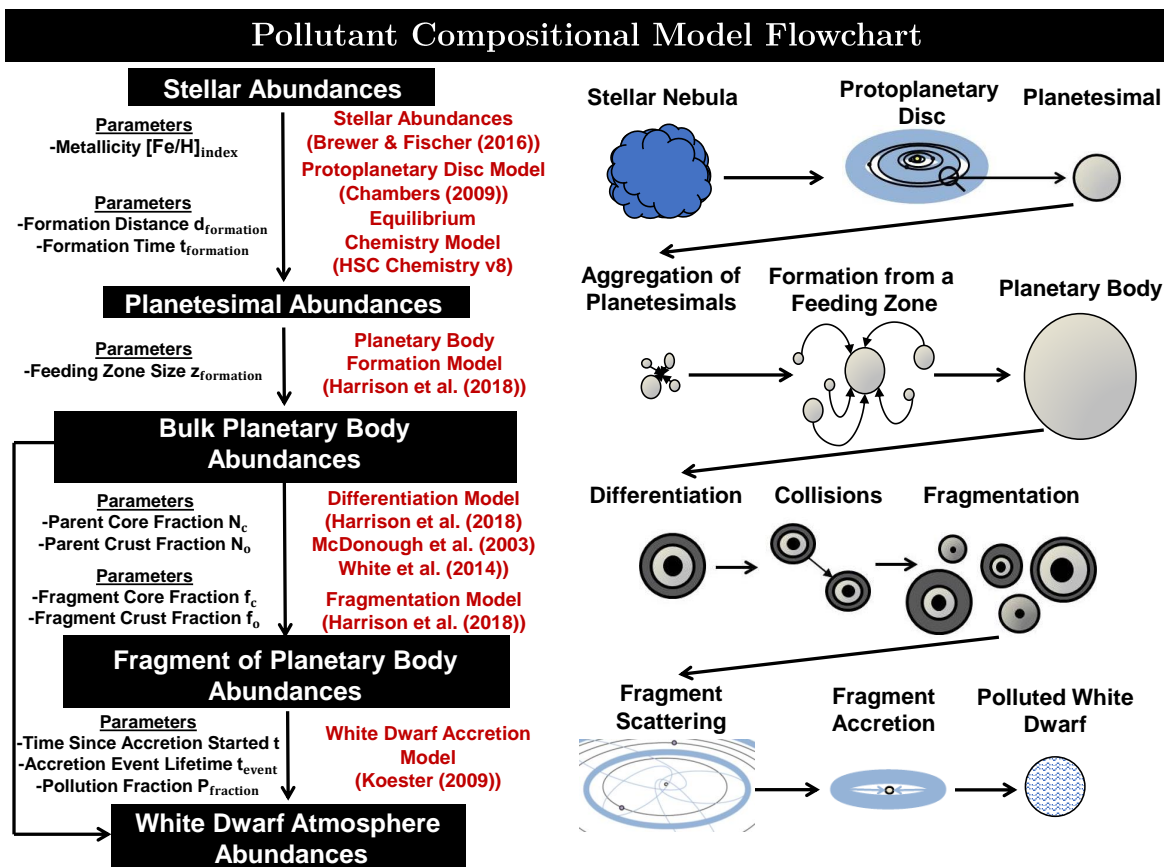
Fig. 2.15 A schematic diagram of the modelled pollution process and all the model free parameters used to recreate white dwarf atmospheric abundances.

2.4 Statistically constraining the model parameters & finding the optimum model

In general when presented with observational data one strives to achieve four main goals:

1. Finding, for a given model, the model free parameters which best explain the data.

2. Finding if the model, when its free parameters are optimised, can reproduce the data to some sufficient level of accuracy.

3. Finding uncertainties on the best fit model parameters, thus, statistically constraining their values.

4. Finding the simplest possible model from a group of models which can reproduce the data to the sufficient level of accuracy, therefore, finding which model parameters, and thus which physical effects, are vital to include and which are not.

Statistical inference methods are generally used to achieve such goals, however, there are two main approaches to statistical inference, the frequentist framework and the Bayesian framework. The frequentist approach dominated scientific research in the 20th century but an increase in computational power in the 21st century has lead to a resurgence of the Bayesian approach. In this section I will outline the most commonly used methods in both frameworks and introduce the method which I employed in order to constrain the origin and geology of the pollutants of white dwarfs in this thesis.

2.4.1 The frequentist approach

The frequentist framework relies on the assumption that only repeatable random events have probabilities and that these probabilities are equal to the frequency of the occurrence of the events when sampled many times. In order to achieve the four goals outlined above, the most common method utilised in the frequentist framework is that of chi-squared minimisation and the calculation of p-values and confidence intervals.

To find and assess how well a particular model, with a given set of free parameters, fits the observed data (with N data points) a chi-squared parameterisation (χ_j^2) can be used where

$$\chi_j^2 = \sum_{i=1}^{N} \frac{\left(m_{\mathrm{i,j}} - x_{\mathrm{i}}\right)^2}{\sigma_i^2} \tag{2.27}$$

and $m_{i,j}$ is the modelled value for the ith observed data point with the jth set of free parameter values, x_i is the ith observed data point value, and σ_i is the uncertainty on the ith observed data point value. A grid of possible model free parameter values is usually created (where j is the total number of combinations of free parameters considered) and a χ^2 value is calculated for each combination (χ_j^2). The minimum value of χ_j^2 (χ_{min}^2) can then be found and the corresponding model free parameter values can be said to be the 'best fit' parameters, therefore, achieving the first goal. If one wishes to gauge a general feeling for how well the χ_{min}^2 model reproduces the data a reduced chi-squared ($\chi_{\text{min, red}}^2$) value can be calculated. Where

$$\chi_{\text{min, red}}^2 = \frac{\chi_{\text{min}}^2}{d} \tag{2.28}$$

and d is the number of degrees of freedom which is simply the number of observed data points included in the calculation minus the number of free parameters in the model. Often if the models required have many necessary free parameters or there are very few data points the $\chi_{\text{min, red}}^2$ becomes undefined and a chi-squared per data point ($\chi_{\text{min, pdp}}^2$) can used which is defined as

$$\chi_{\text{min, pdp}}^2 = \frac{\chi_{\text{min}}^2}{N} \tag{2.29}$$

where N is the total number of data points. If the $\chi_{\text{min, red}}^2$ or $\chi_{\text{min, pdp}}^2$ is close to unity the model and set of parameters are said to produce a sufficient fit to the observed data. If the value is much greater than one then the model poorly reproduces the data and potentially cannot explain the observations, while if the value is much less than one and the best fit model was found simply by minimising the χ^2 one must be cautious as potentially the model is overfitting and is fitting to the noise in the data. $\chi_{\text{min, red}}^2$ values offer a simple way to asses the quality of the fit and therefore can be used to reach the second goal. However, in order to robustly place uncertainties on the model parameters and to find which parameters are required in order to explain the data (the third and fourth goals) $\chi_{\text{min, red}}^2$ should, in most cases, not be used (Andrae et al. (2010)). Instead, p-values and the corresponding confidence intervals should be calculated and utilised.

In order to compare different models with different free parameters, and also compare different combinations of free parameter values within a certain model, the frequentist approach suggests that a hypothesis-style test should be performed. To do this test a p-value is calculated for the fit to the data. The p-value allows one to assess how likely it is that the difference between the model output and the data is

simple down to random chance and therefore allows one to find which models and areas of parameter space can be ruled out as actual bad fits. This allows both goals three and four to be achieved as p-values and their corresponding confidence intervals allow uncertainties to be placed on the 'best fit' model parameters and the requirement for the inclusion of additional model parameters to be found. The χ^2 values for each model can be converted into a p-values using:

$$p_{\chi_j^2,d} = \left(2^{\left(\frac{d}{2}\right)} \Gamma_{\left(\frac{d}{2}\right)} \right)^{-1} \int_{\chi_j^2}^{\infty} t^{\frac{d}{2}-1} e^{-\frac{t}{2}} dt \qquad (2.30)$$

where $\Gamma_x = \int_0^{\infty} t^{x-1} e^{-t} dt$ and d is the number of degrees of freedom. Standard convention is to conclude that a model which produces a fit with a p-value less than 0.317 can be ruled out with a confidence of 1σ, a model which produces a fit with a p-value less than 0.046 can be ruled out with a confidence of 2σ, and a model which produces a fit with a p-value less than 0.003 can be ruled out with a confidence of 3σ. Therefore, confidence intervals of a given statistical significance can be calculated for a given model and models without certain parameters can be ruled out to a given level of statistical significance if their fits are sufficiently poor.

In conclusion, the frequentist approach finds the best fit set of free parameters for a given model using a chi-squared parameterisation. The quality of the fit can then be assessed using a reduced chi-squared parameterisation. The uncertainties on the model parameters can then be calculated by first converting the chi-squared values into p-values then finding the highest and lowest possible values for each model parameter which cannot be rejected to a given statistical significance. Finally, models without a certain free parameter can be rejected to a certain statistical significance using p-values, therefore allowing significances to be found for the requirement of the inclusion of extra parameters.

Such a frequentist approach was originally taken by myself in Harrison et al. (2018) when analysing the atmospheres of polluted white dwarfs. The main advantage the frequentist approach has over the Bayesian approach is its simplicity, however its validity for certain models and scenarios is questionable, especially when one has prior knowledge of the system. Due to the emergence of many easily available Bayesian inference codes, implementing a Bayesian framework in a model has become easier. Therefore, in Harrison et al. (2020, submitted) I took such an approach. The results I will present in this thesis will also use a Bayesian framework. In the next section I will introduce the Bayesian approach, how the approach is commonly applied, and the approach's advantages.

2.4.2 The Bayesian approach

The Bayesian approach utilises Bayes' theorem and assumes that probabilities can be assigned to non-repeatable events and that probabilities can be used to represent the uncertainty in any hypothesis or event. Bayes' theorem states

$$P(A|B) = \frac{P(B|A)\,P(A)}{P(B)} \tag{2.31}$$

where $P(A|B)$ is the probability of A being true given B is true, $P(B|A)$ is the probability of B being true given A is true, $P(A)$ is the probability of A being true, and $P(B)$ is the probability of B being true. When Bayes' theorem is utilised in a Bayesian inference framework $P(A|B)$ is assigned to be the posterior distribution, $P(B|A)$ is the likelihood, $P(A)$ is assigned to be the prior distribution, and $P(B)$ is the Bayesian evidence. The aim of a Bayesian inference model is to start with a prior assumed distribution for each of your model parameters and use Bayes' theorem to calculate the posterior distribution for each parameter. This method allows both the first goals and the third goal to be met. In order to meet the fourth goal the evidence must be calculated as this allows models to be directly compared. The second goal is generally not possible to achieve, and therefore the frequentist reduced chi-squared value is often quoted as a rough number to assess the overall quality of the model fit in Bayesian frameworks. There are two commonly used methods which calculate posterior distributions given prior distributions: Markov chain Monte Carlo (MCMC), and nested sampling.

The Markov chain Monte Carlo (MCMC) method makes use of the fact that the Bayesian evidence is a scalar value rather than a distribution, and therefore can be simply treated as a scaling constant. Thus, there is no need to calculate the evidence directly and in order to find the posterior distribution of a parameter, once a prior distribution is given, only the likelihood needs to be found. In a general sense, MCMC codes work in the following way: a starting value for each parameter is selected, then a new proposed value is generated by adding random noise, which is produced using the proposed distribution, to each starting value. The probability density of the posterior distribution is then calculated for the starting values of the parameters and the proposed values by multiplying the likelihood function with the prior distributions. If the proposed values have a higher probability density then the proposal is accepted. If the proposal has a lower probability density than the starting values then it is randomly decided whether to accept or reject the proposal with a probability equal to the ratio of the starting and proposed probability densities. If the proposal is accepted,

it becomes the next sample in the chain, otherwise, the next sample remains the same as the starting sample. This process continues for a fixed number of steps until ideally a sufficient number of samples have taken place. Each chain consists of a set of walkers which start off at given locations in the parameter space. When the chain starts it is initially in what is often known as the 'burn-in phase', where it is moving towards the distribution's maximum. However, once the chain reaches the maximum the target distribution can take on, the equilibrium value and the posterior can be accurately estimated. MCMC codes therefore require three inputs: the number of walkers, the initial location of the walkers, and the number of steps. Additionally, MCMC codes require that a sufficient number of steps are taken such that the chains can converge and reach equilibrium and that the burn-in phase is removed before the results are analysed. MCMC codes can also be used to calculate the Bayesian evidence, which is required in order to compare models and achieve the fourth goal, however, it is computationally expensive and thus is rarely included as part of the main code.

Nested sampling algorithms calculate the posterior distributions in a fundamentally different way. Instead of calculating the posteriors directly, nested sampling algorithms first calculate the Bayesian evidence by integrating the product of the likelihood and prior distribution over the chosen parameter space. Once the evidence is estimated, the posterior distributions can be calculated as a convenient byproduct using Bayes' theorem. Therefore, Nested sampling codes can meet the first, third and fourth goals simultaneously. Nested sampling codes numerically calculate the Bayesian evidence by investigating progressively increasing likelihood contours such that the likelihood contours contain a set of live points taken from incrementally shrinking ellipsoids. Therefore, nested sampling codes only require one input parameter, the total number of live points. Live points are the locations in the parameter space where the likelihood is calculated. Nested sampling codes also possess a well defined stopping criteria which allows an estimate of the error on the evidence to be calculated. Thus, the number of live points can be adjusted until the user is content with the size of the error on the evidence. This means that Nested sampling codes posses many advantages when compared with MCMC codes. Firstly, nested sampling codes does not have walkers which require initial locations to be specified, which removes a potential fitting issue as suboptimally located walkers can become 'stuck' in local minima. Secondly, nested sampling codes do not have a burn-in phase, and therefore knowing whether convergence has occurred and understanding the criteria for convergence is far less of an issue. Thirdly, and most importantly, nested sampling has the ability to compare models using their Bayesian evidence in a non-computationally expensive manner. For

these reasons a nested sampling algorithm is superior to MCMC for the problems outlined in this thesis and therefore I have used such an algorithm in order to achieve the four goals outlined at the start of this section. I will now fully outline the chosen Nested sampling method and the way it has been implemented in the models used in this thesis.

2.4.3 Constraining the origin & geology of the material which pollutes white dwarfs

In order to select the most probable origin of the pollutant material, rule out areas of parameter space within the models which cannot accurately reproduce the observed atmospheric abundances in the individual white dwarfs, and find which model paramters are required in order to explain the observations, I use the nested sampling algorithm MultiNest (Feroz and Hobson (2008); Feroz et al. (2009); Feroz et al. (2013)) via the python package PyMultiNest (Buchner et al. (2014)).

The validity of a given model is assessed using the Bayesian evidence ($\mathcal{Z}$). This is defined as the integral of the product of the assumed prior distribution for each parameter (π) and the likelihood function ($\mathcal{L}$). The posterior probability distribution for each parameter ($p(\boldsymbol{\theta}|\mathbf{X}_{\mathrm{obs}}, M_i)$) is used to constrain the potential values of each parameter, given the observations. The ratio of the Bayesian evidence (Bayes factor) is used to compare models while the chi-squared per element observed ($\chi^2_{\mathrm{min, \, pdp}}$) is used in order to make sure the best fit is of a sufficient quality.

MultiNest calculates the Bayesian evidence of a model ($\mathcal{Z}$) by numerically integrating the product of the assumed prior distribution for each parameter (π) and the likelihood function ($\mathcal{L}$)

$$\mathcal{Z}(\mathbf{X}_{\mathrm{obs}}|M_i) = \int_{\boldsymbol{\theta}} \mathcal{L}(\mathbf{X}_{\mathrm{obs}}|\boldsymbol{\theta}, M_i) \, \pi(\boldsymbol{\theta}|M_i) \, d\boldsymbol{\theta} \tag{2.32}$$

where $\mathbf{X}_{\mathrm{obs}}$ is a vector containing the abundances observed in the polluted white dwarf's atmosphere, M_i is the model chosen to explain the atmospheric abundances, and $\boldsymbol{\theta}$ is a vector containing the set of parameters included in the chosen model. The likelihood ($\mathcal{L}$) is defined by

$$\ln(\mathcal{L}(\mathbf{X}_{\mathrm{obs}}|\boldsymbol{\theta}, M_i)) = -\frac{1}{2} \sum_{X}^{\mathrm{Ca,Fe,...}} \left(\frac{(X_{\mathrm{obs}} - X_{\mathrm{mod}}(\boldsymbol{\theta}))^2}{\sigma_X^2} + \ln(2\pi\sigma_X^2) \right) \tag{2.33}$$

where the sum is over all the observed elemental abundances, $X_{\mathrm{mod}}(\boldsymbol{\theta})$ is the modelled abundance for a given set of parameters $\boldsymbol{\theta}$, and σ_X is the error on the individual observed elemental abundances. The prior $(\pi(\boldsymbol{\theta}|M_i))$ for each parameter is taken to be a uniform (or log-uniform) distribution between an upper and a lower bound, the priors assumed for each parameter are listed in table 2.4 and discussed in the following section.

The Bayesian evidence is efficiently calculated by MultiNest by exploring progressively increasing iso-likelihood contours in the parameter space such that the iso-likelihood contours contain a set of live points taken from incrementally shrinking ellipsoids. I run the algorithm with 1,500 live points for each model as I found that this was sufficient to produce errors on the log evidence of the order 0.10, while also minimising the run time of the code.

The posterior probability distribution $(p(\boldsymbol{\theta}|\mathbf{X}_{\mathrm{obs}}, M_i))$ for each parameter is found as a convenient byproduct of the evidence calculation, as the posterior is related to the likelihood, evidence, and prior by:

$$p(\boldsymbol{\theta}|\mathbf{X}_{\mathrm{obs}}, M_i) = \frac{\mathcal{L}(\mathbf{X}_{\mathrm{obs}}|\boldsymbol{\theta}, M_i)\,\pi(\boldsymbol{\theta}|M_i)}{\mathcal{Z}(\mathbf{X}_{\mathrm{obs}}|M_i)} \tag{2.34}$$

The updated posterior distributions provide constraints on each parameter given the observations, and thus, can be used to constrain the origin of the pollutant material. In this work for each system I potentially find constraints on each of the 11 parameters in the full model ($[\mathrm{Fe/H}]_{\mathrm{index}}$, t, t_{event}, $d_{\mathrm{formation}}$, $t_{\mathrm{formation}}$, $z_{\mathrm{formation}}$, N_{c}, N_{o}, f_{c}, f_{o}, and P_{fraction}).

In order to compare models and estimate the statistical significance of various pollutant histories (for example, to what significance the white dwarf requires the accretion of a fragment of a differentiated body) a Bayes factor $(\mathcal{B}_{ij})$ can be used. The Bayes factor between two models (i and j) is calculated using:

$$\mathcal{B}_{ij} = \frac{\mathcal{Z}(\mathbf{X}_{\mathrm{obs}}|M_i)}{\mathcal{Z}(\mathbf{X}_{\mathrm{obs}}|M_j)} \tag{2.35}$$

where, as before, $\mathcal{Z}$ is the Bayesian evidence, $\mathbf{X}_{\mathrm{obs}}$ is a vector containing the abundances observed in the polluted white dwarf's atmosphere and M_i and M_j are the models chosen to explain the atmospheric abundances.

The Bayes factor between two models can be converted into a sigma-significance of a given additional parameter using Equation 2.36 (Sellke et al. (2001)).

$$\sigma = \sqrt{2}\,\mathrm{erfcinv}\left(\Re\left(e^{W\left(-\frac{1}{e\mathcal{B}_{ij}}\right)}\right)\right) \tag{2.36}$$

Table 2.4 Prior distributions assumed for the 11 parameters in the full model.

Parameter	Prior	Range
$[\text{Fe/H}]_{\text{index}}$	Uniform	0 to 957
t	Uniform	0 to $t_{\text{event}} + 20\,\text{Myrs}$
t_{event}	Log-uniform	10^{-6} to $10^{2}\,\text{Myrs}$
$d_{\text{formation}}$	Log-uniform	10^{-2} to $R_{\text{disc}}(t_{\text{formation}})\,\text{au}$
$t_{\text{formation}}$	Uniform	0 to $3\,\text{Myrs}$
$z_{\text{formation}}$	Uniform	0 to $0.15\,\text{au}$
N_{c}	Uniform	0 to 0.17
N_{o}	Uniform	0 to 0.25
f_{c}	Uniform	0 to 1
f_{o}	Uniform	0 to 1-f_c
P_{fraction}	Log-uniform	10^{-10} to 10^{-4}

where $\Re$ is the real part of the function, erfcinv is the inverse of the function shown in Equation 2.37,

$$\text{erfc}(x) = \frac{2}{\sqrt{\pi}} \int_{x}^{\infty} e^{-t^2} dt \tag{2.37}$$

and W is the Lambert W function whose defining equation is Equation 2.38,

$$z = W(z)e^{W(z)} \tag{2.38}$$

where z is a complex number. In this thesis I calculate the Bayes factors, and thus the sigma-significance, for the inclusion of the steady state phase, the declining phase, core-mantle differentiation, crustal differentiation, heating during formation, and the presence of water ice for each white dwarf system. For a more detailed discussion of the MultiNest algorithm used in this work to provide fast and robust parameter estimation and model comparisons see Benneke and Seager (2013).

Choice of priors

Bayesian analysis requires prior distributions and ranges for each free parameter to be provided in order to calculate the posterior distributions. The aim is to choose priors that cover the full potential parameter space available to the models, such that they do not influence the model comparison.

The prior on $[\text{Fe/H}]_{\text{index}}$ is trivial as it is a uniform prior over the refined stellar compositional catalogue outlined in Section 2.2.1. This prior therefore simply forces the initial composition of the protoplanetary disc to be one which is in the catalogue.

The model incorporates the temperature experienced by the planetesimals by modelling both their formation time and radial formation location in a protoplanetary disc. I take a uniform prior distribution of formation times ($t_{\text{formation}}$) and allow the planetesimals to form between 0 and 3 Myrs. 3 Myrs was chosen as there is not expected to be sufficient material to form planetesimals in the majority of protoplanetary discs around A-type stars later than 3 Myrs after formation (Ribas et al. (2015)). A log-uniform prior distribution of formation locations ($d_{\text{formation}}$) between the stellar radii and the edge of the protoplanetary disc was chosen as it is expected that pollutants can originate from anywhere in the disc (Bonsor et al. (2011)).

In order to model the fact that planetesimals can be composed of material which formed at a range of radii, a feeding zone parameter is included in the model ($z_{\text{formation}}$). Accretion is a stochastic process, migration and scattering are likely to be important and, therefore, a physically reasonable value of this parameter is difficult to obtain (Kaib and Cowan (2015)). Instead, I chose a uniform prior distribution for the feeding zone size between 0 and 0.15 au as I found that this was not unphysically large for the bodies in question nor did it artificially constrict the model when the code was run.

The maximum parent core fraction (N_{c}) and parent crust fraction (N_{o}) are defined by the differentiation model. The core cannot grow any larger once the mantle contains no Fe and the crust cannot grow any larger once the mantle contains no Ca. By definition the fragment core fraction (f_{c}) and the fragment crust fraction (f_{o}) cannot sum to be greater than unity. The priors set on the differentiation model are therefore chosen to be uniform over the above ranges as outlined in Table 2.4. Additionally, I also do not allow the collisional fragments to be simultaneously enhanced in core-like and crust-like material nor do I allow mantle-like material to be removed from a body without first removing the crust-like material (This alters the prior range and distribution for f_c and f_o given in Table 2.4 to a non-trivial form). This allows improbable fragment compositions to be ignored and more readily correspond to the expected range of fragments formed from protoplanetary collisions (Carter et al. (2018)).

The prior on the pollution fraction was chosen to be log-uniform over a range where the upper limit corresponded to the 3σ limit on the most heavily polluted white dwarf and the lower limit corresponded to the most lightly polluted white dwarf in this thesis. Such a range was found to be sufficiently broad so that all the systems analysed in this thesis could have their pollution fractions robustly constrained.

It is unclear how long each individual white dwarf accretion event lasts. Estimates of such event lifetimes range from tens of years (Wyatt et al. (2014)) to millions of

years (Girven et al. (2012)). Theoretical considerations of Poynting-Robertson drag driven accretion suggest that disc lifetimes for discs with a mass of $\sim 10^{19}$ kg are of the order of millions of years (Rafikov (2011a); Rafikov (2011b)). In this work I chose a log-uniform prior distribution of accretion event lifetimes (t_{event}) ranging from 1 year to 100 million years in order to capture the full extent of possible disc lifetimes.

The prior distribution of the times since accretion started (t) are uniformly distributed between 0 Myrs and 20 Myrs after the accretion event has finished. 20 Myrs after the accretion event was chosen as an upper cut off as it was found to probe sufficiently far into the declining phase to model all the systems analysed in this thesis.

As outlined above it is expected that all the priors chosen are non-informative, which means they have a minimal effect on the constraints generated relative to the effect of the actual data, however, a full discussion of their validity will be presented in Section 2.6.

Model comparison

For each system analysed in this thesis the Bayesian evidence and χ^2 per element is found for various combinations of model parameters as described by Figure 2.16. Only models with the combinations of free parameters outlined in Figure 2.16 were used in order to minimise code run time, while simultaneously robustly investigating whether each main model parameter was necessary. Table 2.5 summarises the free parameters of each model used in this work. Once the various models have been used to fit the data, the model with the highest Bayesian evidence is selected as the optimum model. The χ^2 per element of the model fit is then checked in order to confirm that the 'best' model is not simply the best out of a group of models which all struggle to reproduce the observations. In this thesis a model with a χ^2 per element of less than 1 was considered to be a sufficient fit. By comparing the Bayesian evidence after removing or adding extra parameters a constraint on the necessity for the inclusion of such a parameter can be found. In this thesis I concentrate on the requirement for the inclusion of none-build-up phase accretion (by comparing models where steady state and declining phases are allowed against models where they are not), core-mantle differentiation (by comparing models with f_c as a free parameter against models without f_c as a free parameter), core-mantle-crust differentiation (by comparing models with f_o as a free parameter against models without f_o as a free parameter), heating during formation (by comparing models with $d_{\text{formation}}$ as a free parameter against models without $d_{\text{formation}}$ as a free parameter), and the presence of water ice (by comparing
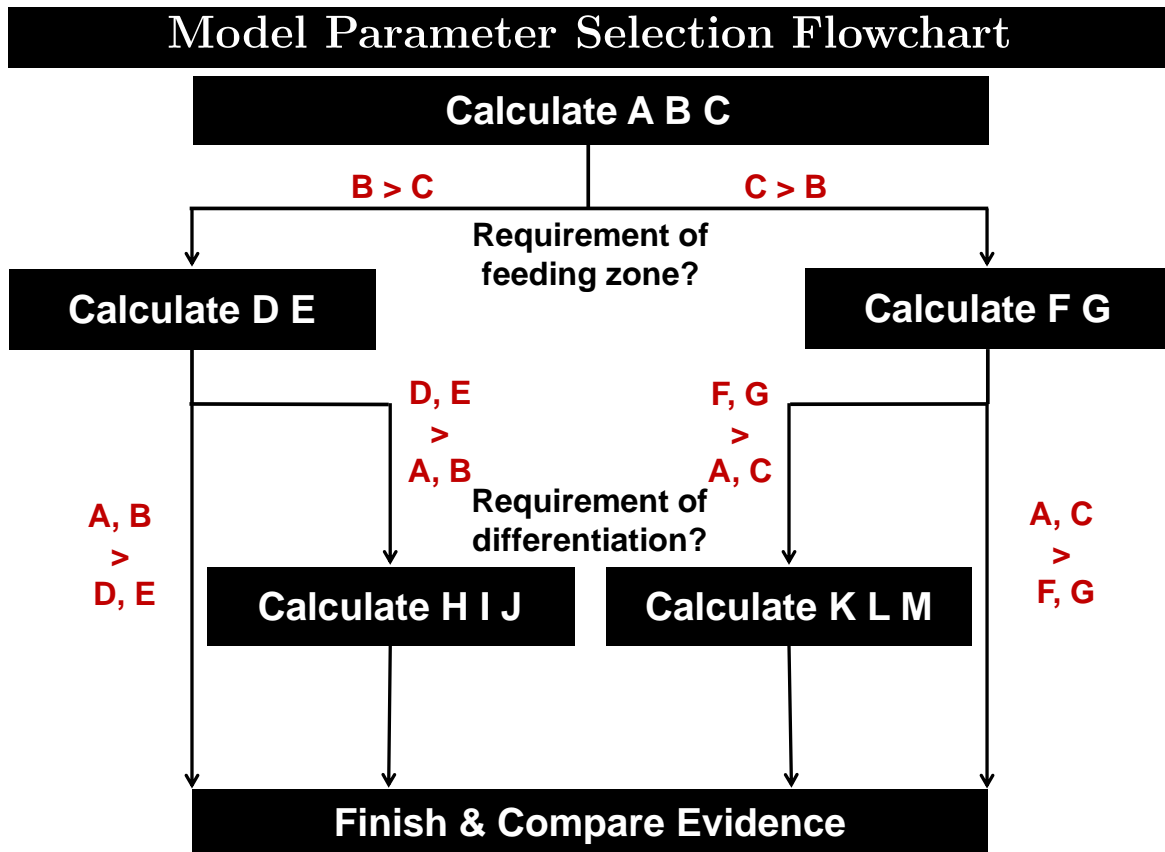
Fig. 2.16 A flowchart showing which model parameters where selected when analysing each system. The logic B>C, for example, is a command to only proceed if the Bayesian evidence of model B is greater than the Bayesian evidence of model C. Such a flowchart minimises run time of the code while also running enough models to constrain the requirement for the pollutant for the system to be: accreting in the declining or steady state phase, significantly heated during formation, partially composed of water ice, or a fragment of a differentiated body.

models where formation past the water ice line is allowed against models where it is not).

Table 2.5 A table describing the models compared in this thesis, in particular the free parameters considered for each model

Model Label	Model Parameters	Model Description
A	$[Fe/H]_{index}$, $P_{fraction}$, t_{event}, t	Primitive planetesimal with no heating
B	$[Fe/H]_{index}$, $P_{fraction}$, t_{event}, t, $d_{formation}$	Primitive planetesimal
C	$[Fe/H]_{index}$, $P_{fraction}$, t_{event}, t, $d_{formation}$, $z_{formation}$	Primitive planetesimal with feeding zone
D	$[Fe/H]_{index}$, $P_{fraction}$, t_{event}, t, $d_{formation}$, f_c	Core-mantle differentiated fragment
E	$[Fe/H]_{index}$, $P_{fraction}$, t_{event}, t, $d_{formation}$, f_c, f_o	Core-mantle-crust differentiated fragment
F	$[Fe/H]_{index}$, $P_{fraction}$, t_{event}, t, $d_{formation}$, $z_{formation}$, f_c	Core-mantle differentiated fragment with feeding zone
G	$[Fe/H]_{index}$, $P_{fraction}$, t_{event}, t, $d_{formation}$, $z_{formation}$, f_c, f_o	Core-mantle-crust differentiated fragment with feeding zone
H	$[Fe/H]_{index}$, $P_{fraction}$, t_{event}, t, $d_{formation}$, f_c, f_o, N_c	Model E with variable parent core fraction
I	$[Fe/H]_{index}$, $P_{fraction}$, t_{event}, t, $d_{formation}$, f_c, f_o, N_o	Model E with variable parent crust fraction
J	$[Fe/H]_{index}$, $P_{fraction}$, t_{event}, t, $d_{formation}$, f_c, f_o, N_c, N_o	Model E with variable parent core and crust fraction
K	$[Fe/H]_{index}$, $P_{fraction}$, t_{event}, t, $d_{formation}$, $z_{formation}$, f_c, f_o, N_c	Model G with variable parent core fraction
L	$[Fe/H]_{index}$, $P_{fraction}$, t_{event}, t, $d_{formation}$, $z_{formation}$, f_c, f_o, N_o	Model G with variable parent crust fraction
M	$[Fe/H]_{index}$, $P_{fraction}$, t_{event}, t, $d_{formation}$, $z_{formation}$, f_c, f_o, N_c, N_o	Model G with variable parent core and crust fraction

2.5   Testing the model on the Solar System

In order to test the validity of model outlined in this chapter, I attempted to recreate the abundances present in some of the Solar System bodies discussed in Chapter 1. In order to test the full model and the statistical framework, I assumed that 10^{20} kg of material with the composition of a given Solar System body was accreted onto a helium dominated white dwarf of mass $0.6 M_\odot$, surface temperature 8,000 K, and convective zone mass to total mass ratio of $10^{-5.527}$. The system was also assumed to be observed in the build-up phase. Such a scenario was chosen in order to probe the full parameter space of the model for a typical polluted white dwarf system and allows the models accuracy and validity to be critically reviewed. It is important to note that some changes have been made to the model such that it is not identical to the model which will be used to analyse white dwarfs. Instead of selecting a random star from the refined Brewer et al. (2016) catalogue when modelling the abundances, a star with solar abundances is chosen each time. Additionally, the protoplanetary disc model outlined previously is adjusted such that it models a disc around a sun-like star of $1 M_\odot$ rather than an A0-type star. Errors on the abundances for all elements were assumed to be 0.05 dex for the chondrites and iron meteorites, and 0.10 dex for the shergottites and the inferred bulk planetary compositions. These errors are approximately the current minimum reported uncertainties available for polluted white dwarf systems, while also being inline with the compositional uncertainties and compositional deviations found in various meteorite samples and planetary interior models (McDonough and Sun (1995); Lodders and Fegley (1998); McDonough (2003); Siebert et al. (2018)).

2.5.1   Reproducing the primitive meteorite suites

Initially, I attempted to fit the abundances of the primitive meteorite suites, namely the CI carbonaceous chondrites and the H ordinary chondrites. As discussed in Chapter 1, the chondrites are primitive meteorites whose abundances have been shown in previous work to be consistent with the solar photosphere in conjunction with a volatile depletion trend (e.g. Lodders (2003)). The CI chondrites are volatile rich and have water ice fractions up to 20% by mass, whereas H chondrites are dry (Sears (2005)).

Figure 2.17 shows the abundances of the CI chondrites given in Lodders and Fegley (1998) and the fit for the model with the highest Bayesian evidence. The x axis displays the key-rock forming elemental abundances in volatility order, increasing from left to right. The x axis is also grouped via the Goldschmidt classification while the y axis is normalised to the average star in the Brewer et al. (2016) catalogue. Such ordering

Fig. 2.17 The fit of the model with the highest Bayesian evidence to the composition of the CI chondrites. The model constrains the material to be primitive, to have undergone formational heating, and to contain water ice as expected. The model also correctly predicts the accretion to be of a 10^{20} kg body in build-up phase.

of the elements allows trends related to incomplete condensation, differentiation and fragmentation, and differential sinking through the white dwarfs atmosphere to be easily noted by eye as highlighted in the figures in Section 2.2. The model can reproduce the abundances in the CI chondrites well, $\chi^2_{pdp} = 0.84$, and correctly predicts that $10^{19.99^{+0.27}_{-0.04}}$ kg of material is accreting in the build-up phase. The material is found to be primitive, as expected, and does not require geological processing. The formation temperature is constrained to be 136.0 ± 0.6 K and therefore, there is a 2.7σ constraint that the pollutant material contains water ice and a 4.7σ constraint that formational heating occurred such that the material has depleted volatile abundances relative to solar.

Figure 2.18 shows the abundances of the H chondrites given in Lodders and Fegley (1998) and the fit for the model with the highest Bayesian evidence. The model can reproduce the abundances in the H chondrites well, $\chi^2_{pdp} = 0.39$, and correctly predicts that $10^{20.27^{+0.05}_{-0.28}}$ kg of material is accreting in the build-up phase. The material is found to not require geological processing and is therefore primitive. The formation temperature is constrained to be $259.4^{+139.6}_{-99.8}$ K and so there is a 10.6σ constraint that formational heating occurred such that oxygen only partially condensed from the Solar nebula.
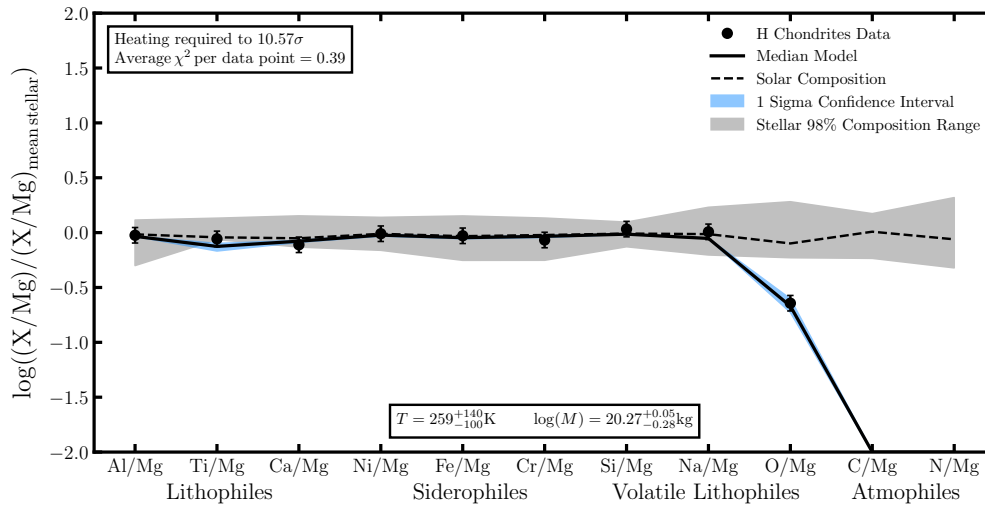
Fig. 2.18 The fit of the model with the highest Bayesian evidence to the composition of the H chondrites. The model constrains the material to be primitive and requires it to have undergone formational heating as expected. The model also correctly predicts the accretion to be of a 10^{20} kg body in build-up phase.

The model presented in this thesis can accurately reproduce the composition of both the CI chondrites and the H chondrites. The model also correctly deduces the pollutant mass and phase of accretion for both bodies. The formation temperature is well constrained for both systems, mainly due to the O and Na abundances, and as expected suggests the CI chondrites formed at lower temperatures than the H chondrites. The model also deduces the presence of water ice in the case of the CI chondrites.

2.5.2   Reproducing the telluric planets and Vesta

As outlined in Chapter 1 the bulk compositions of the Earth, Venus, Mars, Mercury, and Vesta have mainly been constrained using their bulk parameters and the meteoritic samples which originate from them. The compositions presented in McDonough (2003) and Lodders and Fegley (1998) were inputted into the model outlined in this chapter. The Earth, Venus, Mars, and Vesta are thought to be bodies with a generally primitive composition that has not been dramatically changed by differentiation followed by global fragmentation, while Mercury is thought to have had its mantle partially stripped during a giant impact as discussed in Chapter 1. All 5 bodies are expected to have undergone formational heating, and if the currently accepted hypothesis is true that
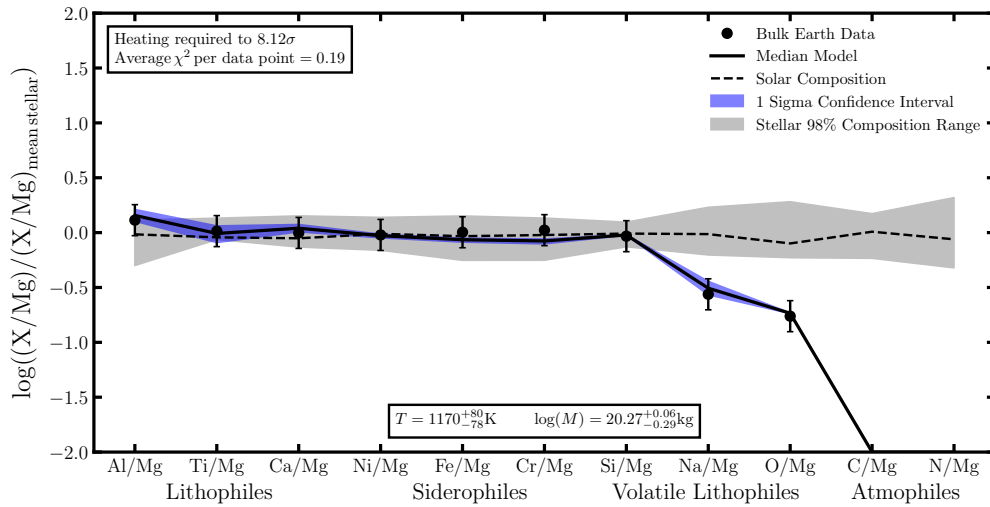
Fig. 2.19 The fit of the model with the highest Bayesian evidence to the composition of bulk Earth. The model constrains the material to be primitive and requires it to have undergone formational heating as expected. The model also correctly predicts the accretion to be of a 10^{20} kg body in build-up phase.

the inner planets formed in situ, then the closer-in bodies should be composed of material which underwent heating at higher temperatures. As introduced in Section 1.1.2 post-nebula volatilisation can deplete the abundances of Na in a rocky world if the body is sufficiently small such that outgassed material can escape from the body. Post-nebula volatilisation is not part of the model outlined thus far, therefore, the formation temperatures derived for the smaller bodies (Mars, Mercury, and Vesta) are more indicative of the maximum temperature reached during a post-nebula phase rather than a formation temperature. This caveat will be discussed further in Section 2.6.

Figure 2.19 shows the model fit with the highest Bayesian evidence for bulk Earth. The model fits the data to a $\chi^2_{\mathrm{pdp}} = 0.19$ and finds that the pollutant is accreting in the build-up phase with an expected pollutant mass of $10^{20.26^{+0.06}_{-0.29}}$ kg. The body is found to not require differentiation and fragmentation to have occurred in order to explain its composition and its formation temperature is constrained to be 1170^{+80}_{-78} K. The model fit requires the inclusion of formational heating to a significance of 8.12σ in order to explain the sub-Solar Na and O abundances.

Figure 2.20 shows the model fit with the highest Bayesian evidence for bulk Venus. The model can fit the data to a $\chi^2_{\mathrm{pdp}} = 0.27$. The model finds the pollutant to be accreting in the build-up phase with an expected pollutant mass of $10^{20.24^{+0.06}_{-0.29}}$ kg.
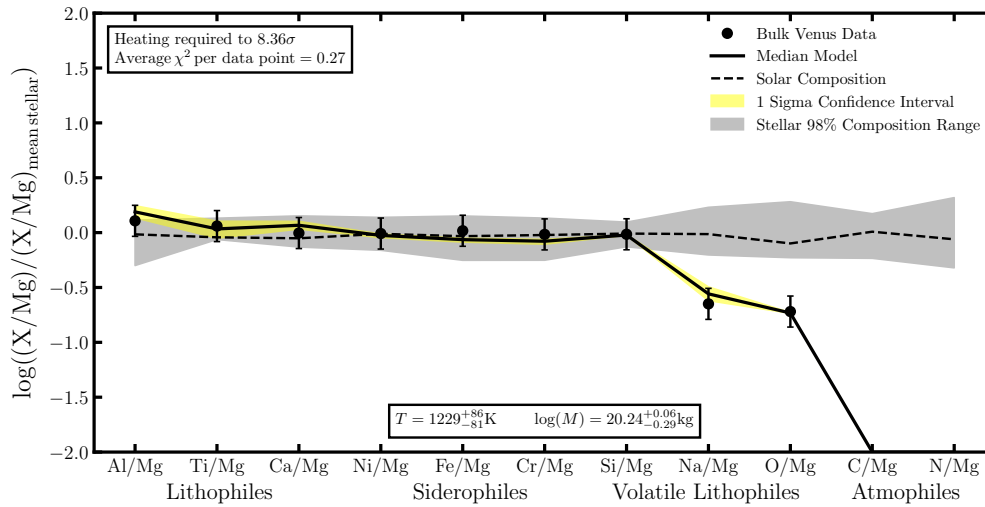
Fig. 2.20 The fit of the model with the highest Bayesian evidence to the composition of bulk Venus. The model constrains the material to be primitive and requires it to have undergone formational heating as expected. The model also correctly predicts the accretion to be of a 10^{20} kg body in build-up phase.

The body is found to have a primitive composition and therefore does not require differentiation and fragmentation to explain its abundances. The formation temperature is constrained to be 1229^{+86}_{-81} K and heating is required to model the abundances to a significance of 8.36σ in order to explain the sub-Solar Na and O abundances.

Figure 2.21 shows the model fit with the highest Bayesian evidence for bulk Mars. The model can fit the data to a $\chi^2_{\mathrm{pdp}} = 0.42$. The model finds the pollutant to be accreting in the build-up phase with an expected pollutant mass of $10^{20.22^{+0.07}_{-0.28}}$ kg. The pollutant is found to be primitive and not require differentiation and fragmentation to explain its composition. The pollutant's formation temperature is constrained to be 1155^{+84}_{-81} K and heating is required to a significance of 7.19σ.

Figure 2.22 shows the model fit with the highest Bayesian evidence for bulk Mercury. The model can fit the data to a $\chi^2_{\mathrm{pdp}} = 0.47$. The model finds the pollutant to be accreting in the build-up phase with an expected pollutant mass of $10^{20.24^{+0.08}_{-0.27}}$ kg. The pollutant is required to be a core-rich fragment of a differentiated body to a significance of 8.09σ and its formation temperature is constrained to be 1413^{+76}_{-38} K and heating is required to a significance of 13.38σ.

Figure 2.23 shows the model fit with the highest Bayesian evidence for bulk Vesta. The model can fit the data to a $\chi^2_{\mathrm{pdp}} = 0.09$. The model finds the pollutant to be accreting in the build-up phase with an expected pollutant mass of $10^{20.25^{+0.08}_{-0.27}}$ kg. The
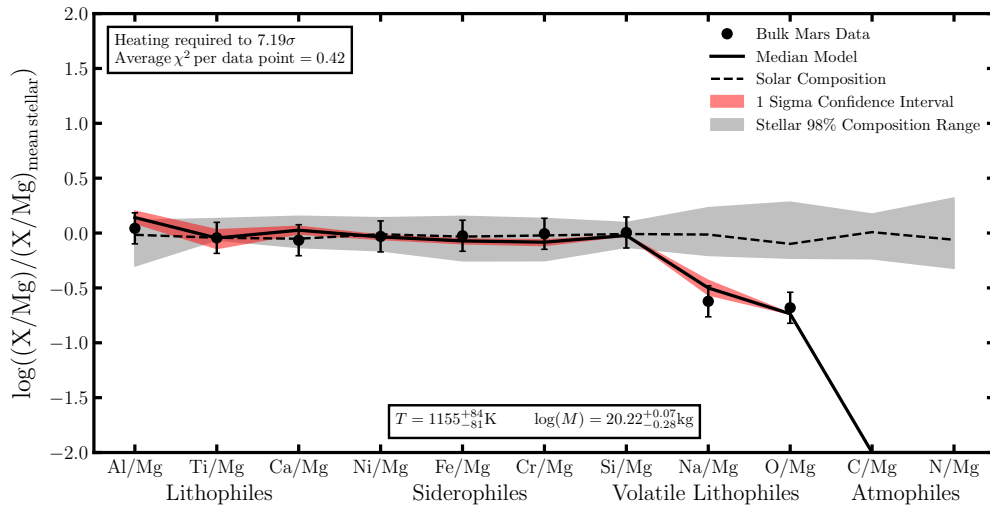
Fig. 2.21 The fit of the model with the highest Bayesian evidence to the composition of bulk Mars. The model constrains the material to be primitive and requires it to have undergone formational heating as expected. The model also correctly predicts the accretion to be of a 10^{20} kg body in build-up phase.
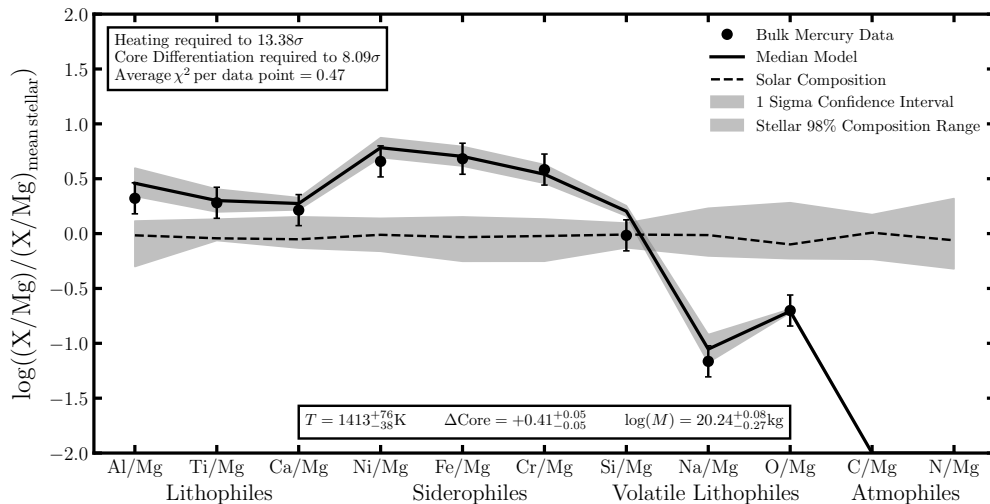
Fig. 2.22 The fit of the model with the highest Bayesian evidence to the composition of bulk Mercury. The model constrains the material to be a core-rich fragment of an originally larger body and requires it to have undergone formational heating. The model also correctly predicts the accretion to be of a 10^{20} kg body in build-up phase.
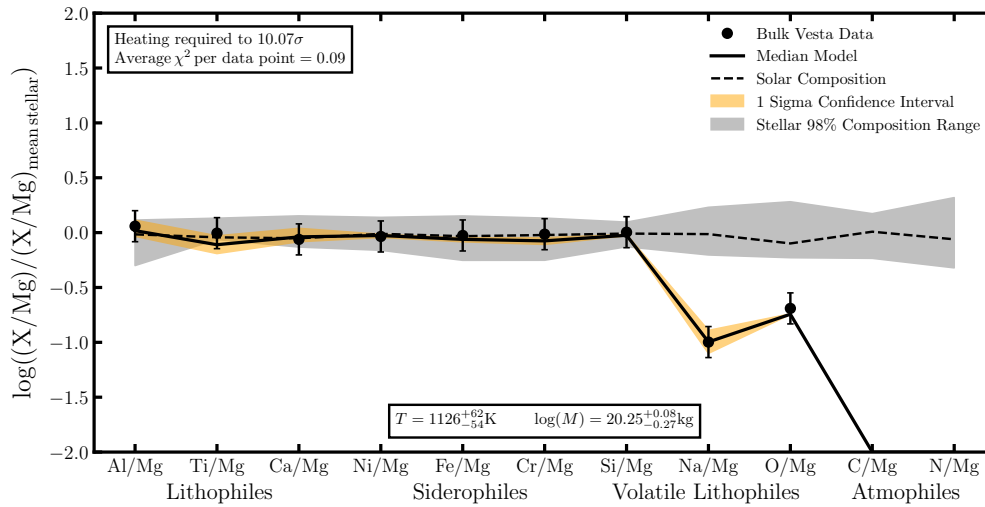
Fig. 2.23 The fit of the model with the highest Bayesian evidence to the composition of bulk Vesta. The model constrains the material to be primitive and requires it to have undergone formational heating as expected. The model also correctly predicts the accretion to be of a 10^{20} kg body in build-up phase.

pollutant is not required to have undergone differentiation and fragmentation and its formation temperature is constrained to be 1126^{+62}_{-54} K and heating is required to a significance of 10.07σ.

The model can accurately reproduce the bulk compositions of the telluric planets and Vesta while also finding the expected formation temperature order for the bodies if one assumes that they formed in situ. The composition of Mercury is explained by Mercury being a core-rich fragment which has had a significant fraction of its mantle stripped as currently hypotheised in the literature (e.g. Benz et al. (1988)) whereas the other 4 bodies are consistent with primitive compositions as expected. Importantly the model also correctly constrains the phase of accretion and pollutant mass for all the bodies.

2.5.3   Reproducing the non-primitive meteorite suites

The composition of the non-primitive meteorites suites offer a unique insight into the differentiation processes which occur in the Solar System. As outlined in Chapter 1 non-primitive meteorites falls into two main classes: Fe meteorites and achondrites. The ability of the model to reproduce the abundances measured for each of these classes was tested by inputting the abundances given in Lodders and Fegley (1998)
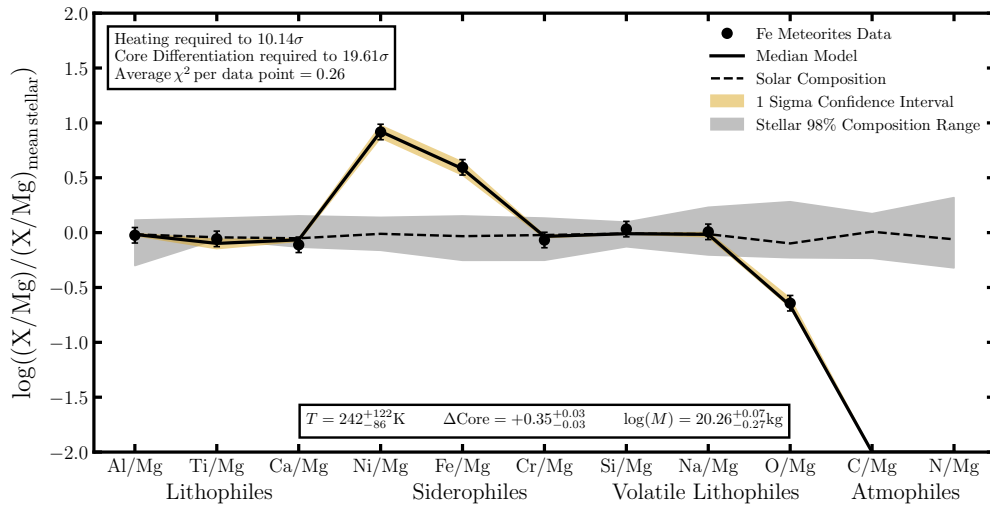
Fig. 2.24 The fit of the model with the highest Bayesian evidence to the composition of a body half composed of type IV Fe meteorite material and half composed of H chondrite material. The model constrains the body to be a core-rich fragment of a differentiated body and requires it to have undergone formational heating as expected. The model also correctly predicts the accretion to be of a 10^{20} kg body in build-up phase.

for the class IV Fe meteorites and the Sheggottites into the model. As introduced in Chapter 1, the Sheggottites are thought to be fragments of the crust of Mars while the Fe meteorites are thought to be fragments of the core of a differentiated asteroid.

Figure 2.24 shows the model fit with the highest Bayesian evidence for the Fe meteorites. As the Fe meteorites do not have a significant lithophile content the data chosen was that for a body composed of 50% Fe meteorite material and 50% H chondrite material. The standard model cannot fit the data accurately due to the Ni/Fe ratio of the iron meteorites being much higher than the Ni/Fe ratio of the Earth, as mentioned in Chapter 1. Therefore, the core composition of the model has been adjusted such that the core is twice as rich in Ni and contains no Cr, such a change allows the model to fit the data to a $\chi^2_{\mathrm{pdp}} = 0.26$. This model finds the pollutant to be accreting in the build-up phase with an expected pollutant mass of $10^{20.26^{+0.07}_{-0.27}}$ kg. As expected the pollutant is required to be a core-rich fragment of a differentiated body to a significance of 19.61σ and its formation temperature is constrained to be 242^{+112}_{-85} K.

Figure 2.25 shows the model fit with the highest Bayesian evidence for the Shergotty meteorites. The standard model cannot fit the data accurately due to the Ni and Cr abundances of the Shergottites. Therefore, as with the Fe meteorites, the core
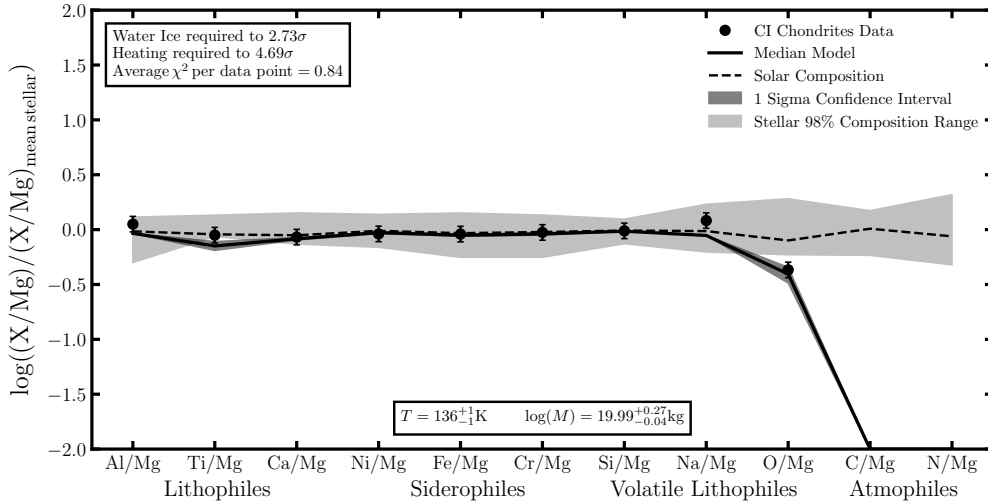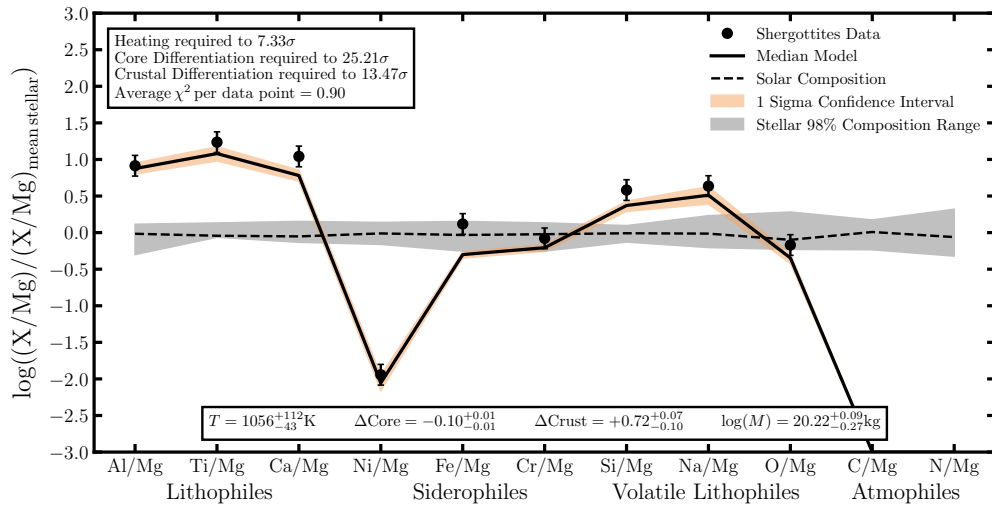
Fig. 2.25 The fit of the model with the highest Bayesian evidence to the composition of the Shergotty meteorites. The model constrains the body to be a crust-rich fragment of a differentiated body and requires it to have undergone formational heating as expected. The model also correctly predicts the accretion to be of a 10^{20} kg body in build-up phase.

composition of the model has been adjusted such that the core is twice as rich in Ni and contains no Cr, such a change allows the model to fit the data to a $\chi^2_{\mathrm{pdp}} = 0.90$. This model finds the pollutant to be accreting in the build-up phase with an expected pollutant mass of $10^{20.22^{+0.09}_{-0.27}}$ kg. As expected the pollutant is required to be a crust-rich fragment of a differentiated body to a significance of 13.47σ. The formation temperature is also consistent with the formation temperature predicted by the model for bulk Mars.

In order to reproduce the compositions of the non-primitive meteorite suites adjustments need to be made to the model in order to account of the fact that differentiation under non-Earth-like conditions produces mantles which have different siderophile abundances. Given the uncertainties on polluted white dwarf data and the detection thresholds for polluted white dwarfs the addition of non-Earth-like differentiation conditions is unlikely to be required to explain the abundances observed in the majority of systems. Therefore, the lack of a robust pressure-varying differentiation model will not pose an issue in the most part. However, a robust differentiation model would be a valuable upgrade to the model in the future.

2.6   Discussion

In this chapter I have presented a model which can help improve the understanding of the origin of white dwarf pollutants by constraining the possible formation scenarios which are compatible with the observed atmospheric abundances. The model takes the observed atmospheric elemental abundances of Al, Ti, Ca, Ni, Fe, Cr, Mg, Si, O, Na, and possibly C and N, and attempts to reproduce a white dwarf atmosphere with a similar composition assuming the accretion of a single planetesimal whose abundances are mainly determined by the initial composition of the protoplanetary disc it formed in, heating processes during formation, and differentiation followed by collisional processing. Using a Bayesian framework constraints are then placed on the model parameters and the most likely formational history of the pollutant material can be found. The model presented is based on many assumptions and, therefore, the results are subject to many caveats. In the subsequent section I will discuss the notable caveats and how they affect the conclusions one can draw from the model outlined in this chapter.

2.6.1   Discussion of caveats

In the model outlined in this chapter I have assumed that the pollution present in the white dwarfs atmospheres is the result of the accretion of one polluting body. Pollution could potentially arise from multiple bodies which were accreted in a similar time frame (Wyatt et al. (2014)), however, it is not anticipated that this would affect the results dramatically, as the abundances are still expected to be dominated by the largest body. It is possible to use the model to test this assumption because if multiple bodies with a similar mass were accreted, one would expect that any signatures of differentiation would be washed out, as it is unlikely that all the bodies would have a similar geological history. Therefore, if a significant fraction of white dwarfs are found to be polluted by fragments of differentiated bodies the assumption of abundances dominated by single bodies would be validated.

When modelling the abundances a key caveat is the phase of accretion which manifests itself mathematically into the model when converting from planetesimal abundances to atmospheric abundances. The model assumed in this thesis is the one outlined in Koester (2009) and therefore does not include the possibility of a thermohaline instability developing in the white dwarf atmosphere. The ability for a thermohaline instability to develop in polluted white dwarf atmospheres is much debated in the literature (Deal et al. (2012); Koester (2014); Bauer and Bildsten

(2018)). However, if such an instability did develop the major consequence would be that polluted white dwarf systems would not reach a steady state phase of accretion. Therefore, again it is possible to use the model to test this assumption, because if thermohaline instabilities did develop in polluted white dwarf atmospheres then it would be impossible to detect any systems in the steady state phase. Thus, the detection of systems whose abundances suggest they are in a steady state phase of accretion would support the argument that thermohaline instabilities do not develop in polluted white dwarf atmospheres.

The modelling of planetesimal abundances in this thesis involves many assumptions. Firstly, the stellar catalogue used to model the initial nebula conditions is assumed to have compositions similar to the compositions of the white dwarf progenitors and the planet forming material around them. Potentially, this could not be the case. However, as outlined when selecting the catalogue, it is not expected that the progenitors of white dwarfs would have formed from nebulae with a dramatically different composition to those modelled. If the stellar sample was found to be invalid the main effect would be that when the model suggests that differentiation and/or heating is required the statistical significance of such a requirement would become weaker if the new sample had a larger range of abundances or stronger if the new sample had a smaller range of abundances.

Another major assumption of the model is that the pollutants are planetesimals whose abundances are dictated when they condense out of a protoplanetary disc in chemical equilibrium. While this is a simplistic assumption, the model can reproduce the major elemental composition of the rocky bodies in the Solar System, as shown in this chapter and in Moriarty et al. (2014). Additionally, as outlined in Chapter 1, evidence from the Earth does suggest a nebula condensation rather than volatilisation origin to the elemental abundances (Palme and O'Neill (2003)). However, the abundance of Mn in many Solar System bodies does suggest that post-nebula volatilisation did occur (Chapter 1; O'Neill and Palme (2008)). I do not take post-nebula volatilisation effects into account in the model outlined in this chapter but taking it into account is not expected to drastically change the conclusions as the majority of elements are depleted in a similar fashion during incomplete condensation and during post-nebula heating. Though it should be noted that due to the potential effects of post-nebula volatilisation the temperatures constrained from the model are effectively the maximum temperatures experienced by the bodies rather than strict formation temperatures. One key exception is Mn, which is not modelled in this chapter but does behave as a volatile in nebula conditions but as a refractory element in post-nebula conditions.

In Chapter 5 I will use the unique behavior of Mn and the few polluted white dwarfs with Mn abundances to investigate this assumption and probe the potential effects of post-nebula volatilisation.

The only major inconsistency in the equilibrium chemistry model and Solar System major elemental observations is the predicted C abundances. This is mainly due to the incompleteness of the HSC chemistry database and a lack of understanding of the cosmochemistry of solid C species. This does not detract from the strong reproduction of the other elemental abundances as C is only a trace species and for the most part in this thesis C abundances of pollutants will not be incorporated into the model fits. The disc model used assumes no vertical mixing and utlilises an alpha parameterisation. The use of this simplistic model is not expected to dramatically effect the results as it is only used to convert protoplanetary disc formation times and distances into temperatures and pressures. Therefore, even if the exact conversion is not robust the temperatures constrained should remain reliable. Planetesimal formation is clearly significantly more complex than the model suggests and planetary migration and dust migration are potentially crucial effects that are not included in the model (Desch et al. (2017a); Desch et al. (2017b)). However, given the model's ability to reproduce the abundances of the Solar System bodies, the inclusion of a more sophisticated disc, chemistry, and planetesimal formation model will likely not effect the results and is likely not necessary.

The final major caveat of the planetesimal abundance model involves the differentiation prescription used. The differentiation model used in this work is Earth-centric as it assumes that the cores of planetary bodies form with the same composition as the Earth's core and the crusts of planetary bodies form with the same composition as the Earth's oceanic crust. This is clearly unrealistic as laboratory experiments have shown that the fraction of siderophilic elements which sequester into the core is dependent on the temperature, pressure, and oxygen fugacity (among other things) at the core-mantle boundary (Bouhifd and Jephcoat (2011); Siebert et al. (2012); Fischer et al. (2015)). However, given the uncertainties on the majority of white dwarf systems, such effects are generally not expected to be required to explain the abundances observed. However, a proxy model which manually adjusts the core abundances of Cr, Ni and the light elements will be implemented if necessary in order to highlight systems which could potentially require non-Earth-like differentiation conditions in order to explain their abundances.

The main caveats involving the statistical framework used in this work involve the number of live points selected and the choice of prior distributions. The number of live

points chosen for each model run was 1,500 as this was found to be sufficient to calculate the log Bayesian evidence to an uncertainty of the order 0.1. Increasing the number of live points would no doubt decrease this uncertainty however it is already small enough that any changes would not effect any of the results presented in this thesis. Regarding the prior distributions, the majority were fixed by the model, however, the formation time, feeding zone size, time since accretion started, accretion event lifetime, and pollution fraction were not. The feeding zone size, time since accretion started, and pollution fraction were tested for various physically realistic ranges and it was found for the white dwarfs analysed in this thesis the ranges were sufficient to be well constrained for all the systems which required them. The ranges for the formation time and accretion event lifetime were constrained by previous studies (Girven et al. (2012); Wyatt et al. (2014); Ribas et al. (2015)). Therefore, these distributions could potentially be changed if new evidence was presented, however, it is not expected that such changes will effect the results presented.

Although the model is subject to many caveats, one major strength is that it can accurately reproduce the abundances of the Solar System bodies. Therefore, although the caveats are important to note, they are not expected to severely affect the usefulness of the model.

2.6.2   Discussion of results

The tests performed on the Solar System bodies presented in this chapter are crucial not just because they validate the model assumed, but they also highlight which elemental abundances are key in providing strong constraints on the origin of planetary material. O is an invaluable element as it allows the accretion of stellar material to be ruled out in favour of the accretion of rocky planetary material. Additionally, as O varies over a wide temperature range it is useful in constraining a body's formation temperature. Na is also a key element in determining the formation temperature of the material as its condensation temperature is $\sim$1,000 K so the Na abundance of a body can easily constrain the formation temperature to be greater than or less than $\sim$1,000 K. Na also allows a key degeneracy between crust-rich material and heated material to be broken. Enhanced Al, Ti, and Ca abundances can be representative of either heating effects or crustal differentiation effects. As Na is a strong lithophile but also a volatile element, crust-rich systems should be rich in Na, while strongly heated systems should be poor in Na, therefore, breaking the degeneracy. Mg and Si are vital benchmark elements as they seldom change with formation temperature or differentation and fragmentation and have long sinking timescales. Mg and Si also make up the majority of the rocks in

the Solar System, therefore, their abundances are crucial when comparing the nature of exo-planetary bodies to Solar System bodies. Si is more variable than Mg so all plotted abundances in this work are ratioed to Mg in order to easily pick out trends in the abundances by eye. Al, Ti, Ca are useful elements because as mentioned previously they probe crust formation and formation temperature as they are lithophilic and refractory, while Fe, Ni, Cr are useful elements as they probe core formation.

Using as many elements as possible when constraining the origin of the polluting material is critical as contradictions between abundances allow trends related to elemental volatility or differentiation to be ruled out. Ideally each system analysed would have two lithophiles, two siderophiles, and two volatiles as well as Mg and Si as this would robustly test the model while allowing degeneracies between the main abundance altering effects to be removed.

The tests on the Solar System bodies also show that it should be possible to determine whether the pollutants were significantly heated during formation, were fragments of differentiated bodies, or were composed of water ice to a high level of statistical significance with the level of uncertainty currently reported for white dwarf atmospheric abundances. The masses of polluting material, the formation location, as well as the phase of accretion should also be possible to constrain given the current state of the art observations.

2.7   Conclusions

In this chapter a method for determining the most probable formation history of the rocky planetary material that pollutes the atmospheres of some white dwarfs was presented. The method attempts to match the abundance patterns observed in the externally polluted white dwarfs' atmospheres to the bulk chemical abundances expected from the accretion of planetesimals which could have formed in protoplanetary discs with a range of initial compositions, at various locations, and with various geological and collisional histories. The strength of the model is that it calculates the statistical significance to which certain formation histories are required. In this chapter the model was tested by attempting to reproduce the abundances of the Solar System bodies. The abundances of the Solar System bodies were well reproduced validating the model and the assumptions made. It was calculated that given the current reported uncertainties on white dwarf atmospheric abundances the presence of water ice should be determinable, along with the requirement for pollutants to be fragments

of differentiated bodies. It is also expected that the mass of the pollutants, the phase of accretion, and the formation location of the pollutants should be constrainable.

Chapter 3

The diversity of white dwarf pollutants

3.1 Introduction

The atmospheric abundances of polluted white dwarfs offer a unique opportunity to study the composition of rocky exo-planetary material. Therefore, understanding and modelling the chemical composition of white dwarf atmospheres can offer insights into the formation and evolution of rocky extrasolar worlds which cannot be found by other means. In this chapter, I use the model outlined in Chapter 2 to fit the abundances of the most heavily polluted white dwarfs in order to constrain the origin and geology of their pollutants. The model aims to constrain four main properties of the white dwarf pollutants: their formation temperature, their mass, the phase of accretion they are observed in, and whether geo-chemical differentiation followed by collisional processing is required to explain their abundances. It should be noted that all constraints on the mass are lower limits unless the system is expected to be in the declining phase, and therefore additional mass present in a circumstellar reservoir can be ruled out. Additionally, it should also be noted that due to observational bias polluted white dwarf systems which accrete low quantities of planetary material are difficult to detect therefore the conclusions drawn in the chapter relate only to the most heaviliy polluted systems. Constraining the four pollutant properties will further the understanding of the formation location of white dwarf pollutants as well as their size, while simultaneously probing the geological processes which occur in exo-planetary systems. When selecting the sample of white dwarfs to analyse in this chapter I chose to only analyse white dwarfs with published abundances and uncertainties of at least 4 elements. This refined the sample to include only white dwarf systems which are

historically the most well studied and thus, the most valuable to constrain. In Section 3.2, I present the results for each system individually, in chronological order of when the abundance measurements were made, and compare my findings to the findings previously published in the literature. In Section 3.3, I summarise and bring together the key results for the individual white dwarf systems analysed and discuss the key findings of this chapter. In Section 3.4, I outline the conclusions of this study.

3.2 Individual Systems

3.2.1 GD362

Table 3.1 displays the stellar data, the atmospheric abundances, and the sinking timescales presented in Zuckerman et al. (2007) and Xu et al. (2013) for the GD362 system. The white dwarf properties and atmospheric abundances, other than the C abundance and the upper limits, were inputted into the model in order to constrain the origin and geology of the polluting material.

Figure 3.1 displays the model fit with the highest Bayesian evidence, which has a χ^2_{pdp} of 0.56. It should be noted that Figure 3.1 poorly represents the actual quality of the fit due to the model mainly struggling to fit Mg (which every element is ratioed to in the figure). A scenario in which the pollutant material is accreting in build-up phase and is a primitive body which has experienced temperatures of the order 1,400 K such that the moderate volatiles were depleted best explains the atmospheric abundances. The model parameters utilised in the optimised model fit are: the stellar metallicity index, the pollution fraction, the accretion event lifetime, the time passed since accretion started, the formation distance, and the feeding zone size. The model produces a 5.87σ constraint on the pollutant being formed through incomplete nebula condensation. The mass of the polluting body is constrained to be above $10^{19.80}$ kg suggesting that the polluting body is at least 25% as massive as Vesta, and therefore, is likely a body equivalent to a large asteroid or minor planet.

Xu et al. (2013) concluded that the pollutant material could potentially be explained by the accretion of a body similar to the Solar System's stony-iron meteorites. The main issue with this hypothesis, as noted by Xu et al. (2013), is that it is difficult to explain how one could form a large enough body with a stony-iron meteorite type composition. As outlined in Chapter 1, stony-iron meteorites are expected to form when differentiated bodies collide and merge before subsequent collisions disrupt the body further. Such a formation process only produces a relatively small mass of

Fig. 3.1 The fit of model with the highest Bayesian evidence to the atmospheric abundances observed in GD362. The polluting material is most likely accreting in build-up phase and is a primitive body which has undergone sufficient heating such that the moderate volatiles incompletely condensed from the nebula.

Table 3.1 Data for GD362 (Zuckerman et al. (2007); Xu et al. (2013)). q is the logarithm of the ratio of the mass of the convective zone to the mass of the white dwarf.

Type	q	$M_{\mathrm{WD}}/M_\odot$	T/K
DBZ	-6.71	0.72	10,500
Element	log(Abundance/He)	log(Sinking Timescale/years)	
Al	-6.40 ± 0.20	5.20	
Ti	-7.95 ± 0.10	4.97	
Ca	-6.24 ± 0.10	5.00	
Ni	-7.07 ± 0.15	5.00	
Fe	-5.65 ± 0.10	5.04	
Cr	-7.41 ± 0.10	5.00	
Mg	-5.98 ± 0.25	5.34	
Si	-5.84 ± 0.30	5.08	
Na	-7.79 ± 0.20	5.34	
O	< -5.14	5.34	
C	-6.70 ± 0.30	5.32	
N	< -4.14	5.34	

stony-iron meteorite type bodies. In this thesis I find that it is possible to explain the abundances of GD362 by processes related to elemental volatility, and therefore run into no such issues. The abundance pattern observed is reproduced well by the composition of material expected to form at temperatures over 1,300 K.

3.2.2 GD40

Table 3.2 displays the stellar data derived in Klein et al. (2010), the atmospheric abundances given in Klein et al. (2010) and Jura et al. (2012), and the sinking timescales presented in Xu et al. (2013) for the GD40 system. These white dwarf properties and abundances, other than the C abundance and the N upper limit, were inputted into the model in order to constrain the origin and geology of the polluting material.

Figure 3.2 displays the model fit with the highest Bayesian evidence, which is a strong fit to the data with a χ^2_{pdp} of 0.39. A scenario in which the pollutant material is accreting in build-up phase, is primitive in composition, and has experienced temperatures of the order 1,200 K best explains the atmospheric abundances. The model parameters utilised in the optimised model fit are: the stellar metallicity index, the pollution fraction, the accretion event lifetime, the time passed since accretion started, and the formation distance. The model produces a 4.56σ constraint on the pollutant requiring incomplete nebula condensation to explain the abundances. Measurements of the Na abundance in the system would allow the model to further constrain the formation temperature, however the high temperature of the white dwarf means the detection of Na is unlikely. The mass of the body is constrained to be above $10^{19.90}$ kg suggesting that the polluting body is at least 30% the mass of Vesta. Therefore, is likely of a similar size to a large asteroid or minor planet.

Initially in the literature the pollutant of GD40 was classified as potentially being a fragment of a differentiated body (Klein et al. (2010)), however, further study and improved uncertainty estimates suggested that the material was in fact consistent with being primitive (Jura et al. (2012); Xu et al. (2013)). In Jura et al. (2012) the heavily depleted O, S, and C abundances were used to conclude that the polluting body formed well inside the various ice lines and did not contain substantial water. The model outlined in this thesis supports the conclusion that the polluting material is most likely primitive and has experienced sufficient formational heating such that it is not rich in ice species.
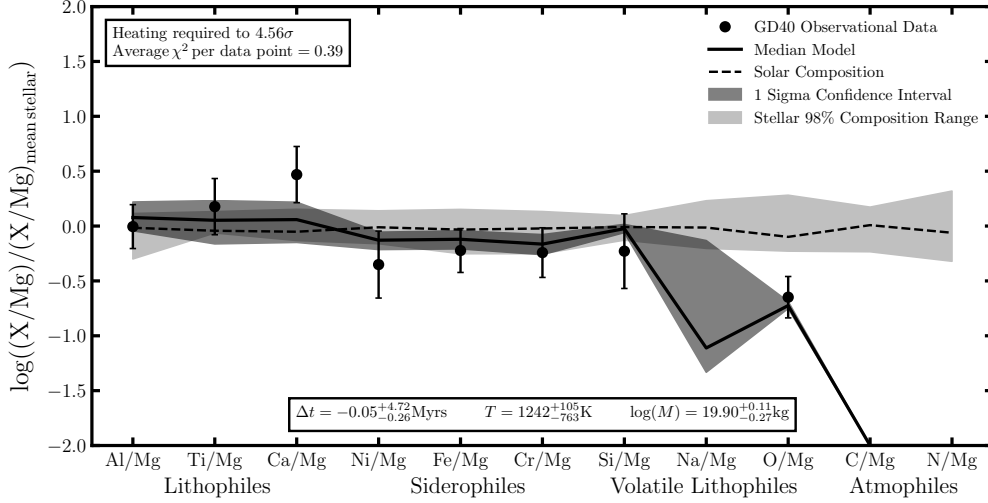
Fig. 3.2 The fit of model with the highest Bayesian evidence to the atmospheric abundances observed in GD40. The polluting material is consistent with being primitive, modified only due to incomplete condensation, and accreting in the build-up phase.

Table 3.2 Data for GD40 (Klein et al. (2010); Jura et al. (2012); Xu et al. (2013)).

Type	q	$M_{\mathrm{WD}}/M_\odot$	T/K
DBZ	-5.85	0.60	15,300
Element	log(Abundance/He)	log(Sinking Timescale/years)	
Al	-7.35 ± 0.12	6.08	
Ti	-8.61 ± 0.20	5.69	
Ca	-6.90 ± 0.20	5.71	
Ni	-7.84 ± 0.26	5.79	
Fe	-6.47 ± 0.12	5.75	
Cr	-8.31 ± 0.16	5.72	
Mg	-6.20 ± 0.16	6.08	
Si	-6.44 ± 0.30	6.00	
Na	—	6.08	
O	-5.62 ± 0.10	6.04	
C	-7.80 ± 0.20	6.04	
N	< -8.8	6.04	

3.2.3 G241-6

Table 3.3 displays the stellar data derived in Zuckerman et al. (2010), the atmospheric abundances given in Zuckerman et al. (2010) and Jura et al. (2012), and the sinking timescales presented in Xu et al. (2013) for the G241-6 system. These white dwarf properties and atmospheric abundances, other than the upper limits, were inputted into the model in order to constrain the origin and geology of the polluting material.

Figure 3.3 displays the model fit with the highest Bayesian evidence, which has a χ^2_{pdp} of 0.22. A scenario in which the pollutant material is accreting in build-up phase, has experienced temperatures of the order 300 K, and is a mantle-rich fragment of a differentiated body best explains the atmospheric abundances. The model parameters utilised in the optimised model fit are: the stellar metallicity index, the pollution fraction, the accretion event lifetime, the time passed since accretion started, the formation distance, and the fragment core fraction. The model produces a 3.91σ constraint on the pollutant requiring incomplete nebula condensation and a 1.48σ constraint on the pollutant being a mantle-rich fragment of a differentiated body. The mass of the body is constrained to be above $10^{19.80}$ kg suggesting that the polluting body is at least 25% the mass of Vesta and is therefore a similar size to a large asteroid or minor planet.

In Jura et al. (2012) the pollutant material was classified as being primitive and forming at temperatures such that S was fully condensed from the disc while O and C were incompletely condensed ($\sim$600 K). Jura et al. (2012) also suggested the possibility that the system was in the declining phase of accretion to explain the low Fe and Ni abundances and high S abundance. In this thesis I conclude that the system is unlikely to be in declining phase due to the unaffected abundances of Ca and Ti, and therefore, the most likely explanation is that G241-6 is accreting a mantle-rich fragment of a larger differentiated body in the build-up phase. Due to the O abundance suggesting the pollutant is lacking in water ice but is rich in FeO, I reach a similar conclusion to Jura et al. (2012) regarding the formation temperature.

3.2.4 GD61

Table 3.4 displays the stellar data derived in Farihi et al. (2011) and the atmospheric abundances and sinking timescales presented in Farihi et al. (2013) for the GD61 system. These white dwarf properties and abundances, other than the upper limits, were inputted into the model in order to constrain the origin and geology of the polluting material.
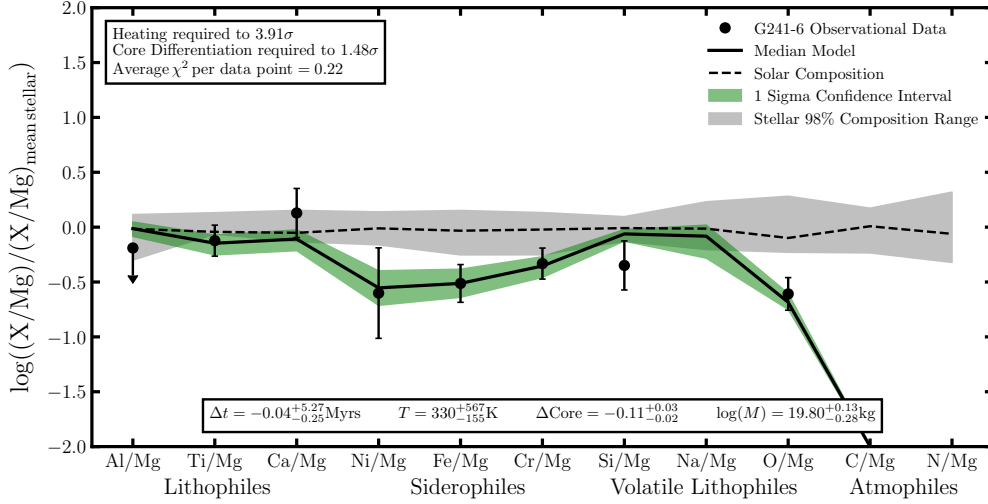
Fig. 3.3 The fit of model with the highest Bayesian evidence to the atmospheric abundances observed in G241-6. The polluting material is most likely a mantle-rich fragment of a differentiated body which condensed from the nebula at temperatures sufficient to cause the body to contain no water ice. The system is most likely accreting in the build-up phase.

Table 3.3 Data for G241-6 (Zuckerman et al. (2010); Jura et al. (2012); Xu et al. (2013)).

Type	q	$M_{\mathrm{WD}}/M_\odot$	T/K
DBZ	-5.85	0.60	15,300
Element	log(Abundance/He)	log(Sinking Timescale/years)	
Al	< -7.7	6.08	
Ti	-8.97 ± 0.10	5.69	
Ca	-7.30 ± 0.20	5.71	
Ni	-8.15 ± 0.40	5.79	
Fe	-6.82 ± 0.14	5.75	
Cr	-8.46 ± 0.10	5.72	
Mg	-6.26 ± 0.10	6.08	
Si	-6.62 ± 0.20	6.00	
Na	—	6.08	
O	-5.64 ± 0.11	6.04	
C	< -8.5	6.04	
N	< -8.8	6.04	

Figure 3.4 displays the model fit with the highest Bayesian evidence, which can reproduce the data well with a χ^2_{pdp} of 0.05. A scenario in which the pollutant material is accreting in build-up phase, is rich in water ice, and is a mantle-rich fragment of a differentiated body best explains the atmospheric abundances. The model parameters utilised in the optimised model fit are: the stellar metallicity index, the pollution fraction, the accretion event lifetime, the time passed since accretion started, the formation distance, and the fragment core fraction. The model produces a 4.91σ constraint on the pollutant requiring incomplete nebula condensation, a 2.43σ constraint on the pollutant containing water ice, and a 8.44σ constraint on the pollutant being a mantle-rich fragment. The pollutant of GD61 therefore provides strong evidence that core-mantle differentiation is occurring in exo-planetary systems and that water ice can survive in planetary bodies until the white dwarf phase. If a Ni and a Cr abundance could be constrained for GD61 it would potentially allow constraints to be placed on the mass of the parent body. If the Ni/Fe ratio was significantly less than Earth's mantle and the Cr/Fe ratio was significantly higher than Earth's mantle this would suggest core-mantle differentiation occurred at much lower pressures, thus an asteroid-sized parent body. The mass of the polluting body is constrained to be above $10^{18.49}$ kg suggesting that the polluting body is at least 1% as massive as Vesta.

Farihi et al. (2013) concluded that the pollutant material had a substantial water ice fraction and was most likely a mantle-rich body due to the excess O abundance and the low Fe abundance. The results presented in this thesis further support this conclusion, while also providing the statistical significance for the conclusion that the system accreted a differentiated fragment.

3.2.5 NLTT43806

Table 3.5 displays the stellar data, the atmospheric abundances, and the sinking timescales presented in Zuckerman et al. (2011) for the NLTT43806 system which were inputted into the model in order to constrain the origin and geology of the polluting material.

Figure 3.5 displays the model fit with the highest Bayesian evidence, which produces a good fit with a χ^2_{pdp} of 0.27. The model parameters utilised in the optimised model fit are: the stellar metallicity index, the pollution fraction, the accretion event lifetime, the time passed since accretion started, the formation distance, the fragment core fraction, and the fragment crust fraction. A scenario in which the pollutant material is accreting in the steady state phase and is a crust-rich fragment of a differentiated body best explains the atmospheric abundances. The model produces a 1.85σ
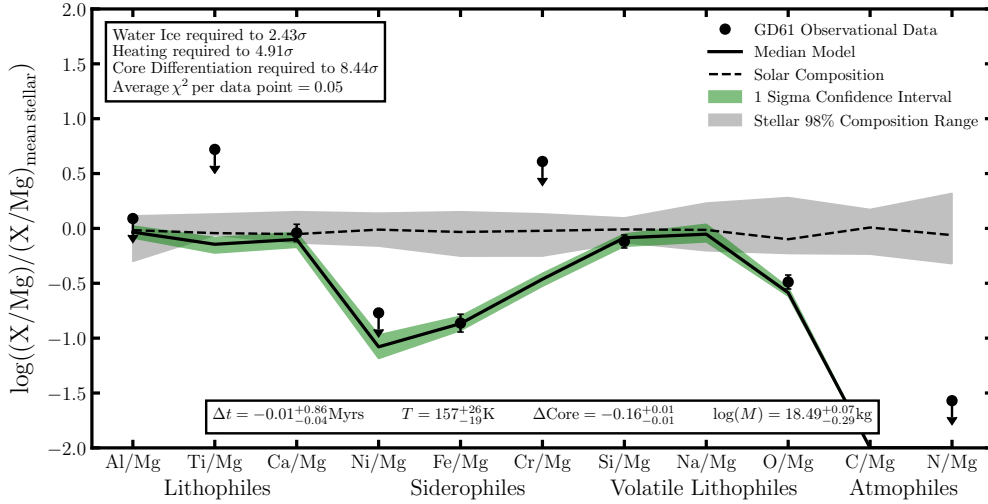
Fig. 3.4 The fit of model with the highest Bayesian evidence to the atmospheric abundances observed in GD61. The polluting material is most likely a mantle-rich fragment of a differentiated body which is partial composed of water ice and the system is most likely accreting in the build-up phase.

Table 3.4 Data for GD61 (Farihi et al. (2011); Farihi et al. (2013)).

Type	q	$M_{\rm WD}/M_\odot$	T/K
DBZ	-6.82	0.71	17,300
Element	log(Abundance/He)	log(Sinking Timescale/years)	
Al	< -7.8	5.24	
Ti	< -8.6	4.89	
Ca	-7.90 ± 0.06	4.89	
Ni	< -8.8	4.93	
Fe	-7.60 ± 0.07	4.93	
Cr	< -8.0	4.93	
Mg	-6.69 ± 0.05	5.26	
Si	-6.82 ± 0.04	5.16	
Na	< -6.8	5.26	
O	-5.95 ± 0.04	5.23	
C	< -9.1	5.24	
N	< -8.0	5.24	

constraint on the pollutant being in the steady state phase and a 3.46σ constraint on the pollutant being a crust-rich fragment. The pollutant of NLTT43806 therefore provides strong evidence that crustal differentiation is occurring in exo-planetary systems and that such fragments can survive until the white dwarf phase. If an O abundance was obtained for this system it would allow a constraint to be placed on whether the pollutant contained water ice. The total mass of the polluting body is predicted to be above $10^{19.39}$ kg, however this value is not well constrained as the system is in steady state and therefore it is difficult to know exactly how long the system has been accreting.

Zuckerman et al. (2011) concluded that the pollutant material was most likely a crust-rich body due to the similarities between the pollutant abundances and the abundances of the Earth's crust. Similar conclusions were made in Xu et al. (2013). The results presented in this thesis further support the conclusion that the material accreted is likely a fragment of an exo-planetary bodies crust, while also providing the statistical significance for such a conclusion.

3.2.6 HS2253+8023

Table 3.6 displays the stellar data, the atmospheric abundances, and the sinking timescales presented in Klein et al. (2011) for the HS2253+8023 system all of which were inputted into the model, other than the upper limits, in order to constrain the origin and geology of the polluting material.

Figure 3.6 displays the model fit with the highest Bayesian evidence, which has a $\chi^2_{\rm pdp}$ of 0.48. A scenario in which the pollutant material is accreting in build-up phase and is a primitive body best explains the atmospheric abundances. The model parameters utilised in the optimised model fit are: the stellar metallicity index, the pollution fraction, the accretion event lifetime, the time passed since accretion started, and the formation distance. The model produces a 3.10σ constraint on the pollutant requiring incomplete nebula condensation. The mass of the body is constrained to be above $10^{19.56}$ kg suggesting that the polluting body is at least 10% the mass of Vesta and therefore is of a similar size to a large asteroid or minor planet.

Klein et al. (2011) concluded that the pollutant material was likely dry and similar in composition to bulk Earth, these conclusions were then supported by Xu et al. (2013). The results presented in this thesis support this conclusion as I find the system can be readily explained by the accretion of primitive material which does not contain a significant fraction of water ice.
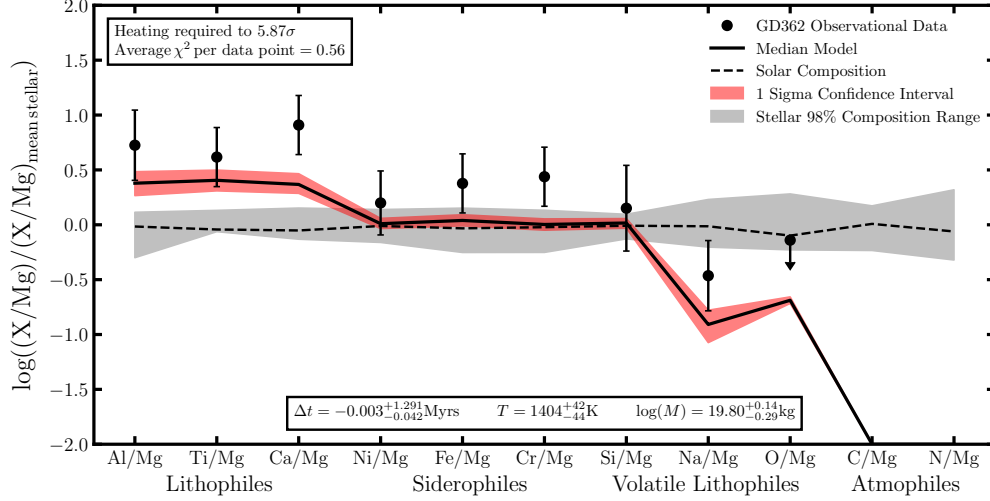
Fig. 3.5 The fit of model with the highest Bayesian evidence to the atmospheric abundances observed in NLTT43806. The polluting material is most likely a crust-rich fragment of a differentiated body accreting in the steady state phase.

Table 3.5 Data for NLTT43806 (Zuckerman et al. (2011)).

| Type	q	$M_{\text{WD}}/M_\odot$	T/K
DAZ	-7.571	0.573	5,900
Element	log(Abundance/H)	log(Sinking Timescale/years)	
Al	-7.60 ± 0.17	4.23	
Ti	-9.55 ± 0.14	4.05	
Ca	-7.90 ± 0.19	4.14	
Ni	-9.10 ± 0.17	3.97	
Fe	-7.80 ± 0.17	4.00	
Cr	-9.55 ± 0.22	4.02	
Mg	-7.10 ± 0.13	4.28	
Si	-7.20 ± 0.14	4.20	
Na	-8.10 ± 0.14	4.31	
O	—	4.31	
C	—	4.31	
N	—	4.31	

Fig. 3.6 The fit of model with the highest Bayesian evidence to the atmospheric abundances observed in HS2253+8023. The polluting material is most likely accreting in build-up phase and is a primitive body which has experienced sufficient heating to contain no water ice.

Table 3.6 Data for HS2253+8023 (Klein et al. (2011)).

Type	q	$M_{\mathrm{WD}}/M_\odot$	T/K
DBZ	-6.48	0.84	14,400
Element	log(Abundance/He)	log(Sinking Timescale/years)	
Al	< -6.7	4.92	
Ti	-8.74 ± 0.04	4.73	
Ca	-7.00 ± 0.10	4.78	
Ni	-7.32 ± 0.20	4.68	
Fe	-6.17 ± 0.05	4.71	
Cr	-8.00 ± 0.06	4.74	
Mg	-6.12 ± 0.08	4.93	
Si	-6.28 ± 0.06	4.93	
Na	< -6.8	4.93	
O	-5.38 ± 0.12	5.00	
C	—	5.05	
N	—	5.05	

3.2.7   PG1225-079

Table 3.7 displays the stellar data, the atmospheric abundances, and the sinking timescales presented in Klein et al. (2011) and Xu et al. (2013) for the PG1225-079 system. The white dwarf properties and atmospheric abundances, other than C and the upper limits, were inputted into the model in order to constrain the origin and geology of the polluting material.

Figure 3.7 displays the model fit with the highest Bayesian evidence, which has a χ^2_{pdp} of 0.07. A scenario in which the pollutant material is a primitive body which is accreting in the build-up phase and has experienced temperatures of $\sim$1,400 K such that the moderate volatiles were depleted best explains the atmospheric abundances. The model parameters utilised in the optimised model fit are: the stellar metallicity index, the pollution fraction, the accretion event lifetime, the time passed since accretion started, the formation distance, and the feeding zone size. The model produces a 9.15σ constraint on the pollutant being the product of incomplete nebula condensation. The mass of the polluting body is constrained to be above $10^{19.62}$ kg suggesting that the polluting body is at least 15% as massive as Vesta, and therefore, is likely a body equivalent to a large asteroid or minor planet.

Xu et al. (2013) concluded that the pollutant material had no Solar System analogue and had abundances which were difficult to explain but were likely due to post-nebula processing. In this thesis I find that it is possible to explain the abundances of PG1125-079 by nebula condensation processes. The abundance pattern observed is reproduced well by the composition of material expected to form at temperatures over 1,300 K. The lack of a depletion in the siderophiles rules out the accretion of crust-rich material as an explanation for the high lithophile abundances.

3.2.8   SDSS J0738+1835

Table 3.8 displays the stellar data, the atmospheric abundances, and the sinking timescales presented in Dufour et al. (2012) for the SDSS J0738+1835 system which were inputted into the model in order to constrain the origin and geology of the polluting material.

Figure 3.8 displays the model fit with the highest Bayesian evidence, which has a χ^2_{pdp} of 0.33. A scenario in which the pollutant material is a differentiated body which has had its crust partially stripped best explains the atmospheric abundances. The model parameters utilised in the optimised model fit are: the stellar metallicity index, the pollution fraction, the accretion event lifetime, the time passed since accretion
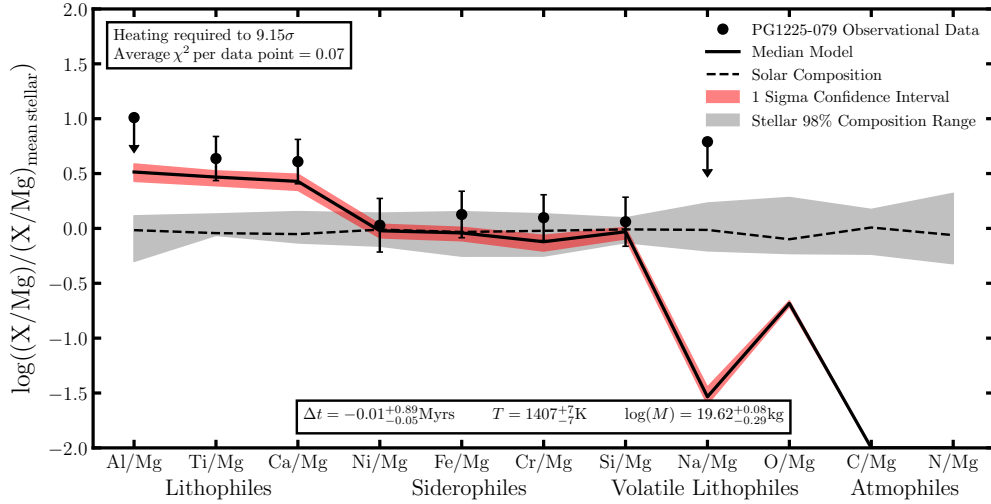
Fig. 3.7 The fit of model with the highest Bayesian evidence to the atmospheric abundances observed in PG1225-079. The polluting material is most likely observed in the build-up phase and is a primitive body which has undergone sufficient heating such that the moderate volatiles incompletely condensed from the nebula.

Table 3.7 Data for PG1225-079 (Klein et al. (2011); Xu et al. (2013)).

Type	q	$M_{\mathrm{WD}}/M_\odot$	T/K
DBZ	-5.02	0.58	10,800
Element	log(Abundance/He)	log(Sinking Timescale/years)	
Al	< -7.84	5.56	
Ti	-9.45 ± 0.02	5.26	
Ca	-8.06 ± 0.03	5.28	
Ni	-8.76 ± 0.14	5.36	
Fe	-7.42 ± 0.07	5.32	
Cr	-9.27 ± 0.06	5.28	
Mg	-7.50 ± 0.20	5.68	
Si	-7.45 ± 0.10	5.48	
Na	< -8.26	5.64	
O	< -5.54	5.65	
C	-7.80 ± 0.10	5.74	
N	—	5.74	

Fig. 3.8 The fit of model with the highest Bayesian evidence to the atmospheric abundances observed in SDSSJ0738+1835. The polluting material is most likely a differentiated body which has had its crust stripped and is partially composed of water ice.

Table 3.8 Data for SDSSJ0738+1835 (Dufour et al. (2012)).

Type	q	$M_{WD}/M_{\odot}$	T/K
DBZ	-6.41	0.841	14,000
Element	log(Abundance/He)	log(Sinking Timescale/years)	
Al	-6.39 ± 0.11	5.24	
Ti	-7.95 ± 0.11	5.01	
Ca	-6.23 ± 0.15	5.04	
Ni	-6.31 ± 0.10	5.06	
Fe	-4.98 ± 0.09	5.05	
Cr	-6.76 ± 0.12	5.03	
Mg	-4.68 ± 0.07	5.26	
Si	-4.90 ± 0.16	5.25	
Na	-6.36 ± 0.16	5.24	
O	-3.81 ± 0.19	5.24	
C	—	5.26	
N	—	5.26	

started, the formation distance, the fragment core fraction, the fragment crust fraction, and the parent body crust fraction. The model produces a 2.62σ constraint on the pollutant being partially composed of water ice and a 2.18σ constraint on the pollutant being a differentiated crustally-stripped body. The mass of the polluting body is constrained to be at least $\sim 10^{21}$ kg, however due to the potential for the system to be in the steady state phase this constraint has large uncertainties. Regardless the mass required is still exceptionally high and the body is at least 10% the mass of Pluto.

Dufour et al. (2012) concluded that the pollutant abundances were potentially due to the accretion of a body which had its crust removed, while Xu et al. (2013) suggested that the system was primitive due to its similarity when compared with bulk Earth. The results presented in this thesis support the conclusions presented in Dufour et al. (2012), while also providing the statistical significance for such conclusions. The key elements which supports the crust-stripped model are Al, Ti, Ca and Na which are all depleted relative to Mg as would be expected if a thick crust rich in the lithophiles was removed. Although the model strongly predicts the presence of water ice the accretion of an icy body is potentially uncertain, as not only does the star not show sufficient polluting H (a 2.97σ disagreement), but Dufour et al. (2012) questioned the quality of the lines used when deriving the O abundance. The model presented here could easily be rerun if updated abundances were found.

3.2.9   PG0843+516

Table 3.9 displays the stellar data, the atmospheric abundances, and the sinking timescales presented in Gänsicke et al. (2012) for the PG0843+516 system which were inputted into the model in order to constrain the origin and geology of the polluting material.

PG0843+516 cannot be modelled to a χ^2_{pdp} of less than 1 by any model or combination of free parameters in the traditional setup. However, this is due to a higher than expected Cr abundance and a lower than expected Ni abundance which is potentially due to differentiation occurring under non-Earth-like conditions as described in Chapter 1 and Chapter 2. I therefore manually changed the parent core abundances such that all the Cr was sequestered in the core, while the fraction of Ni in the core was 5 times lower than that of the Earth's core as such changes seem reasonable in light of the work of Fischer et al. (2015). Figure 3.9 displays the model fit with the highest Bayesian evidence after the parent core abundances were changed, the model now has a strong fit with a χ^2_{pdp} of 0.62. A scenario in which the pollutant material is accreting in the steady state phase and is a core-rich fragment of a differentiated body best explains
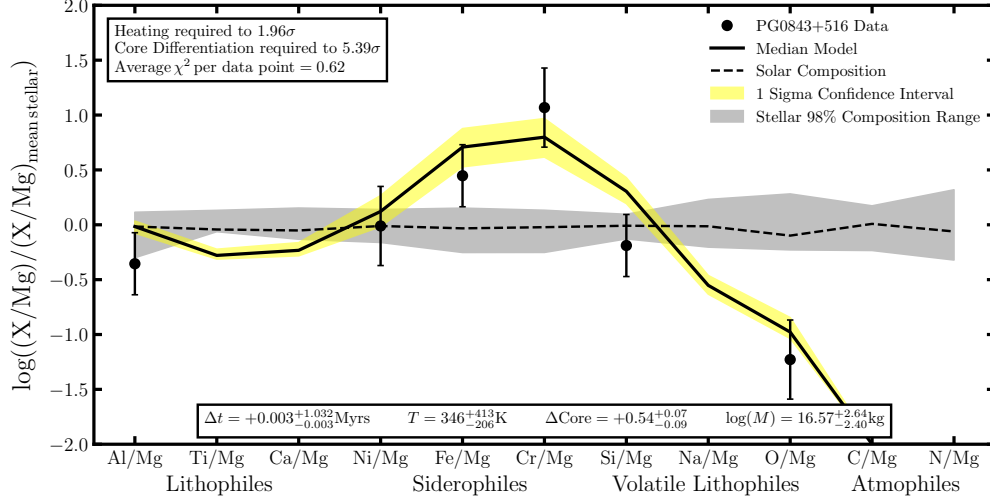
Fig. 3.9 The fit of model with the highest Bayesian evidence to the atmospheric abundances observed in PG0843+516. The high Cr abundance and low Ni abundance cannot be accurately fitted unless the parent core abundances are modified as outlined in Chapter 2. The polluting material is most likely a core-rich body which has undergone sufficient heating such that it contains no water ice.

Table 3.9 Data for PG0843+516 (Gänsicke et al. (2012)).

Type	q	$M_{\mathrm{WD}}/M_{\odot}$	T/K
DAZ	-16.599	0.704	23,095
Element	log(Abundance/H)	log(Sinking Timescale/years)	
Al	-6.50 ± 0.20	-2.22	
Ti	—	-2.46	
Ca	—	-2.44	
Ni	-6.30 ± 0.30	-2.60	
Fe	-4.60 ± 0.20	-2.57	
Cr	-5.80 ± 0.30	-2.52	
Mg	-5.00 ± 0.20	-2.23	
Si	-5.20 ± 0.20	-2.28	
Na	—	-2.70	
O	-5.00 ± 0.30	-2.52	
C	—	-2.22	
N	—	-2.40	

the atmospheric abundances. The model parameters utilised in the optimised model fit are: the stellar metallicity index, the pollution fraction, the accretion event lifetime, the time passed since accretion started, the formation distance, and the fragment core fraction. The model produces a 1.96σ constraint on the pollutant being the product of incomplete nebula condensation and a 5.39σ constraint on the pollutant being a core-rich fragment. The mass of the polluting body is poorly constrained due to the fact that the incredibly short sinking timescales (less than 3 days) mean the system must be in the steady state phase and the time period for which the system has been in such a phase is difficult to know.

Gänsicke et al. (2012) concluded that the pollutant material was most likely a dry core-rich body due to the enhanced Fe and the lack of an O excess. Xu et al. (2013) also concluded that the system was accreting a non-primitive body but stated that the large uncertainties suggested this conclusion was not certain. The results presented in this thesis support the conclusion that the accreting body is core-rich, while also providing the statistical significance for such a conclusion. However, further study of this system with a more complete, self consistent, differentiation model is required as it would potentially allow the parent body's mass to be constrained as well as confirming the results presented here.

3.2.10   SDSS J1228+1040

Table 3.10 displays the stellar data, the atmospheric abundances, and the sinking timescales presented in Gänsicke et al. (2012) for the SDSS J1228+1040 system. The white dwarf properties and atmospheric abundances, other than C and the upper limits, were inputted into the model in order to constrain the origin and geology of the polluting material.

Figure 3.10 displays the model fit with the highest Bayesian evidence, which has a χ^2_{pdp} of 0.27. As with GD362 it should be noted that the seemingly poor fit in Figure 3.10 is due to the fact the plot is displayed as a ratio to Mg. A scenario in which the pollutant material is a primitive body which is accreting in steady state and has experienced temperatures over $1,300\,\text{K}$ such that the moderate volatiles were depleted best explains the atmospheric abundances. The model parameters utilised in the optimised model fit are: the stellar metallicity index, the pollution fraction, the accretion event lifetime, the time passed since accretion started, the formation distance, and the feeding zone size. The model produces a 3.53σ constraint on the pollutant being the product of incomplete nebula condensation. The mass of the polluting body is poorly constrained due to the fact that the incredibly short sinking timescales (less
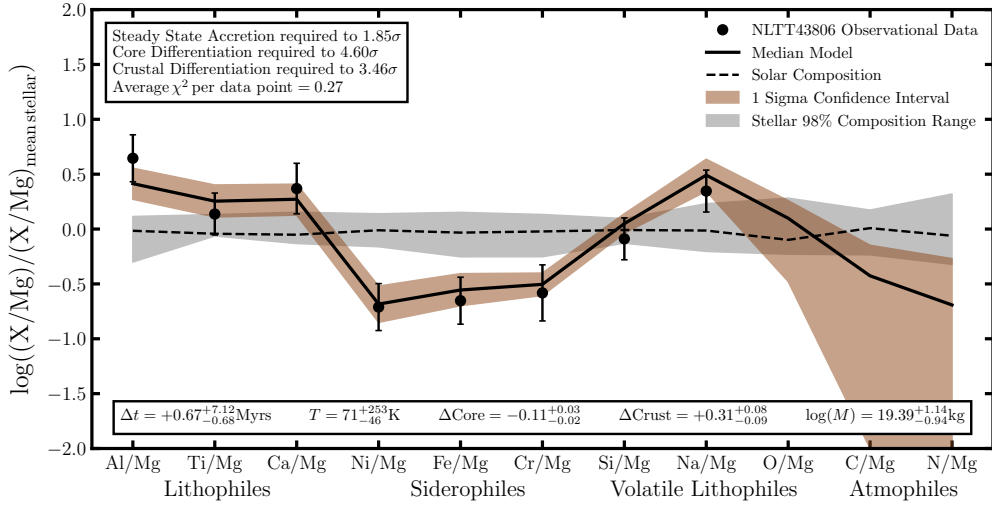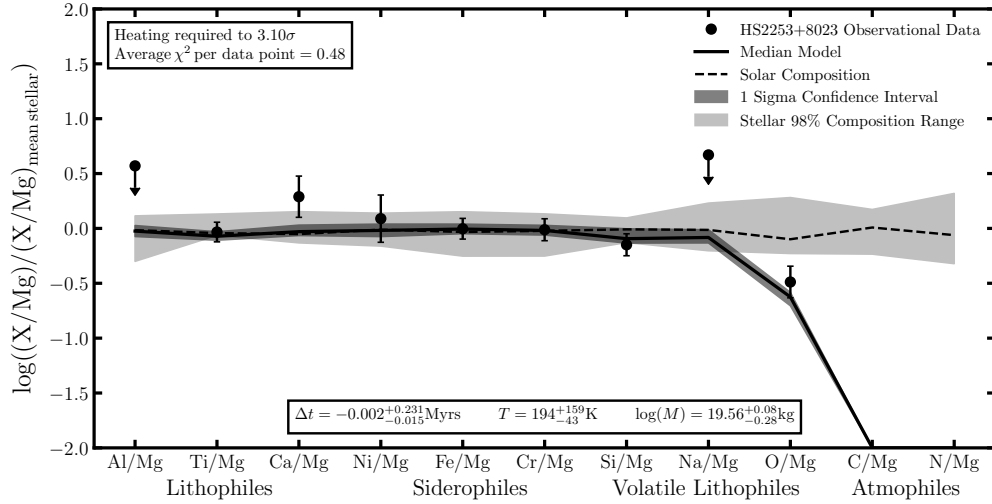
Fig. 3.10 The fit of model with the highest Bayesian evidence to the atmospheric abundances observed in SDSSJ1228+1040. The polluting material is most likely a primitive body accreting in steady state which has undergone sufficient heating such that the moderate volatiles incompletely condensed from the nebula.

Table 3.10 Data for SDSSJ1228+1040 (Gänsicke et al. (2012)).

Type	q	$M_{\mathrm{WD}}/M_\odot$	T/K
DAZ	-16.663	0.689	20,900
Element	log(Abundance/H)	log(Sinking Timescale/years)	
Al	-5.75 ± 0.20	-2.28	
Ti	—	-2.51	
Ca	-5.70 ± 0.20	-2.46	
Ni	< -6.50	-2.63	
Fe	-5.20 ± 0.30	-2.62	
Cr	< -6.00	-2.56	
Mg	-5.20 ± 0.20	-2.24	
Si	-5.20 ± 0.20	-2.34	
Na	—	-2.71	
O	-4.55 ± 0.20	-2.55	
C	-7.50 ± 0.20	-2.35	
N	—	-2.47	

than 3 days) mean the system must be in steady state and the time period for which it has been in steady state is difficult to constrain.

Gänsicke et al. (2012) concluded that the pollutant material was most likely a dry body with a similar composition to bulk Earth. The results presented in this thesis find that the enhanced abundances of Al and Ti suggest that it is more likely that the polluting material has experienced higher temperatures than bulk Earth and is depleted in the moderate volatiles in comparison. Analysis of the gas disc in the system by Manser et al. (2019) suggested the presence of a dense likely core-rich planetesimal in orbit around the white dwarf. Therefore, the photospheric abundances do not seem to be linked with the orbiting body as if this were the case one would expect the atmosphere to show evidence of the accretion of mantle-rich material. However, further study of the system's photosphere would be useful in investigating the link between the orbiting material and the material in the white dwarf's atmosphere.

3.2.11 G29-38

Table 3.11 displays the stellar data, the atmospheric abundances, and the sinking timescales presented in Xu et al. (2014) for the G29-38 system. The white dwarf properties and atmospheric abundances, other than C and the upper limits, were inputted into the model in order to constrain the origin and geology of the polluting material.

Figure 3.11 displays the model fit with the highest Bayesian evidence, which has a χ^2_{pdp} of 0.23. A scenario in which the pollutant material is accreting in steady state and is a primitive body which has experienced temperatures of $\sim 1,400\,\mathrm{K}$ such that the moderate volatiles were depleted best explains the atmospheric abundances. The model parameters utilised in the optimised model fit are: the stellar metallicity index, the pollution fraction, the accretion event lifetime, the time passed since accretion started, the formation distance, and the feeding zone size. The model produces a 5.66σ constraint on the pollutant being the product of incomplete nebula condensation and a 1.08σ constraint on the system being in the steady state phase of accretion. The mass of the polluting body is poorly constrained due to the fact that the incredibly short sinking timescales (less than a year) mean the system is likely in steady state and the time period for which it has been in steady state is difficult to constrain.

Xu et al. (2014) concluded that the pollutant material must have undergone post-nebula processing namely differentiation and collisions to explain the high Ti and Ca abundances. In this thesis I do not reach such a conclusion as I find that condensational
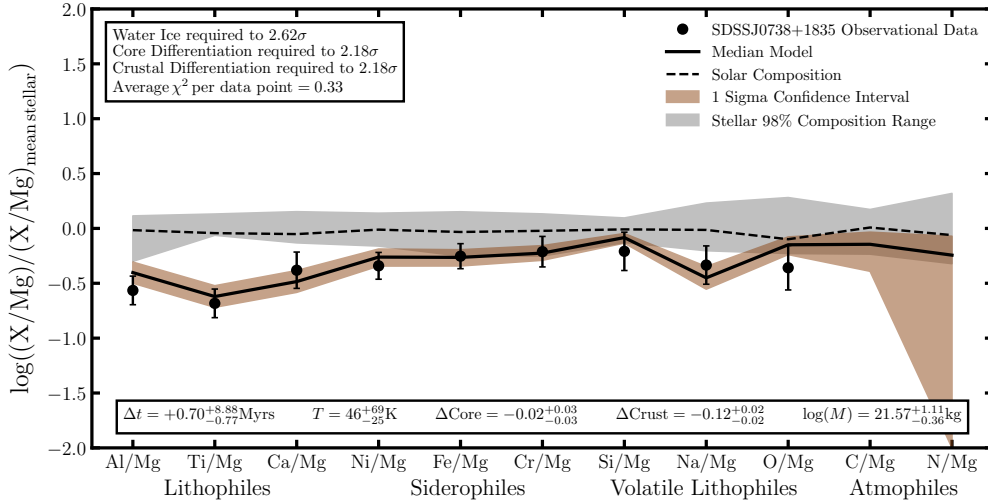
Fig. 3.11 The fit of model with the highest Bayesian evidence to the atmospheric abundances observed in G29-38. The polluting material is most likely accreting in the steady state phase and is a primitive body which has undergone sufficient heating such that the moderate volatiles incompletely condensed from the nebula.

Table 3.11 Data for G29-38 (Xu et al. (2014)).

Type	q	$M_{WD}/M_\odot$	T/K
DAZ	-13.90	0.85	11,800
Element	log(Abundance/H)	log(Sinking Timescale/years)	
Al	< -6.1	-0.47	
Ti	-7.90 ± 0.16	-0.57	
Ca	-6.58 ± 0.12	-0.70	
Ni	< -7.3	-0.72	
Fe	-5.90 ± 0.10	-0.68	
Cr	-7.51 ± 0.12	-0.62	
Mg	-5.77 ± 0.13	-0.60	
Si	-5.60 ± 0.17	-0.34	
Na	< -6.7	-0.68	
O	-5.00 ± 0.12	-0.35	
C	-6.90 ± 0.12	-0.11	
N	< -5.7	-0.19	

processes can explain the abundance pattern observed without invoking planetary differentiation. The Fe and Cr abundances along with the Na upper limit make the accretion of crust-rich material less likely than material which has experienced temperatures of the order $1,400\,K$.

3.2.12   SDSS J1242+5226

Table 3.12 displays the stellar data, the atmospheric abundances and the sinking timescales presented in Raddi et al. (2015) for the SDSS J1242+5226 system. These abundances, other than the upper limits, and white dwarf properties were inputted into the model in order to constrain the origin and geology of the polluting material.

Figure 3.12 displays the model fit with the highest Bayesian evidence, which has a χ^2_{pdp} of 0.69. A scenario in which the pollutant material is rich in water ice and is a mantle-rich fragment of a differentiated body which is accreting in build-up phase best explains the atmospheric abundances. The model parameters utilised in the optimised model fit are: the stellar metallicity index, the pollution fraction, the accretion event lifetime, the time passed since accretion started, the formation distance, and the fragment core fraction. The model produces a 2.46σ constraint that the pollutant contains water ice and a 1.35σ constraint on the pollutant being a mantle-rich fragment. The mass of the polluting body is constrained to be at least $10^{21.57}\,kg$, this exceptionally high mass is due to the incredibly strong pollution observed in this system. The polluting body is at least a quarter of the mass of Pluto.

In Raddi et al. (2015) the pollutant material was classified as being an icy mantle-rich object due to an apparent O excess and the low Fe abundance. In this thesis I arrive at the same conclusions, while also placing statistical constraints on the results. It should be noted that the statistical constraint on the requirement for the system to be a mantle-rich fragment would be much larger if the Ni lower limit could be incorporated into the fit. If the Ni abundance was found it could offer a unique insight into the mass of the parent body as the Ni/Fe ratio is sensitive to the conditions at the core-mantle boundary. Similarly, if an Al abundance was derived for the system a constraint on the system being a crust-stripped body would also emerge as currently, although such a model is the best fit as it can explain the low Na abundance, given the amount of additional free parameters involved, the Bayesian evidence is still lower than that of a simple mantle-rich model.

Fig. 3.12 The fit of model with the highest Bayesian evidence to the atmospheric abundances observed in SDSSJ1242+5226. The polluting material is most likely observed accreting in the build-up phase and is a mantle-rich body which is composed in part of water ice.

Table 3.12 Data for SDSSJ1242+5226 (Raddi et al. (2015)).

Type	q	$M_{\rm WD}/M_{\odot}$	T/K
DBZ	-5.40	0.59	13,000
Element	log(Abundance/He)	log(Sinking Timescale/years)	
Al	< -6.50	6.34	
Ti	-8.20 ± 0.20	5.95	
Ca	-6.53 ± 0.10	6.00	
Ni	< -7.30	6.08	
Fe	-5.90 ± 0.15	6.04	
Cr	-7.50 ± 0.20	6.00	
Mg	-5.26 ± 0.15	6.38	
Si	-5.30 ± 0.06	6.23	
Na	-7.20 ± 0.20	6.34	
O	-4.30 ± 0.10	6.34	
C	< -4.70	6.36	
N	< -5.00	6.34	

3.2.13   SDSS J0845+2257

Table 3.13 displays the stellar data, the atmospheric abundances, and the sinking timescales presented in Wilson et al. (2015) for the SDSS J0845+2257 system. The white dwarf properties and atmospheric abundances, other than the upper limits and the C abundance were inputted into the model in order to constrain the origin and geology of the polluting material.

Figure 3.13 displays the model fit with the highest Bayesian evidence, which has a χ^2_{pdp} of 0.11. A scenario in which the pollutant material is accreting in the steady state phase and is a core-rich fragment of a differentiated body best explains the atmospheric abundances. The model parameters utilised in the optimised model fit are: the stellar metallicity index, the pollution fraction, the accretion event lifetime, the time passed since accretion started, the formation distance, and the fragment core fraction. The model produces a 3.03σ constraint on the pollutant being the product of incomplete nebula condensation and a 2.12σ constraint on the pollutant being a core-rich fragment. Measurements of the Na abundance in the system would allow the model to further constrain the formation temperature, however the high temperature of the white dwarf means the detection of Na is unlikely. The mass of the polluting body is estimated to be above $10^{20.58}$ kg however this value is not well constrained as the system is in steady state and therefore it is difficult to know exactly how long the system has been accreting.

Wilson et al. (2015) concluded that the pollutant material was most likely a dry core-rich body due to the enhanced Fe and Ni abundances and the lack of an O excess. The results presented in this thesis further support this conclusion, while also providing the statistical significance for such conclusions. Additionally, Wilson et al. (2015) hinted that the core-rich nature of the body could be explained by mantle removal during the giant branches due to the star's increased luminosity sublimating the upper layers. The results presented here to do not support that argument, and instead support a collisional explanation for the partial removal of the body's mantle, due to the lack of a heating signature in the refractory abundances.

3.2.14   WD1536+520

Table 3.14 displays the stellar data, the atmospheric abundances, and the sinking timescales presented in Farihi et al. (2016) for the WD1536+520 system. The white dwarf properties and atmospheric abundances, other than the upper limits, were
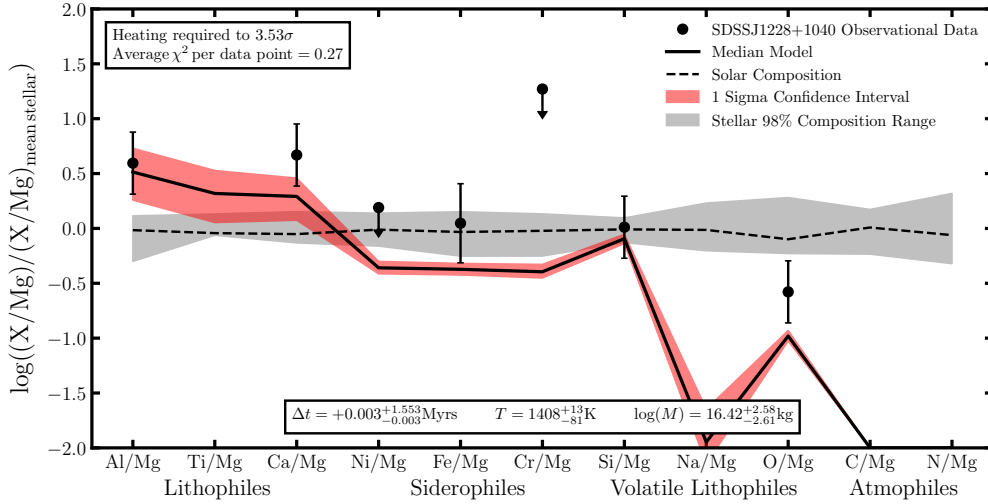
Fig. 3.13 The fit of model with the highest Bayesian evidence to the atmospheric abundances observed in SDSSJ0845+2257. The polluting material is most likely a core-rich fragment of a differentiated body accreting in the steady state phase which has experienced sufficient heating such that it does not contain any water ice.

Table 3.13 Data for SDSSJ0845+2257 (Wilson et al. (2015)).

Type	q	$M_{\rm WD}/M_\odot$	T/K
DBZ	-8.40	0.679	19,780
Element	log(Abundance/He)	log(Sinking Timescale/years)	
Al	-5.70 ± 0.15	4.08	
Ti	< -7.15	3.77	
Ca	-5.95 ± 0.10	3.99	
Ni	-5.65 ± 0.30	3.64	
Fe	-4.60 ± 0.20	3.94	
Cr	-6.44 ± 0.30	3.72	
Mg	-4.70 ± 0.15	4.08	
Si	-4.80 ± 0.30	4.08	
Na	—	4.08	
O	-4.25 ± 0.20	3.99	
C	-4.90 ± 0.20	4.18	
N	< -6.30	4.18	

Fig. 3.14 The fit of model with the highest Bayesian evidence to the atmospheric abundances observed in WD1536+520. The polluting material is most likely a primitive body which has undergone sufficient heating such that it does not contain any water ice and is accreting in the steady state phase.

Table 3.14 Data for WD1536+520 (Farihi et al. (2016)).

Type	q	$M_{WD}/M_\odot$	T/K
DBZ	-11.60	0.58	20,800
Element	log(Abundance/He)	log(Sinking Timescale/years)	
Al	-5.38 ± 0.15	2.15	
Ti	-6.84 ± 0.15	2.10	
Ca	-5.28 ± 0.15	2.16	
Ni	—	1.98	
Fe	-4.50 ± 0.15	1.99	
Cr	-5.93 ± 0.15	2.01	
Mg	-4.06 ± 0.15	2.22	
Si	-4.32 ± 0.15	2.09	
Na	—	2.22	
O	-3.40 ± 0.15	2.48	
C	< -4.20	2.42	
N	—	2.42	

inputted into the model in order to constrain the origin and geology of the polluting material.

Figure 3.14 displays the model fit with the highest Bayesian evidence, which has a χ^2_{pdp} of 0.31. A scenario in which the pollutant material is accreting in the steady state phase and is a primitive body best explains the atmospheric abundances. The model parameters utilised in the optimised model fit are: the stellar metallicity index, the pollution fraction, the accretion event lifetime, the time passed since accretion started, and the formation distance. The model produces a 3.65σ constraint on the pollutant being the product of incomplete nebula condensation and a 1.68σ constraint on the system being in the steady state phase. The mass of the polluting body is poorly constrained due to the fact that the system is likely in the steady state phase and the time period for which it has been in such a phase is difficult to constrain.

Farihi et al. (2016) concluded that the pollutant material was most likely dry due to a lack of an O excess and generally similar in composition to bulk Earth. The results presented in this thesis support this conclusion as I find the system can be readily explained by the accretion of primitive material which does not contain a significant fraction of water ice, while also providing statistical constraints on the heating required and the phase of accretion.

3.2.15 SDSS J1043+0855

Table 3.15 displays the stellar data, the atmospheric abundances and the sinking timescales presented in Melis and Dufour (2017) for the SDSS J1043+0855 system. These white dwarf properties and atmospheric abundances, other than C and the upper limits, were inputted into the model in order to constrain the origin and geology of the polluting material.

Figure 3.15 displays the model fit with the highest Bayesian evidence, which has a χ^2_{pdp} of 0.88. A scenario in which the pollutant material has experienced temperatures of the order $500\,\mathrm{K}$, is a mantle-rich fragment of a differentiated body, and is accreting in the steady state phase best explains the atmospheric abundances. The model parameters utilised in the optimised model fit are: the stellar metallicity index, the pollution fraction, the accretion event lifetime, the time passed since accretion started, the formation distance, and the fragment core fraction. The model produces a 3.91σ constraint on the pollutant being a product of incomplete nebula condensation and a 1.48σ constraint on the pollutant being a mantle-rich fragment. The mass of the polluting body is poorly constrained as the incredibly short sinking timescales (less
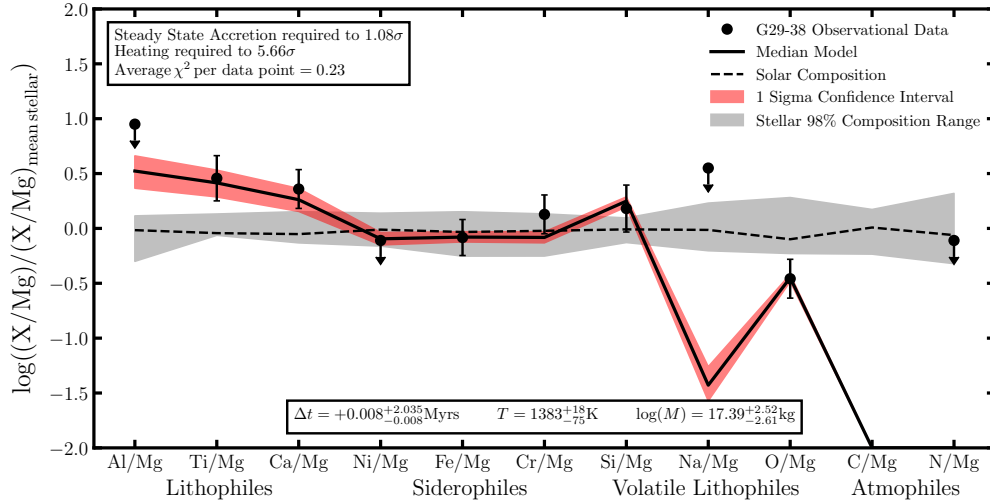
Fig. 3.15 The fit of model with the highest Bayesian evidence to the atmospheric abundances observed in SDSSJ1043+08556. The polluting material is most likely a mantle-rich body which has undergone sufficient heating such that it contains no water ice and is observed to be accreting in the steady state phase.

Table 3.15 Data for SDSSJ1043+0855 (Melis and Dufour (2017)).

Type	q	$M_{WD}/M_\odot$	T/K
DAZ	-16.645	0.626	18,330
Element	log(Abundance/H)	log(Sinking Timescale/years)	
Al	-7.06 ± 0.30	-2.23	
Ti	< -7.00	-2.44	
Ca	-5.96 ± 0.20	-2.36	
Ni	-7.38 ± 0.30	-2.56	
Fe	-6.15 ± 0.30	-2.58	
Cr	< -6.50	-2.47	
Mg	-5.11 ± 0.20	-2.16	
Si	-5.33 ± 0.50	-2.31	
Na	—	-2.16	
O	-4.90 ± 0.20	-2.48	
C	-6.15 ± 0.30	-2.32	
N	—	-2.32	

than 3 days) mean the system must be in steady state and the time period for which it has been in steady state is difficult to know.

In Melis and Dufour (2017) the pollutant material was classified as being a mantle-rich object which formed at temperatures high enough such that water ice was not sequestered into the body. In this thesis I arrive at the same conclusions, while also placing statistical constraints on the results. Melis and Dufour (2017) also hinted that the low Al abundance was potentially due to a crust stripping event, however I find that such an event is not required to explain the abundances as such an event would also decrease the Ca abundance, therefore, producing a worse quality fit.

3.2.16   WD1425+540

Table 3.16 displays the stellar data, the atmospheric abundances, and the sinking timescales presented in Xu et al. (2017) for the WD1425+540 system which were inputted into the model in order to constrain the origin and geology of the polluting material.

Figure 3.16 displays the model fit with the highest Bayesian evidence, which has a χ^2_{pdp} of 0.20. A scenario in which the pollutant material is observed accreting in build-up phase and is a primitive body which is rich in water ice, carbon ices, and nitrogen ices best explains the atmospheric abundances. The model parameters utilised in the optimised model fit are: the stellar metallicity index, the pollution fraction, the accretion event lifetime, the time passed since accretion started, and the formation distance. The model produces a 3.98σ constraint on the pollutant being composed partially of water ice. The mass of the polluting body is constrained to be above $\sim 10^{18.8}$ kg suggesting that the polluting body is at least 3% as massive as Vesta. Xu et al. (2017) concluded that the pollutant material was similar to a Solar System Kuiper belt object due to its stellar level abundances of the extreme volatiles O, C and N. The results presented in this thesis support this conclusion and I find that water ice is required to a 3.98σ significance. The high abundances of C and N constrain the formation temperature to be less than 80 K supporting the conclusion that this body formed in a region analogous to the Solar Systems Kuiper belt. It is important to note that the accretion of stellar material or ISM material can be ruled out for this system as it is a DBZ white dwarf. The H abundance in the atmosphere of WD1425+540 is -4.20 ± 0.10, therefore the Fe/H ratio is -3.95 ± 0.17 which is 3.24σ from an average metallicity star and thus the material accreting is H depleted in comparison to ISM material and stellar material. As H does not diffuse out of the atmosphere and there is sufficient H for all the O to be in the form of H_2O, all the C to be in the form of CH_4,
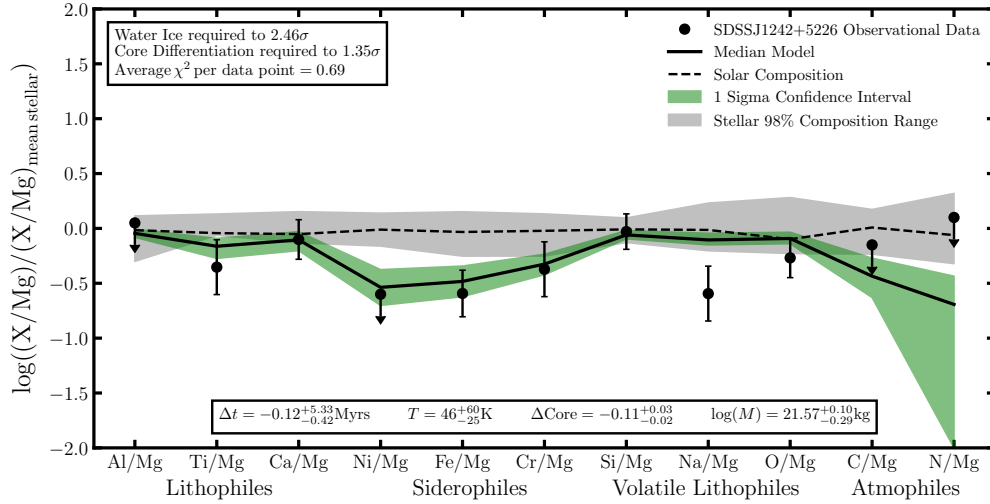
Fig. 3.16 The fit of model with the highest Bayesian evidence to the atmospheric abundances observed in WD1425+540. The polluting material is most likely accreting in the build-up phase and is a primitive body which is rich in water ice, carbon ices and nitrogen ices. An entirely stellar composition is ruled out due to the fact that H does not dominate the polluting material.

Table 3.16 Data for WD1425+540 (Xu et al. (2017)).

Type	q	$M_{\mathrm{WD}}/M_{\odot}$	T/K
DBZ	-5.495	0.562	14,490
Element	log(Abundance/He)	log(Sinking Timescale/years)	
Al	—	6.12	
Ti	—	5.93	
Ca	-9.26 ± 0.10	5.93	
Ni	-9.67 ± 0.20	5.94	
Fe	-8.15 ± 0.14	5.92	
Cr	—	5.94	
Mg	-8.16 ± 0.20	6.12	
Si	-8.03 ± 0.31	6.11	
Na	—	6.12	
O	-6.62 ± 0.23	6.11	
C	-7.29 ± 0.17	6.16	
N	-8.09 ± 0.10	6.12	

and all the N to be in the form NH$_3$ the conclusion that the material must be cometary and ice-rich is robust.

3.2.17   WD0446-255

Table 3.17 displays the stellar data, the atmospheric abundances, and the sinking timescales presented in Swan et al. (2019) for the WD0446-255 system which were inputted into the model in order to constrain the origin and geology of the polluting material.

Figure 3.17 displays the model fit with the highest Bayesian evidence, which has a χ^2_{pdp} of 0.41. A scenario in which the pollutant material is a crust-rich fragment of a differentiated body which experienced temperatures of the order 1,000 K and is accreting in the build-up phase best explains the atmospheric abundances. The model parameters utilised in the optimised model fit are: the stellar metallicity index, the pollution fraction, the accretion event lifetime, the time passed since accretion started, the formation distance, the fragment core fraction, and the fragment crust fraction. The model produces a 4.16σ constraint on the pollutant being the product of incomplete nebula condensation and a 2.22σ constraint on the pollutant being a crust-rich fragment. The mass of the polluting body is constrained to be above $10^{20.29}$ kg suggesting that the polluting body is at least 70% as massive as Vesta.

Swan et al. (2019) concluded that the pollutant material was dry and similar in composition to the Silicate Earth. The results presented in this thesis further support this conclusion, while also providing the statistical significance for such conclusions.

3.2.18   WD2216-657

Table 3.18 displays the stellar data, the atmospheric abundances, and the sinking timescales presented in Swan et al. (2019) for the WD2216-657 system. The white dwarf properties and atmospheric abundances, other than the upper limits, were inputted into the model in order to constrain the origin and geology of the polluting material.

Figure 3.18 displays the model fit with the highest Bayesian evidence, which has a χ^2_{pdp} of 0.04. A scenario in which the pollutant material is a primitive body which is observed in the declining phase best explains the atmospheric abundances. The model parameters utilised in the optimised model fit are: the stellar metallicity index, the pollution fraction, the accretion event lifetime, the time passed since accretion started, and the formation distance. The model produces a 4.65σ constraint on the accretion
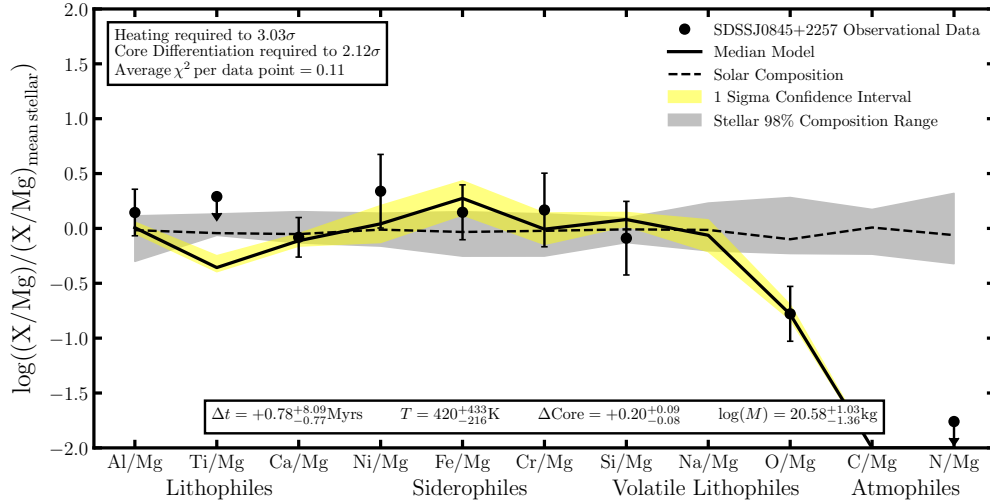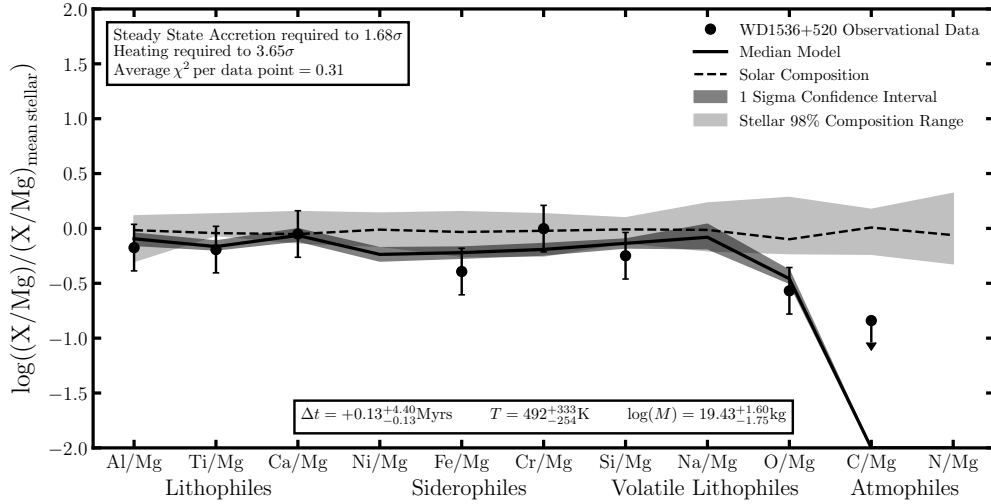
Fig. 3.17 The fit of model with the highest Bayesian evidence to the atmospheric abundances observed in WD0446-255. The polluting material is most likely a crust-rich fragment of a differentiated body which has experienced sufficient heating such that it contains no water ice and is accreting in the build-up phase.

Table 3.17 Data for WD0446-255 (Swan et al. (2019)).

Type	q	$M_{\rm WD}/M_\odot$	T/K
DBZ	-5.2	0.58	10,120
Element	log(Abundance/He)	log(Sinking Timescale/years)	
Al	-7.3 ± 0.3	6.41	
Ti	-8.8 ± 0.1	6.16	
Ca	-7.4 ± 0.1	6.21	
Ni	-8.2 ± 0.1	6.22	
Fe	-6.9 ± 0.1	6.20	
Cr	-8.5 ± 0.1	6.18	
Mg	-6.6 ± 0.1	6.42	
Si	-6.5 ± 0.1	6.42	
Na	-7.9 ± 0.1	6.39	
O	-5.8 ± 0.1	6.40	
C	—	6.47	
N	—	6.40	

event being over. The pollutant of WD2216-657 therefore offers a unique insight into the mass of white dwarf pollutants as it is known that there is no material left to accrete in a circumstellar reservoir. The mass of the polluting body is constrained to be $10^{20.64}$ kg suggesting that the polluting body is 1.6 times as massive as Vesta. Such a result strongly supports the conclusion that white dwarf pollutants observed thus far are equivalent to large asteroids or minor planets.

Swan et al. (2019) concluded that the pollutant material was most likely primitive and in the declining phase. The results presented in this thesis further support this conclusion, while also providing the statistical significance for such conclusions and additionally constraining the mass of the pollutant body.

3.2.19   WD2157-574

Table 3.19 displays the stellar data, the atmospheric abundances, and the sinking timescales presented in Swan et al. (2019) for the WD2157-574 system. The white dwarf properties and atmospheric abundances, other than the upper limits, were inputted into the model in order to constrain the origin and geology of the polluting material.

Figure 3.19 displays the model fit with the highest Bayesian evidence, which has a χ^2_{pdp} of 0.29. A scenario in which the pollutant material is a mantle-rich fragment of a differentiated body accreting in steady state best explains the atmospheric abundances. The model parameters utilised in the optimised model fit are: the stellar metallicity index, the pollution fraction, the accretion event lifetime, the time passed since accretion started, the formation distance, and the fragment core fraction. The model produces a 1.41σ constraint on the pollutant being a mantle-rich fragment. The mass of the polluting body is poorly constrained due to the fact that the system is likely in steady state and the time period for which it has been in steady state is difficult to know.

Swan et al. (2019) concluded that the pollutant material was likely similar in composition to bulk Earth and explained the high Ni/Fe abundance as potentially due to stellar compositional variance. The results presented in this thesis suggest that stellar chemical variation alone is not sufficient to explain the abundances and that the pollutant is likely a mantle-rich fragment.

3.2.20   WD2115-560

Table 3.20 displays the stellar data, the atmospheric abundances, and the sinking timescales presented in Swan et al. (2019) for the WD2115-560 system. The white dwarf properties and atmospheric abundances, other than the upper limits, were
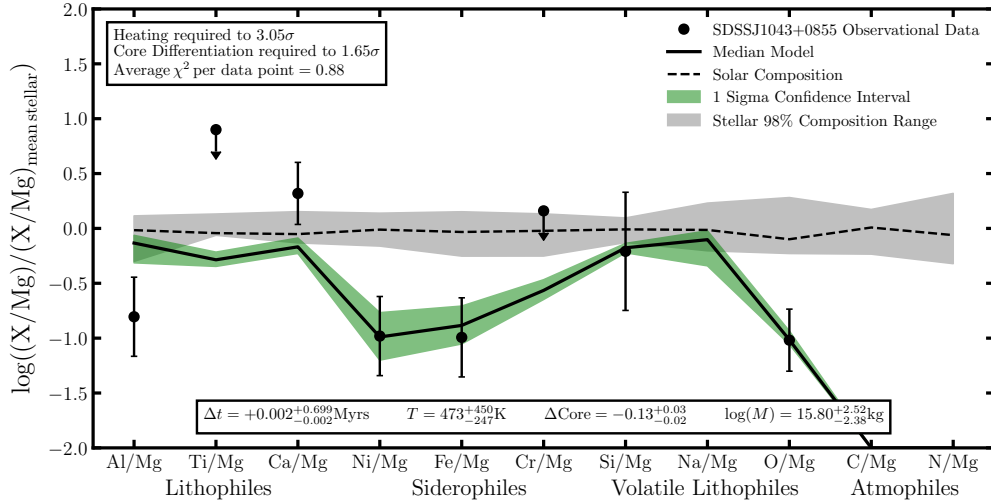
Fig. 3.18 The fit of model with the highest Bayesian evidence to the atmospheric abundances observed in WD2216-657. The polluting material is most likely a primitive body which has been observed after accretion has finished, such a system provides a unique insight into the mass of white dwarf pollutants.

Table 3.18 Data for WD2216-657 (Swan et al. (2019)).

Type	q	$M_{\mathrm{WD}}/M_\odot$	T/K
DBZ	-5.1	0.61	9,120
Element	log(Abundance/He)	log(Sinking Timescale/years)	
Al	—	6.26	
Ti	-10.6 ± 0.1	5.99	
Ca	-9.0 ± 0.1	6.04	
Ni	—	6.07	
Fe	-8.0 ± 0.2	6.04	
Cr	—	6.02	
Mg	-7.1 ± 0.1	6.28	
Si	—	6.27	
Na	< -8.5	6.25	
O	< -6.5	6.25	
C	—	6.30	
N	—	6.25	

Fig. 3.19 The fit of model with the highest Bayesian evidence to the atmospheric abundances observed in WD2157-574. The polluting material is most likely a mantle-rich fragment of a differentiated body accreting in the steady state phase.

Table 3.19 Data for WD2157-574 (Swan et al. (2019)).

Type	q	$M_{WD}/M_\odot$	T/K
DAZ	-8.6	0.63	7,010
Element	log(Abundance/H)	log(Sinking Timescale/years)	
Al	-8.1 ± 0.1	3.71	
Ti	—	3.65	
Ca	-8.1 ± 0.1	3.72	
Ni	-8.8 ± 0.1	3.58	
Fe	-7.3 ± 0.1	3.56	
Cr	—	3.62	
Mg	-7.0 ± 0.1	3.72	
Si	-7.0 ± 0.1	3.74	
Na	—	3.77	
O	< -3.8	3.96	
C	< -3.6	3.98	
N	< -3.0	3.99	

inputted into the model in order to constrain the origin and geology of the polluting material.

Figure 3.20 displays the model fit with the highest Bayesian evidence, which has a χ^2_{pdp} of 0.19. A scenario in which the pollutant material is a primitive body accreting in steady state best explains the atmospheric abundances. The model parameters utilised in the optimised model fit are: the stellar metallicity index, the pollution fraction, the accretion event lifetime, the time passed since accretion started, and the formation distance. The mass of the polluting body is poorly constrained due to the fact that the system is likely in steady state and the time period for which it has been in steady state is difficult to know. Few constraints can be placed on the polluting body due to the lack of abundances.

Swan et al. (2019) concluded that the pollutant material was likely similar in composition to bulk Earth. The results presented in this thesis support this conclusion as I find the system can be readily explained by the accretion of primitive material.

3.2.21 WD1232+563

Table 3.21 displays the stellar data, the atmospheric abundances, and the sinking timescales presented in Xu et al. (2019) for the WD1232+563 system. The white dwarf properties and atmospheric abundances, other than the upper limits, were inputted into the model in order to constrain the origin and geology of the polluting material.

Figure 3.21 displays the model fit with the highest Bayesian evidence, which has a χ^2_{pdp} of 0.94. A scenario in which the pollutant material is a primitive body accreting in the steady state phase which has a composition rich in water ice best explains the atmospheric abundances. The model parameters utilised in the optimised model fit are: the stellar metallicity index, the pollution fraction, the accretion event lifetime, the time passed since accretion started, and the formation distance. The model produces a 3.90σ constraint on the pollutant containing water ice and a 2.33σ constraint on the system accreting material in steady state. The system has the longest sinking timescales of any system the model predicts to be in steady state, of the order $10^{5.5}$ years. In order for this system to settle into a steady state of accretion the accretion event would be required to have a duration of the order of $1\,\text{Myr}$. The mass of the polluting body is constrained to be above $10^{21.17}\,\text{kg}$ suggesting that the polluting body is at least 5 times as massive as Vesta, and therefore, is likely a body equivalent to a large asteroid or minor planet.

Xu et al. (2019) concluded that the pollutant material was likely primitive however the high O abundance was puzzling, due to a lack of H in the DBZ star which would
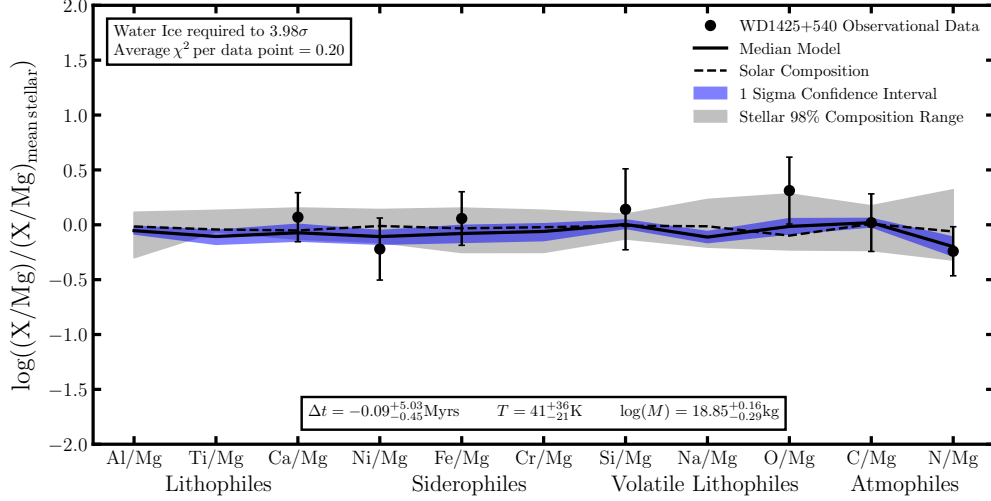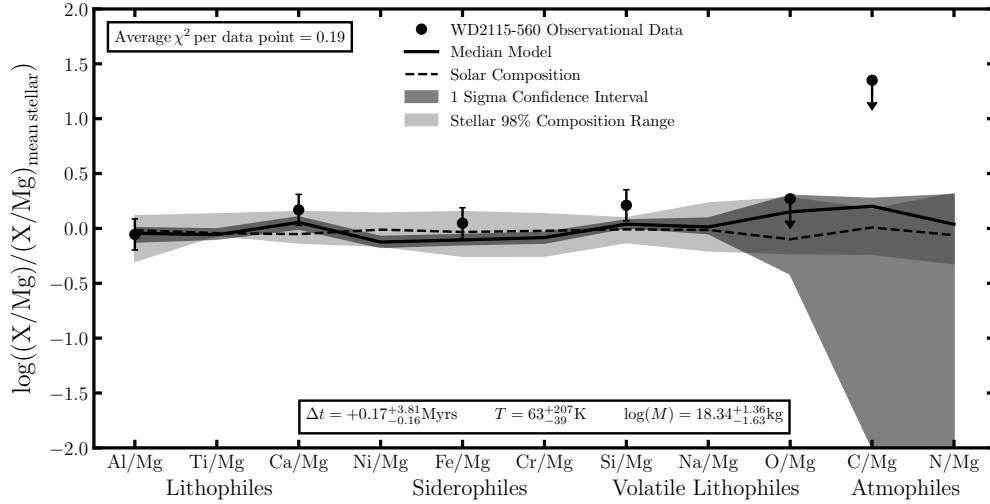
Fig. 3.20 The fit of model with the highest Bayesian evidence to the atmospheric abundances observed in WD2115-560. The polluting material is most likely a primitive body accreting in steady state, however any further constraints are not possible due to a lack of abundances.

Table 3.20 Data for WD2115-560 (Swan et al. (2019)).

Type	q	$M_{\mathrm{WD}}/M_\odot$	T/K
DAZ	-10.3	0.58	9,600
Element	log(Abundance/H)	log(Sinking Timescale/years)	
Al	-7.6 ± 0.1	2.88	
Ti	—	2.82	
Ca	-7.4 ± 0.1	2.90	
Ni	—	2.77	
Fe	-6.4 ± 0.1	2.75	
Cr	—	2.76	
Mg	-6.4 ± 0.1	2.89	
Si	-6.2 ± 0.1	2.90	
Na	—	2.94	
O	< -5.0	3.11	
C	< -4.3	3.13	
N	< -4.0	3.15	
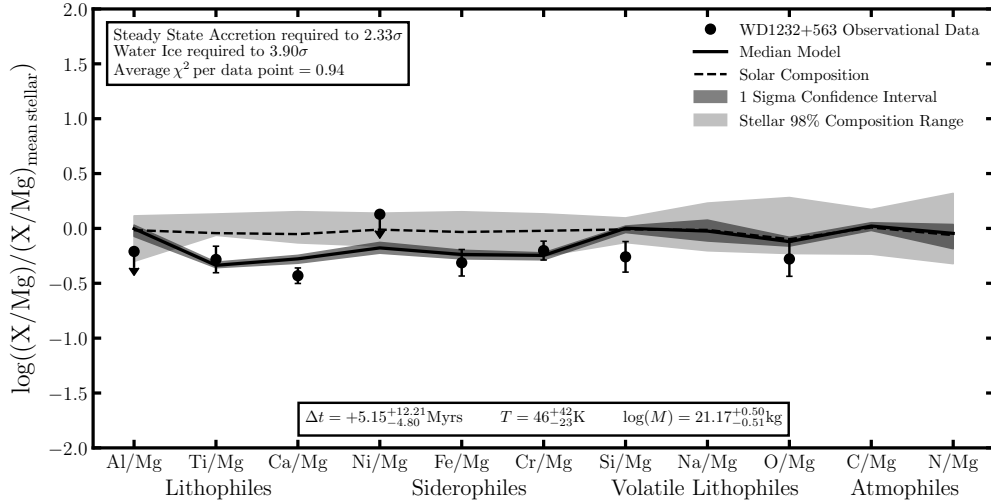
Fig. 3.21 The fit of model with the highest Bayesian evidence to the atmospheric abundances observed in WD1232+563. I find that the best fit model is one in which the system is in steady state and is water ice rich. However, the lack of H pollution puts such an explanation into question.

Table 3.21 Data for WD1232+563 (Xu et al. (2019)).

Type	q	$M_{WD}/M_{\odot}$	T/K
DBZ	-5.924	0.773	11,787
Element	log(Abundance/He)	log(Sinking Timescale/years)	
Al	< -7.50	5.71	
Ti	-8.96 ± 0.11	5.45	
Ca	-7.69 ± 0.05	5.50	
Ni	< -7.30	5.52	
Fe	-6.45 ± 0.11	5.50	
Cr	-8.16 ± 0.07	5.47	
Mg	-6.09 ± 0.05	5.72	
Si	-6.36 ± 0.13	5.72	
Na	—	5.69	
O	-5.14 ± 0.15	5.70	
C	—	5.75	
N	—	5.70	

be expected if the pollutant was ice rich. The results presented in this thesis find the same conclusion that the O abundance requires the pollutant to contain water ice. The expected abundance of H given the other elemental abundances is -5.00 ± 0.30 which is 2σ from the observed H abundance of -5.90 ± 0.15 so while I do not model atmospheric H as a pollutant, as it is not necessarily related to the metals currently in the atmosphere, I do suggest that this system is studied further in order to understand the tension between the O abundance and the H abundance.

3.2.22   WD1551+175

Table 3.22 displays the stellar data, the atmospheric abundances, and the sinking timescales presented in Xu et al. (2019) for the WD1551+175 system. The white dwarf properties and atmospheric abundances were inputted into the model in order to constrain the origin and geology of the polluting material.

Figure 3.22 displays the model fit with the highest Bayesian evidence, which has a high χ^2_{pdp} of 1.25. Potentially this poor fit could be due to processes which are altering the composition of the pollutant body which have not been modelled in this work or it could simply be down to the uncertainties being underestimated. The element which is most difficult to fit is O as its observed abundance is higher than the model can produce in conjunction with the super stellar refractory abundances. A scenario in which the pollutant material is a primitive body accreting in build-up phase which has experienced temperatures above $1,300\,\mathrm{K}$ such that it is depleted in the moderate volatiles best explains the atmospheric abundances. The model parameters utilised in the optimised model fit are: the stellar metallicity index, the pollution fraction, the accretion event lifetime, the time passed since accretion started, and the formation distance. If the model fit is trusted the model produces a 7.58σ constraint on the pollutant being the product of incomplete nebula condensation. The mass of the polluting body is constrained to be above $10^{20.16}\,\mathrm{kg}$ suggesting that the polluting body is at least 50% as massive as Vesta, and therefore, is likely a body equivalent to a large asteroid or minor planet.

Xu et al. (2019) concluded that the pollutant material was likely a refractory-rich body which formed at high temperatures. The results presented in this thesis support this conclusion, however, further study is recommended in order to explain the high O abundance.
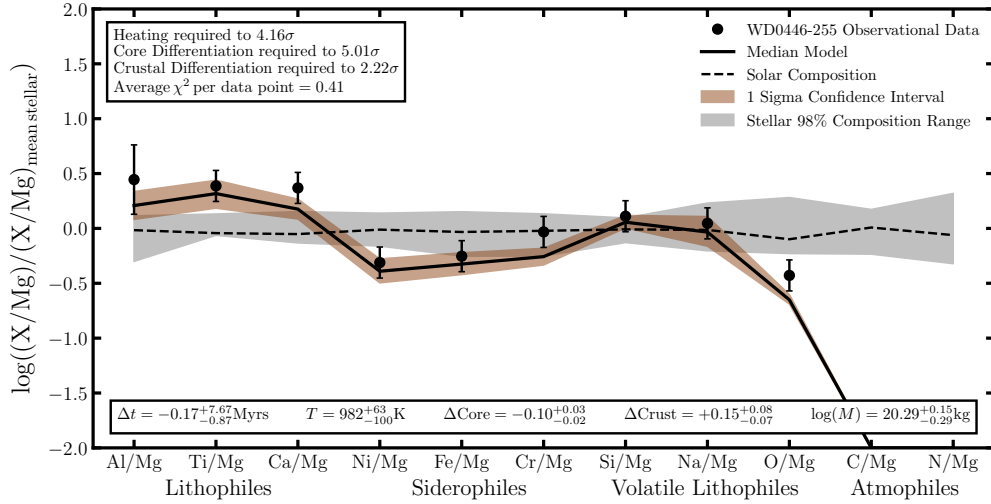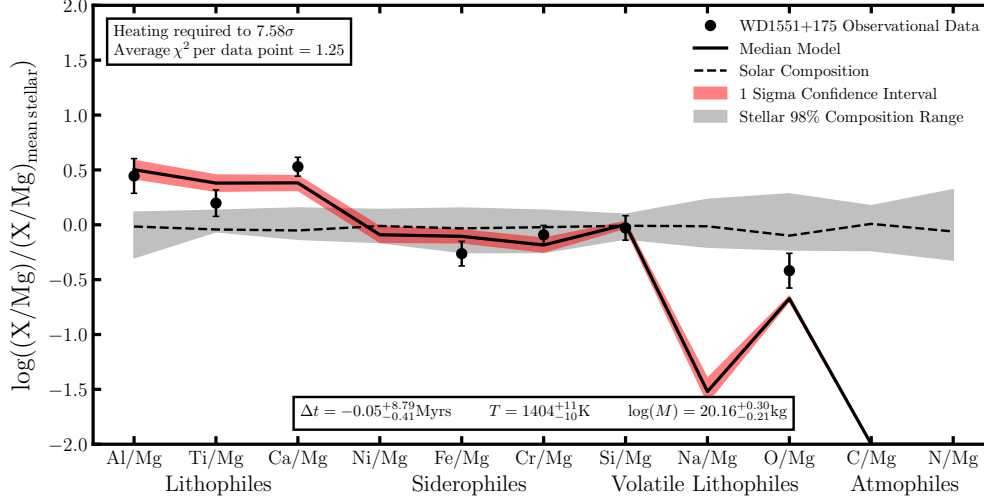
Fig. 3.22 The fit of model with the highest Bayesian evidence to the atmospheric abundances observed in WD1551+175. The polluting material is most likely a primitive body accreting in build-up phase which has undergone sufficient heating such that the moderate volatiles incompletely condensed from the nebula. However, the modelled fit to the data is not particularly strong.

Table 3.22 Data for WD1551+175 (Xu et al. (2019)).

Type	q	$M_{\mathrm{WD}}/M_\odot$	T/K
DBZ	-5.691	0.603	14,756
Element	log(Abundance/He)	log(Sinking Timescale/years)	
Al	-6.99 ± 0.15	5.92	
Ti	-8.68 ± 0.11	5.72	
Ca	-6.93 ± 0.07	5.76	
Ni	—	5.76	
Fe	-6.60 ± 0.10	5.75	
Cr	-8.25 ± 0.07	5.73	
Mg	-6.29 ± 0.05	5.94	
Si	-6.33 ± 0.10	5.93	
Na	—	5.92	
O	-5.48 ± 0.15	5.94	
C	—	5.98	
N	—	5.95	

3.2.23   WD2207+121

Table 3.23 displays the stellar data, the atmospheric abundances, and the sinking timescales presented in Xu et al. (2019) for the for the WD2207+121 system which were inputted into the model in order to constrain the origin and geology of the polluting material.

Figure 3.23 displays the model fit with the highest Bayesian evidence, which has a χ^2_{pdp} of 0.34. A scenario in which the pollutant material is a primitive body accreting in the steady state phase which formed at temperatures of the order $200\,\mathrm{K}$ best explains the atmospheric abundances. The model parameters utilised in the optimised model fit are: the stellar metallicity index, the pollution fraction, the accretion event lifetime, the time passed since accretion started, and the formation distance. The model produces a 2.04σ constraint on the pollutant being the product of incomplete nebula condensation. The mass of the polluting body is constrained to be above $10^{20.65}\,\mathrm{kg}$ suggesting that the polluting body is at least 1.8 times as massive as Vesta.

Xu et al. (2019) concluded that the pollutant material was similar to bulk Earth in composition and was potentially icy. I find that a scenario in which the pollutant material is primitive is also the best explanation for the atmospheric abundances, however, given the O abundance I find that it is not necessary to suggest that the pollutant contains water ice.

3.2.24   WD1145+017

Table 3.24 displays the stellar data, the atmospheric abundances, and the sinking timescales presented in Fortin-Archambault et al. (2020) for the WD1145+017 system. The white dwarf properties and atmospheric abundances, other than C and the upper limits, were inputted into the model in order to constrain the origin and geology of the polluting material.

Figure 3.24 displays the model fit with the highest Bayesian evidence, which has a χ^2_{pdp} of 0.19. A scenario in which the pollutant material is a primitive body accreting in build-up phase easily explains the atmospheric abundances. The model parameters utilised in the optimised model fit are: the stellar metallicity index, the pollution fraction, the accretion event lifetime, the time passed since accretion started, and the formation distance. Given the uncertainties on the O abundance the model does not require the pollutant to contain water ice nor does it require it to be the the product of incomplete nebula condensation as both scenarios can explain the data. The mass of the polluting body is constrained to be above $10^{20.68}\,\mathrm{kg}$ suggesting that the polluting
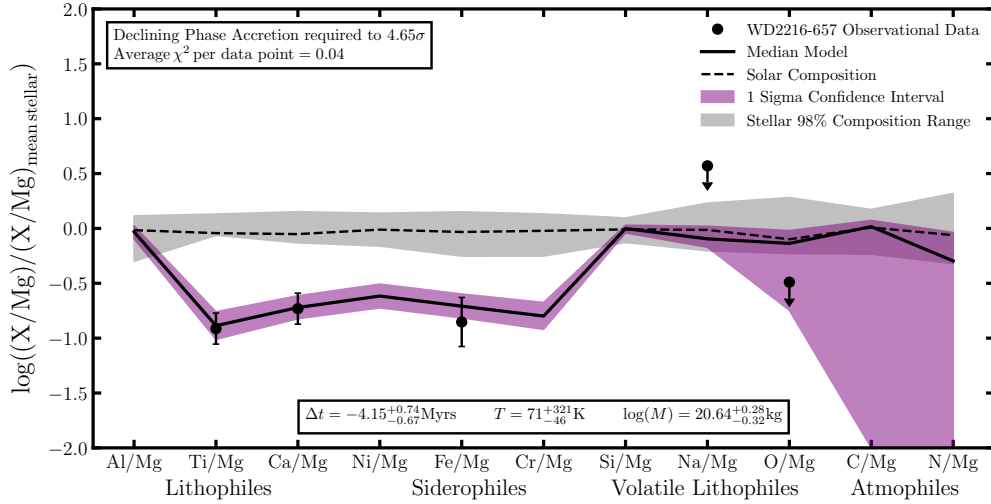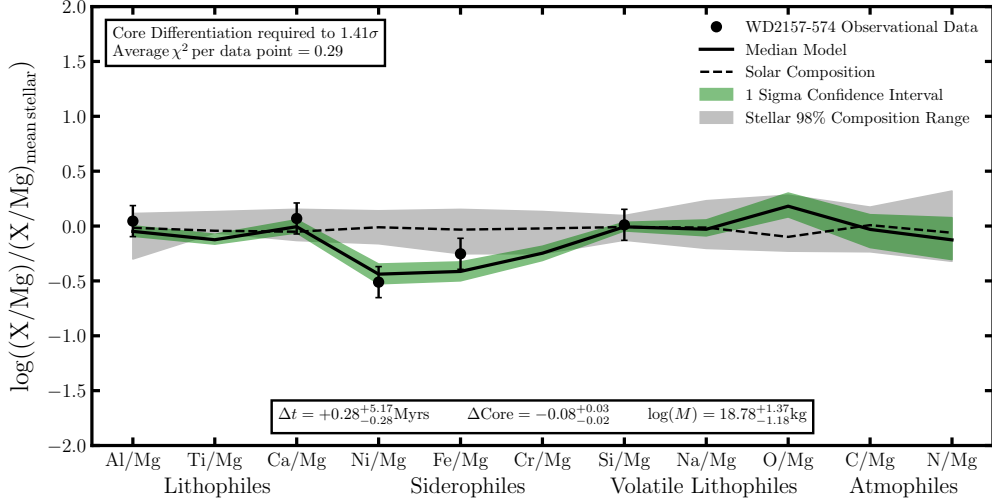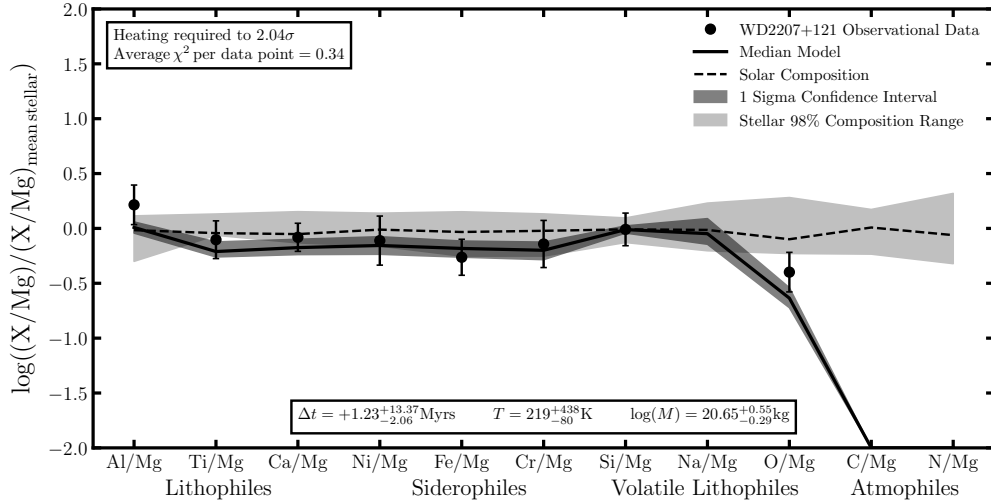
Fig. 3.23 The fit of model with the highest Bayesian evidence to the atmospheric abundances observed in WD2207+121. The polluting material is most likely a primitive body which is accreting in the steady state phase and has experienced sufficient heating such that it contains no water ice.

Table 3.23 Data for WD2207+121 (Xu et al. (2019)).

Type	q	$M_{WD}/M_\odot$	T/K
DBZ	-5.591	0.574	14,752
Element	log(Abundance/He)	log(Sinking Timescale/years)	
Al	-7.08 ± 0.15	6.02	
Ti	-8.84 ± 0.14	5.82	
Ca	-7.40 ± 0.08	5.85	
Ni	-7.55 ± 0.20	5.86	
Fe	-6.46 ± 0.13	5.84	
Cr	-8.16 ± 0.19	5.83	
Mg	-6.15 ± 0.10	6.03	
Si	-6.17 ± 0.11	6.02	
Na	—	6.02	
O	-5.32 ± 0.15	6.03	
C	—	6.08	
N	—	6.04	
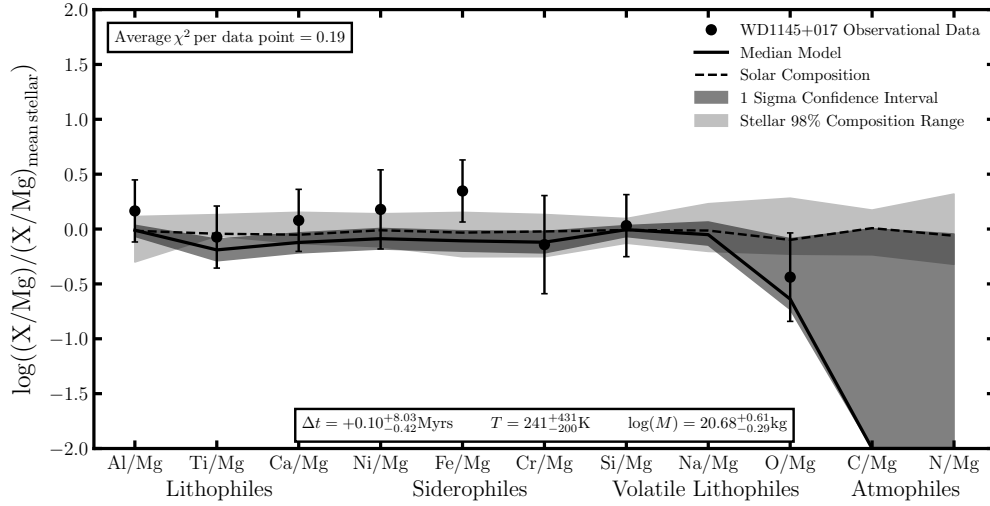
Fig. 3.24 The fit of model with the highest Bayesian evidence to the atmospheric abundances observed in WD1145+017. The polluting material is most likely a primitive body accreting in build-up phase.

Table 3.24 Data for WD1145+017 (Fortin-Archambault et al. (2020)).

Type	q	$M_{\mathrm{WD}}/M_\odot$	T/K
DBZ	-5.819	0.656	14,500
Element	log(Abundance/He)	log(Sinking Timescale/years)	
Al	-6.89 ± 0.20	5.80	
Ti	-8.57 ± 0.20	5.58	
Ca	-7.00 ± 0.20	5.62	
Ni	-7.02 ± 0.30	5.63	
Fe	-5.61 ± 0.20	5.61	
Cr	-7.92 ± 0.40	5.60	
Mg	-5.91 ± 0.20	5.81	
Si	-5.89 ± 0.20	5.80	
Na	—	5.79	
O	-5.12 ± 0.35	5.80	
C	-7.50 ± 0.40	5.85	
N	< -7.00	5.81	

body is at least 1.85 times as massive as Vesta, and therefore, is likely a body equivalent to a large asteroid or minor planet.

Fortin-Archambault et al. (2020) concluded that the pollutant material had a similar composition to bulk Earth. The results presented in this thesis agree with this conclusion. With such large abundance uncertainties very little can be constrained about the system other than the accretion of a primitive body with a mass similar to that of a minor planet can sufficiently explain the observations. The detection of disintegrating material orbiting the white dwarf (Vanderburg et al. (2015)) potentially supports the conclusion that the system is currently accreting material. Further investigation into the material orbiting WD1145+017 and whether its dynamical properties can be explained by material with a homogeneous composition, as suggested by the primitive nature of the material in the photosphere, would be a worthwhile endeavor.

3.3   Summary and discussion

In this chapter I have analysed the atmospheric abundances present in 24 of the most heavily polluted white dwarf systems currently known. In this section I summarise and discuss the results found as well as reflecting on the diversity of white dwarf pollutants in general.

Crucially, the model presented in Chapter 2 can explain the abundances of all but one system to a χ^2_{pdp} less than unity. This not only validates the model but also suggests that the abundances of rocky exo-planetary bodies are mainly dictated by the three processes modelled in Chapter 2: the initial composition of the protoplanetary disc, thermodynamic conditions during condensation, and differentiation followed by collisional processing and fragmentation. Understanding the major factors which influence the composition of rocky bodies is vital as the statistical significances derived in this chapter are found by comparing the model fits with other model fits, therefore, reproducing the abundances well validates the results and statistical significances presented.

The majority of the systems analysed in this chapter, 14/24, are well explained by a scenario in which they are accreting primitive material, material that matches the composition of nearby stars in combination with a condensation temperature dependent trend without any need for any further processing. This is not unexpected, as not only are the majority of Solar System bodies primitive, but not all rocky bodies are expected
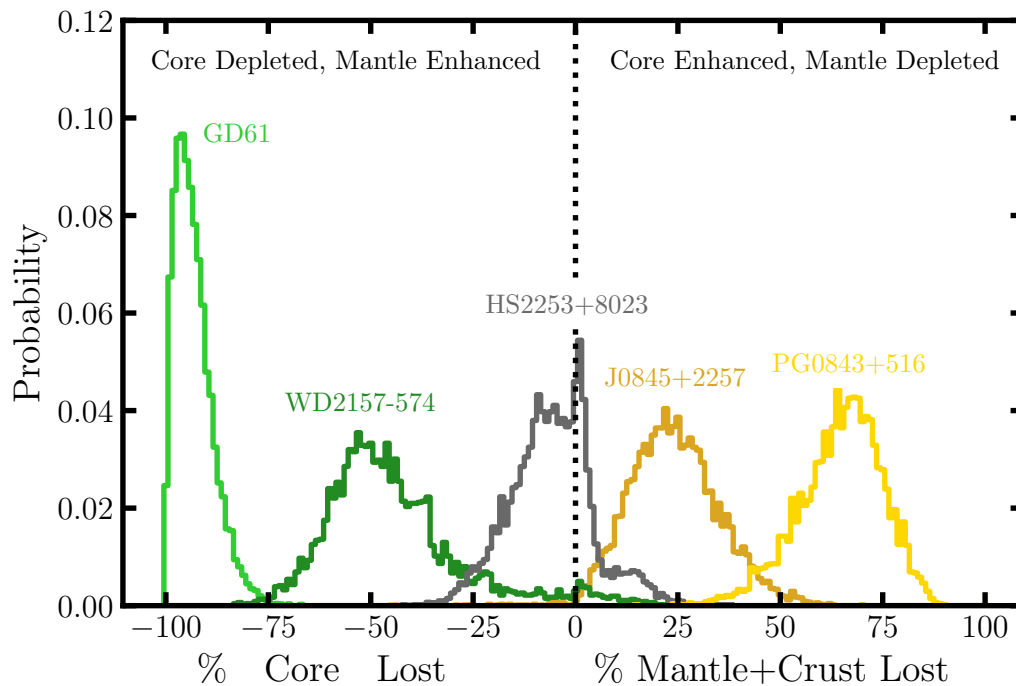
Fig. 3.25 The posterior distributions of the percentage of core/mantle+crust lost for 5 polluted white dwarf systems. The material which pollutes white dwarfs ranges from extremely core-depleted to extremely core-rich.

to differentiate and not all collisions between differentiated bodies are expected to produce fragments with a notable excess of core-like, mantle-like, or crust-like material.

However, not all polluted white dwarf systems are consistent with the accretion of primitive material. The results found in this chapter present strong evidence for differentiation, collisions, and fragmentation occurring in exo-planetary systems. In 10/24 systems the model with the highest Bayesian evidence is one in which the pollutant material is a fragment of a larger differentiated body and for 6 of these systems such a model is required to a statistical significance of at least 2σ. Of the 6 systems: 2 systems are required to be accreting core-rich fragments, 1 system is required to be accreting a mantle-rich fragment, 2 systems are required to be accreting crust-rich fragments, and 1 system is required to be accreting a crust-stripped fragment. Therefore, white dwarfs offer a unique insight into the geological and collisional processes which occur in exo-planetary systems and their polluting material provides evidence that geological differentiation into cores, mantles, and crusts occurs in the rocky worlds present in exo-planetary systems in a similar manner to rocky worlds present in the Solar System.

The accretion of fragments of differentiated bodies also suggests that white dwarfs are often polluted by single bodies rather than multiple bodies, as the abundance patterns would likely be washed out if multiple bodies were accreting simultaneously. Thus, the assumption of single body pollution taken in Chapter 2 is therefore somewhat validated. Additionally, as only one system, PG0843+516, requires non-Earth-like differentiation conditions to explain its abundances the assumption that a full self consistent differentiation model is not yet required to analyse white dwarf pollutants is justified. However, even though the uncertainties on many white dwarf abundances would make meaningful constraints on non-Earth-like differentiation difficult, such an advanced differentiation model would still be valuable in order to fully validate the results and potentially constrain the nature of the parent bodies of white dwarf pollutants.

Figure 3.25 displays the posterior distributions for the fraction of core or mantle and crust lost for 5 of the polluted white dwarf systems analysed. Due to their low siderophile abundances GD61 and WD2157-574 are modelled to be depleted in core-like material (greens), while J0845+2257 and PG0843+516 are modelled to be depleted in mantle-like material due to their high siderophile abundances (yellows). HS2253+8023 is shown as an example of the posterior for a primitive body which does not require differentiation followed by collisional processing. The x axis is scaled as such so that the scale is centered at zero and so there is no artificial scaling based on the initial sizes of the core, mantle, and crust. Figure 3.25 highlights how the systems analysed in this chapter provide evidence for a wide range of core mass fractions. The frequency of each type of fragment is difficult to assess with only 10 systems, however, the discovery of at least one crust-rich, core-rich, mantle-rich and crust-stripped body indicates that the results so far are likely consistent with an even spread of core mass fractions as predicted by models of protoplanetary collisions (Carter et al. (2015); Carter et al. (2018)).

As shown in Chapter 2, the volatile abundances, in particularly Na and O, can be used to constrain the formation temperature of the polluting material. The majority of systems analysed in this work, 14/24, have abundances consistent with dry rocky material which formed between 1,300 K and 200 K. This reinforces the conclusion that the majority of white dwarf pollutants are bodies originating in the inner regions of white dwarf planetary systems and have low volatile budgets similar to many Solar System asteroids.

5 systems are required to be partially composed of water ice to a statistical significance of greater than 2σ. The presence of water ice in all of these systems has
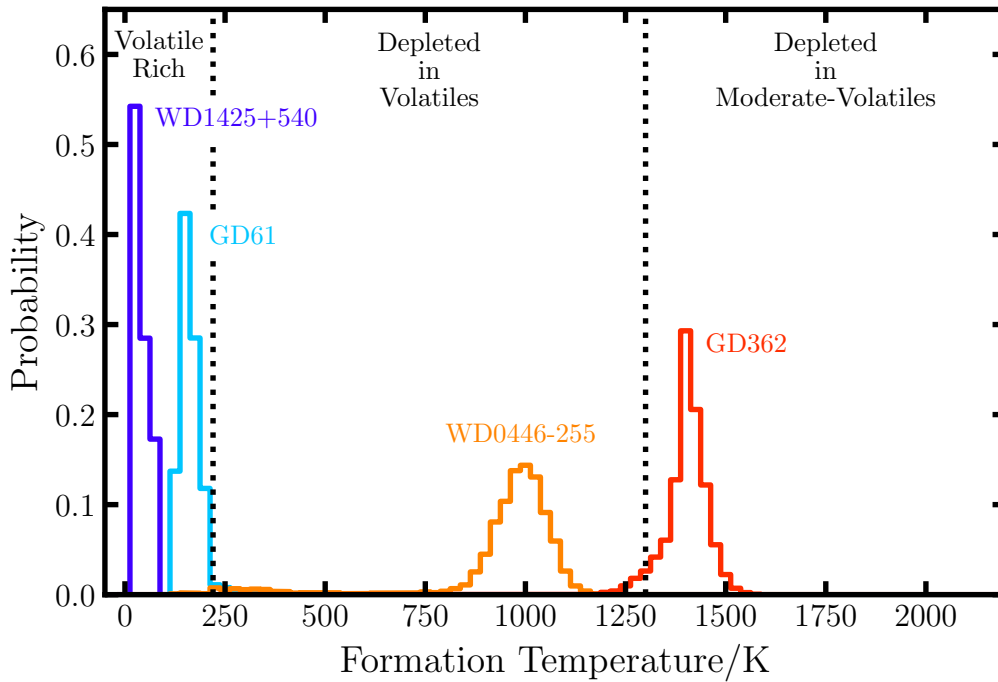
Fig. 3.26 The posterior distributions of the formation temperature for the pollutants of 4 white dwarf systems. The material which pollutes white dwarfs ranges from icy volatile rich material to material which is depleted in the moderate-volatiles.

been concluded previously (Dufour et al. (2012); Farihi et al. (2013); Raddi et al. (2015); Xu et al. (2017); Xu et al. (2019)) by calculating whether there is an O excess relative to the amount which could be sequestered in oxides. The presence of water in 2 of these systems is debated due to low abundances of polluting H (Dufour et al. (2012): Xu et al. (2019)), however, for 3 systems the abundances of polluting H are consistent with the accretion of water. Therefore, there is strong evidence for the presence of water ice in multiple white dwarf systems which suggests that it is possible to pollute white dwarfs with material which originates exterior to the water ice line.

Unexpectedly, the abundances of 5 systems require pollutant material which condensed out of the nebula at temperatures of the order of 1,400 K. Although high temperature condensates like CAIs are found in the Solar System there are no large bodies which are predominately composed of them. One important difference between the Solar System and the systems around the progenitors of polluted white dwarfs is that the host stars were most likely A-types. Therefore, temperatures above 1,400 K during the protoplanetary disc phase can last for longer and be maintained at further

distances from the host star. Using the protoplanetary disc model outlined in Chapter 2, I find that in order to reach temperatures greater than 1,400 K the planetesimals would need to have formed interior to 2.75 AU. It is important to note that not all bodies orbiting the progenitors of white dwarfs will survive until the white dwarf phase. Bodies which reside closer to their host star are less likely to survive as the 3 main effects which remove bodies orbiting evolved stars: stellar engulfment, Yarkovsky drift, and YORP (Yarkovsky–O'Keefe–Radzievskii–Paddack) spin-up are all more effective at removing bodies closer to the star (Bottke et al. (2006); Veras et al. (2014a); Veras et al. (2016); Mustill et al. (2018)). Using the predicted masses of the pollutants it is possible to estimate the minimum location a body could have formed at and survived. If this calculation is performed one finds that the bodies must have formed earlier than 0.32 Myrs in order to form far enough from the star to survive to the white dwarf phase but close enough to the star to be heated to temperatures greater than 1,400 K. Such early formation times are plausible and therefore the pollution of white dwarfs by such bodies with no Solar System equivalent is potentially not unexpected.

Figure 3.26 displays the posterior distributions for the formation temperature of the material which pollutes 4 white dwarfs. Due to the abundances of O, C, and N the pollutant of WD1425+540 is required to be an ice-rich Kuiper belt analogue, while the high O abundance present in GD61 requires its pollutant to contain a significant fraction of water ice. The Na and O abundances of WD0446-255 allows its formation temperature to be constrained more precisely suggesting a dry pollutant which formed at ∼1,000 K. The enhanced refractory (Al, Ti, Ca) and depleted moderate volatile (Mg, Si, Fe) of the pollutant of GD362 suggest a formation temperature of the order 1,400 K. Figure 3.26 highlights how the systems analysed in this chapter provide evidence for a wide range of formation temperatures, and thus, formation locations. The frequency of bodies polluting white dwarfs as a function of radial distance from the star is hard to quantify with such a small sample, however, with 3(5) ice-rich bodies, 14 dry bodies, and 5 bodies depleted in moderate volatiles a scenario in which pollutants have an equal probability of accreting onto the white dwarf regardless of formation location seems consistent with the observations as suggested in Bonsor et al. (2011). Such a conclusion also reinforces the prior distribution assumed for the formation location in the model.

The model fits also constrain the phase of accretion a system is likely to be in. As the effects of the mode of accretion are more subtle the constraints often are not as strong, however, they still provide useful information. Of the 24 systems analysed 11

Table 3.25 A summary of the best-fit phases of accretion for the 24 white dwarfs analysed in this chapter. All systems with sinking timescales above $\sim$1 Myrs are not expected to be in steady state while all systems with sinking timescales below $\sim$0.1 Myrs are expected to be in steady state.

System	$\log(t_{\text{sink, Mg}})$	Phase of Accretion	System	$\log(t_{\text{sink, Mg}})$	Phase of Accretion
WD0466-255	6.42	Build-up	GD 61	5.26	Build-up
J1242+5226	6.38	Build-up	J0738+1835	5.26	Steady State
WD2216-657	6.28	Declining (4.65σ)	HS2253+8023	4.93	Build-up
WD1425+540	6.12	Build-up	NLTT43806	4.28	Steady State (1.85σ)
GD40	6.08	Build-up	J0845+2257	4.08	Steady State
G241-6	6.08	Build-up	WD2157-574	3.72	Steady State
WD2207+121	6.03	Steady State	WD2115-560	2.89	Steady State
WD1551+175	5.94	Build-up	WD1536+520	2.22	Steady State (1.68σ)
WD1145+017	5.81	Build-up	G29-38	-0.60	Steady State (1.08σ)
WD1232+563	5.72	Steady State (2.33σ)	J1043+0855	-2.16	Steady State
PG1225-079	5.68	Build-up	PG0843+516	-2.23	Steady State
GD362	5.34	Build-up	J1228+1040	-2.24	Steady State

are expected to be in the build-up phase, 12 are expected to be in the steady state phase, and 1 is expected to be in the declining phase.

Table 3.25 highlights the best-fit phases of accretion for each system and whether there are any statistical constraints on the system being in such a phase rather than either of the other two. The best fit for all systems with sinking timescales below $\sim$0.1 Myrs is the steady state phase, while no system with a sinking timescale above $\sim$1 Myrs is predicted to be in the steady state phase. The systems with sinking timescales between 0.1 Myrs and 1 Myrs have best-fit models which suggest they can be in either steady state or in build-up. Therefore, given it takes roughly 5 sinking timescales to settle into the steady state phase (Koester (2009)), the abundances provide constraints on the accretion event lifetimes and suggest that they are of the order of a few Myrs which is consistent with the results presented in Girven et al. (2012). The constraints on 4 systems to be in the steady state phase hint that thermohaline instabilities do not occur in some white dwarf atmospheres as the unique signature created by steady state accretion can not be reproduced if thermohaline instabilities did occur or by any other effects modelled in this work.

There is a strong constraint, 4.65σ, on WD2216-657 being in the declining phase and for the accretion event to have finished $\sim$4 Myrs ago. Such a system offers a unique insight into the mass of white dwarf pollutants as there is no longer any material left to accrete so the mass constraint provided by the model is no longer a lower limit. The mass of the body is constrained to be $20.64^{+0.28}_{-0.32} \log(\text{kg})$ suggesting that the polluting body is 1.6 times as massive as Vesta. Such a result adds further support to the conclusion that the white dwarf pollutants observed thus far are equivalent to large asteroids or minor planets as has previously been concluded in the literature (Jura

(2006); Jura and Young (2014)). It is important to note though that smaller bodies potentially also pollute white dwarfs, however as they are more difficult to observe they are unlikely to form part of the sample analysed in this thesis. The model required to fit the abundances of J0738+1835 requires the parent body to have had a crust which is $\sim$ ten times thicker than the Earth's crust relative to the size of the body. A crust of such size is not unexpected for subterrestrial size bodies due to their increased surface area to volume ratio (Lodders and Fegley (1998); Clenet et al. (2014)), thus, the pollutant of J0738+1835 provides further evidence that the pollutants of white dwarfs are equivalent to large asteroids or minor planets.

Two systems which fulfilled the selection criteria and whose abundances were published in Swan et al. (2019) have not been modelled in this chapter, WD0449-259 and WD1350-162. Unusually, these two systems have atmospheric abundances dominated by Na and are predicted to have Na sinking timescales which are shorter than Mg. Therefore, their abundances cannot be explained by the model presented in this thesis. The Na abundance in these two systems could be explained if the white dwarfs preferentially accreted the outer layers and the volatile species of the body initially before subsequently accreting the inner layers and the refractories. Because this would allow for a phase in which all the Na from a body was in the white dwarf's convective zone while the majority of its Ca, Fe, Mg etc. remained in a circumstellar reservoir yet to be accreted. Such a hypothesis would require further exploration for two main reasons: firstly, to confirm if the physical and chemical timescales on which sublimation and accretion processes occur could produce white dwarf atmospheres with two distinct compositional phases, and secondly, to confirm why only a minority of systems are found in such a phase. If such a hypothesis were found to be plausible it would also predict a population of core-rich moderate-volatile depleted systems which have so far not been found.

As expected the results presented in this chapter are broadly the same as the results presented in Harrison et al. (2018) where the same systems were analysed but with a frequentist statistical approach rather than a Bayesian one. The only results which differ are for the systems SDSS J1228+1040 and SDSS J1242+5226. SDSS J1228+1040 is no longer best explained as a primitive ice-rich body but instead is best explained as a primitive refractory rich body. SDSS J1242+5226 still is required to be a mantle-rich fragment of a differentiated body which contains water ice but it no longer requires crustal-stripping to explain its Na abundance. The main advantages of the Bayesian approach are that it take into account the prior information known about the systems and also allows the distributions of each model parameter, and therefore the constraints

on the requirement of each parameter, to be computed in a self consistent manner without the need for splitting the model into a discrete grid.

3.4   Conclusions

In this chapter I have presented how the model outlined in Chapter 2 can reproduce the atmospheric abundances of 24 externally polluted white dwarfs. The abundance patterns present in the atmospheres of the white dwarfs analysed cannot be explained by the accretion of stellar material or the ISM due to their depleted O abundances, as previously suggested in the literature (Farihi et al. (2010a); Jura and Young (2014)). However, the atmospheric abundances for 23 of the 24 systems can be well fitted, $\chi^2_{\mathrm{pdp}} < 1$, by a scenario in which they have accreted planetary material further supporting the planetary body accretion hypothesis and validating the model used.

The optimum model for 10 of the 24 systems analysed required them to have accreted fragments of differentiated bodies. For 6 systems the accretion of such a fragment is required to a significance of greater than 2σ. The discovery of core-rich, mantle-rich, crust-rich, and crust-stripped pollutants, and the roughly even spread in core mass fractions found is an expected outcome of the collisional processing (Carter et al. (2015); Carter et al. (2018)). Therefore, the polluting material in some white dwarf systems provides evidence that geological differentiation into cores, mantles, and crusts occurs in the rocky worlds present in exo-planetary systems in a similar manner to rocky worlds present in the Solar System. The accretion of fragments of differentiated bodies also suggests that white dwarfs are often polluted by single bodies because if multiple bodies polluted white dwarfs simultaneously the frequency of such systems would be lower.

The analysis in this chapter suggests that white dwarf pollutants form at a wide range of formation temperatures and thus originate from a wide range of formation locations. Therefore, the scattering of planetary bodies into a white dwarf's tidal radius is potentially equally efficient over a large range of semi-major axes. At least 3 systems require the presence of water ice in their pollutants to a statistical significance of 2σ, while 5 pollutants require formation temperatures of the order $1,400\,\mathrm{K}$ to explain their enhanced refractory abundances. Potentially such results are not unexpected as water ice is expected to avoid sublimation until it is accreted onto the white dwarf (Jura and Xu (2010a); Malamud and Perets (2016)) and the progenitors of white dwarfs produce much hotter inner disc conditions in comparison to the Sun.

The chemical abundances present in the atmospheres of polluted white dwarfs can also be used to constrain the phase of accretion a system is in. In this chapter I found that systems with sinking timescales below $\sim$0.1 Myrs are likely in the steady state phase while systems with sinking timescales above $\sim$1 Myrs are likely in the build-up phase. These results in combination with the constraints on NLTT43806, WD1536+520, and WD1232+563 to be in the steady state phase not only suggest that thermohaline instabilities do not develop in some polluted white dwarfs but additionally suggest that accretion event lifetimes are of the order of Myrs.

One system, WD2216-657, is constrained to be in the declining phase with a statistical significance greater than 4σ. Therefore, the mass of the pollutant can be constrained as it is known that there is no material left to be accreted. I find the pollutant had a mass of $10^{20.64}$ kg suggesting that the polluting body is 1.6 times as massive as Vesta. Additionally, the lower limit mass estimates for the remaining 23 systems all suggest pollutants at least as massive as large Solar System asteroids. These results strongly supports the conclusion that the white dwarf pollutants observed to date are equivalent to large asteroids or minor planets as previously concluded in the literature (e.g. Jura and Young (2014)).

Chapter 4

Analysing a large population of white dwarf pollutants

4.1 Introduction

This chapter aims to further investigate the origin of white dwarf pollutants by analysing the large sample of white dwarf atmospheric abundances derived by Hollands et al. (2017). This study offers another test of the validity of the model outlined in Chapter 2 while also potentially providing additional support to the conclusions found in Chapter 3. The analysis of a much larger sample allows more robust constraints to be placed on the frequency of pollutant material which has undergone differentiation, the average formation location of white dwarf pollutants, the average mass of white dwarf pollutants, and the average lifetimes of white dwarf accretion events. However, the observational biases present in the sample must be well understood in order to draw meaningful numbers from the analysis, and attempt to understand the material present in exo-planetary systems. In Section 4.2, I outline the polluted white dwarf data analysed in this work. In Section 4.3, I present the individual results for each system analysed, in Section 4.4 I present the constraints derived for the population as a whole, and in Section 4.5 I summarise the results. In Section 4.6, I discuss the caveats of the work and the implications of the results. The conclusions of this study are outlined in Section 4.7.

4.2   The Hollands et al. (2017) catalogue

The analysis focuses on the 230 externally polluted cool DZ white dwarfs presented in Hollands et al. (2017). The sample was selected by Hollands et al. (2017) by searching for white dwarf stars whose colour was shifted away from the usual white dwarf track. When sufficiently polluted, the colour of DZ white dwarfs become modified and therefore, such a search could easily identify a large sample of polluted white dwarfs. For all the white dwarfs in the sample atmospheric abundance measurements of Ca, Mg, and Fe relative to He were derived, and in some cases, Ti, Ni, Cr and Na abundances were also found.

Table A.1 lists the abundances used in this work, alongside convective zone masses, sinking timescales and uncertainty estimates. I note here that uncertainties on the relative abundances were not found in Hollands et al. (2017) and are extremely time consuming to calculate and therefore, I utilise a conservative estimate of the expected uncertainty for each element in each system calculated using the signal to noise ratios (S/N) of the relevant spectra and considering the relative line strengths of each element. This is analogous to the procedure Hollands et al. (2017) used to calculate the uncertainty of the surface temperature measurements for the sample of white dwarfs. The uncertainty on the measurement of the atmospheric elemental abundance of an element X relative to He in dex is given by:

$$\sigma_X = \sqrt{\sigma_{\text{systematic}}^2 + \left(\frac{1.28}{(\text{S/N})}\right)^2} \tag{4.1}$$

where $\sigma_{\text{systematic}}$ is the assumed systematic error for the atmosphere elemental abundance relative to He in dex and (S/N) is the median signal to noise ratio of the spectra between 4500 and 5500 Å. The constant of proportionately 1.28 was chosen such that the uncertainties on the weakest lines in the noisiest spectra were 0.43 dex, given this was the maximum possible error on an individual elemental abundance for a 1σ detection (Hollands et al. (2017)). For the very best spectra in the sample, systematic uncertainty dominates. For elements with the highest line strength (Ca, Fe, and Na) this uncertainty is expected to be of the order 0.05 dex (Hollands et al., 2017). For elements with weaker line strengths (Cr, Mg, Ni, and Ti) the systematic errors are expected to be of the order 0.10 dex (Hollands et al., 2017).

Of the 230 systems with published abundances in Hollands et al. (2017) only 208 systems will be analysed in this chapter as 22 of the white dwarfs have magnetic fields stronger than 1 MG, and therefore their spectral features have been modified

substantially by Zeeman splitting (Hollands et al. (2017)). The 22 systems have been cut from the sample as the Hollands et al. (2017) model does not include magnetic fields and therefore the abundances and errors derived for such systems may not be valid.

4.3 Individual system constraints

The 208 polluted white dwarf atmospheric abundances outlined in Section 4.2 were fitted using the model described in Chapter 2. For each system the Bayesian evidence and χ^2 per element was found for various combinations of model parameters. The 'best' model is defined as the model which has the highest Bayesian evidence. The χ^2 per element of the model fit is then checked in order to confirm that the 'best' model is not simply the best out of a group of models which all struggle to reproduce the observations. In this work a model with a χ^2 per element of less than 1 was considered to be a sufficient fit. By comparing the Bayesian evidence after removing or adding extra parameters a constraint on the necessity for the inclusion of such a parameter can be found. In this chapter, for the individual systems I concentrate on the requirement for the inclusion of none-build-up phase accretion, core-mantle differentiation, core-mantle-crust differentiation, and heating during formation. A full set of figures containing the fits for each system is given in the appendix.

4.3.1 Primitive planetesimals accreting in build-up phase

For 135 systems the model with the highest Bayesian evidence is the model in which the abundances can be explained by the build-up phase accretion of a primitive planetesimal whose composition falls within the proxy for the range of initial compositions in protoplanetary discs. Therefore, 65% of all systems in the Hollands et al. (2017) sample can be easily be explained by such a scenario. For 47 of these systems Na was observed and therefore it can be robustly concluded that heating during formation was insufficient to cause the incomplete condensation of Na out of the nebula gas. Figure 4.1 highlights the abundances and model fits for four such example systems. The abundances are given relative to Mg, normalised to the mean star in the stellar sample, given in increasing volatility order, and grouped by the goldschmidt classification in order to allow abundance signatures relating to differential sinking, incomplete condensation, and geological processes to be displayed if they are present. Figure 4.4 displays the posterior distributions of the temperature for two of the example systems

(blue and cyan), it highlights how having stellar abundances of Na constrains the material to have formed below 1000 K.

4.3.2 Primitive planetesimals which have experienced formational heating, accreting in build-up phase

For 20 systems the model with the highest Bayesian evidence is a model in which the abundances can be explained by the build-up phase accretion of a primitive planetesimal which experienced sufficient temperatures during formation such that incomplete nebula condensation occurred. For 10 systems this heating is required in order to deplete the volatile element Na. Figure 4.2 highlights the abundances of four such systems and their modelled fits. The other 10 systems require the heating to not just deplete the volatiles (Na, O, etc.) but also deplete the moderate-volatiles (Mg, Si, etc.). Figure 4.3 highlights the abundances of four such systems and their modelled fits. Systems which require heating to explain their abundances are potential probes of the formation temperature of white dwarf pollutants, and thus, the formation location of exo-planetary bodies in white dwarf planetary systems. Figure 4.4 displays the posterior distributions of the temperature for six of the example systems (two only require the heating to deplete their volatiles while four require heating to deplete both the volatiles and moderate-volatiles). Figure 4.4 highlights how atmospheric abundances can effectively constrain the formation temperatures of pollutants. Figure 4.4 also highlights how the pollutants in the Hollands et al. (2017) sample show a wide range of formation temperatures, thus, a wide range of formation locations.

4.3.3 Fragments of differentiated planetesimals accreting in build-up phase

For 28 systems the model with the highest Bayesian evidence is one in which the white dwarf is accreting in the build-up phase a fragment of a larger parent body which underwent geo-chemical differentiation and formed a core and a mantle or a core, a mantle, and a crust. Figure 4.5 highlights the abundances and model fits for 4 of the 9 systems whose highest evidence model requires the accretion of a core-rich fragment. Figure 4.6 highlights the abundances and model fits for 4 of the 5 systems whose highest evidence model requires the accretion of a mantle-rich fragment. Figure 4.7 highlights the abundances and model fits for 4 of the 12 systems whose highest evidence model requires the accretion of a crust-rich fragment. Figure 4.8 displays the posterior distributions of the fraction of core or the fraction of crust and mantle
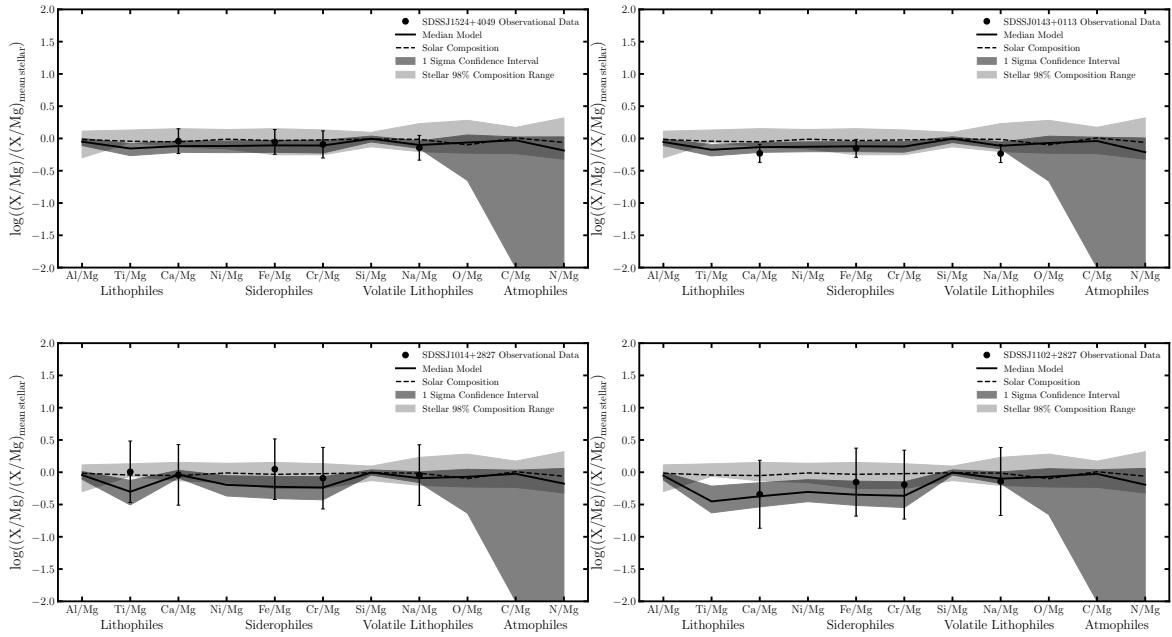
Fig. 4.1 Four example systems whose abundances are consistent with the accretion in build-up phase of a planetesimal whose composition is derived from the range of initial compositions found in planetesimal forming discs. In total 135/208 (65%) systems can be explained this way.
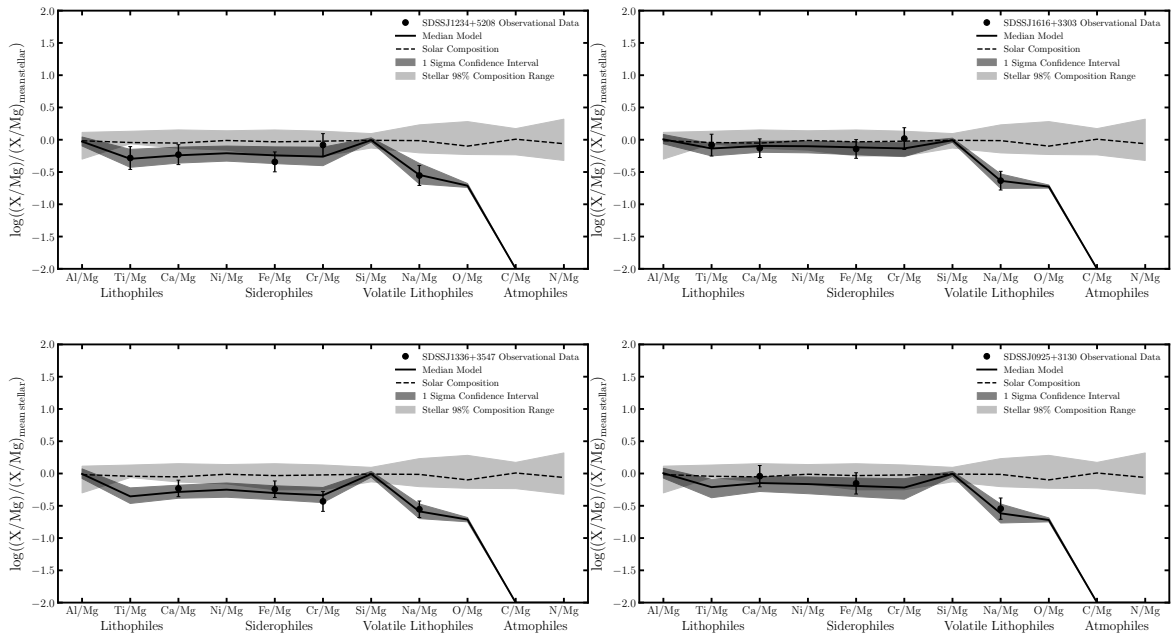
Fig. 4.2 Four example systems (of 10/208) in which Na is depleted relative to the range of initial conditions considered. I hypothesise that sufficient heating was experienced during formation to lead to the incomplete condensation of Na. 9 systems require such heating to a significance of at least 2σ.
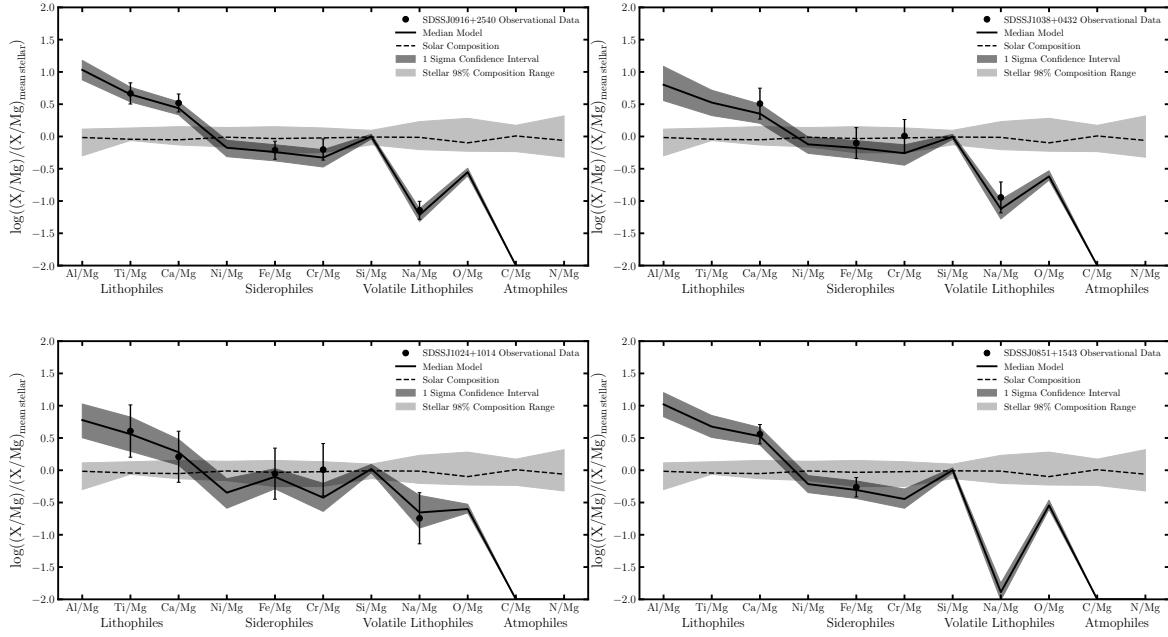
Fig. 4.3 Four example systems (of 10/208) whose abundances are such that the highest Bayesian evidence model is one where they accrete a primitive planetesimal which has experienced sufficient heating to cause depletion of the moderate volatiles (Mg, Fe, Si etc.), and therefore relative enhancements in the refractories (Al, Ti, Ca etc.). 8 systems require such heating to a significance of at least 2σ.
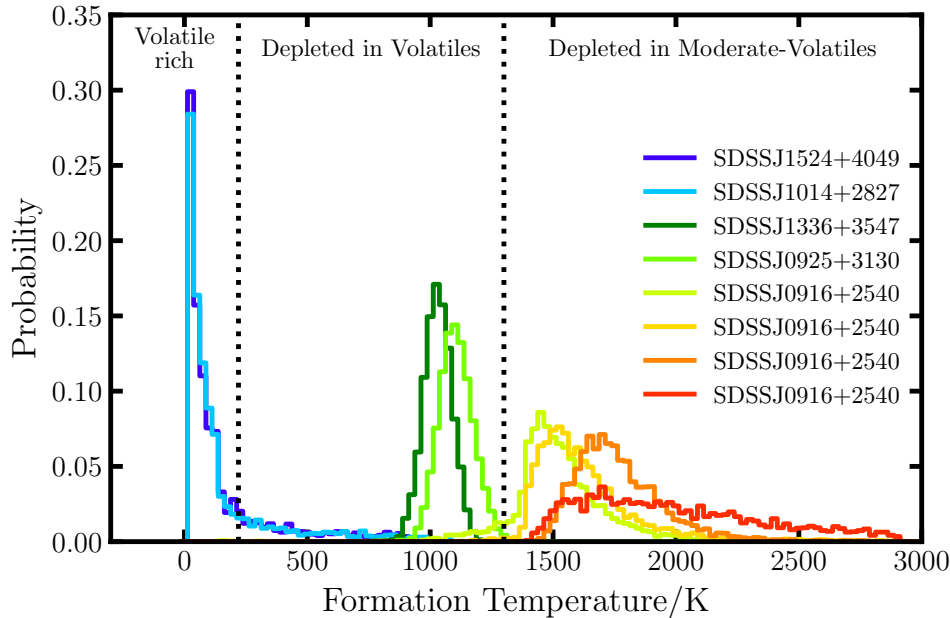
Fig. 4.4 The posterior distributions of formation temperature for the polluted white dwarf systems where the model with the highest Bayesian evidence is model A (no heating, coloured in blues), model B (with heating, coloured in greens), or model C (with heating and feeding zone, coloured in yellow through to red). The plotted distributions indicate the range of temperatures that would lead to the abundances observed in these polluted white dwarfs. The Na abundance is crucial in distinguishing between formation at >1,000K and <1,000K.

lost in order to explain the abundances observed. The x axis is scaled as such so that the scale is centered at zero and so there is no artificial scaling based on the initial sizes of the core, mantle, and crust. Two of the systems shown require the accretion of a mantle-rich collisional fragment (greens), two of the systems shown require the accretion of a core-rich collisional fragment (yellows), while the remaining two example systems require no differentiation or fragmentation and are best explained by the accretion of primitive material (greys) and are plotted for comparison.

4.3.4 Primitive planetesimals or fragments of differentiated planetesimals observed in the declining phase

For 4 systems the model with the highest Bayesian evidence is one in which the abundances can be explained if the system is observed in the declining phase after accreting a primitive planetesimal (2 cases) or a fragment of a differentiated planetesimal (2 cases). Figure 4.9 highlights the abundances and model fits for all four of the systems whose highest evidence model requires declining phase accretion. 3 of the systems require declining phase accretion to above a significance of 2σ. Given the sinking timescales for the white dwarfs studied in this work this is not unexpected as polluting material will remain observable for millions of years after accretion has finished. Knowledge of the phase of accretion of a white dwarf is incredibly useful. If a system is in the declining phase accretion must have ceased, and therefore, the mass in the atmosphere can be converted into the total mass of the polluting body. The calculation no longer yields a lower limit, as there cannot be any material left in a close-in circumstellar orbit which is yet to accrete. Such systems are a unique probe into the mass of the polluting bodies. Figure 4.10 highlights the posterior distributions on the masses of the polluting bodies which are constrained to be in the declining phase from their atmospheric abundances, along with the posterior for WD2216-657 from Chapter 3. The masses found in this work range from bodies as massive as 31% that of Pluto down to 3% that of Vesta.

4.3.5 Core-rich fragments that have experienced moderate-volatile depletion, accreting in build-up phase

For 13 systems the model with the highest Bayesian evidence is one in which the white dwarf is accreting, in build-up phase, a core-rich fragment of body which formed at sufficiently high temperatures such that the moderate volatile species failed to fully condense from the nebula. Figure 4.11 highlights the abundances of four such systems

Fig. 4.5 Four example systems (of 9/208) whose abundances are such that the highest Bayesian evidence model is one where they accrete a core-rich fragment of a differentiated planetesimal. 4 systems require such differentiation and collisional processing to a significance of at least 2σ.

Fig. 4.6 Four example systems (of 5/208) whose abundances are such that the highest Bayesian evidence model is one where they accrete a mantle-rich fragment of a differentiated planetesimal. 3 systems require such differentiation and collisional processing to a significance of at least 2σ.

Fig. 4.7 Four example systems (of 12/208) whose abundances are such that the highest Bayesian evidence model is one where they accrete a crust-rich fragment of a differentiated planetesimal. 4 systems require such differentiation and collisional processing to a significance of at least 2σ.
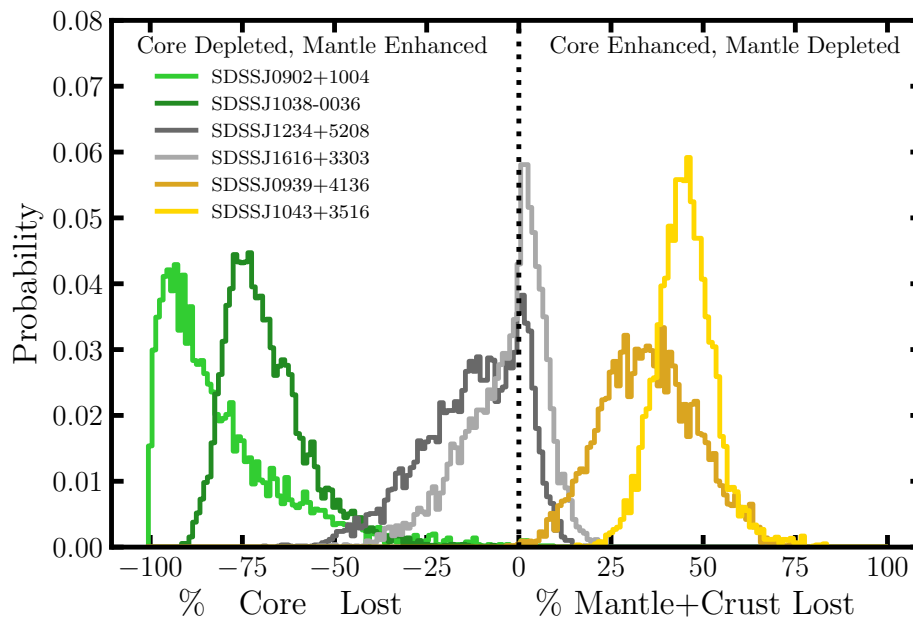
Fig. 4.8 The posterior distributions of the fraction of core-like material or mantle-crust-like material lost for the polluting planetesimals in 6 white dwarf systems. Of the systems plotted two are required to be depleted in core material and rich in mantle material (greens), two are required to be depleted in mantle-crust material and rich in core material (yellows), and the final two systems do not require differentiation or collisional processing are shown for comparison (greys).

and the model fits. The high frequency of such systems is not generally expected and no systems similar to this were found in Chapter 2. I will discuss various hypotheses to explain these systems in Section 4.6.

4.3.6 Potential requirement for differentiation under non-Earth-like conditions

The remaining 10 systems could not be reproduced to the required χ^2 per element threshold by the standard model outlined in Chapter 2. However, when the abundances were inspected it became clear that for 9 of the systems this was due to contradictions between the relative abundances of Cr or Ni and the other siderophile elements. This is potentially not unexpected, as the model used in this work assumes that when a core forms in a planetary body it has a composition identical to that of the Earth's core. The Earth's core composition is to some extent dictated by the pressure, temperature, and oxygen fugacity at which differentiation occurred at, therefore, if the pollutants were fragments of bodies which differentiated under different conditions the core compositions would likely deviate from that of the Earth. In order to probe whether this is indeed the case the initial core composition was manually changed from the Earth's core composition to be either more or less Cr or Ni rich as described in Chapter 2. Each of the 9 systems were then re-fitted with the new model in order to quantify whether such changes could explain the atmospheric abundances. A fully self consistent differentiation model is required in order to investigate these systems robustly and would be incredibly valuable as this would allow constraints to be placed on the parent bodies of the pollutants for the first time. However, this is beyond the scope of this thesis. The results I shall present are simply to highlight how these abundances could be explained by variable conditions during the differentiation process. Figure 4.12 and Figure 4.13 show the abundances of four of the 9 systems and highlight on the left panels the best-fits with Earth-like core abundances and on the right panels the improved best-fits with altered core abundances.

4.4 Population constraints

Constraints on the population as a whole are useful for probing the origin of the 'average' white dwarf pollutant. Such constraints can either be found by examining the frequency of each different best fit model or by summing the posterior distributions of each parameter for each individual system. It should be noted that both methods

are subject to the observational biases in the sample, namely that high relative Ca and Fe abundances potentially generate larger colour shifts, thus, moderate volatile depleted, crust-rich, and core-rich pollutants may be more easily detected than primitive pollutants.

Figure 4.14 is a grid which contains the frequency of white dwarf systems whose atmospheric abundances suggest that they accreted planetary material which was primitive or geologically processed or whether significant heating occurred during formation. The black text indicates the numbers excluding the 10 poor fits outlined in Section 4.3.6, while the red text indicates the numbers produced when 9 of the systems are refitted once the core compositions have been manually altered. Summing the posteriors could potentially offer deeper insights into the 'average' white dwarf pollutant and offer additional constraints when compared with just observing the spread in the population frequency grid. However, this is not the case for all parameters.

For pollutant formation temperatures many systems do not have Na abundance measurements and therefore their temperatures are not constrained and remain at the prior distributions. Additionally, even if the system has a Na abundance measurement if it is stellar it will only constrain the posterior to be below 1,000 K. Therefore, categorising the systems in the 3 rows outlined in Figure 4.14 and observing the spread in formation temperatures using Figure 4.4 provides as much information as the summed posterior would in an easier to digest format less influenced by the prior distributions.

For the core/crust mass fractions the major issue with summing the posterior distributions of the population is that not all systems require differentiation into a core, crust, and mantle. Therefore, they do not have have posteriors for such parameters. For such systems one could model them with the extra unnecessary parameters included, however this would introduce a bias to slightly core-rich fragments, as given the uncertainties and limited number of elements, a slightly core-rich fragment in the steady state/declining phase produces primitive results. Therefore, when discussing the frequency of differentiation it is more useful to use the data given in Figure 4.14 and the spread given in Figure 4.8 rather than attempt to sum the posteriors.

When discussing constraints on the masses of the pollutants and the accretion event lifetime a summed posterior will not be influenced by such issues, as the posteriors are not heavily dependent on specific elements nor are the parameters not necessary for all systems. Additionally, the summing of posteriors will produce useful constraints on the 'average' white dwarf pollutant and therefore would be useful to investigate. Figure 4.15 displays the summed posterior for the mass accreted for the 203 systems

which can be reproduced to a χ^2 of less than 1 and are not required to be in the declining phase. It must be noted that such constraints on the mass are only lower limits as these systems most likely have material which is yet to be accreted residing in a circumstellar reservoir. Figure 4.16 displays the summed posterior for the accretion event lifetime for all 207 systems which can be reproduced to a χ^2 of less than 1.

4.5   Results summary

The key results presented in this chapter are:

- The abundances observed in the majority (133/208) of the systems in the Hollands et al. (2017) sample can be explained by the build-up phase accretion of a primitive planetesimal whose composition lies within the range of compositions expected to be present in protoplanetary discs.

- 20 systems require the build-up phase accretion of a primitive planetesimal which has experienced heating during its formation. 10 systems require such heating to have caused the incomplete condensation of the volatile species, while 10 systems require such heating to have caused the incomplete condensation of the moderate-volatile species.

- The abundances observed in 28 systems require models which invoke geo-chemical differentiation followed by fragmentation in order to be explained. To a statistical significance of greater than at least 2σ, 4 systems require the accretion of a core-rich fragment, 3 systems require the accretion of a mantle-rich fragment, and 4 systems require the accretion of a crust-rich fragment.

- 13 systems have abundances which can only be readily explained by the build-up phase accretion of core-rich fragments of bodies which formed at sufficiently high temperatures such that the moderate volatile species failed to fully condense from the nebula.

- 9 systems have abundances which potentially can be explained by the accretion of fragments of differentiated bodies which differentiated under conditions dissimilar to that of the Earth such that the relative ratios of the siderophiles are altered.
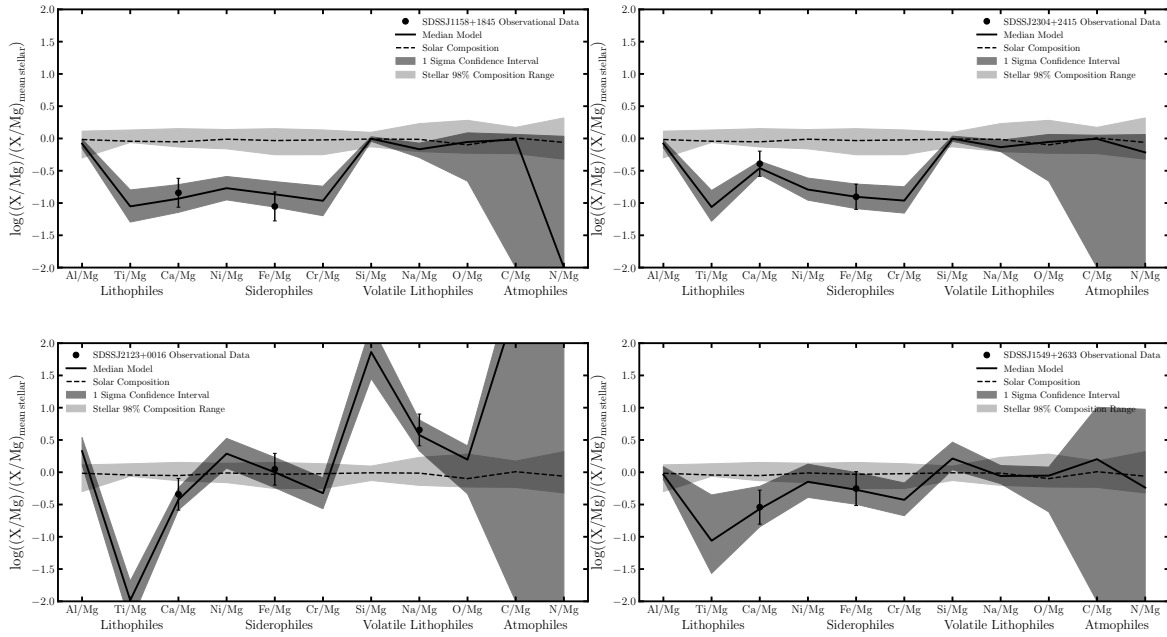
Fig. 4.9 All four systems whose abundances are such that a model where the pollutant material is accreting in the declining phase provides the highest Bayesian evidence. 3 systems require declining phase accretion to a significance of at least 2σ.
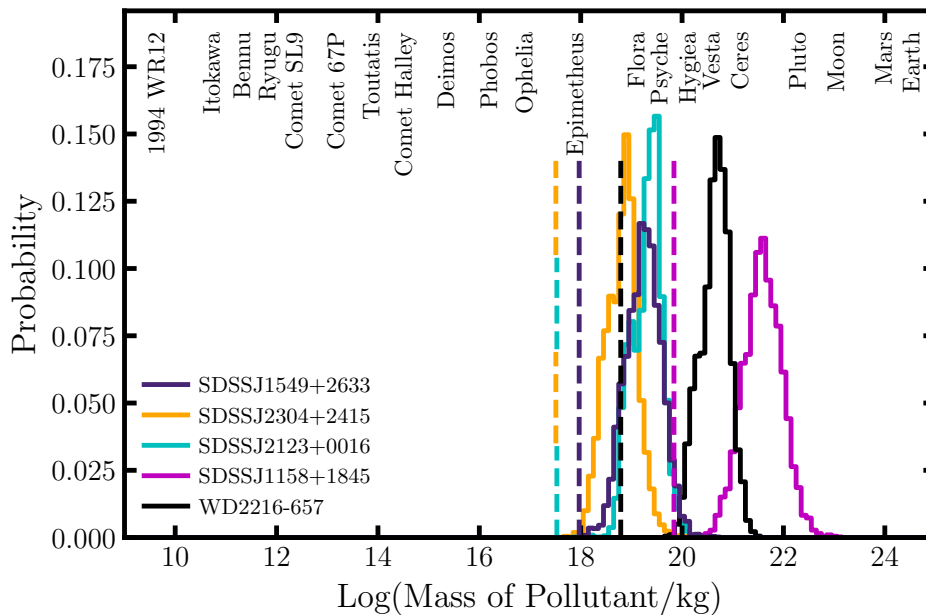
Fig. 4.10 The posterior distributions for the total mass accreted onto the four polluted white dwarfs whose abundances suggest that they are in the declining phase during the whole accretion event. Such constraints can be made as given the systems are in the declining phase there is no mass currently accreting and therefore no mass left in a close-in circumstellar reservoir. The dashed lines indicate the mass of pollutant material currently in the atmosphere. The posterior for WD2216-657 from Chapter 3 is also plotted.
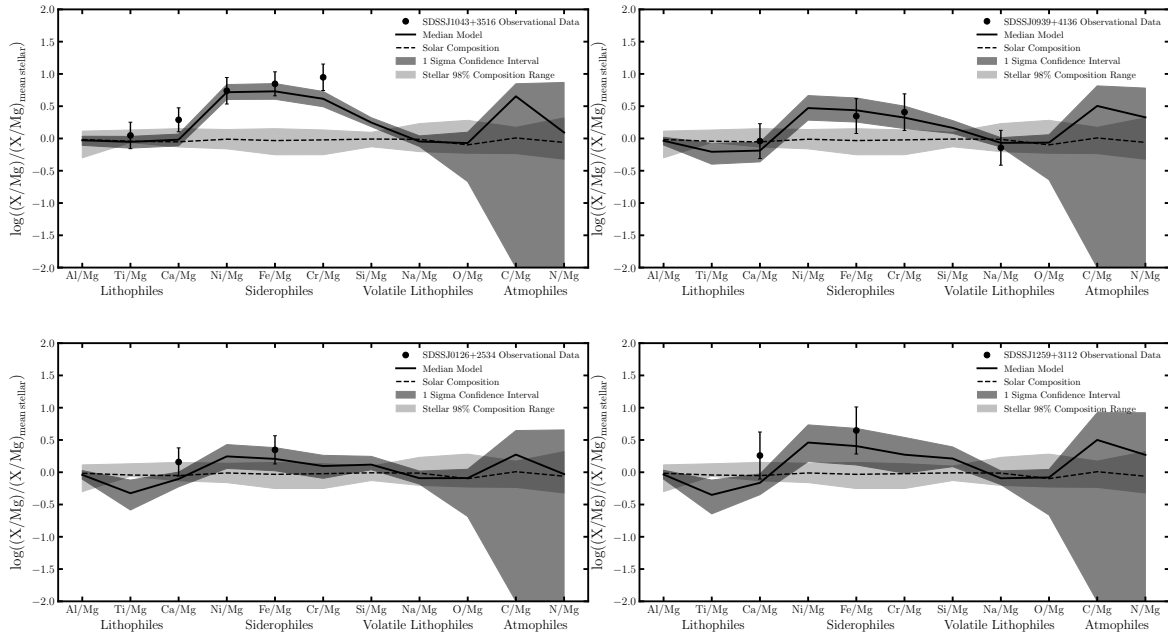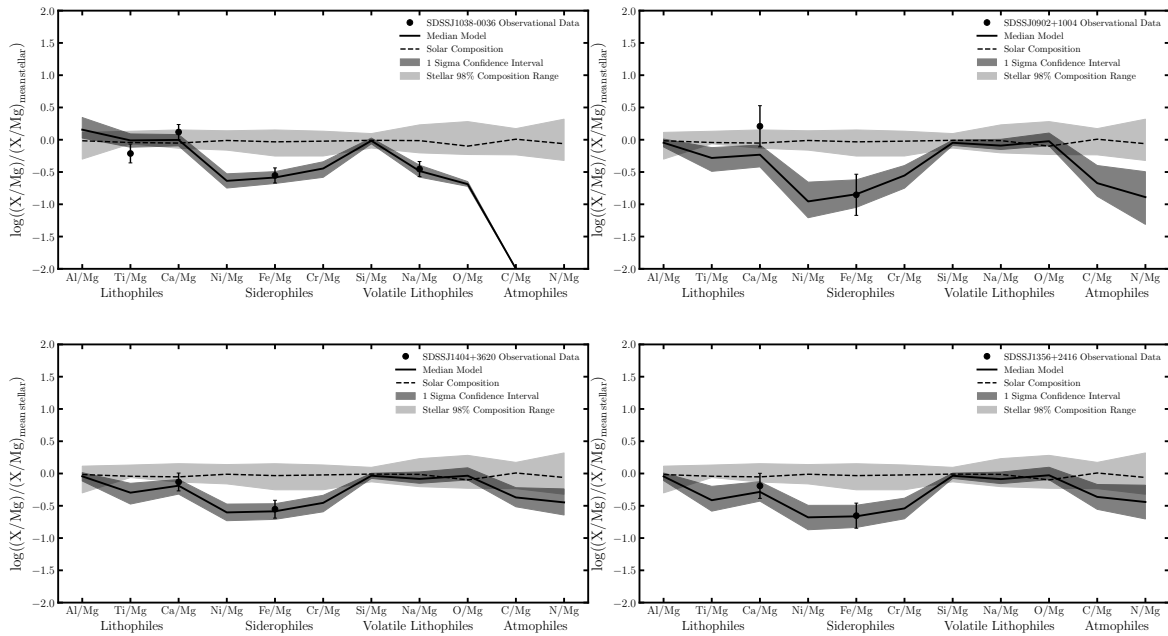
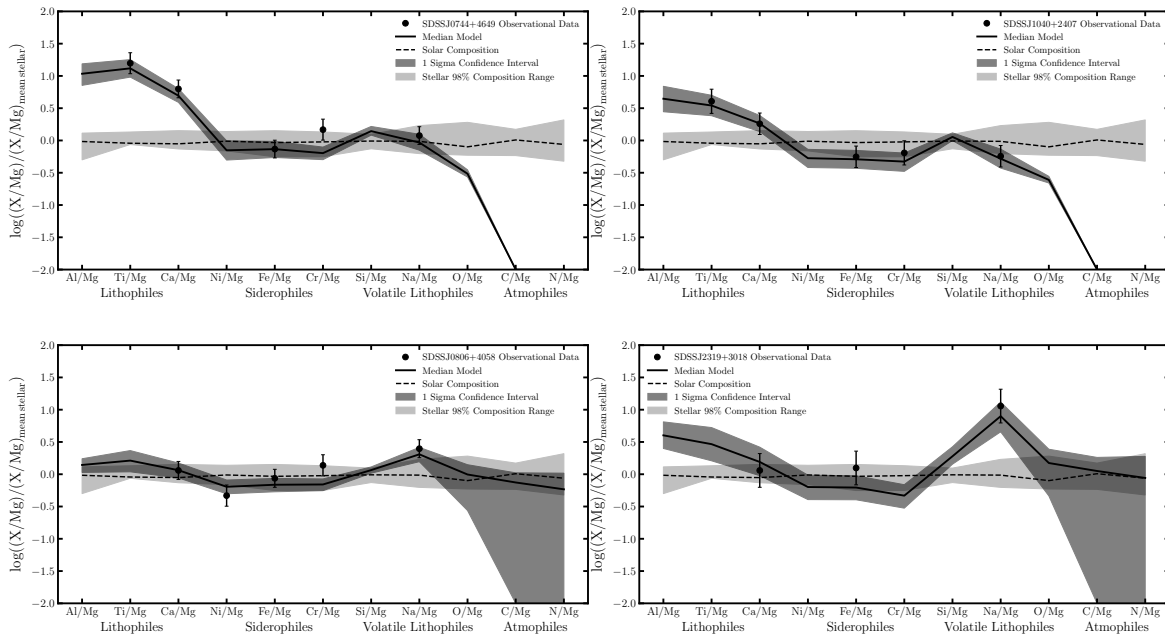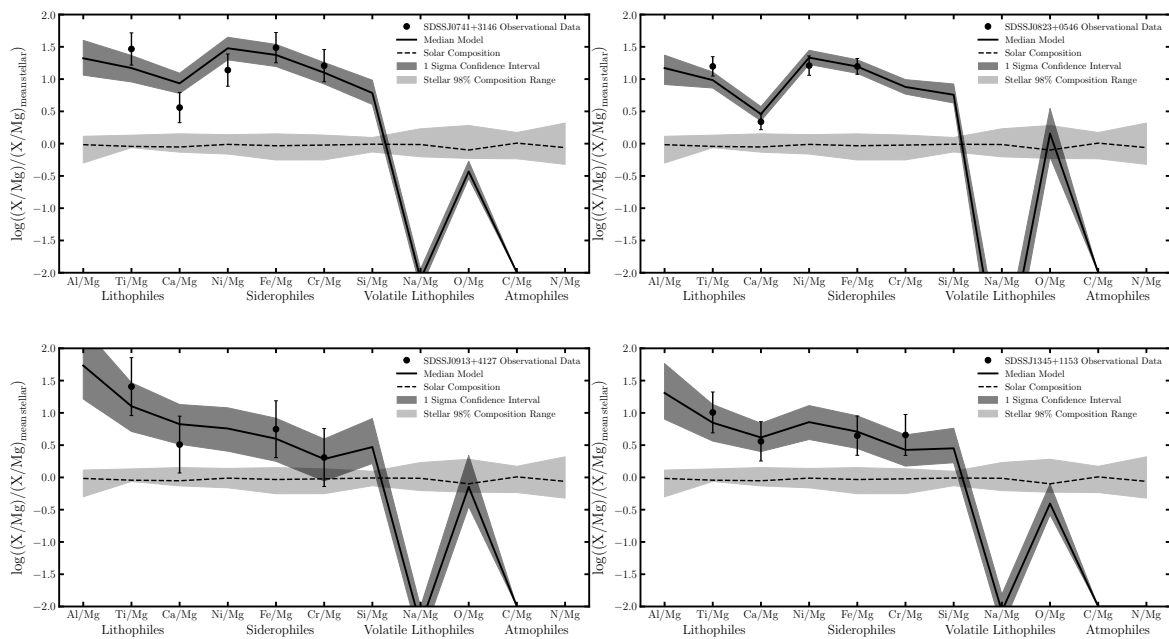Fig. 4.11 Four example systems (of 13/208) whose abundances are such that the highest Bayesian evidence model is one where they accrete a core-rich fragment of a differentiated planetesimal which has experienced sufficient heating such that the moderate volatiles (Mg, Fe, Si etc.) are depleted. 12 systems require such heating, differentiation and collisional processing to a significance of at least 2σ.
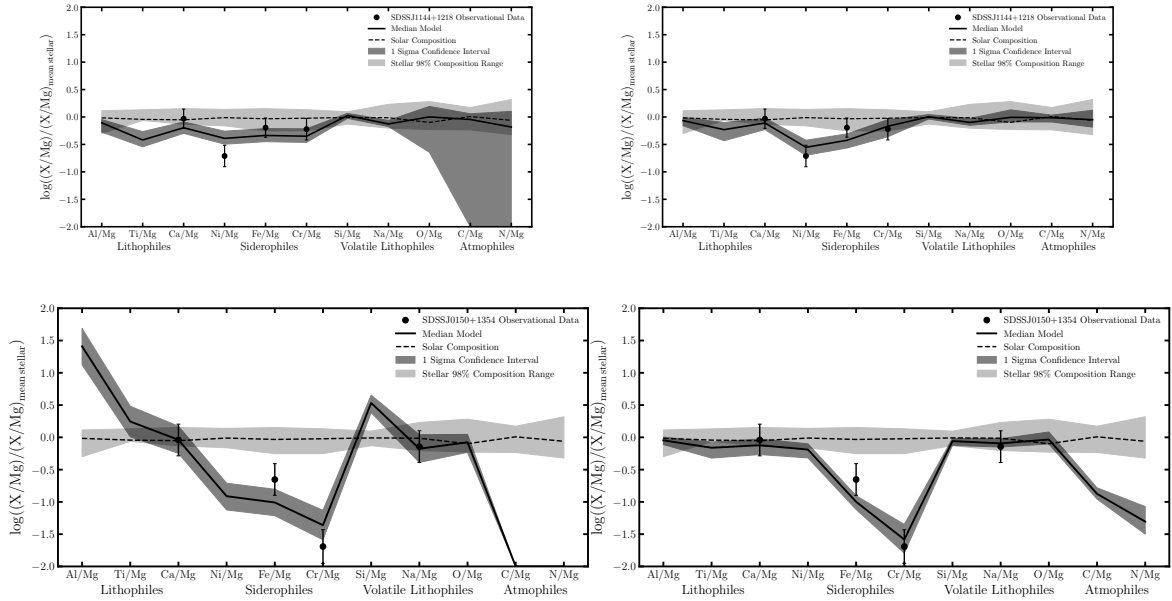
Fig. 4.12 2 of the 9 systems for which modifying the abundances of the cores which form from Earth-like to ones which can be more Ni or Cr rich/poor allows their abundances to be modelled to a sufficient accuracy. The left hand panels show the highest evidence model with an Earth-like core composition, whereas the right hand panels show the highest evidence model with an altered core composition.
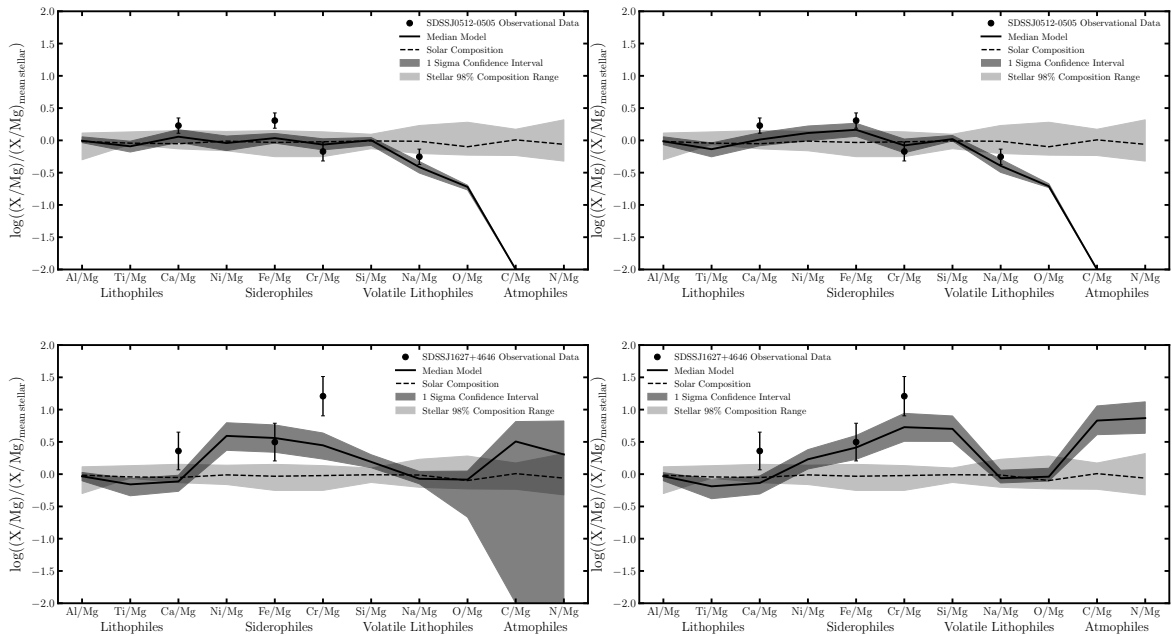
Fig. 4.13 2 of the 9 systems for which modifying the abundances of the cores which form from Earth-like to ones which can be more Ni or Cr rich/poor allows their abundances to be modelled to a sufficient accuracy. The left hand panels show the highest evidence model with an Earth-like core composition, whereas the right hand panels show the highest evidence model with an altered core composition.

Population Frequency Grid	Primitive 157 75%	Core-rich 24(28) 14%	Mantle-rich 5(10) 5%	Crust-rich 12 6%
Volatile-rich 162(169) 81%	**137**	**11(13)**	**4(9)**	**10**
Depleted in Volatiles 13(14) 7%	**10**	**0(1)**	**1**	**2**
Depleted in Moderate Volatiles 23(24) 12%	**10**	**13(14)**	**0**	**0**

Unclassified due to poor best model fit 10(1)

Fig. 4.14 A grid containing the frequency of white dwarf systems whose atmospheric abundances suggest that they accreted planetary material which was primitive or geologically processed or whether significant formational heating occurred. The black text indicates the results of the model fits where the differentiation model used Earth's core abundances, whereas the red text indicates the results of the model fits where the initial core composition could be altered from that of the Earth. If no red text is present the number with the modified model is identical to the number found by the original set up.
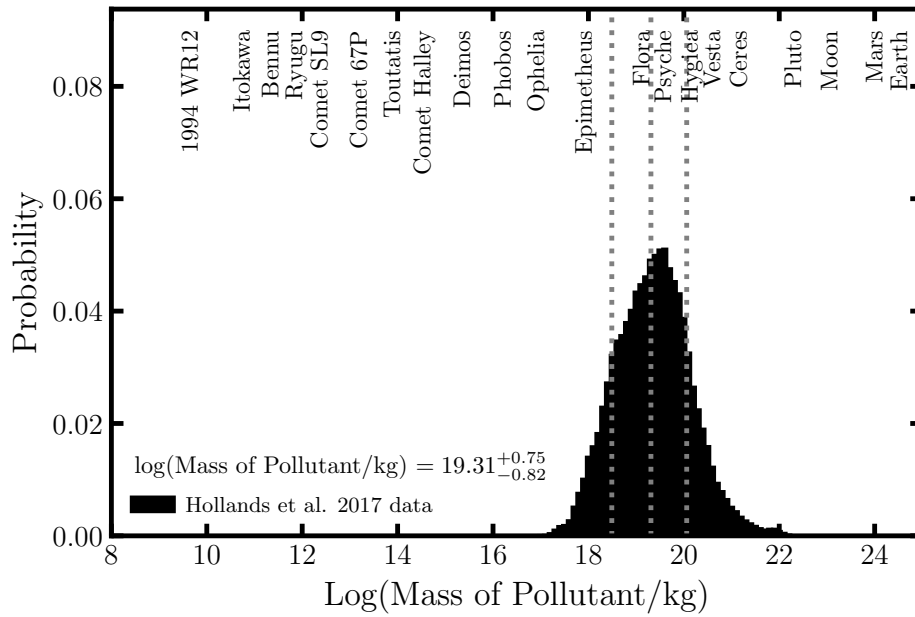
Fig. 4.15 Summed posterior distribution for the mass accreted for the 203 systems which can be reproduced to a χ^2 of less than 1 and are not required to be in the declining phase. The grey dashed lines represent the median value and the one sigma range.
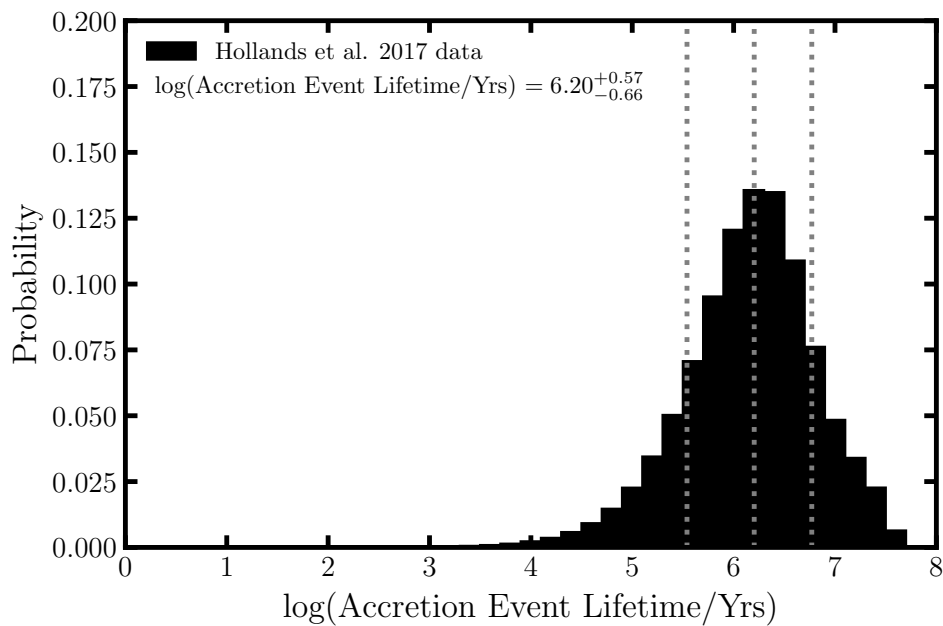
Fig. 4.16 Summed posterior distribution for the accretion event lifetime of all 207 systems which can be reproduced to a χ^2 of less than 1. The grey dashed lines represent the median value and the one sigma range.

- Only the abundances present in one system (SDSS J1351+2645) cannot be reconciled by the model outlined in this work. This is due to an extraordinary high Ti abundance which is $\sim$200 times higher than that of the average stellar abundance.

- 4 systems are predicted to be in the declining phase where accretion has ceased and the pollutant material is simply sinking out of the convective zone. Such systems allow the masses of polluting bodies to be constrained as it is known that no material is still to be accreted and resides in a reservoir close to the star. The masses found in this work range from bodies as massive as 31% that of Pluto down to 3% that of Vesta.

- Using the systems which are currently in the build-up phase, the average white dwarf pollutant body is at least $10^{19.3}$ kg, which corresponds to being at least 8% the mass of Vesta.

- The constraints generated for the population as a whole on the accretion event lifetimes suggest that white dwarf accretion events last on average $1.6^{+4.3}_{-1.2}$ Myrs.

4.6 Discussion

The aim of this work is to improve the understanding of rocky exo-planetary bodies by constraining the origin of the planetary bodies which pollute the large sample of white dwarfs whose atmospheric abundances were derived in Hollands et al. (2017). In order to constrain the origin of the large sample of planetary bodies I use the model outlined in Chapter 2. In the next section I discuss the notable caveats of the data and how they potentially affect the conclusions of this study. For a discussion of the caveats of the model see Chapter 2.

4.6.1 Discussion of caveats

The analysis presented here is based on the elements detected in Hollands et al. (2017). For many objects there is relatively little information available as only Mg, Fe and Ca are detected. For such systems unless Ca is enhanced relative to Mg it is not possible to probe heating effects. Therefore, I conclude that most of these systems are primitive material which have not been heated substantially during formation, when the detection of further elements might verify a different reality. I note here that the

model constrains the parameter values and the necessity of parameters to be included based on the observed abundances and the priors assumed.

The estimation of the uncertainties on the observed abundances is key to the Bayesian model conclusions. Whilst the full time consuming analysis for each individual system has not been completed, the error estimation is regarded (Equation 4.1) to be conservative. Thus, the conclusions drawn, based on the statistical significance to which certain systems require heating, differentiation, and declining phase accretion remain valid.

The model framework outlined in this study finds the statistical significance of various origins by comparing the abundances predicted for various models with various combinations of free parameters. Therefore, if the abundances of exo-planetesimals were determined by additional factors which are not incorporated into the model the conclusions would not be valid. However, as the model can reproduce the abundances of the rocky bodies in the Solar System and the abundances of the 207/208 pollutants analysed in this work to a χ^2 per element values of less than one I do not expect that any major factors are missing.

When I consider the distribution of pollutants found from the modelling, it is crucial to consider how the sample of white dwarfs was selected. In Hollands et al. (2017) polluted white dwarfs were found by searching for white dwarf stars whose colour was shifted away from the usual white dwarf track. One potential bias of this selection method is that crust-rich fragments, core-rich fragments, and bodies which have experienced depletion to their moderate volatiles are more easily detected due to their high Ca or Fe abundances, which lead to a large shift in color. This will not effect the constraints generated for individual systems, however, it should be noted as a potential explanation for the high fraction of crust-rich fragments and core-rich moderate-volatile depleted pollutants. Additionally, the sample will only contain the most heavily polluted systems, as higher levels of pollution produce larger colour shifts. Therefore, it should be known that the masses of the polluting bodies constrained in this chapter are likely not the masses of the average white dwarf pollutant but are instead biased towards the most massive pollutants.

4.6.2   Discussion of results

In this work the majority of systems in the Hollands et al. (2017) sample are found to be easily reproduced by a scenario in which the star is accreting primitive unprocessed and unheated material in the build-up phase. Given the long sinking timescales, the majority of systems accreting in build up phase matches expectations. It is also

unsurprising that the accreted material is often primitive, and thus, has refractory abundances which match those expected for its original planetesimal forming disc, as the majority of Solar System bodies have refractory abundances which match that of the solar photosphere, and thus their natal disc. This result also reinforces the findings of Chapter 3 which suggested that primitive pollutants were the most common.

This study provides evidence for the occurrence of heating and the depletion of volatiles in the planetary material accreting onto many white dwarfs. Na is the crucial element in constraining such processes. Na has a condensation temperature of $\sim$1,000 K, the lowest of any element studied. Na abundances similar to that observed in stellar photospheres are indicative of formation temperatures lower than $\sim$1,000 K while depleted abundances can constrain formation temperatures higher than $\sim$1,000 K. I find that 56 systems have Na abundances consistent with stellar while 20 systems have depleted Na abundances. Such systems are potential probes of the formation temperature of white dwarf pollutants and thus the formation location of exo-planetary bodies in white dwarf planetary systems. If the temperatures are converted into formation locations in a protoplanetary disc around an A-type star, 56 systems are required to have accreted bodies which formed exterior to $\sim$5 AU. Whereas, 20 systems are required to have accreted bodies which formed interior to $\sim$5 AU. Therefore as previously concluded in Chapter 3, white dwarf pollutants have a range of formation locations.

10 systems analysed in this work require not just incomplete condensation of Na but also incomplete condensation of the moderate-volatiles such as Fe and Mg. Systems whose pollutants have experienced such extreme heating have been discussed before in Chapter 3 and are especially interesting as they have no Solar System equivalent (Xu et al. (2013)). If the formation temperatures constrained are converted into formation locations in a protoplanetary disc around an A-type star these bodies formed are required to have formed interior to $\sim$2 AU. Given the mass of the pollutant bodies one can estimate the time at which formation must have occurred such that the bodies could have survived the giant branch evolution of the star without being engulfed or spun to break up by the YORP effect. The material accreted by these systems must have formed earlier than $\sim$0.12 Myrs after the protoplanetary disc formed otherwise it would have to have formed so close to the host star that it would not be able to survive the giant branch evolution of the star and pollute the star during the white dwarf phase. Therefore, as concluded in Chapter 3, such systems are potentially not unexpected in polluted white dwarf systems, however they are interesting objects as

their internal composition will be drastically different to that of the rocky Solar System bodies.

From the population of white dwarfs analysed in this chapter, if one only concentrates on systems with a Na abundance or a constraint for the requirement of incomplete nebula condensation: 56 systems formed below 1000 K, 14 formed between 1000 K and 1300 K, and 24 formed above 1300 K. Given the potential observational biases the high fraction of super heated bodies is not unexpected, therefore a more robust comparison would be to compare the systems with stellar Na and the systems with depleted Na, a ratio of 56:14 suggests that the majority of pollutants formed exterior to ∼5 AU. Given the sample size and the volume of the planetary system which forms at temperatures less than 1000 K, this result is consistent with an even spread in formation locations of white dwarf pollutants suggested in Bonsor et al. (2011) and Chapter 3.

The accretion of fragments of differentiated bodies onto white dwarfs has been proposed due to atmospheric abundances which are rich in the siderophiles/lithophiles (Zuckerman et al. (2011); Xu et al. (2013); Wilson et al. (2015)). In Chapter 3, I showed how such conclusions are robust and how the abundances of some polluted white dwarfs are difficult to explain in any other way. The results presented in this work agree with these previous conclusions and find strong statistical evidence that some systems are accreting fragments of differentiated bodies. Hollands et al. (2018) identified 4, 3, and 2 systems as having extreme Ca, Fe, and Mg abundances and attributed this to the accretion of crust-rich, core-rich, and mantle-rich fragments. The strength of my analysis is that not only can I provide statistical significances for the requirement of such systems to have accreted fragments of differentiated bodies, I can also find evidence for differentiation and collisional processing in less extreme systems. My analysis finds that of the Ca-rich systems outlined by Hollands et al. (2018) only 1 can be attributed to being crust-rich (SDSS J0744+4649 to 5σ significance) while the other 3 systems (SDSS J1033+1809, SDSS J1055+3725, and SDSS J1351+2645) have extreme Ca abundances due to heating and are inconsistent with being crust-rich due to the abundances of Fe. The 3 Fe-rich systems (SDSS 1043+3516, SDSS J0741+3146, and SDSS J0823+0546) are all indeed found to be core-rich to at least 5σ however both SDSS J0741+3146 and SDSS J0823+0546 also require extreme heating in order to explain their Ca and Ti abundances. Of the 2 Mg-rich systems, SDSS J0956+5912 is found to be mantle-rich to a statistical significance of 1.9σ, while SDSS J1158+1845 is found to be in the declining phase rather than being intrinsically mantle-rich material.

This study provides strong evidence for the occurrence of planetary differentiation and planetary collisions in exo-planetary systems. In total I find that 28 systems require the accretion of fragments of differentiated bodies to a statistical significance of at least 2σ, while the model with the highest Bayesian evidence for 50 systems is one in which the white dwarf accretes a fragment of a differentiated body. Crucially, it also appears that the differentiation occurring in these systems is likely happening in a similar fashion to the differentiation which occurred in the Solar System i.e. the formation of siderophile-rich cores and lithophile-rich crusts.

24% of the systems analysed have potentially accreted fragments of differentiated bodies. Such a fraction requires the majority of bodies to be differentiated in exo-planetary systems, as collisions are often not disruptive enough to produce massive mantle-rich or core-rich fragments (Bonsor et al. (2020)). However, as noted in Section 4.6.1, fragments rich in crust/core material may be detected more easily than primitive material. The frequency of mantle/crust-rich pollutants to core-rich pollutants is less affected by the observational biases of the sample and is 22:28. This is consistent with the roughly equal amount of core-rich and mantle/crust-rich pollutants is predicted by studies of the collisional evolution of planetary bodies (Carter et al. (2015); Carter et al. (2018); Bonsor et al. (2020)). It is important to note that, as mentioned in Chapter 3, these systems also provide evidence that the observed abundances are often dominated by a single body, as multiple bodies would struggle to produce such a strong signature of differentiation. If multiple bodies were accreted simultaneously then the main affect to the results would be that potentially many of the primitive systems would be combinations of differentiated bodies rather than actually primitive material. Additionally, one would also expect systems which appear simultaneously polluted by core-rich and crust-rich material, however, the lack of such systems provides further evidence that often the pollutants are single bodies.

For 13 systems the model with the highest Bayesian evidence is one in which the abundances can be explained by the build-up phase accretion of the core-rich fragments of bodies which formed at sufficiently high temperatures such that the moderate volatile species failed to fully condense from the nebula. The frequency of bodies with such an origin was not expected nor is it easy to reconcile. One possible explanation is that heating during the giant branch evolution of the star erodes the mantles of differentiated planetary bodies by a significant amount and many of their moderate volatiles can be outgassed. Another possible explanation is that the accretion process which transports material onto the white dwarf preferentially accretes the upper layers and most volatile layers of a body initially then accretes the refractory layers and inner layers of a body

subsequently and such systems are observed at late accretion times. Both hypotheses need further testing in order to resolve this issue, however, a potential strength of the latter hypothesis is that it could also explain the peculiar Na abundances in the 2 systems published in Swan et al. (2019) and discussed in Chapter 3.

I note here that an increase in the Mg sinking timescale has previously been suggested as an explanation for not just these systems but the Hollands et al. (2017) sample in general by Turner and Wyatt (2019). However, there are two key observations which suggest that the Mg timescales are correct. Firstly, a system wide change in the Mg sinking timescale would contradict the majority of white dwarf systems in the sample which can be explained with no such issues. Secondly, Figure 4.11 shows how for the systems in question simply reducing the Mg sinking timescale would cause a contradiction between Ca and Ti (as the Ca abundance would become too low when compared with the Ti abundance) and the systems could not be accurately reproduced. The characteristic hook in the abundances between Ti, Ca, and Ni is indicative of heating, as Ti is more refractory than Ca so it is likely that heating processes are responsible for the abundances in these systems. The main reasons for the discrepancy in results between Turner and Wyatt (2019) and this work are the uncertainty prescriptions used and the compositional models used. In Turner and Wyatt (2019) elemental errors were not incorporated into the analysis so although they found the mean Mg abundances to be generally too low for their model to explain they could not evaluate the statistical significance of the deviation. Additionally, as they did not include the potential for heating and condensation effects, which I find contribute to the composition of potentially up to 10% of the systems analysed, they had no mechanism which reduced the Mg abundance relative to Ca, thus, any system which had abundances which are typical of incomplete nebula condensation could not be explained.

For 4 systems the model with the highest Bayesian evidence is one in which accretion has finished and the systems are observed in the declining phase, for 3 of these systems declining phase accretion is required to at least 2σ. Knowledge of the phase of accretion of a white dwarf is incredibly useful information because if accretion has ceased the mass in the atmosphere, combined with the sinking timescales, can be converted into the total mass of the polluting body. This calculation no longer yields a lower limit as there cannot be any material left in a circumstellar orbit which is yet to accrete. Such systems are a unique probe into the mass of the polluting bodies and, as shown in Figure 4.10, the bodies polluting white dwarfs are found to have masses between just ∼3% of Vesta and ∼15 times Vesta. Figure 4.15 shows how the majority of white dwarf

pollutants are at least 1% the mass of Vesta and the 'average' pollutant has a mass of at least 8% of Vesta. These results reinforce what has previously been concluded in the literature (Farihi et al. (2010a); Girven et al. (2012)) as I also find that the pollutants which have been observed to date have masses similar to that of large Solar System asteroids.

Laboratory experiments show that Ni behaves in a more siderophilic fashion at lower pressures while Cr behaves in a less siderophilic fashion at lower pressures (Bouhifd and Jephcoat (2011); Siebert et al. (2012); Fischer et al. (2015)). Therefore if the parent bodies which fragmented in order to produce the white dwarf pollutants differentiated under different conditions the relative ratios of the siderophiles may be incompatible with the model used to fit the abundances. Indeed in 9 systems I find such contradictions in the siderophiles and I showed if one manually depletes/enhances the core in Cr and Ni then the abundances can be explained by the accretion of fragments of differentiated bodies which differentiated under conditions dissimilar to that of the Earth. Such systems need to be investigated further, however, I highlight in this work that such a study could potentially use the abundances to constrain the size of the parent bodies from which the collisional fragments derive. In combination with the masses derived from systems in the declining phase this could probe whether the pollutants of white dwarfs are asteroids and fragments of asteroids or if they are fragments of planet-sized bodies.

The accretion event lifetime for a system can be constrained from the abundances because the duration of accretion effects the probability that the system will be observed in build-up vs steady state vs declining phase (Figure 2.13). The accretion event lifetimes for the whole population of white dwarf systems suggests that the accretion events last $1.6^{+4.3}_{-1.2}$ Myrs. This result is consistent with the result derived in Girven et al. (2012) and is consistent with the theoretical predictions of Rafikov (2011a) and Rafikov (2011b). It is also consistent with the results presented in Chapter 3, which found a disc lifetime of the order of a few Myrs would explain the spread in the phases of accretion observed. It is important to note that these results contradict the results of Wyatt et al. (2014) where the accretion rates of cool DAZ white dwarfs seem to be higher in comparison with hot DAZ white dwarfs which implies disc lifetimes of the order of tens of years. A potentially explanation for this contradiction in timescales between the work presented in this thesis and in Wyatt et al. (2014) is that the accretion rates in Wyatt et al. (2014), which are calculated from the Ca abundances alone assuming a bulk-earth composition, create a bias. As cooler white dwarfs will likely form from more massive main sequence stars potentially they are more likely to

produce refractory enhanced pollutants, therefore, using the Ca abundances alone will over estimate the accretion rate in old white dwarf systems more often than in young white dwarf systems. However, more work clearly needs to be done to investigate this bias and the disc lifetimes of polluted white dwarf systems in general.

4.7   Conclusions

In this chapter I present how the method outlined in Chapter 2 reproduces the abundance patterns observed in a large population of polluted white dwarfs by modelling the chemical composition expected if the white dwarf stars accreted planetesimals which could form in protoplanetary discs with a range of initial compositions, at various temperatures, and with various geological and collisional histories.

The model is able to explain all 208 systems in the Hollands et al. (2017) sample to χ^2 per element values of less than one, apart from SDSS J1351+2645, whose Ti abundance is too extreme to reproduce. I use this as evidence that the initial composition of the planetesimal forming disc, formational heating, and differentiation and collisions are the key processes that determine the abundances of exo-planetary bodies, as is the case in our Solar System.

In our Solar System, the refractory abundances of most meteorites are consistent with solar abundances. In this work, I provide observational evidence that many exo-planetesimals have refractory abundances that match those of their host-stars. This is shown by the 135/208 systems whose abundances fit within the range of abundances seen in nearby stars. A match between stellar and planetary abundances is crucial in determining the composition of exoplanets (e.g. Dorn et al. (2017)). My findings validate this hypothesis.

Heating is a key process in determining the abundances of Solar System bodies, from the refractory enhanced Ca-Al inclusions, to the volatile depleted Earth and to a lesser extent the volatile depleted chondritic meteorites. I provide evidence that similar processes occur in exo-planetary systems. The composition of the material which pollutes 20 white dwarfs systems is required to have experienced significant heating during formation in order to explain the atmospheric abundances. 10 systems require such heating to have caused the incomplete condensation of the volatile species, such as Na, while 10 systems require such heating to have caused the incomplete condensation of the moderate-volatile species, such as Mg.

My analysis supports the idea that differentiation and collisions are common processes in exo-planetary systems and that differentiation occurs in a similar manner

in exo-systems as it does in the Solar System. The abundances reported for 50/208 systems are such that they require that the white dwarfs accreted either a core-rich, mantle-rich, or crust-rich body, of which at least 11 systems require this to a statistical significance of greater than 2σ. It is, therefore, unlikely that multiple bodies dominate the material accreted in these systems as if multiple bodies did accrete onto the white dwarfs simultaneously such signatures would not be present.

My analysis provides evidence that the white dwarf pollutants currently observed are typically the size of large asteroids. The evidence is three-fold. Firstly, for the four systems constrained to be in the declining phase, the total mass accreted during the accretion event can be determined. The masses found for such systems range from bodies as massive as 31% that of Pluto down to 3% that of Vesta. Secondly, the spread of minimum masses derived for the population suggests that the majority white dwarf pollutants observed are at least as massive as 1% that of Vesta. Thirdly, there are five systems where I present tentative evidence that the abundances can only be explained by the accretion of a fragment of a parent body that differentiated at lower pressures than Earth, and thus was smaller in size. However, further study and the inclusion of a robust differentiation model is required in order to probe these systems further. It should be noted that observational limits mean that only the most heavily polluted white dwarf systems are currently known, therefore white dwarfs could also potentially be polluted by much smaller bodies than those suggested in this thesis.

The accretion event lifetimes for the population of pollutants can also be constrained from their abundances and in this work the accretion events were constrained to last $1.6^{+4.3}_{-1.2}$ Myrs on average. Such a result is consistent with the observational properties of polluted white dwarfs (Girven et al. (2012)) and theoretical predictions of white dwarf pollution (Rafikov (2011a); Rafikov (2011b)), however, it should be noted that such disc lifetimes make it potentially difficult to explain the difference in accretion rates of hot white dwarfs and cool white dwarfs.

Chapter 5

Probing planet formation using the Mn/Na abundance ratio of white dwarf pollutants

5.1 Introduction

The loss and gain of volatile elements during planet formation is key for setting a planet's subsequent climate, geodynamics, and habitability. As introduced in Section 1.1 most rocky planet forming material originates in protoplanetary discs, when hot circumstellar gas condenses into solid matter at the midplane of the disc (Chambers (2004); Chambers (2009); Williams and Cieza (2011)). Through the subsequent growth of dust particles into ever larger aggregates: pebbles, planetary embryos and eventually terrestrial planets are formed. However as outlined in Chapter 1, despite this subsequent processing, the bulk composition of both Earth and the chondrites are well explained using such a nebula condensation model (Anders (1964); Wasson and Kallemeyn (1988); Lodders (2003); Palme and O'Neill (2003); Lodders (2010); Siebert et al. (2018)). The refractory elemental abundances of the chondrites match those of the Sun, whilst the volatile elements, are depleted relative to the Sun in accordance with their individual elemental condensation temperatures (McDonough and Sun (1995); McDonough (2003); Lodders (2003)). Different thermal conditions in the solar nebula have imparted a fundamental compositional fingerprint on planetary material through condensation processes. How universal this process is to planet formation is a key question, one which can be answered through study of extrasolar rocky material.

As discussed extensively in previous chapters, it is possible to probe the abundances of planetary material from outside the Solar System by observing metal features in the atmospheres of white dwarfs (Jura and Young (2014)). White dwarfs are the faint remnants of the cores of stars like the Sun, and theoretically they should have atmospheres only composed of H and He (Althaus et al. (2010); Koester (2013)). The metal features observed in many white dwarfs are thought to be present due to the accretion of rocky planetary bodies (Jura and Young (2014); Farihi (2016)). As the properties of the metal spectral features can be used to constrain the relative abundances of the metals in white dwarf atmospheres' (Koester (2009); Koester (2010)), polluted white dwarfs can probe the composition of exo-planetary bodies and test whether nebula condensation can explain the abundances found. In Chapter 3 and Chapter 4, I showed how such a condensation model can explain the abundances present in the majority of systems.

Nebula condensation is not the sole process which determines the composition of rocky planetary material. As introduced in Section 1.1.2, the composition of bodies can be significantly altered post formation (O'Neill and Palme (2008)). Significant melting and the formation of a global magma ocean can occur on rocky planetary bodies due to high energy planetary impacts and the decay of short lived radioactive isotopes (Keil (2000); Chambers (2004); Day and Moynier (2014); Pringle et al. (2014); Wang and Jacobsen (2016); Hin et al. (2017); Siebert et al. (2018)). This heating, referred to in this work as post-nebula volatilisation, causes the preferential loss of volatile elements, especially on less massive bodies which do not have sufficient surface gravity to stop the thermal escape of the vapour (O'Neill and Palme (2008); Pringle et al. (2014)). Post-nebula volatilisation occurs at higher pressures and in more oxidising conditions than solar nebula condensation (Visscher and Fegley (2013)). Thus, individual elemental behaviours and volatilities may be significantly different and the abundance signatures created need not match those expected from nebula condensation (Sossi and Fegley (2018)). The atmospheric compositions of polluted white dwarfs could, therefore, potentially provide evidence for post-nebula volatilisation in exo-planetary bodies, noting that for white dwarfs there is the additional complexity that the planetary bodies must survive the star's giant branch evolution, and may also potentially experience strong heating processes due to the increased luminosity of the host star.

As well as trends related to volatility, planetary compositions can be altered by large scale melting and the segregation of siderophilic elements into a planetary core. Collisions between differentiated bodies can separate core and mantle material and

can lead to the production of bodies with bulk compositions dissimilar to those of the bodies that condensed out of the stellar nebula. As introduced in Chapter 1, iron meteorites and the achondrites are examples which provide evidence for the occurrence of this process in the Solar System (Scott and Wasson (1975); Lodders and Fegley (1998); Scott (2013); Michel et al. (2015)). As planetary differentiation preferentially moves siderophilic elements into the core and lithophilic elements into the mantle and crust, planetary bodies are no longer homogeneous, thus, disruptive collisions may produce fragments which are enhanced/depleted in siderophilic or lithophilic elements. As presented in Chapter 3 and Chapter 4, the atmospheric compositions of polluted white dwarfs can be used to provide evidence of planetary differentiation and collisional processing in exo-planetary systems due to observations of siderophile/lithophile rich/poor atmospheric compositions.

Figure 5.1 is a modified version of Figure 1 from Siebert et al. (2018) (Data sources are O'Neill and Palme (2008); Dauphas et al. (2014); Palme and O'Neill (2014); Brewer et al. (2016); Siebert et al. (2018)). The positions of the Solar System bodies in $\log(Mn/Na)$ and $\log(Mn/Mg)$ space can be readily explained by three processes: condensation from the solar nebula (blue), planetary differentiation (green), and post-nebula volatilisation (red).

Mn is a siderophile while Na and Mg are lithophiles, hence, the Mn/Na ratio and the Mn/Mg ratio of a body can be altered by differentiation, collisions, and fragmentation. Evidence for this is found in the abundances of silicate Earth where Mn is depleted relative to bulk Earth while Na and Mg are not (McDonough (2003); Palme and O'Neill (2014); Siebert et al. (2018)). The green vector on Figure 5.1 corresponds to the abundances expected for increasingly mantle-rich collisional fragments of differentiated bodies.

Mn and Na are both volatile elements in solar nebula conditions with 50% condensation temperatures of 1,158 K and 958 K respectively, while Mg is a non-volatile element with a 50% condensation temperature of 1,336 K (Lodders (2003)). Therefore, bodies which experienced hotter formation temperatures are expected to have higher Mn/Na ratios and lower Mn/Mg ratios. Evidence for this is found in the abundances of the chondrites and bulk Earth (O'Neill and Palme (2008); Siebert et al. (2018)) which lie along the blue condensation vector plotted on Figure 5.1.

The relative volatility of Mn and Na is heavily dependent on the oxygen fugacity and the pressure at which the condensation/volatilisation process is occurring. Impact generated silicate melting (post-nebula volatilisation) would have occurred under much more oxidising conditions and at much higher pressures than nebula condensation
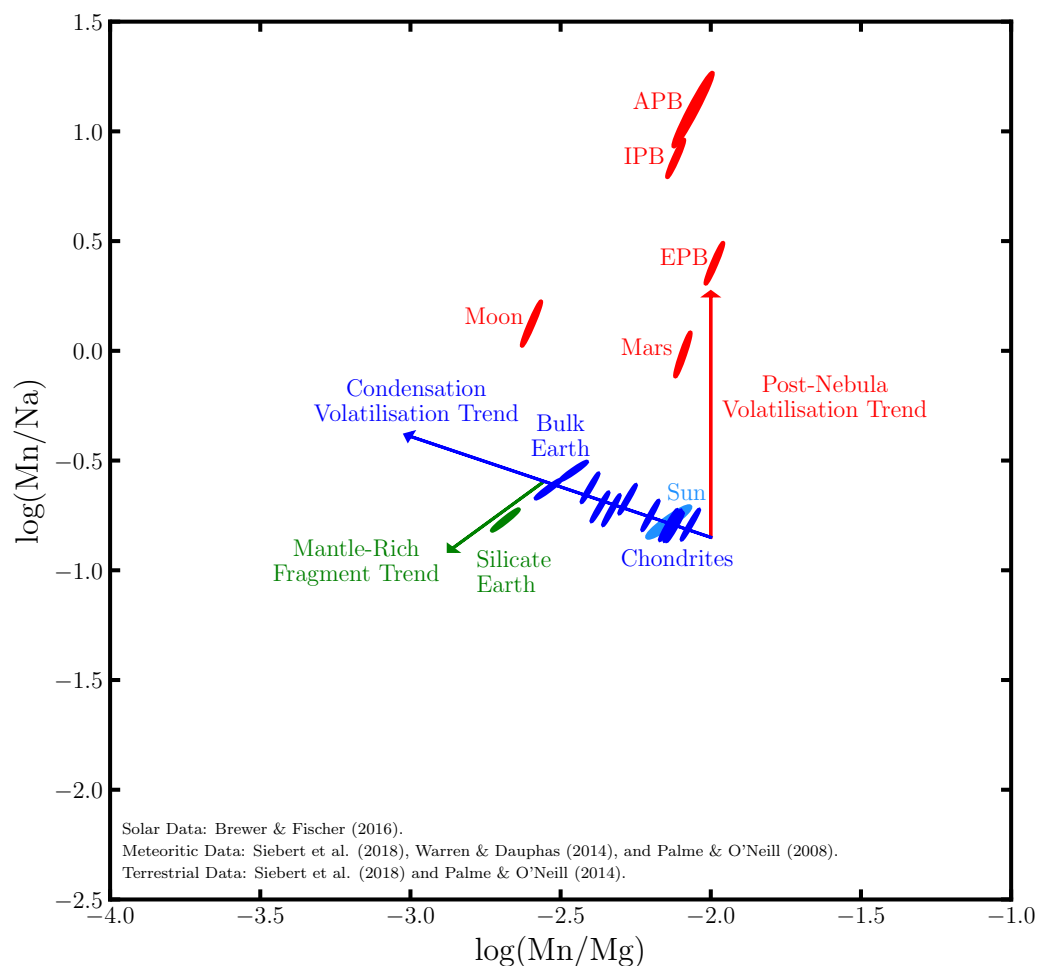
Fig. 5.1 A modified version of Figure 1 from Siebert et al. (2018). The Mn/Na and Mn/Mg ratios of Solar System bodies and fragments can be explained by three processes: condensation from the solar nebula (blue), planetary differentiation (green), and post-nebula volatilisation (red). The three coloured arrows indicate trends relating to the three processes based on starting with initially solar abundance values. Errors are displayed as 1σ error ellipses as regular error bars do not capture the correlation between the axes.

(Visscher and Fegley (2013); O'Neill and Palme (2008); Siebert et al. (2018)). Such conditions would cause Na to become much more volatile relative to Mn and Mg, and thus, would cause preferential loss of Na, leading to enhanced Mn/Na ratios but unchanged Mn/Mg ratios (O'Neill and Palme (2008); Pringle et al. (2014)). Evidence for post-nebula volatilisation is found in the super-chondritic Mn/Na ratios of Mars, the Moon, the Angrite parent body, the Ibitira parent body, and the Eucrite parent body. This process is described by the composition of objects moving along the red vector in Figure 5.1.

By finding the Mn, Mg, and Na abundances of rocky bodies in exo-planetary systems one can attempt to answer two main questions: Firstly, do the three processes of nebula condensation, differentiation, and post-nebula volatilisation occur regularly in other planetary systems? Secondly, are these three processes the major factors which determine the bulk composition of rocky exo-planetary bodies or are additional key processes taking place?

In this chapter I use the Mn/Na ratio and the Mn/Mg ratio of the exo-planetary bodies which pollute white dwarfs to assess whether the three processes known to alter the Mn/Na ratio and Mn/Mg ratio in the Solar System can explain the abundances observed. In order to investigate whether such effects are likely ancient or recent I also investigate whether the effect of post-main sequence stellar evolution is expected to alter the composition of the rocky bodies which pollute white dwarfs. In Section 5.2, I outline the polluted white dwarf data used, in Section 5.3 I outline the post-main sequence heating model used, in Section 5.4 I discuss the caveats of my work and my results, and in Section 5.5 I state the conclusions.

5.2   Polluted white dwarf data

Currently the most direct method for measuring the bulk composition of rocky bodies in exo-planetary systems is by observing the atmospheres of externally polluted white dwarfs. As introduced in Chapter 1, externally polluted white dwarfs are cool white dwarf stars with metal features in their spectra (Jura and Young (2014)). Metal absorption lines have been detected in more than one thousand cool white dwarfs (Weidemann (1960); Zuckerman and Reid (1998); Kepler et al. (2016); Hollands et al. (2017); Coutu et al. (2019)). The polluting metals must have been accumulated in the upper atmospheres of the cool white dwarf stars relatively recently because the cooling ages of the white dwarfs (of the order tens of millions of years to billions of years) are far longer than the time it takes for the metals to sink out of the upper

Table 5.1 The polluted white dwarf atmospheric abundances used in this work. The atmospheric abundances were derived in Dufour et al. (2012); Hollands et al. (2017); Swan et al. (2019); Zuckerman et al. (2007).

System	[Mg/He]	[Na/He]	[Mn/He]
GD362	-5.98 ± 0.25	-7.79 ± 0.20	-7.47 ± 0.10
J0738+1835	-4.68 ± 0.07	-6.36 ± 0.16	-7.11 ± 0.10
WD0446-255	-6.60 ± 0.10	-7.90 ± 0.10	-9.10 ± 0.10
J1535+1247	-7.36 ± 0.10	-8.72 ± 0.05	-9.80 ± 0.20

atmosphere and become unobservable (of the order days to millions of years) (Koester (2009); Jura and Young (2014)). For the white dwarf stars in question the polluting metals cannot originate from the interstellar medium, the fallback of the star's giant branch winds, or the radiative levitation of primordial metals (Farihi et al. (2010b); Jura and Young (2014); Farihi (2016); Veras (2016); Preval et al. (2019)). It is now widely accepted that for these stars the polluting material is of an exo-planetary origin, and therefore, by measuring the relative abundances of the metals in the polluted white dwarf atmospheres a unique insight into the bulk compositions of exo-planetary rocky material can be found (Jura and Young (2014); Farihi (2016); Veras (2016)).

Table 5.1 contains the atmospheric abundances for the four polluted white dwarfs investigated in this work. The atmospheric abundances were derived in Dufour et al. (2012); Hollands et al. (2017); Swan et al. (2019); Zuckerman et al. (2007) and they are currently the only white dwarfs which have measured abundances of Mn, Mg, and Na in their atmospheres. Six other white dwarfs are known to have two of the three elements of interest in their atmospheres, however, with only upper limits at best on the third elemental abundance I do not investigate these white dwarfs in this work.

As discussed in Chapter 2, the abundances in Table 5.1 cannot necessarily be directly compared to the Solar System bodies. This is because the differential sinking times of Mn, Na, and Mg through the white dwarf's photosphere cause fractionation of the photospheric abundances away from that of the accreting material. For example, for Mn, Na, and Mg in the atmosphere of GD362 the sinking times are 0.10, 0.22, and 0.22 Myrs respectively (Xu et al. (2013)). As highlighted in Figure 2.13, the abundances tend from those of the accreted body ('build-up phase') to a modified value dependent on the sinking timescales when accretion and diffusion settle into a steady state phase (Koester (2009)). Once accretion has finished, abundances decrease in a 'declining phase' (Koester (2009)). In Chapter 3 and Chapter 4, a Bayesian model is used to assess the most likely state of each body. The model finds that for GD362, J1535+1247,

Table 5.2 The polluted white dwarf data adjusted to account for differential sinking which is plotted in Figure 5.2. The abundances for GD362, J1535+1247, and WD0446-255 assume the polluting material is accreting in build-up phase while the abundances for J0738+1835 assume that the polluting material is accreting in steady state.

System	[Mn/Mg]	[Mn/Na]
GD362	-1.49 ± 0.27	$+0.32 \pm 0.22$
J0738+1835	-2.20 ± 0.12	-0.54 ± 0.19
WD0446-255	-2.50 ± 0.14	-1.20 ± 0.14
J1535+1247	-2.44 ± 0.22	-1.08 ± 0.21

and WD0446-255 the accreting material is most likely in the build-up phase while J0738+1835 is likely to be in a steady state accretion phase.

Table 5.2 outlines the expected abundance ratios of the rocky material that pollutes the white dwarfs GD362, WD0446-255, J1535+1247, and J0738+1835. These abundances can now be directly compared to those of the Solar System rocky bodies.

The abundance ratios from Table 5.2 of these four polluted white dwarfs are shown in Figure 5.2. An additional grey shaded region is added to account for the fact that in exo-planetary systems the initial composition of the stellar nebula may differ from that of the solar nebula. I model this potential variation using the same sample of nearby stars outlined in Chapter 2 (Brewer et al. (2016)).

Figure 5.2 highlights a diversity in the relative abundances of Mn, Mg, and Na in rocky exo-planetary bodies. The abundances of WD0446-255, J1535+1247, and J0738+1835 can be easily explained by condensation followed by differentiation and finally fragmentation of the body. As shown in Chapter 2 and Chapter 3, this conclusion holds when all the derived abundances are analysed, not just Na, Mg, and Mn. The crucial insight from this is that the Mn, an element which displays different behaviour in nebula vs post-nebula conditions, is explained by condensation processes. Thus, the decision to use a condensation model in Chapter 2 is somewhat validated as for these systems post-nebula volatilisation doesn't seem to have effected the abundances. A full discussion about these three polluted white dwarfs is given in Chapter 2 and Chapter 3 and no further discussion will take place here. The Mn/Na abundance of GD362 is inconsistent with condensation volatilisation ($>3\sigma$) and, as shown in Chapter 2, the abundances of the detected siderophile elements are inconsistent with the material being a fragment of a larger body which differentiated and was subsequently collisionally processed. The elemental abundances seen in GD362 are, therefore, difficult to explain without invoking post-nebula volatilisation.
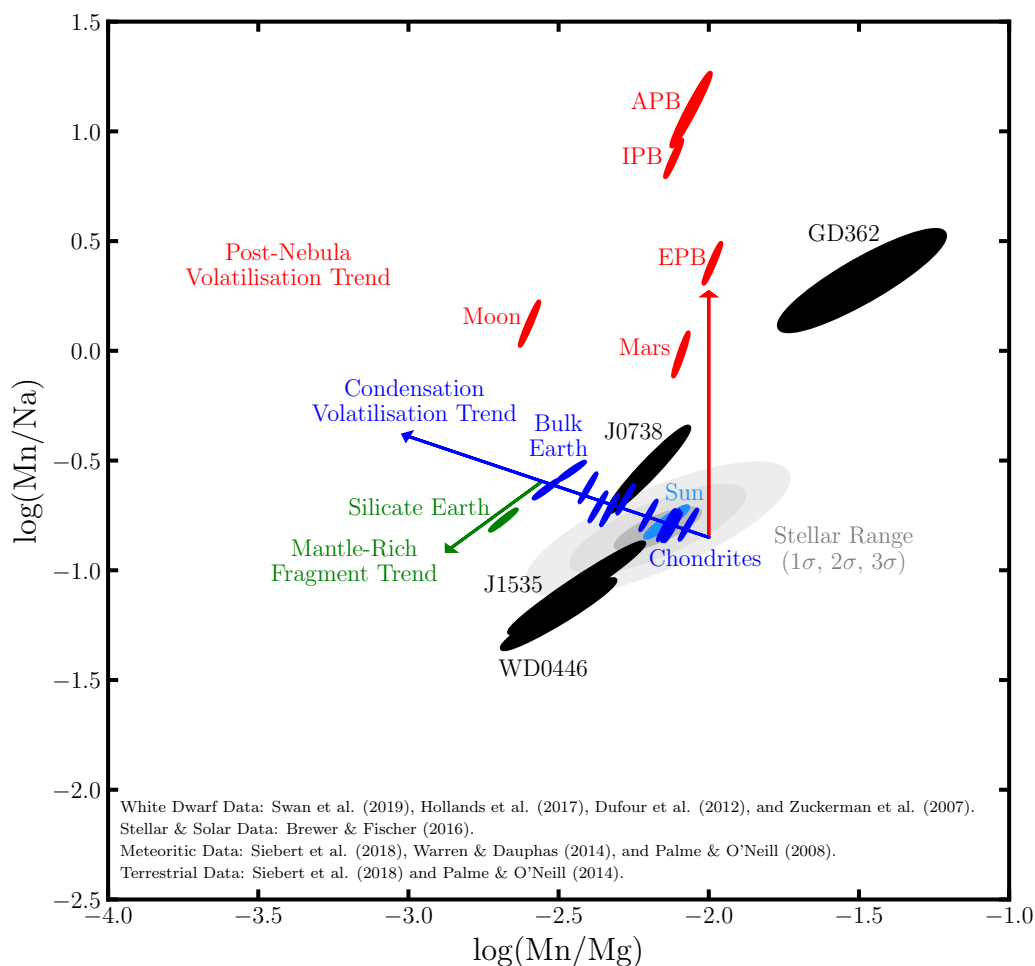
Fig. 5.2 The Mn/Na and Mn/Mg ratios of the bodies which pollute white dwarfs (Table 5.2) are plotted onto Figure 5.1. The white dwarf data (black) suggests that the three processes: condensation from the stellar nebula (blue), planetary differentiation (green), and post-nebula volatilization (red) may have occurred in exo-planetary systems, as the pollutant body ratios appear to have been moved along vectors away from the initial stellar abundance values (grey area). The errors are again displayed as 1σ error ellipses as regular error bars do not capture the correlation between the axes.

As the material that pollutes GD362 survived the giant branch evolution of the star, it is possible that devolatilisation could have occurred during the post-main sequence, when the luminosity of the star increases by many orders of magnitude. In order to investigate this possibility in Section 5.3 I model the compositional changes expected to occur to an asteroid in the GD362 system during the post-main sequence evolution of the host star.

5.3 Modelling volatile loss during the post-main sequence

When the progenitor of a white dwarf (a star with initial mass under 8-11 solar masses (Siess (2007))) evolves off the main sequence, it will go through phases where its luminosity exceeds 10,000 times the luminosity of the Sun and its radius exceeds a few astronomical units. During this post-main sequence evolution the equilibrium temperatures of the bodies which orbit the star can increase dramatically. Therefore, rocky bodies could potentially experience significant heating causing them to lose their volatile species.

5.3.1 The conditions required to remove Na preferentially to Mn

To estimate whether post-main sequence heating during the host star's giant branch evolution could heat an asteroid sufficiently to vaporise Na, whilst not vaporising Mn (or the whole asteroid for that matter), and produce the observed Mn/Na ratio in the pollutant body of GD362, one must first estimate the sublimation temperatures of the Na and Mn species expected to be present on extrasolar asteroids.

In this work I used the software package HSC chemistry version 8 to produce vaporisation curves for Na and Mn. For Na I inputted 100 kmol of solid Na2O and 1000 kmol of gaseous O into HSC chemistry and allowed it to equlibrate assuming the Na and O could only be in the form of the species listed in Table 5.3. I tracked the percentage of Na in gaseous form as a function of temperature and pressure and the vaporisation curve was defined as the line in pressure temperature space at which over 10 percent of the Na was in the gas. For Mn I performed an analogous procedure, however in this case I inputted 100 kmol of solid MnO and 1000 kmol of gaseous oxygen into HSC chemistry and allowed it to equilibrate assuming the Mn and O could only be in the form of the species in Table 5.3. I varied the abundances of the excess gaseous

Table 5.3 The possible solid, liquid, and gaseous species that were allowed to form when running the HSC Chemistry v. 8.0 equilibrium chemistry program to determine the behaviour of Na and Mn when heated assuming they are in oxide form.

Gaseous Species	Liquid Species	Solid Species
Na	Na	Na
Na_2O	Na_2O	Na_2O
Na_2		NaO_3
NaO		NaO_2
Na_2O_2		Na_2O_2
O		
O_2		
Gaseous Species	Liquid Species	Solid Species
Mn	Mn	Mn
MnO	MnO	MnO
MnO_2	Mn_2O_7	MnO_2
O		Mn_2O_3
O_2		Mn_3O_4

O in both cases to as low as 100 kmol and found that this only caused the sublimation temperatures to vary by ∼50 K and in both cases this variation caused the sublimation temperatures to increase. Therefore, any variability in the abundance of available O will not dramatically effect the conclusions.

The vaporisation curves found are strong functions of pressure. Therefore, in order to calculate the temperature at which Na starts to vaporise from an externally heated asteroid, one must know the pressure at which the potential vaporisation is occurring. Assuming that the atmosphere of the heated body is solely composed of the Na that is vaporised from its surface and the major factor contributing to atmospheric loss is Jeans loss, one can find the steady state mass of the atmosphere, and hence the surface pressure.

The steady state mass of the atmosphere M_{atmo} is defined as

$$M_{\mathrm{atmo}} = \Phi \tau_{\mathrm{escape}}. \tag{5.1}$$

The mass of Na vapourised per second, Φ is:

$$\Phi = \frac{4\pi R_{\mathrm{ast}}^2 \sigma \epsilon T^4}{C_{\mathrm{Na}}}, \tag{5.2}$$

where R_{ast} is the radius of the asteroid, σ is the stefan-boltzmann constant, ϵ is the emissivity of the asteroid, T is the surface temperature, and C_{Na} is the latent heat of vaporisation of Na.

The Jeans escape timescale, τ_{escape} is given by

$$\tau_{\mathrm{escape}} = \sqrt{\frac{2\pi k R_{\mathrm{ast}}^4 T}{G^2 M_{\mathrm{ast}}^2 \mu}} \frac{e^\lambda}{(1+\lambda)}, \tag{5.3}$$

where

$$\lambda = \frac{GM_{\mathrm{ast}}\mu}{kR_{\mathrm{ast}}T}, \tag{5.4}$$

k is the boltzmann constant, M_{ast} is the mass of the asteroid, G is the gravitational constant, and μ is the mean molecular mass of the atmosphere.

As the gravitational surface pressure is defined as

$$P = \frac{GM_{\mathrm{ast}}M_{\mathrm{atmo}}}{4\pi R_{\mathrm{ast}}^4}, \tag{5.5}$$

surface pressure can be written as a function of asteroid surface temperature, asteroid radius and asteroid mass:

$$P = \sqrt{\frac{2\pi k \sigma^2 \epsilon^2 T^9}{\mu C_{\mathrm{Na}}^2}} \frac{e^{\frac{GM_{\mathrm{ast}}\mu}{kR_{\mathrm{ast}}T}}}{\left(1 + \frac{GM_{\mathrm{ast}}\mu}{kR_{\mathrm{ast}}T}\right)}. \tag{5.6}$$

Figure 5.3 shows how for externally heated spherical black body asteroids of density 3000 kgm^{-3} and Bond albedo 0.035 the surface pressure varies with surface temperature and asteroid mass. The body is assumed to have no initial atmosphere and the steady state atmosphere produced is only composed of vapourised Na. The four solid lines shown correspond to four different asteroid masses and highlight how larger asteroids retain larger atmospheres and, therefore, require larger temperatures to cause vaporisation. I find that in the minimum mass scenario (where I assume all of the asteroid is currently in the white dwarfs atmosphere and none is left in a disc around the star, the value used is 6.31×10^{19} kg (Xu et al. (2013))) for temperatures above 1,186 K, and below 2,344 K, Na will vaporise from the surface while Mn will not. I also find that even if the mass of the asteroid polluting GD362 is 100 times larger than the minimum mass scenario, the above quoted temperatures vary by less than 40 K.
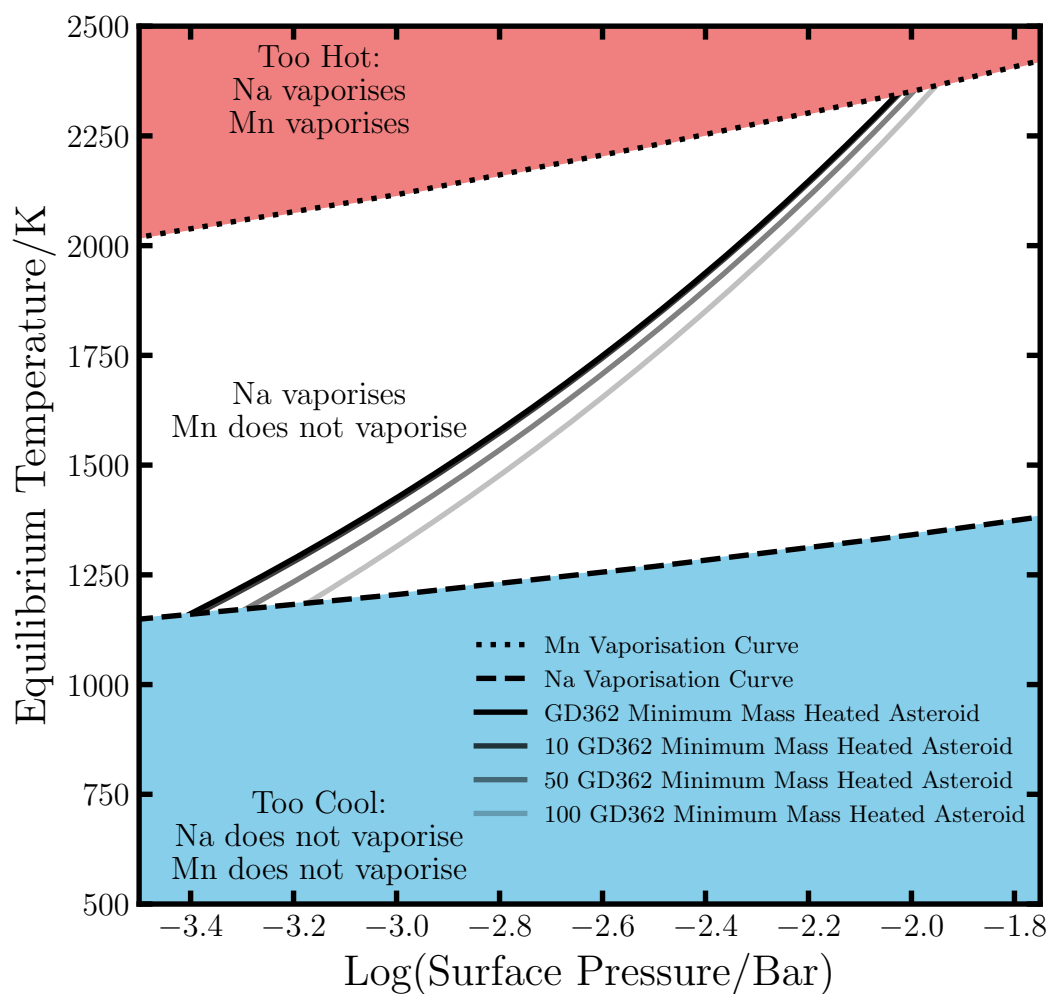
Fig. 5.3 The solid lines show the equilibrium temperature of an externally heated asteroid as a function of surface pressure and asteroid mass. The white region indicates the region of interest where Na vaporises but Mn does not. The Mn and Na vaporisation curves were found using the software package HSC Chemistry version 8 (For further details see Section 3.1).

5.3.2 Can post-main sequence heating remove Na preferentially to Mn?

The evolution of the luminosity of the progenitor to GD362 is calculated using the single star evolution (SSE) code (Hurley et al. (2013)). The code was run assuming an initial stellar mass of 3.2 solar masses. The mass of the white dwarf GD362 is 0.72 solar masses (Xu et al. (2013)). The value of 3.2 solar masses was chosen because it is the initial stellar mass which, given the star is solar metallicity, results in the formation of a white dwarf of 0.72 solar masses (Meng et al. (2008)). The stellar luminosity calculated can then be converted into an equilibrium temperature which is a function of radial distance from the star and can then be compared to the required vaporisation conditions. However, not all bodies in the planetary system will survive until the white dwarf phase. Bodies with close-in orbits (small radial distances from the star) can be either engulfed by the star as it expands or be spun to break up as the star's luminosity increases.

The Yarkovsky–O'Keefe–Radzievskii–Paddack (YORP) effect causes asteroids to become spun up by stellar radiation (Rubincam (2000)). On the giant branches, when the star's luminosity greatly increases, asteroids may be spun up to the point of break up (Veras et al. (2014a)). Smaller bodies which are closer to the star are easier to destroy due to the YORP effect. Therefore, for GD362, the YORP effect would be maximised for the case where the polluting asteroid only has mass equal to that of the material in the atmosphere (minimum mass assumption). The code presented in Veras et al. (2014a) calculates that if the body was interior to 0.4 AU it would be spun to break up during the giant branch, assuming the body was the minimum possible mass.

During post-main sequence evolution, the radii of a star can increase by orders of magnitude, potentially causing bodies which orbit too close to the star to become engulfed and destroyed. Whilst strong stellar winds during this phase of radial expansion cause the orbits of bodies around the star to migrate outwards, this is often not enough to stop engulfment (Mustill and Villaver (2012); Adams and Bloch (2013)). Using the analytical expression given in Adams and Bloch (2013), for the minimum mass case for GD362, I find that the body would be engulfed inside of 0.46 AU. The parameter values inputted into the analytical expression were those given by the SSE code for a 3.2 solar mass star: An initial AGB stellar mass of 3.2 solar masses, an initial AGB stellar radius of 1.22 au, and an AGB duration time of 0.96 Myrs. The gamma parameter was set to a value of 1 in order to minimise the engulfment radius. Larger bodies are engulfed more readily, and therefore, need to orbit further from the star in order to avoid destruction (Mustill and Villaver (2012); Adams and Bloch (2013)). Thus,

for all possible masses of the pollutant of GD362, engulfment will be the dominant factor in determining the closest orbit the body could have been on and survived to the white dwarf phase. Therefore, in order to consider the case of maximum heating, and therefore maximum Na loss, I take the minimum mass assumption as it allows the body orbit closer to the star without being destroyed.

Figure 5.4 displays the equilibrium temperature of a spherical black body asteroid of Bond albedo 0.035 orbiting a 3.2 solar mass star as a function of radial distance from the star and time. The luminosity as a function of time was calculated using the SSE code (Hurley et al. (2013)). The grey area is the region for which an asteroid of density 3000 kgm^{-3} and radius 170km (the minimum mass assumption) would be destroyed by stellar engulfment (Adams and Bloch (2013)). The regions where Mn and Na vaporise were taken from Figure 5.3 assuming the minimum mass scenario. By assuming the minimum mass scenario I minimise the size of the grey area, thus, maximising the size of the region where Na can be vaporised from the surface while Mn is retained.

Figure 5.4 highlights how the surface of an asteroid of radius 170km orbiting the progenitor of the star GD362 would be at temperatures such that Na vaporises while Mn would not for potentially up to 4 million years. Figure 5.4 additionally displays that the vaporisation of Na could occur on all bodies interior to approximately 8 AU.

5.3.3 Can post-main sequence heating produce a significant change to a body's Mn/Na ratio?

In order to calculate whether a sufficient fraction of the Na from the body can be vaporised and lost, thus, altering the bulk composition of the asteroid, one must calculate how the temperature of the interior of the asteroid evolves during the post-main sequence.

Thoroughly investigating this would require a complete asteroid interior model. However, due to the uncertainty on the mass of the asteroid and the abundances in this work, I feel it suitable to use a simple heat diffusion model in order to calculate a maximum possible volume heated and, therefore, the maximum fraction of Na lost.

In order to calculate the temperature of the interior at a given depth and at a given time I assume the asteroid is a sphere. Therefore, the relevant heat diffusion equation is:

$$\frac{\partial T}{\partial t} = \frac{\kappa}{\rho C_b} \frac{1}{r^2} \frac{\partial}{\partial r}\left(r^2 \frac{\partial T}{\partial r}\right).$$

(5.7)
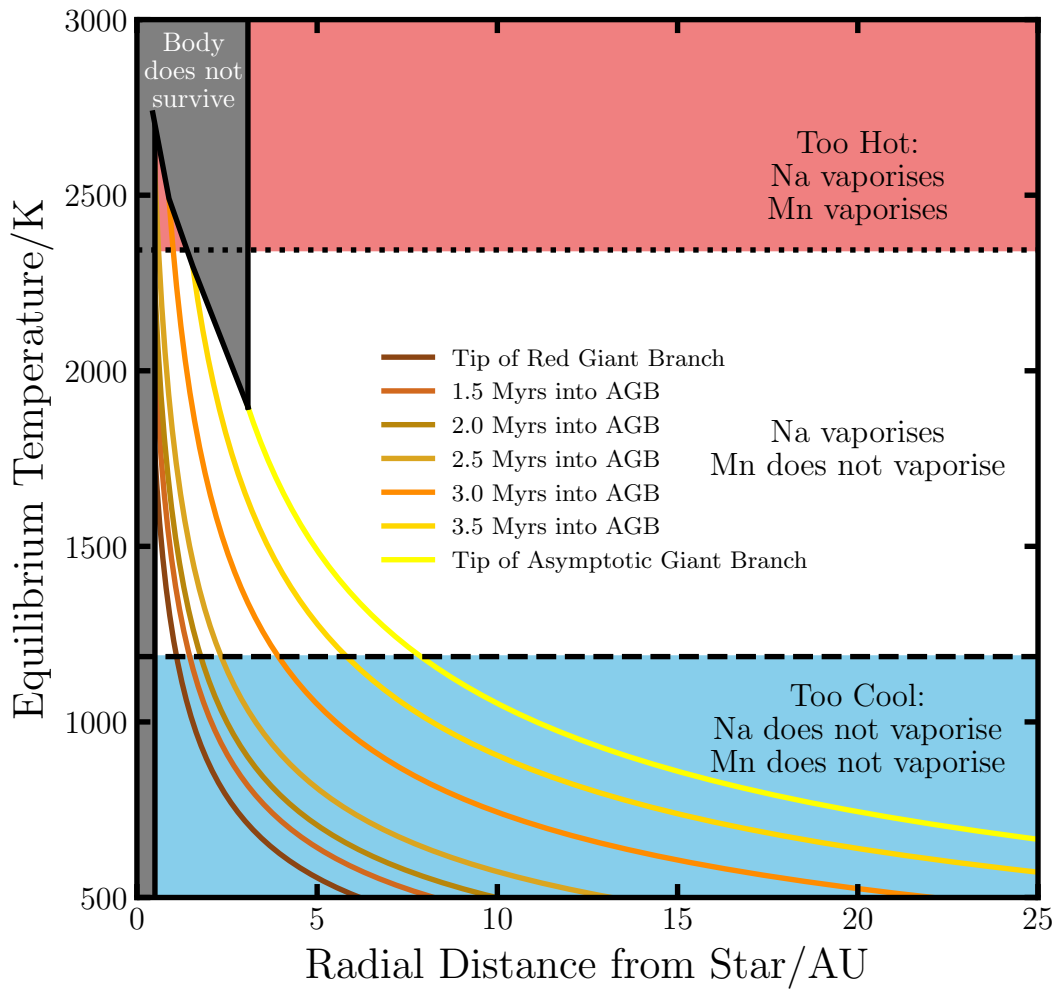
Fig. 5.4 The solid lines show the equilibrium temperature of a spherical black body asteroid as a function of radial distance from an initially 3.2 solar mass star at various epochs which are 0.5 Myrs apart. If the equilibrium temperatures enter the white region Na can be vaporised from the surface while Mn is retained. The grey area is the region for which an asteroid of density 3000 kgm^{-3} and radius 170km would be destroyed by stellar engulfment which in this scenario dominates over the YORP effect (Adams and Bloch (2013); Veras et al. (2014a)). For further details see Section 3.2.

where T is the temperature of the asteroid at a given distance from the centre r and a given time t, κ is the thermal conductivity of the asteroid, ρ is the density of the asteroid, and C_b is the heat capacity of the asteroid.

The boundary conditions for an isothermal sphere of radius a are:

$$T(a,t) = T_1 \qquad T(r,0) = T_0. \tag{5.8}$$

Assuming a steady state is reached the solution must have the form

$$T = A + \frac{B}{r}, \tag{5.9}$$

therefore, the following substitution can be used

$$B(r,t) = r(T(r,t) - T_1). \tag{5.10}$$

Equation 5.7 then becomes

$$\frac{\partial B}{\partial t} = \frac{\kappa}{\rho C_b} \frac{\partial^2 B}{\partial r^2}, \tag{5.11}$$

and the boundary conditions become

$$B(a,t) = 0 \quad B(r,0) = r(T_0 - T_1) \quad B(0,t) = 0. \tag{5.12}$$

The solution to Equation 5.11 is

$$B(r,t) = \frac{2a}{\pi}(T_1 - T_0) \sum_{n=1}^{\infty} \frac{(-1)^n}{n} sin\left(\frac{n\pi r}{a}\right) e^{-\frac{\kappa n^2 \pi^2 t}{\rho C_b a^2}}, \tag{5.13}$$

therefore the solution to Equation 5.7 is

$$T(r,t) = T_1 + \frac{2a}{\pi r}(T_1 - T_0) \sum_{n=1}^{\infty} \frac{(-1)^n}{n} sin\left(\frac{n\pi r}{a}\right) e^{-\frac{\kappa n^2 \pi^2 t}{\rho C_b a^2}}. \tag{5.14}$$

This solution can then be used to calculate the temperature at a given depth inside the asteroid during the post-main sequence evolution of the star. In this work, I make the simplistic assumption that if part of the asteroid gets to the temperature required to vaporise Na on the surface, then it is possible for the Na to be lost to this depth. This will certainly be an overestimate as, firstly, the temperature required to vaporise Na will actually be higher the deeper in the asteroid due to the increased pressure and, secondly, being at depth inside the asteroid will make it more difficult for the Na to out-gas and leave the asteroid once it does vaporise.

The distribution of Na in the asteroid may not be uniform. Hence, if I wish to find the fraction of Na it is possible to heat, I need to estimate the fraction of Na at a given depth. In this work I calculate two end member assumptions. Firstly, a case where Na is distributed homogeneously throughout the whole body which is analogous to the asteroid being primitive and undifferentiated. Secondly, a case where Na is mainly sequestered in the upper layers of the asteroid. This is analogous to the asteroid being differentiated into a core, a mantle, and a crust. In this work I assume the maximum size core a body of radius 170 km could differentiate into is 85 km and the maximum thickness of the crust is 6 km. 6 km was chosen as if I fix the composition of this crust to be the same as the Earth's oceanic crust (White and Klein (2014)) at 6km thickness there would be no Ti left in the mantle therefore the crustal composition would need to change. Assuming no Na is sequestered into the core and the crust has the same composition as the Earth's oceanic crust then 17% of the body's Na is in the first 6 km and 83% of the body's Na is in the next 79 km.

Figure 5.5 shows the percentage of volume heated for the minimum mass assumption asteroid during the post-main sequence evolution of GD362, as a function of radial distance from the star. I assume a heat capacity of 840 $Jkg^{-1}K^{-1}$ and a thermal conductivity of 2 $Js^{-1}m^{-1}K^{-1}$. As outlined earlier, as orbital migration occurs during the evolution of the star the radial locations in Figure 5.5 can be taken to be the initial orbital distances and, therefore, the percentage of volume heated is an upper bound. The volume required to be heated to fit the abundance observed in GD362 to within the 1σ uncertainties depends on the distribution of Na in the body. Figure 5.5 shows the volumes required for a homogeneous body and a maximally differentiated one. Figure 5.5 shows that it is very difficult to heat a large fraction of the body on the post-main sequence. Thus, it is not possible to produce the observed abundances to within their 1σ uncertainties. This is mainly due to the timescales of heat diffusion being longer than the time it takes to evolve through the post-main sequence evolution. In fact, Figure 5.5 shows that any body orbiting outside of the first astronomical unit will only experience heating to a very small fraction of the body.

Figure 5.6 is an updated version of Figure 5.2 with the maximum possible change estimated from this work due to post-main sequence heating. Two vectors are plotted; the longer vector assumes the body is differentiated, whereas the shorter vector assumes the body is homogeneous. I emphasise that these vectors are upper limits for what post-main sequence heating could achieve in terms of Mn/Na fractionation, as I assume the mass of the pollutant is the minimum possible mass, therefore, maximising both its volume heated and the proximity to the star. The vectors were calculated assuming
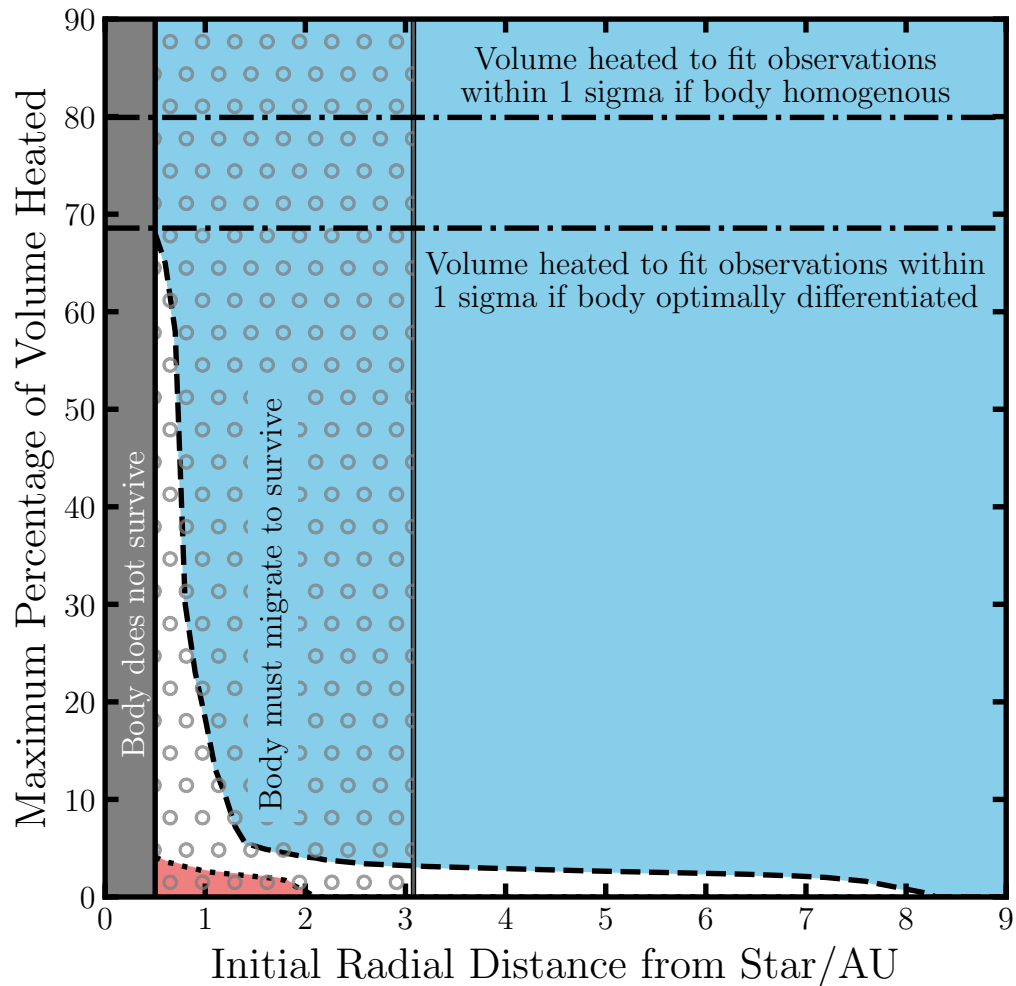
Fig. 5.5 The percentage of the volume of a spherical 170km radius 3000 kgm^{-3} density asteroid which is heated to a given temperature as a function of radial distance from the star. The white area is the region where the asteroid is heated to a temperature such that Na on the surface would vaporise while Mn on the surface would not, while the red area is the region where both surface Mn and Na vaporise, and the blue area is the region where temperature is sufficiently low such that neither Mn or Na vaporise. The percentage of volume heated is for a fixed radial location whereas in reality due to stellar mass loss all bodies will migrate outward over time, therefore, this plot highlights the maximum possible percentage heated at a given starting radial location.

all Na heated to the surface sublimation temperature is lost from the system and that the body is on an optimal orbit where it is as close to the host star as possible without being engulfed.

Figure 5.6 highlights that it is not possible to produce the abundance pattern seen in the pollutant of GD362 to within the quoted 1σ error bars with post-main sequence stellar heating.

5.4 Discussion

The main aim of this work was to investigate how volatiles are lost in exo-planetary bodies. In the Solar System, Mn and Na abundances suggest that there are three key processes: nebula condensation, differentiation and fragmentation, and post-nebula volatilisation. In order to probe these effects in exo-planetary systems I utilise the Mn, Mg, and Na abundances of the planetary material that has accreted onto white dwarfs. This method does come with additional assumptions and complications, most notably an extra potential phase of volatile loss on the giant branches whilst the star evolves to become a white dwarf. Evidence from the four white dwarfs investigated suggests that only condensation, differentiation and post-nebula volatilisation are required, and the simple model rules out heating on the giant branches as a likely explanation for the observed Mn/Na abundance of GD362. I now discuss the validity of the results and justify the assumptions made in the simple post-main sequence heating model.

5.4.1 Discussion of caveats

In order to discuss the validity of the results I must first address the validity of white dwarfs as a 'laboratory' to study the composition of exo-planetary material. Currently, white dwarfs offer a unique insight into the bulk composition of exo-planetary bodies which can not be offered by the study of exoplanet masses and radii or atmospheric compositions. As discussed in Chapter 1, the prevailing explanation for the presence of metals in cool white dwarf atmospheres is the accretion of exo-planetary material. In this work I assume that the metals originate from one body and that they can be related to the elemental abundances of the exo-planetary body accreted via consideration of the relevant sinking timescales. The assumption of single pollutants has been discussed in earlier chapters and has been validated by the results found in Chapter 3 and Chapter 4. It is also possible that GD362 is not accreting material in the build-up phase and the abundances in the atmosphere are related to the abundances of the
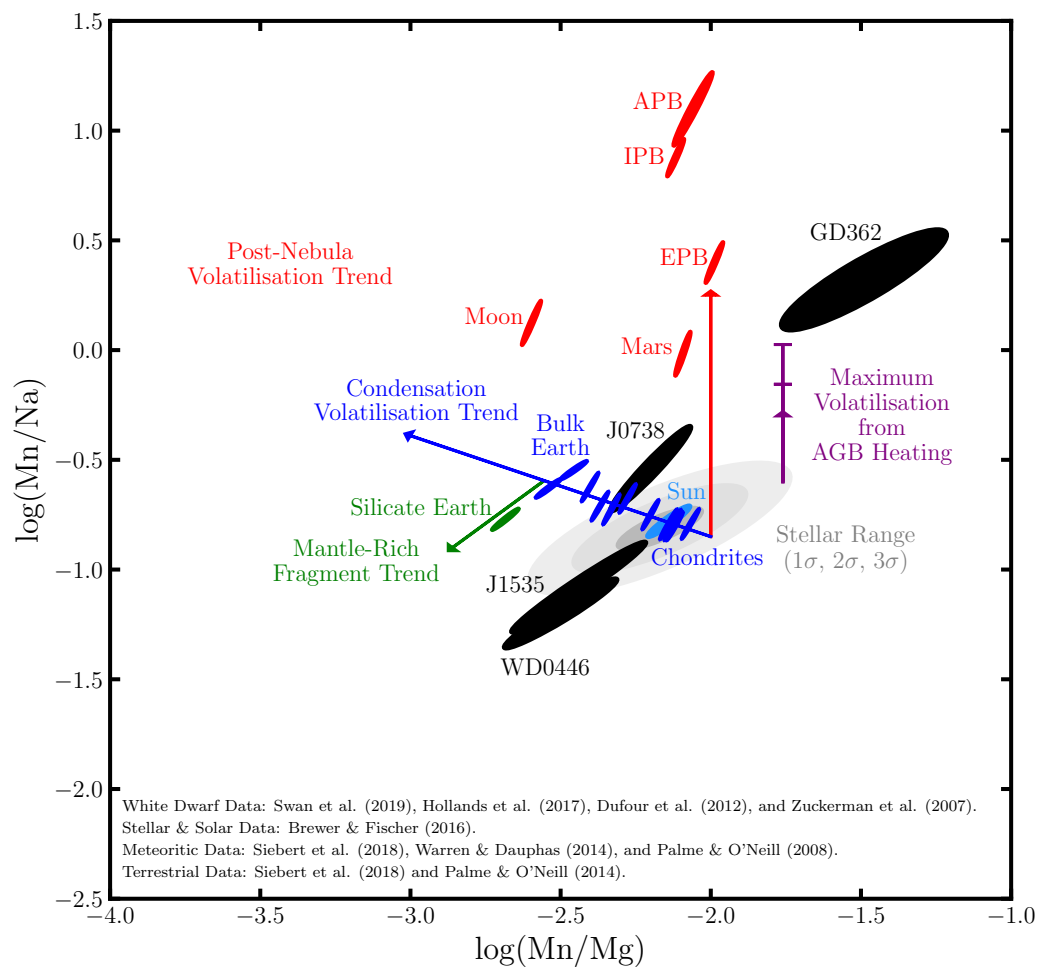
Fig. 5.6 An updated version of Figure 5.2 which includes a purple vector which indicates the maximum possible change in composition which could be attributed to heating during the post-main sequence evolution of the star. The lower cap is the limit assuming the asteroid is homogeneous, whereas, the higher cap is the limit assuming a scenario where Na is easier to remove due to the fact it is mainly sequestered in the upper layers of the asteroid. For further details see Section 3.3.

accreting material in a manner dissimilar to those calculated in this work. However, as Mn sinks faster than Na, if GD362 was in fact in a different phase of accretion the true Mn/Na ratio of the original body would in fact be even higher. Therefore, I do not expect the assumptions regarding the link between polluted white dwarf atmospheres and exo-planetary compositions to affect the results.

Only four white dwarf systems have measurements of the elements required to probe the nature of planetary volatile loss (Mg, Mn, and Na). The lack of observations are due to the fact that only sufficiently heavily polluted white dwarfs that lie in a narrow temperature range $(9,000\,\text{K-}14,000\,\text{K})$produce strong enough Mn and Na absorption features for both elements to be simultaneously detected. Therefore, in order to robustly conclude that only condensation, differentiation and post-nebula volatilisation are required to explain the abundances in exo-planetary material additional observations of heavily polluted white dwarf systems within the relevant temperature range will be required.

The major caveats which affect the validity of the results involve the simple model I established in order to rule out post-main sequence heating as an alternative explanation for the enhanced Mn/Na ratio of GD362. The major caveats of the model can be separated into two categories. Caveats which have been designed specifically so that they maximise the post-main sequence heating effect, and caveats which do not, and therefore, could potentially affect the conclusions of this work. The following assumptions are ones which could potentially alter the conclusions of this work:

- *Modelling the post main-sequence*: The duration of the giant branches, the maximum luminosity on the giant branches, and the closest possible orbit for which a body can survive to the white dwarf phase are all functions of the initial main sequence mass of the star. A longer duration for the AGB phase would lead to increased heating and could potentially explain the observed signature. For GD362 to spend significantly longer on the giant branch than I have modelled, given its observed mass of 0.72 ± 0.02 solar masses (Xu et al. (2013)), GD362 would need an initial metallicity higher than 3 times solar or lower than one third solar, in either of these cases, GD362 would have an initial mass which was considerably less than than 3.2 solar masses and therefore spend longer on the giant branch (Meng et al. (2008)). However, the majority of nearby stars do not have metallicities which are this extreme, therefore, it is unlikely that the metallicity of GD362 could be such that the conclusions would be affected (Brewer et al. (2016)).

- *Modelling Na loss*: In this work I assumed chemical equilibrium would be reached when calculating the sublimation temperature of Na and Mn and that sublimation would occur in an environment with plentiful oxygen. It is not obvious whether these assumptions will hold. However, I expect this will not influence the conclusions because regardless of the exact temperature required to vaporise Na, unless it is substantially lower, it will remain difficult to heat a large enough volume of the body to create the observed elevated Mn/Na ratio.

- *Modelling silicate vapour escape*: In order to calculate the surface pressure of the body it is assumed that the vaporised Na escapes the planetary body via Jeans escape. In reality many escape mechanisms may be at work, for example the hydrodynamic and sputtering escape mechanisms. If these escape mechanisms are important, their efficiency will cause a reduction in surface pressure, which will decrease the vaporisation temperature of Na and will potentially allow it to be more readily lost. However, this decrease is not expected to be drastic enough to change the conclusions as Na will still be difficult to vaporise from deep inside the body's interior.

The following assumptions have been designed such that they maximise the potential for the abundances in GD362's atmosphere to be explained by post-main sequence heating:

- The mass of the polluting body is equal to the total mass of the metals in the atmosphere of GD362. Less massive bodies can survive closer in orbits and can have more of their total volume heated in a given time therefore minimising the mass of a body maximises the potential heating it can experience.

- The pollutant body has an atmosphere solely composed of material which sublimates from its surface. This lowers the total surface pressure and therefore the sublimation temperatures.

- The chosen model parameters for the asteroid survival models presented in Adams and Bloch (2013) and Veras et al. (2014a) have been set such that the destruction distances for planetesimals during the evolution of the star are minimised.

- The pollutant body can survive on a stellar-surface-skimming orbit.

- Any Na which reaches the sublimation criteria can escape from the polluting body.

- The pollutant can be a differentiated body with a thick crust and a core that has a radius of half that of the body, allowing the majority of the Na to be sequestered in the upper layers of the pollutant.

5.4.2 Discussion of results

This work has shown that the Mg, Na, and Mn abundances of three of the analysed polluted white dwarf systems can be well explained by condensation and differentiation processes. This provides further evidence to suppliment the evidence given in Chapter 3 and Chapter 4 that the main processes which determined the bulk composition of the rocky worlds in the Solar System have determined the bulk composition of the rocky worlds in exo-planetary systems. This result also reinforces the validity of the assumption taken in the model outlined in chapter 2 that condensation effects usually dominate over post-nebula volatilisation effects.

The most significant result of this work is that one polluted white dwarf system, GD362, requires post-nebula volatilisation. GD362 is a historically significant system as it was the first polluted white dwarf to have the abundances of the metals in its atmosphere measured in detail (Zuckerman et al. (2007)). Additionally, GD362 has abundance measurements of 16 different metal elements the most of any single system to date (Zuckerman et al. (2007); Xu et al. (2013)). The differences between the depletion of volatiles due to incomplete condensation from the nebula, and the depletion of volatiles due to post-nebula heating are well understood (O'Neill and Palme (2008); Visscher and Fegley (2013); Siebert et al. (2018)). The enhanced Mn/Na ratio of GD362 is a signature of post-nebula volatilisation and crucially I find that the required volatilisation cannot be easily produced during the post-main sequence evolution of the star. This is not unexpected as previous work has shown that post-main sequence heating does not produce sufficient heat to sublimate the majority of the water ice present in some minor planetary bodies (Malamud and Perets (2016); Malamud and Perets (2017); Malamud and Perets (2017)). As post-main sequence heating struggles to provide the required volatilisation this implies that the planetesimal which pollutes GD362 underwent a period of formational heating such that it developed a global magma ocean once the stellar nebula had dissipated. This process is predicted to have occurred on many of the Solar System's minor bodies and is therefore not unexpected. The heat required to form the global magma ocean is expected to be generated by a

combination of impact heating from planetary collisions and short lived radioactive nucleotides. This heating must have been able to melt deep inside of the planetesimal in order to remove the required fraction of Na. The feasibility of this mechanism is not calculated in this chapter, however, I note that the position of GD362 on Figure 5.6 is not dissimilar to that of Vesta (the Eucrite parent body, EPB). Therefore, it seems likely that the same process predicted to have removed volatiles from Vesta could devolatilise the pollutant of GD362.

The Mn/Mg ratio of GD362 is potentially difficult to explain. As highlighted by Figure 5.2, it is simply possible that the progenitor star had an unusually low Mg abundance. However, the analysis of all the elements present in the atmosphere given in Chapter 3, found that the pollutant of GD362 was likely a primitive body and that the estimated Mg value is likely too low, and re-observation would potentially yield a higher abundance measurement. Additional observations of polluted white dwarf systems could yield more systems with enhanced Mn/Na ratios and add further weight to the conclusions presented here, and therefore, would be a worthwhile project. The enhanced Al, Ti, and Ca abundances of GD362 also need explanation if post-nebula volatilisation is preferred to nebula condensation and a full model which takes both processes into account would need to be created. Such a model is beyond the scope of this thesis, however, it would be of value as it could further test the results presented in this chapter. Additionally, further modelling to investigate whether post-main sequence heating can contribute to smaller changes in the Mn/Na ratio of planetary bodies would be of great interest, especially once more white dwarf systems with Mn and Na abundances are discovered.

5.5 Conclusions

Volatile loss is a key process in rocky planetary bodies. Mn and Na trace the loss of volatiles and, crucially, can distinguish between volatile loss occurring under two physical-chemical regimes. The first regime is volatile loss due to incomplete condensation of the nebula gas early in a system's evolution. The second regime is volatile loss due to heating processes late in a system's evolution after the nebula gas has dissipated. The Mn to Na ratio and Mn to Mg ratio observed in the material accreted by polluted white dwarfs can be used to provide evidence for condensation processes and post-nebula volatilisation occurring in exo-planetary systems. In this study I found that the abundances present in the material polluting J0738+1835, J1535+1247, and WD0446-255 are consistent with a scenario in which the material condensed out of a

protoplanetary disc, before undergoing differentiation and collisional processing, and then finally accreting onto the white dwarf. However, the Mn/Na ratio of the material polluting the star GD362 cannot be explained by condensation volatilisation processes ($>3\sigma$). I hypothesise that the enhanced Mn/Na ratio is a signature of post-nebula volatilisation. I show that any alterations to the composition of the material orbiting GD362, that could develop due to heating during the giant branch evolution of the star, are not significant enough to increase the Mn/Na ratio to match that observed in GD362. Even if the polluting body was suitably small, suitably differentiated, and orbited its host star on a surface grazing orbit I still cannot explain the abundances to within their 1σ error bars. Therefore, I conclude it is most likely that the volatile loss that occurred on the pollutant of GD362 after the dissipation of the nebula gas was due to impact heating, which created a global magma ocean, allowing Na to be efficiently outgassed, similar to the process experienced by small rocky bodies of the Solar System. Therefore, GD362 may provide evidence for the occurrence of global magma oceans and post-nebula volatilisation in exo-planetary systems.

Chapter 6

Modelling the effect of planetesimal formation temperature on the exoplanet mass-radius relation

6.1 Introduction

In Section 1.1, the observational techniques which are used to detect exoplanets, and subsequently derive their radii and masses were introduced. These observations offer a glimpse into the nature of extrasolar planets, however, as discussed in Section 1.1 measurements of the mass and radius of exoplanets alone cannot precisely determine the interior composition of the exoplanets. The degeneracy in exoplanet mass-radius solutions can be reduced, and the interior composition can be somewhat constrained, if the host star's photospheric abundances are observed and it is assumed that planets are composed of material which condenses out of a protoplanetary disc with a composition identical to that of the host star's photosphere (Dorn et al. (2015); Dorn et al. (2017)). As outlined in Chapter 4, the frequency of primitive material accreting onto white dwarf stars suggests that such an assumption is a valid one, as white dwarf observations show that the majority of exo-planetary material has a refractory composition identical to that which is expected for its host star. Theoretically the assumption is expected to hold as at temperatures cooler than $\sim$1,200 K all of the major rocky forming species (Si, Mg, Fe) will condense out of the disc, and therefore, planets composed of such condensates will have abundances of the major rocky forming species identical to the host star's (Bond et al. (2010); Moriarty et al. (2014)). Further support for such an assumption is given by observations of the Solar System planets: Earth, Venus, and

Mars, which are expected to have similar major rock forming elemental abundances as they all follow the same mass-radius trend (Figure 1.8). However, in the hot inner parts of the protoplanetary disc bodies may form from condensates which are dominated by refractory elements (Al, Ti, Ca) and are depleted in moderately volatile elements (Si, Mg, Fe etc.) relative to the host star (Lodders (2003); Lodders (2010); Bond et al. (2010)). The prevalence of such refractory dominated condensates is not well understood, however, as shown in Chapter 3 and Chapter 4, polluted white dwarf observations suggest such bodies may be potentially plentiful in certain exoplanetary systems. Therefore, in such systems exoplanets may potentially form with drastically different internal compositions to those traditionally assumed. These exotic compositions may create rocky planets with unusual radii for a given mass. If this were the case the existence of such refractory dominated exoplanets could potentially be probed by searching for close-in rocky exoplanets and comparing their masses and radii measurements to the masses and radii expected for planets formed of traditional material and refractory dominated material.

As highlighted in Figure 1.8 observed Earths and super-Earths have a variety of bulk densities indicative of variability in their internal composition and interior structure. It is understood that even if all planets inherit refractory elemental abundances from their star, deviations in bulk density are possible via various mechanisms. Geochemical differentiation creates planetary cores which are significantly more dense than planetary mantles, therefore, mantle stripping due to giant impacts (Benz et al. (1988)) or tidal disruption events (Rappaport et al. (2013)) can create planets with increased densities. Planets with decreased densities can be formed if they contain either water-rich ice layers or thick volatile-rich atmospheres (Zeng et al. (2019)). The uncertainties on the masses of many exo-planets are sufficiently large such that constraining information from their density and analysing any possible density deviations is not possible. However, there are two rocky planets in the K-dwarf system HD 219134 (Gillon et al. (2017)) which have sufficient precision on their mass estimates as to offer useful insights into such density deviation effects. HD 219134b and HD 219134c do not follow the same mass-radius trend, in fact they have a $\sim$10% difference in bulk density. Gillon et al. (2017) suggested that HD 219134b potentially has a thick H/He atmosphere and the density difference could be explained that way. However, Dorn and Heng (2018) showed that if evaporative loss is considered H and He atmospheres can be ruled out for both HD 219134b and HD 219134c. Dorn and Heng (2018) suggested that the density difference could be caused by a difference in secondary atmospheric compositions. In this chapter I first explore the possibility that the density difference

Table 6.1 Stellar data for HD 219134 (Motalebi et al. (2015)).

Parameter	HD 219134
$M_* \; [M_\odot]$	0.78 ± 0.02
$R_* \; [R_\odot]$	0.778 ± 0.005
$L_* \; [L_\odot]$	0.265 ± 0.002
$T_* \; [K]$	4699 ± 16

between HD 219134b and HD 219134c can be explained by an additional mechanism, the formation of planets with abundances dominated by refractory elements. I then outline the magnitude of the deviations in planetary density such planets would display as well as the likelihood of these deviations occurring. Secondly, I investigate the viability of other possible explanations for the low density of HD 219134b. The research outlined in this chapter was done in collaboration with Caroline Dorn, Amy Bonsor, and Thomas Hands, therefore, I outline in detail only the work done by myself, while briefly summarising the work done by others.

6.2   The HD 219134 system

The HD 219134 system is a single star system which resides 6.5 parsecs from the Sun and contains at least 5 planets. Table 6.1 displays the stellar data for the system as derived in Motalebi et al. (2015) while Table 6.2 displays the planetary data for the inner most two planets as derived in Gillon et al. (2017). The planet hosting star is a K-dwarf while HD 219134b and HD 219134c are super-Earth planets on sub-week orbits. HD 219134b has a bulk density of $1.15 \pm 0.13 \; \rho_\oplus$ while HD 219134c has a bulk density of $1.26 \pm 0.14 \; \rho_\oplus$, therefore, although both planets are predominantly rocky in nature they have a density difference of the order of 10%, which if true cannot be easily explained. Given the magnitude of the uncertainties on the density it is possible that there is no density difference, however, in this chapter I will assume the density difference is real. In the next section, I present a model which calculates the bulk composition of a planet based on the compositions of the planetesimals which it accretes during formation.

6.3   Planetary composition model

In order to model the bulk composition of the rocky planets HD 219134b and HD 219134c I employ a simple model which has been shown to recreate, to first

Table 6.2 Bulk planetary data for HD 219134b and HD 219134c (Gillon et al. (2017)).

Parameter	HD 219134b	HD 219134c
M [$M_\oplus$]	4.74 ± 0.19	4.36 ± 0.22
R [$R_\oplus$]	1.602 ± 0.055	1.511 ± 0.047
ρ [$\rho_\oplus$]	1.15 ± 0.13	1.26 ± 0.14
a [AU]	0.03876 ±0.00047	0.06530 ±0.00080

order, the bulk composition of the rocky bodies in the Solar System (Moriarty et al. (2014); Chapter 2). The model assumes that rocky planets form via the aggregation of rocky planetesimals which have condensed out of a protoplanetary disc in chemical equilibrium. The composition of the protoplanetary disc is assumed to be identical to the stellar nebula, whilst the compositions of the planetesimals are determined by the compositions of the solid species found when minimising the Gibbs free energy at the pressures and temperatures present in the mid-plane of the protoplanetary disc. In order to compare these compositions to that of the planets, I consider that the planets would form out of material that condensed out of the nebula within a small feeding zone around each planet's orbital location. Thus, the bulk compositions found are functions of the size of the feeding zone from which the planet accreted planetesimals (Δr), the time when the planetesimals condensed out of the disc (t), and the distance from the star at which the planet formed (r). The compositions predicted by the model also depend on the mass and the composition of the host star as the mass of the host star affects the evolution of the protoplanetary disc while the composition of the host star is used as initial conditions for the equilibrium chemistry model (M_* and $[X/H]_*$). Figure 6.1 is a schematic diagram outlining the model, the mean temperature of the condensates which compose the planet (T) is often a more useful parameter to discuss than the formation distance as its effect on the planet composition, and therefore planet internal structure, is less dependent on the formation time and feeding zone size.

6.3.1 Viscous irradiated protoplanetary disc model

The Gibbs free energy of the system, and thus the composition of the solids formed depends on the pressure and temperature at which condensation occurs. In order to consider reasonable pressures and temperatures for the inner regions of the protoplanetary disc, and in order to convert these temperatures and pressures into radial locations within the disc and formation times for the solid condensates, I consider a simple protoplanetary disc model. I use the theoretical model derived in Chambers (2009),

Fig. 6.1 A schematic diagram of the planetary composition model taken from Dorn et al. (2018).

which models the viscous accretion of gas heated by the star. This model has been previously used for the modeling of planetesimal formation in protoplanetary discs (Moriarty et al. (2014)) and super-Earths (Alessi et al. (2016)). This model ignores any vertical or radial mixing, and as will be discussed further later, any radial drift. All of these processes may be of critical importance in a realistic protoplanetray disc.

The Chambers model is a disc model with an alpha parameterization which divides the disc into 3 sections; an inner viscous evaporating region, an intermediate viscous region, and an outer irradiated region. For the calculations in this work I have assumed disc parameters of $s_0 = 33\,AU$, $\kappa_0 = 0.3\,\mathrm{m^2 kg^{-1}}$, $\alpha = 0.01$, $\gamma = 1.7$, $\mu = 2.4$, and $M_* = 0.78 M_\odot$ following Chambers (2009) and Motalebi et al. (2015). I also assume that the mass of the protoplanetary disc is directly proportional to the mass of the host star according to $M_0 = 0.1 M_*$ (Chambers (2009); Andrews et al. (2013)). The temperature and radius of the star in the protoplanetary disc phase are assumed to be functions of the stellar mass in the form derived in Siess et al. (2000). The relations used in this work to calculate the disc mass, the initial stellar radius, and the initial stellar temperature as a function of stellar mass are consistent with the values given in Stepinski (1998) and Chambers (2009) for a solar mass star.

The full analytical expressions for the pressure and temperature of the mid-plane of the disc as a function of radial location (r) and time (t) are presented in Chapter 2. The temperature-radial location curves for the model disc around HD 219134 are plotted as a function of time in Figure 6.2. The pressure-radial location curves and pressure-temperature space mapped out by the model disc around HD 219134 is displayed in Figure 6.3 and Figure 6.4.
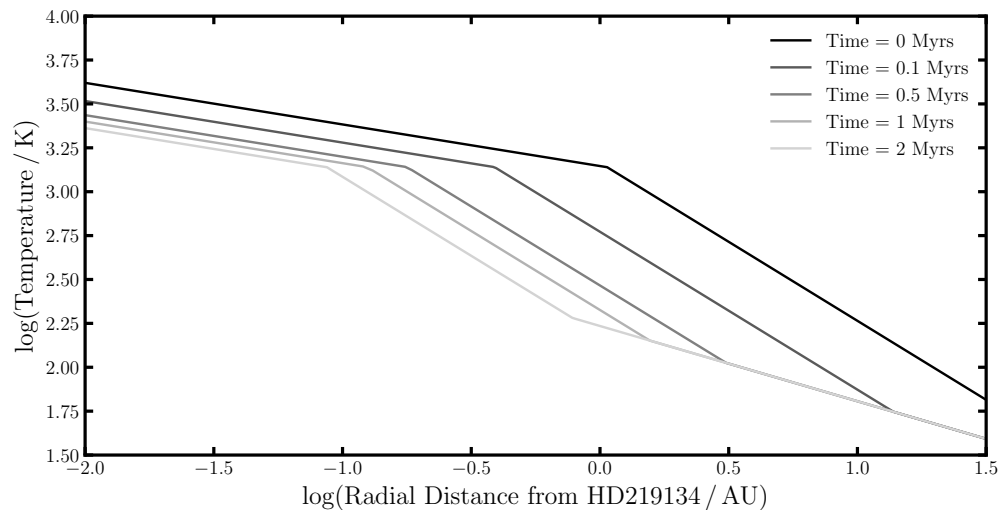
Fig. 6.2 Midplane temperature as a function of radial distance in a protoplanetary disc around HD 219134 as derived by the Chambers (2009) analytical model.
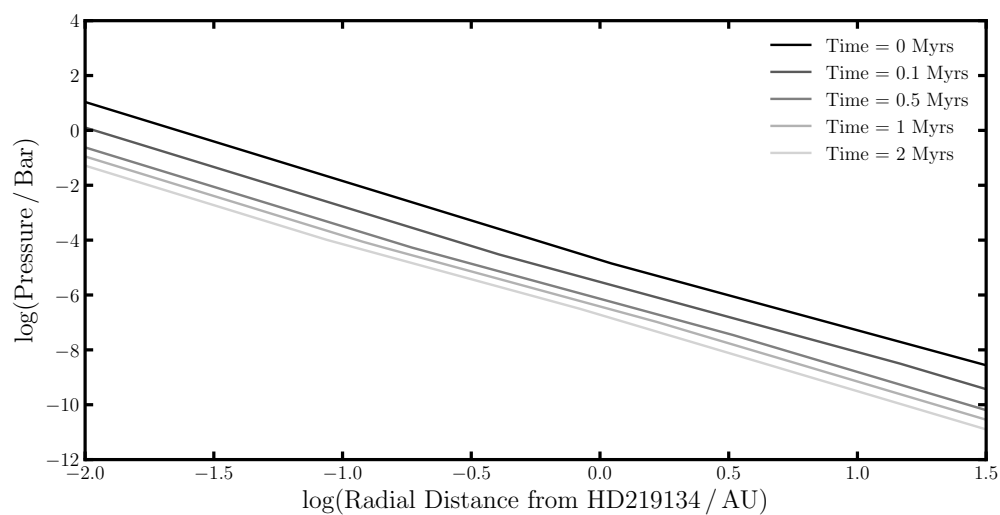
Fig. 6.3 Midplane pressure as a function of radial distance in a protoplanetary disc around HD 219134 as derived by the Chambers (2009) analytical model.
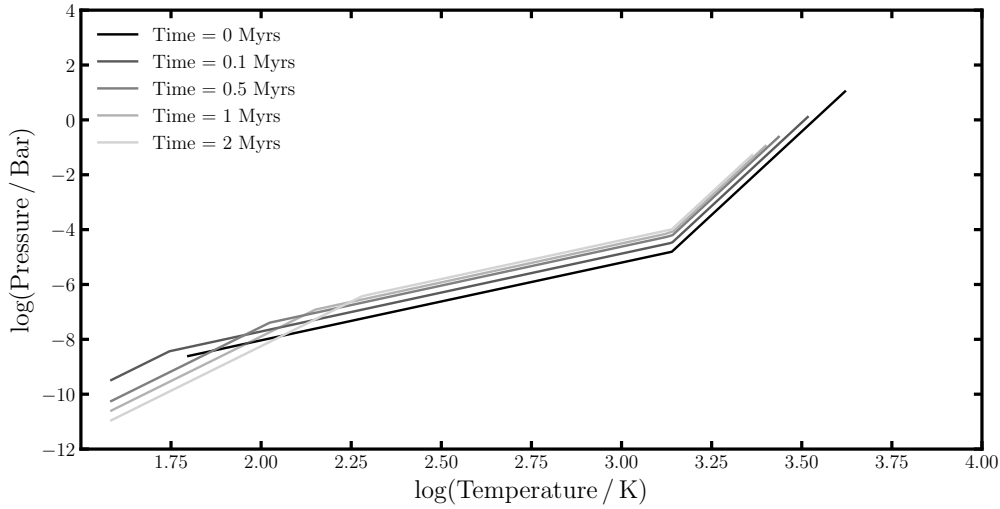
Fig. 6.4 The midplane pressure-temperature space mapped out by the protoplanetary disc around HD 219134 as derived by the Chambers (2009) analytical model.

6.3.2 Equilibrium chemistry condensation model

I use the commercial Gibbs free energy minimisation package in HSC Chemistry version 8 to model the compositions of the solid species at the pressures and temperatures expected to be present in the protoplanetary disc (Section 6.3.1). As the pressures and temperatures in the disc are a function of the formation time and the radial location (t, r), so are the planetesimal compositions.

HSC chemistry version 8 was set up in the same way as in Bond et al. (2010), Moriarty et al. (2014), and Chapter 2, which all used the software to model planetesimal compositions. The gaseous elements inputted, the list of gaseous species included in the model, and the list of solid species included in the model are the same as in Chapter 2 (They are displayed in Table 2.1, Table 2.2, and Table 2.3). The initial inputted gaseous abundances for the case of the HD 219134 system are displayed in Table 6.3.

The abundances for the nearby star HD 219134 have been measured by many groups within the literature (Thévenin (1998); Prieto et al. (2004); Luck and Heiter (2005); Valenti and Fischer (2005); Mishenina et al. (2013); Ramírez et al. (2013); Maldonado et al. (2015); Da Silva et al. (2015)). Table 6.3 lists the median stellar abundances from the *Hypatia catalog* (Hinkel et al. (2014)) after outliers were removed and assuming the Hydrogen abundance is 10^{12} kmol. Outliers are those that lie beyond the range of possible abundances in stars with metallicities similar to HD 219134 based on Brewer et al. (2016). This criteria was chosen as the uncertainities on the

Table 6.3 The inputted gaseous elemental abundances, the values are in kmol and are representative of the initial stellar nebula of HD219134 ((Hinkel et al., 2014)).

Element	Input
Al	4.46×10^6
C	3.71×10^8
Ca	2.75×10^6
Cr	6.17×10^5
Fe	3.47×10^7
H	1.00×10^{12}
He	8.51×10^{10}
Mg	4.32×10^7
N	7.42×10^7
Na	2.29×10^6
Ni	2.19×10^6
O	6.02×10^8
P	2.82×10^5
S	1.62×10^7
Si	3.68×10^7
Ti	1.41×10^5

Brewer et al. (2016) catalogue are far smaller than the uncertainties on the majority of measurements of the HD219134 system. The C/O ratio of HD 219134 is assumed to be 0.62, as this is the value found when the outliers are removed the *Hypatia catalog* (Hinkel et al. (2014)). If the actual C/O ratio of HD 219134 was outside the range of 0.25-0.75, our calculated disc chemistry could significantly differ. However, Brewer et al. (2016) showed that most FGK stars cluster around sub-solar C/O ratios of 0.44 and no super-solar C/O ratios of greater than 0.75 were detected among the 958 sample stars which are confirmed to be on the main-sequence.

A caveat to the model is that the Gibbs free energy minimisation is only performed on a limited list of species, however, as these elements and species are the most abundant in the rocky debris in the Solar System this is not thought to be a major limitation. The only major species missing from the list, that are expected to possibly alter the results of this work, are the complex carbon macromolecules which are found in many asteroids and meteorites (Pizzarello et al. (2006)) and whose formation mechanism is not yet understood. However, as it is expected that the carbon abundance in the disc is sufficiently low with respect to the overall metal abundances, these molecules will be trace species and therefore their contribution to the overall planetesimal composition in the inner disc will be negligible.
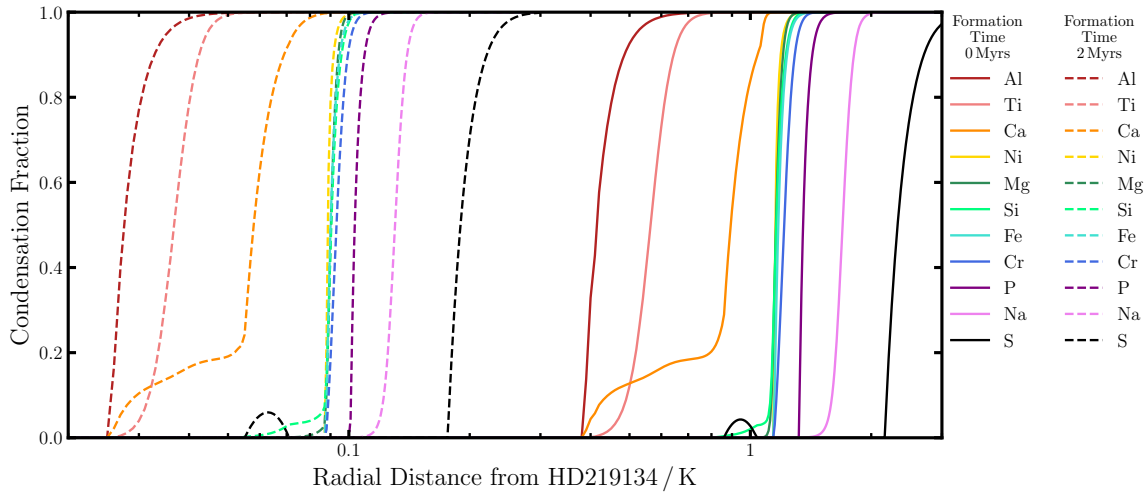
Fig. 6.5 The fraction of all modelled elements which are in solid species rather than gaseous species as a function of radial formation location for an initially HD 219134 composition gas at formation time equals 0 Myrs and formation time equals 2 Myrs.

Figure 6.5 shows how the ratio of each element in solid state relative to gaseous state changes with increasing radial separation (r) from the host star at the two extremes of formation time (t=0 Myrs and t=2 Myrs) for a HD 219134 input chemistry and disc model. Figure 6.6 is a modified version of Figure 6.5 where I plot the condensation fraction against temperature rather than radial separation for the two extremes of formation time. Figure 6.5 and Figure 6.6 illustrate how the model can reproduce the expected condensation series found in Lodders (2003) and Lodders (2010). The figures also emphasize how the order of condensation of the elements analysed is invariant over time and how the condensation temperatures for each element only change by $\sim$100 K for the two end member cases. Two million years is taken to be a general time span for which gas in the protoplanetary can be present. However, this is potentially an extreme case as recent disc surveys suggest that the majority of planetesimal formation occurs very early for discs similar to those investigated here and maybe limited to < 1 Myr (Tychoniec et al. (2018)).

6.3.3   Planetesimal aggregation model

The planetesimal compositions found using the equilibrium chemistry model and the protoplanetary disc model are a function of formation time and formation location (t, r). In reality a body the size of a planet will incorporate material from a range of
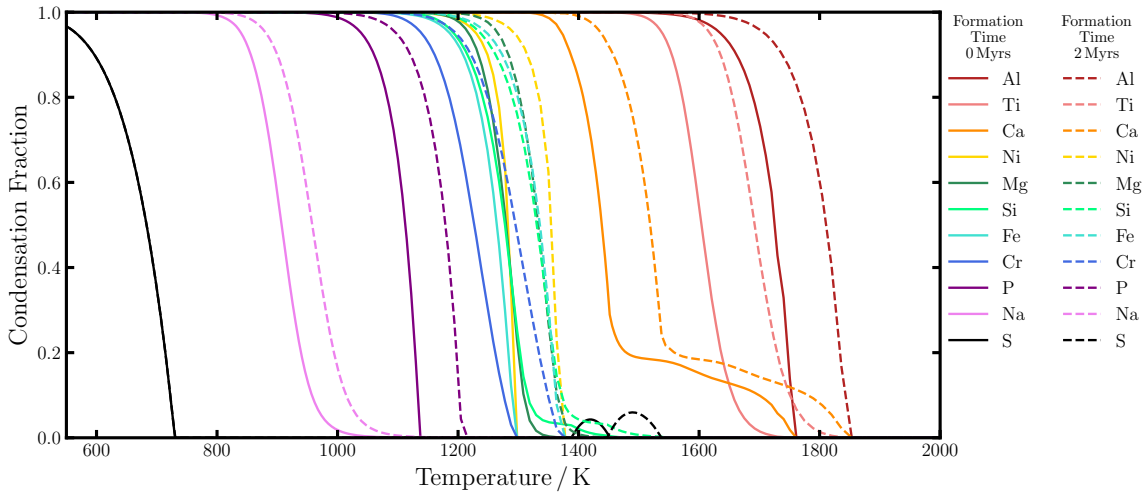
Fig. 6.6 The fraction of all modelled elements which are in solid species rather than gaseous species as a function of temperature for an initially HD 219134 composition gas at formation time equals 0 Myrs and formation time equals 2 Myrs.

formation locations and possibly a range of formation times and the radial drift of planetesimal could play an important role in the condensates a body aggregates.

In order to somewhat account for these effects, I consider a model in which the material that forms the planets originates from a range of formation locations described by a Gaussian distribution centered at distance r and with a width of Δr. Thus, I have three free parameters, the formation location, r, which is equivalent to the mean of the normal distribution, the feeding zone parameter, Δr, which is equivalent to the standard deviation of the normal distribution and the formation time of the planetesimals which comprise the planet, t. Figure 6.1 outlines the parameters of the model for a given formation time.

The feeding zone Δr is generally mass dependent in oligarchic growth and is often set to a maximum of 10 Hill radii (Ida and Lin (2004)). For planet b at 1 AU ($t = 0$ Myrs) this maximum equals 0.18 AU, while at 0.1 AU ($t = 2$ Myrs) it is 0.018 AU. Larger effective feeding zones may be realized as a result of scattering of planetesimals by neighboring planets. In this chapter I will now specify feeding zone sizes in terms of planetary Hill radii to clarify my assumptions. No N-bodys simulations were computed in order to predict the amount of mass available to form a planet, therefore, it was assumed that it was possible to form multiple earth masses of such high temperature condensates. This assumption will be addressed in the Section 6.5.

The modelled exoplanetary compositions found here were then used as inputs for the exoplanet interior model outlined in Dorn et al. (2017) and the variation in the

mass radius curves produced as a function of formation time (t), formation radius (r), and feeding zone size (Δr) were investigated for the HD 219134 system.

6.3.4 Exo-planet interior model

The calculated compositions from the condensation model are used as bulk constraints for the rocky interiors of the planets. The employed interior model uses self-consistent thermodynamics and is described fully in Dorn et al. (2015). It is assumed that the interiors are purely rocky and are composed of pure iron cores with silicate mantles. The mantles comprise the oxides Na_2O–CaO–FeO–MgO–Al_2O_3–SiO_2 (model chemical system NCFMAS). Mantle mineralogy is assumed to be dictated by thermodynamic equilibrium and computed by free-energy minimization (Connolly (2005)) as a function of composition, interior pressure and temperature. The Gibbs free-energy minimization procedure yields the amounts, mineralogy, and density of the stable minerals. For the core density profile, an equation of state fit of solid state iron in the hcp (hexagonal close-packed) structure is provided by Bouchet et al. (2013). An adiabatic temperature profile is assumed for both mantle and core. Figure 6.7 shows the mass fraction of each of the key elements used in the interior model as a function of formation temperature for a specified formation time (Myrs) and feeding zone size (5 Hill radii for planet b). For temperatures below $\sim$1,200 K the majority of all rock forming species are fully condensed out of the disc and therefore any changes in bulk density between planets composed of material which formed below this temperature are negligible. At higher formation temperatures (>1,200 K), planets become very rich in Ca and Al and depleted in Fe.

The calculated compositions of Fe, Si, Mg, Al, Ca, and Na are then used to compute the mineralogy and the corresponding bulk density for the given planet masses M_c = 4.36$M_\oplus$ and M_b = 4.74$M_\oplus$. For rock compositions where the sum of calcium and aluminium oxides exceed $\sim$80 wt%, no stable solutions for the mineralogy can be found, on Figure 6.7 this is represented by a composition outside of the dashed line.
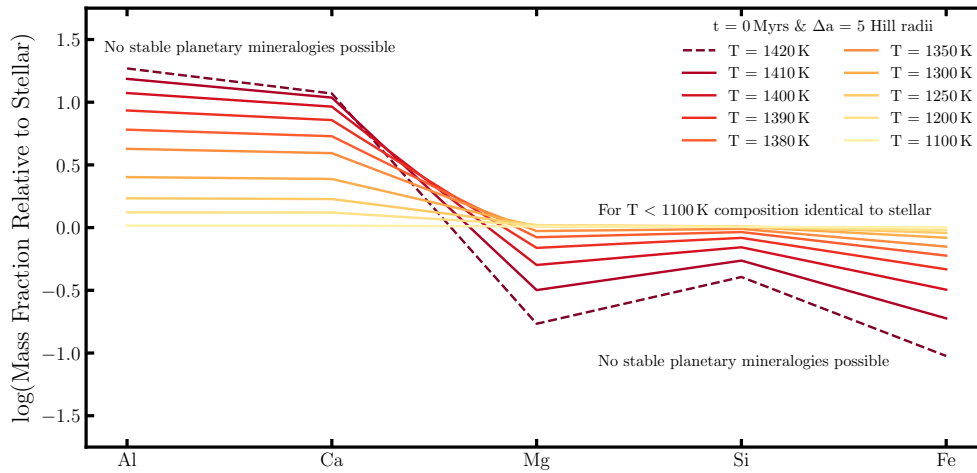
Fig. 6.7 The mass fraction of a planet as a function of formation temperature for a formation time of 0 Myrs and a feeding zone size of 5 Hill radii. No stable mineralogies are possible for compositions outside of the dashed line (1,420 K at formation time equals 0 Myrs).

6.4 Explaining the compostional difference between HD 219134b and HD 219134c

6.4.1 The accretion of high temperature condensates during the formation of planet b

Figure 6.8 demonstrates, that compositions dominated by Mg, Si, and Fe corresponding to $T_{cond} < 1,200$K explain bulk densities that fit planet c's bulk density $\rho_c = 1.26 \pm 0.14 \, \rho_\oplus$. The low density of planet b ($\rho_b = 1.15 \pm 0.13 \, \rho_\oplus$) could be explained with condensates formed at high temperatures, being rich in Ca and Al and depleted in Fe. In that case, planet b has no core. Thus, the density difference can be related to a difference in rock composition, due to a difference in formation temperature, of the solids out of which planets b and c are built, and hence a difference in their formation location at given times. Density differences of up to ~15% can be produced by the accretion of high temperature condensates in the most extreme cases.

Dorn et al. (2018) showed that it is difficult to switch the positions of the two planets relative to the host star, therefore, they most likely formed in their present order and then migrated together into the inner disc. Dorn et al. (2018) also showed
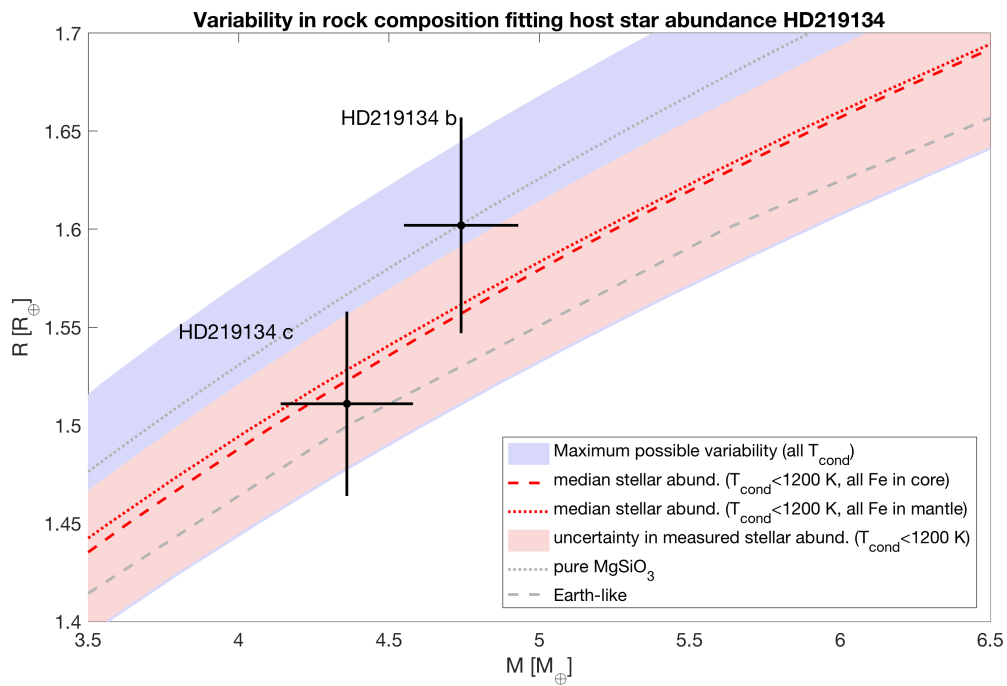
Fig. 6.8 A plot taken from Dorn et al. (2018) showing the mass and radius of HD 219134 b and c compared to various modelled interiors. The variability of purely rocky planets forming at different times and locations within the disc is highlighted by the blue area. Purely rocky interiors that are built from temperate condensates ($T_{\mathrm{cond}} < 1,200\mathrm{K}$) lie within the red area, which respects the uncertainty in measured stellar abundances. Interiors that fit the median stellar abundance follow the red curves. The difference between the dashed and dotted red curves is due to the degeneracy between iron-free mantles with pure iron cores and core-free interiors with all iron in the mantle, respectively.

that migration models which place the planets in their final locations are compatible with initial differences in formation location which produce the required compositional differences such that planet b may be formed from high temperature condensates while planet c is built from condensates below 1200 K. The two planets were also shown not to trap in resonance if subjected to such migration.

In the following subsection I outline the possibility that the compositional difference between planets b and c arose due to effects other than that of high temperature condensates. It is important to note that to within the 1σ level both planets are consistent with no compositional difference, however for this work I shall assume that the interior difference is real.

6.4.2   A higher volatile fraction for planet b

In this section I discuss whether the density difference between HD 219134b and HD 219134c can be explained solely by the planets having different volatile layer fractions while neglecting any differences in rock composition due to high temperature condensates as discussed in the previous section.

There are three main types of volatile layers which could decrease the density of HD 219134b: the presence of a primordial atmosphere, the presence of an outgassed atmosphere, and the presence of water-rich layers in the planets interior.

A primordial atmosphere on planet b

H-dominated primordial atmospheres for both planets have been excluded by Dorn and Heng (2018). This is because evaporative loss due to radiation from the host star efficiently erodes either planet's atmosphere on a short timescale. The timescales required to erode H-rich atmospheres which can produce the observed density difference would be lost on roughly 10 Myr timescales implying that the atmospheres must be of higher mean-molecular weight. Dorn et al. (2018) investigated whether primordial atmospheres composed of H_2, He, H_2O, and CO_2 could reproduce the observations while surviving against atmospheric loss for at least 100 Myrs. Dorn et al. (2018) found that a primordial H-atmosphere was excluded while a helium-atmosphere was also shown to be unlikely for planet b which agreed with results previously published in Dorn and Heng (2018). Atmospheres composed of H_2O or CO_2 could in principle explain the observations, however, in the next section I outline whether a planet similar to HD 219134b could ever form such an atmosphere.

A high mean-molecular weight atmosphere on planet b

Outgassed higher mean molecular weight atmospheres composed of H_2O or CO_2 can originate from two main mechanisms. The outgassing of material early in the planet's history during a magma ocean stage or outgassing of material later during the solid state evolution of the planet.

Atmospheres which are outgassed during the solid state evolution of the planet are continuously replenished over geological timescales. The rate of outgassing depends on many parameters, however, planet mass, planet age, thermal state, and convection regime dominate. The thermal state and convective regime are difficult parameters to constrain observationally. However, planets which are older and more massive than Earth are expected to experience less outgassing than Earth-like planets (Valencia et al. (2007); Van Heck and Tackley (2011); Tackley et al. (2013); Noack and Breuer (2014)). Dorn et al. (2018) estimated that the maximum outgassing rate for planets similar to HD 219134b and HD 219134c is a factor of a few lower than the estimates of evaporative loss rates for the planets (Kite et al. (2009)). The uncertainties on both loss and outgassing rates are significant, however, volcanic replenishment of the planet b's atmosphere seems unrealistic given its continuous erosion by stellar irradiation.

Dorn et al. (2018) also calculated an estimate for the maximum mass of a primordial atmosphere outgassed during the magma ocean stage. A back of the envelope estimate showed that even if the amount of gas lost during the magma ocean stage was maximised while minimising the expected atmospheric loss from stellar irradiation, HD 219134 would not be able to have retained a significant high mean-molecular weight primary atmosphere.

Additionally, and most importantly, there is no reason to believe that planet b could have either a primordial atmosphere or an outgassed high mean-molecular weight atmosphere, while planet c could not, since both planets are similar in mass. Also planet b is closer to the host star, and it is expected that this has always been the case, therefore, it would lose any atmosphere more quickly than planet c and therefore most likely has a less substantial atmospheric component.

Water-rich layers inside planet b

In principle the low density of planet b could be explained easily by the planet containing a water-rich layer which is roughly a few percent of the planet's mass. However, requiring planet b to contain a significant amount of water ice while planet c contains a negligible amount would only be possible if planet b formed outside of

planet c and both planets exchanged their positions after their formation. As outlined earlier in this section, Dorn et al. (2018) showed that the repositioning of the planets during migration is not likely.

In summary, assuming that the difference in densities between HD 219134b and HD 219134c is real, it is unlikely that it is due to planet b having a massive atmosphere while planet c does not. While high mean-molecular weight atmospheres can explain the densities of planet b (Dorn and Heng (2018); Dorn et al. (2018)), they are unlikely to have survived to the present day, especially only on planet b and not planet c. Planet b is also unlikely to have water-rich layers while planet c does not, as it is not expected that planet b could have accreted more water-rich material than planet c given dynamical evolution models predict that planet b has always resided interior to planet c (Dorn et al. (2018)). The accretion of a substantial amount of planetesimals which condensed out of the protoplanetary disc at sufficiently high temperatures such that they were enhanced in the refractory elements and depleted in Fe have been shown to produce less dense planets (Dorn et al. (2018)). In the context of HD 219134b and HD 219134c this explanation is feasible as planet b resides interior to planet c and is the less dense. Additionally migration from distances of the order 1 AU to the current locations of the planets were shown to be consistent both dynamically and compositionally. The major caveat to this model is whether there is enough mass in the inner regions of the disc to form the majority of a $\sim 5 M_{\oplus}$ planet, this assumption, along with the other model assumptions and the implications of the results outlined in this chapter, will be discussed in the next section.

6.5   Discussion

The primary aim of the work was to model whether the formation temperature of the planetesimals which aggregate to form a planet affect the bulk mass radius relation of the planet eventually formed. The secondary aim was to probe whether such planets could offer an explanation to the density difference between two super-Earth planets which reside in the K dwarf system HD 219134. Modelling planetesimal formation using a simple protoplanetary disc and chemical equilibrium model suggested that it is possible to form refractory-rich material, and when combined with an exo-planetary interior model stable minerologies were found which had densities of up to $\sim 15\%$ less than that of a planet with an Earth-like composition. This model was then shown to be able explain the mass and radius of HD 219134b with a model in which the planet accreted a substantial amount of its mass from high temperature condensates

enhanced in Al and Ca and depleted in Fe, while, as expected, the mass and radius of HD 219134c could be explained by the planet having a purely rocky composition whose formation only required the aggregation of condensates which formed at below 1,200 K with their full stellar complement of rock forming elements. Other potential explanations for the low density of HD 219134b were shown to be less likely than the accretion of high temperature condensates, however, there are many caveats to the modeling and, therefore, there are caveats to exactly what can be drawn from these results. In the next section I discuss the major caveats which could potentially alter the conclusions, before then discussing the major consequences of this research.

6.5.1   Discussion of caveats

The major caveats of the modelling done in the chapter involve the assumptions and set-up of the disc model, chemistry model. I assume that the composition of the planetesimals, which go on to form the planets, are dictated when they condense out of a protoplanetary disc in chemical equilibrium. While such an assumption is simplistic it should not affect the conclusions of this work as equilibrium condensation is clearly a key process in determining the bulk composition of rocky worlds as such a model has been shown to reproduce the major elemental abundances of the rocky bodies in the Solar System (Moriarty et al. (2014); Chapter 2). The use of the simplistic disc model is not expected to dramatically effect the results of this work as it is effectively only used to convert protoplanetary disc formation times and distances into temperatures and pressures. Therefore, while the planetary formation locations required to generate high temperature condensates may be uncertain the temperatures required remain robust.

The assumption that could affect the conclusions arrived at in this chapter the most is the assumption that there is enough mass in the inner disc to form a $\sim 5 \mathrm{M_\oplus}$ super-Earth. No N-bodys simulations were computed in order to robustly predict the amount of mass available to form a planet. The disc model used predicts that the available mass in solids between 0.8 and 1.2 AU at 0 Myr is $\sim 0.5 \mathrm{M_\oplus}$. In order to form a planet on the order of $5 \mathrm{M_\oplus}$, the disc properties would have to be adjusted. The disc would either need to be more massive ($M_0 = 0.5 M_*$ instead of $M_0 = 0.1 M_*$) or the surface density gradient would need to be steeper ($\Sigma(r, t) \propto (r/s_0)^{-\frac{37}{19}}$ instead of $\Sigma(r, t) \propto (r/s_0)^{-\frac{24}{19}}$). Such changes to the disc model may not be unrealistic, as the exact initial parameters expected in protoplanetary discs is not well understood, and the influence of the presence of the outer more massive planets and radial drift of planetesimals from outer disc regions may allow the mass available in planetesimals in

the innermost disc region to increase in a non-negligible fashion. However, any future work on the formation of such refractory dominated planets will need to address the issue of creating bodies with enough mass in a robust manner.

6.5.2   Discussion of results

In this work I have shown that, by combining multiple simple models, it is theoretically possible for planets to form from high temperature condensates. Crucially, such planets occupy a significantly different position in mass-radius space. In order to investigate whether these planets exist in reality I discussed the case of HD 219134 and argued that the density difference between HD 219134b and HD 219134c is likely due to a difference in rock composition instead of a difference in volatile layer thickness. While planet c can be explained by a composition dominated by silicates and iron, planet b can be explained by a composition dominated by a Ca and Al with no Fe core. This drastic difference in rock composition has implications on their possible interior dynamics, magnetic fields, and atmospheric properties. Magnetic fields which are generated by convective Fe, as with the Earth, cannot exist for planet b. If interactions between the magnetic fields of a host star and its planet become detectable (Saur et al. (2013)), HD 219134 would become an interesting target to investigate as the signatures for planet b and c could significantly differ if the refractory-enhanced planet model is true. Similarly, HD 219134 has characteristics which suggest the properties of the atmospheres of its planets should be observable and Gillon et al. (2017) suggested the system was a viable target for transit transmission spectroscopy with the Hubble Space Telescope (HST) or occultation emission spectroscopy with the James Webb Space Telescope (JWST). If the atmospheric properties of HD 219134b and HD 219134c are observed it would be insightful as it would allow the hypothesis that planet b's low density is due to a thick atmosphere to be either confirmed or ruled out. Additionally, if planet b is composed of refractory rich material it could have an unusual atmospheric composition, as atmospheres outgassed from a planet with such an interior would likely not resemble a terrestrial atmosphere. This could potentially offer a useful method to identify other rocky worlds with exotic compositions without the need for high precision mass measurements and intra-system comparable planets.

Further observations of HD 219134 will allow improvements on the precision on planet radii and masses. Dorn et al. (2018) showed that if 50 further transits were observed for both planets and 2000 new RV measurements the uncertainty in the density ratio would become of the order 6%. Such an improved uncertainty would allow the scenario in which both planets are scaled-up analogues with no considerable

difference in their bulk densities to be ruled out. These observations could therefore reinforce the possibility that a new sub classification of super-Earths, ones which are formed from high-temperature condensates, exist.

6.6 Conclusions

In this chapter I demonstrated that if one assumes that rocky planets are built up of planetesimals which condensate out of cooling protoplanetary discs it is potentially possible for close-in planets to form which are enhanced in the refractory elements (Al, Ca etc.) and depleted in the moderately volatile elements (Mg, Si, Fe etc.). These refractory dominated planets are composed of material which formed at high temperatures such that most of the traditional rock-forming species were vaporised and thus, they are products of incomplete condensation. The compositional differences of such planets could cause them to have a bulk density up to 15% lower than that of a planet composed of Earth-like material. Therefore, such planets offer a potential explanation for close-in rocky worlds with unexpectedly low densities. If such planets exist their interior dynamics, outgassing histories, atmosphere evolution, and magnetic fields may be fundamentally different than what we know from rocky Solar System planets. Identifying Ca and Al-rich planets is impossible from bulk density alone as low density planets could easily be explained by having volatile-rich layers either as an atmosphere or inside the interior. Therefore, such volatile-rich models must be ruled out in order to suggest that a planet is a potential refractory-rich candidate. The HD 219134 system hosts a potential candidate for such a refractory dominated planet, a close-in super-Earth HD 219134b. The existence of a twin planet, HD 219134c, with a similar mass but higher bulk density (consistent with that of regular rocky material) exterior to the planet suggests that volatile-rich explanations are unlikely. A relatively simple migration model predicts that it is difficult for the positions on the planets to switch and that the current locations of the planets are compatible with migration from the locations expected to form high temperature condensates early in the planetary system. The uncertainties on the masses of the planets in the HD 219134 system are still such that it is possible that both planets do not in fact have a density difference to a 1σ significance. However, the expected uncertainties provided by PLATO should allow the mass estimates to be refined such that it will potentially be possible to rule out a scenario in which both planets have a similar density. PLATO will also provide mass estimates for other planetary systems and therefore could potentially find evidence for more exotic worlds which have formed from high temperature condensates.

Chapter 7

Conclusions and Future Work

7.1 Conclusions

The realisation that many white dwarfs accrete exo-planetary material has given astronomers a unique insight into the composition of exo-planetary bodies. In this thesis I have created a model which can reproduce the atmospheric abundances present in polluted white dwarfs. The model constrains the most likely origin of the polluting material by considering the heating, geochemical differentiation, and collisional processes experienced by the planetary body accreted, as well as the gravitational sinking of planetary material through the white dwarf atmosphere. The constraints generated by the model allow the formational and geological processes which occur in exo-planetary systems to be investigated. Knowledge of the geology and bulk composition of exo-planetary bodies will be crucial if one wishes to understand the nature of the rocky exoplanets which will be discovered in the coming years, as measurements of the masses and radii of the worlds will be degenerate for a variety of internal compositions. Once telescopes have the capacity to determine the atmospheric composition of rocky exoplanets, a planet's habitability will potentially be constrainable; however, a detailed understanding of the planets interior and geological history will be crucial in generating such constraints.

In Chapter 2, I outlined the model I created and subsequently validated it by showing how it could reproduce the major elemental abundances present in the rocky material in the Solar System. In Chapter 3, I presented how the model could reproduce the atmospheric abundances present in 24 of the most heavily polluted white dwarfs, while in Chapter 4 I used the model to fit the abundances derived by Hollands et al. (2017) for 208 polluted white dwarfs. I found, as is the case in the Solar System, that the refractory abundances of the majority of white dwarf pollutants match those expected

for their main-sequence host stars. Therefore, my findings validate the hypothesis that planetary abundances can be inferred by measuring host star abundances, as is frequently done when using mass-radius measurements to probe exoplanet interior compositions (e.g. Dorn et al. (2017)). However, not all exo-planetary bodies were found to be primitive; strong evidence for the accretion of core-rich, mantle-rich, crust-rich, or crust-stripped material was found in at least 17 systems. Therefore, my analysis also supports the idea that differentiation and collisions are common processes in exo-planetary systems. Crucially, thus far the abundances observed in all systems suggest that differentiation processes and geological processes occur in a similar fashion in exo-planetary systems as they do in the Solar System. White dwarfs which have accreted fragments of differentiated bodies also provide evidence that it is unlikely that multiple bodies dominate the material accreted in most systems, as if multiple bodies accreted simultaneously, such signatures would not be so frequently present.

The Na abundances of pollutants in the Hollands et al. (2017) catalogue and the pollutants outlined in Chapter 3 provide evidence for a spread in white dwarf pollutant formation temperatures. 49 systems have stellar level Na abundances, and therefore require formation temperatures below 1,000 K similar to the Solar System chondritic meteorites, while 15 systems have depleted Na abundances and therefore require formation temperatures of ∼1,100 K, like bulk Earth. 29 systems were found to require formation temperatures of ∼1,400 K and while such refractory dominated bodies are not found in the Solar System, they are potentially not unexpected in white dwarf systems, as the progenitors of white dwarfs were earlier types, and thus produce hotter inner disc conditions for longer and over a wider range of radii. The O abundances of the pollutants discussed in Chapter 3 further support a spread in pollutant formation temperatures. The majority of pollutants have O abundances consistent with that expected if no water ice was present in the planetary bodies accreted and therefore formed at temperatures greater than ∼200 K. However, at least 3 systems were found to require pollutants which are partially composed of water ice to a statistical significance of greater than 2σ. These results confirm the conclusions drawn in previous studies and suggest that water ice can be sequestered in planetary bodies in exo-planetary systems. The accretion of water ice is not unexpected, as it is thought that water ice present in a planetary body can avoid sublimation until it is accreted onto the white dwarf (Jura and Xu (2010a); Malamud and Perets (2016)). The analysis performed in this thesis finds that white dwarf pollutants have formation temperatures ranging from 40 K to 1,400 K suggesting that scattering of planetary bodies into a white dwarf's tidal radius is possibly equally efficient across a wide range semi-major axes.

The atmospheric abundances present in at least 4 white dwarf systems suggest that the material accreting onto the stars has reached the steady state phase. As the steady state phase is not expected to be reached if white dwarf atmospheres are susceptible to thermohaline instabilities, these systems provide evidence that the conditions present in some H dominated and He dominated white dwarf atmospheres do not allow such instabilities to develop, in concurrence with Koester (2014). 5 systems were constrained to be in the declining phase, thus, the total mass accreted during the accretion event could be determined. The masses found for such systems range from bodies as massive as 31% that of Pluto down to 3% that of Vesta, further supporting the hypothesis that the white dwarf pollutants currently observed are large asteroids or minor planets. The size of the Hollands et al. (2017) sample allowed the model to constrain the average polluted white dwarf accretion event lifetime. The accretion event lifetimes were constrained to be of the order of a few Myrs, reinforcing the conclusions derived in Chapter 3 from the systems constrained to be in the steady state phase and in Girven et al. (2012).

The model outlined in Chapter 2, and used in Chapters 3 and 4, assumed that only condensation volatilisation processes were important in determining the composition of a planetary body. However, post-nebula volatilisation processes are known to have occurred in some Solar System bodies (Chapter 1). Although both processes effect most elements in a similar manner, the Mn/Na ratio of a body is sensitive to the volatilisation process. In Chapter 5, I investigated the importance of post-nebula volatilisation in determining a planetary body's bulk composition, and whether there is evidence for post-nebula volatilisation occurring in white dwarf planetary systems. I analysed how incomplete nebula condensation and volatile loss after the dissipation of the nebula produce observable differences in a planetary body's Mn/Na ratio. I showed that for the majority of polluted white dwarf systems with observed Mn and Na abundances, the Mn/Na ratios are consistent with condensation-based volatilisation. However, for one system, GD362, the Mn/Na ratio of the polluting material cannot be explained by condensation volatilisation processes ($>3\sigma$), and instead requires post-nebula volatilisation. I additionally showed how heating during the giant branches cannot significantly alter the Mn/Na ratio of a body, and therefore the pollutant of GD362 likely underwent ancient post-nebula volatile loss due to impact heating in a similar manner to some of the small rocky bodies in the Solar System. The ability to explore such processes beyond the Solar System not only improves our understanding of the Solar System but probes how universal such processes are.

The discovery of refractory-rich material in the atmospheres of polluted white dwarfs in Chapter 3 and Chapter 4 suggests that potentially substantial planetary bodies can form from high temperature condensates. In Chapter 6, I investigated whether a planet made of such material would be observably different from a planet made of traditional rocky material, and whether there was any evidence for such planets currently. I demonstrated that the radius of an exoplanet of a given mass is somewhat dependent on the temperature at which its composite planetesimals formed. If a significant fraction of the mass of an exoplanet is in the form of high temperature condensates, which are enhanced in the refractory elements (Al, Ca etc.) and depleted in the moderate-volatile elements (Mg, Si, Fe etc.), its bulk density can be up to 15% lower than that of a planet composed of Earth-like material. Such planetary compositions could be probed by PLATO and offer a potential explanation for any close-in rocky worlds discovered with unexpectedly low densities. The HD219134 system hosts a potential candidate for such a refractory dominated planet, a close-in super-Earth HD219134b. The existence of an exterior twin planet, HD219134c, with a similar mass but higher bulk density, consistent with that of regular rocky material, suggests that volatile-rich explanations are unlikely.

7.2   Future work

While my research has furthered the understanding of white dwarf planetary systems and the geological processes which take place in exo-planetary systems there is still much to be gained from both observational and theoretical research.

There are currently only ∼250 externally polluted white dwarfs with multiple metal abundances derived from their spectra. While such a population has offered great insights into white dwarf planetary systems, as discussed in this thesis, a larger sample would test the model further and probe for potential evidence of non-Solar-System-like geologies. In the coming years, Gaia is expected to confirm the discovery of over 200,000 white dwarfs (Gentile Fusillo et al. (2019)) and potential follow up optical spectroscopy with X-Shooter, WEAVE, DESI, SDSS-V, and 4MOST will allow those which are polluted to be identified and the pollutant abundances to be constrained. Such a sample would also allow the frequency of various pollutant origins to be better understood. With a sample of thousands of polluted white dwarfs, many more will be in the correct temperature range for the simultaneous detection of Na and Mn; this would allow the frequency of systems which have undergone post-nebula volatilisation to be found.

Potential improvements to the main model outlined in this thesis would be to include elements such as P, S, and Mn in the model fitting process. This is not trivial; firstly, there is currently no stellar sample with all of the required elements and sufficiently low uncertainties, and secondly, the HSC chemistry model would need to be adjusted from the Bond et al. (2010) prescription, which would require a detailed analysis of all the relevant species to include for each new element. Another useful addition, as mentioned throughout this thesis, would be the inclusion of a fully self consistent differentiation model, which formulates the core abundances of the parent body as functions of the thermodynamic conditions at the core-mantle boundary during differentiation. This inclusion could validate some of the results presented in this thesis, and allow constraints to be placed on the mass of the parent bodies of white dwarf pollutants.

Two key unsolved issues in the field of white dwarf atmospheric abundances are the frequency of core-rich moderate-volatile depleted pollutants and the two Na dominated systems published in Swan et al. (2019). Both peculiarities could potentially be resolved if accretion from the disc during the white dwarf stage preferentially accretes the upper layers and most volatile layers of a body initially, followed by the refractory layers and inner layers of a body subsequently. The initial phase would produce Na dominated atmospheres, while the second phase would produce core-rich moderate-volatile depleted atmospheres. This hypothesis needs further testing, as the timescales on which disruption and sublimation take place have to be reconciled with the white dwarf sinking timescales to allow such distinct phases to be observable in some but not all polluted white dwarf systems.

References

Adams, F. C. and Bloch, A. M. (2013). Evolution of planetary orbits with stellar mass loss and tidal dissipation. *The Astrophysical Journal Letters*, 777:L30.

Adams, W. S. (1914). An A-Type Star of Very Low Luminosity. *Publications of the Astronomical Society of the Pacific*, 26(155):198.

Adams, W. S. (1915). The spectrum of the companion of sirius. *Publications of the Astronomical Society of the Pacific*, 27:236.

Alessi, M., Pudritz, R. E., and Cridland, A. J. (2016). On the formation and chemical composition of super earths. *Monthly Notices of the Royal Astronomical Society*, 464(1):428–452.

Alexander, R. D., Clarke, C. J., and Pringle, J. E. (2006a). Photoevaporation of protoplanetary discs – i. hydrodynamic models. *Monthly Notices of the Royal Astronomical Society*, 369(1):216–228.

Alexander, R. D., Clarke, C. J., and Pringle, J. E. (2006b). Photoevaporation of protoplanetary discs – ii. evolutionary models and observable properties. *Monthly Notices of the Royal Astronomical Society*, 369(1):229–239.

Althaus, L. G., Córsico, A. H., Isern, J., and García-Berro, E. (2010). Evolutionary and pulsational properties of white dwarf stars. *The Astronomy and Astrophysics Review*, 18(4):471–566.

Althaus, L. G., De Gerónimo, F., Córsico, A., Torres, S., and García-Berro, E. (2017). The evolution of white dwarfs resulting from helium-enhanced, low-metallicity progenitor stars. *Astronomy and Astrophysics*, 597:A67.

Anders, E. (1964). Origin, age, and composition of meteorites. *Space Science Reviews*, 3(5-6):583–714.

Anderson, O. and Isaak, D. (2002). Another look at the core density deficit of earth's outer core. *Physics of the Earth and Planetary Interiors*, 131(1):19 – 27.

Andrae, R., Schulze-Hartung, T., and Melchior, P. (2010). Dos and don'ts of reduced chi-squared. *arXiv e-prints*, page arXiv:1012.3754.

Andrews, S. M. (2020). Observations of protoplanetary disk structures.

Andrews, S. M., Rosenfeld, K. A., Kraus, A. L., and Wilner, D. J. (2013). The Mass Dependence between Protoplanetary Disks and their Stellar Hosts. *The Astrophysical Journal*, 771:129.

Asphaug, E. and Reufer, A. (2014). Mercury and other iron-rich planetary bodies as relics of inefficient accretion. *Nature Geoscience*, 7(8):564–568.

Basilevsky, A. T. and Head, J. W. (2003). The surface of venus. *Reports on Progress in Physics*, 66(10):1699–1734.

Bauer, E. B. and Bildsten, L. (2018). Increases to inferred rates of planetesimal accretion due to thermohaline mixing in metal-accreting white dwarfs. *The Astrophysical Journal*, 859(2):L19.

Benneke, B. and Seager, S. (2013). How to Distinguish between Cloudy Mini-Neptunes and Water/Volatile-dominated Super-Earths. *The Astrophysical Journal*, 778(2):153.

Benz, W., Slattery, W. L., and Cameron, A. (1988). Collisional stripping of mercury's mantle. *Icarus*, 74(3):516 – 528.

Bhatia, G. K. and Sahijpal, S. (2017). Did 26al and impact-induced heating differentiate mercury? *Meteoritics and Planetary Science*, 52(2):295–319.

Birch, F. (1964). Density and composition of mantle and core. *Journal of Geophysical Research*, 69(20):4377–4388.

Blum, J. R. (2018). Dust evolution in protoplanetary discs and the formation of planetesimals. *Space Science Reviews*, 214:1–19.

Boehler, R. (2000). High-pressure experiments and the phase diagram of lower mantle and core materials. *Reviews of Geophysics*, 38(2):221–245.

Boltzmann, L. (1884). Ableitung des Stefan'schen Gesetzes, betreffend die Abhängigkeit der Wärmestrahlung von der Temperatur aus der electromagnetischen Lichttheorie. *Annalen der Physik*, 258(6):291–294.

Bond, G. (1862). On the Companion of Sirius, by Prof. G. Bond, Director of the Observatory of Harvard College. *Astronomische Nachrichten*, 57:131.

Bond, H. E., Bergeron, P., and Bédard, A. (2017). Astrophysical Implications of a New Dynamical Mass for the Nearby White Dwarf 40 Eridani B. *The Astrophysical Journal*, 848(1):16.

Bond, J. C., Lauretta, D. S., and O'Brien, D. P. (2010). Making the Earth: Combining dynamics and chemistry in the Solar System. *Icarus*, 205:321–337.

Bonsor, A., Carter, P. J., Hollands, M., Gänsicke, B. T., Leinhardt, Z., and Harrison, J. H. D. (2020). Are exoplanetesimals differentiated? *Monthly Notices of the Royal Astronomical Society*, 492(2):2683–2697.

Bonsor, A., Farihi, J., Wyatt, M. C., and van Lieshout, R. (2017). Infrared observations of white dwarfs and the implications for the accretion of dusty planetary material. *The Monthley Notices of the Royal Astronomical Society*, 468:154–164.

Bonsor, A., Mustill, A. J., and Wyatt, M. C. (2011). Dynamical effects of stellar mass-loss on a kuiper-like belt. *The Monthly Notices of the Royal Astronomical Society*, 414:930–939.

Bonsor, A. and Veras, D. (2015). A wide binary trigger for white dwarf pollution. *The Monthly Notices of the Royal Astronomical Society*, 454:53–63.

Bottke, Jr., W. F., Vokrouhlický, D., Rubincam, D. P., and Nesvorný, D. (2006). The yarkovsky and yorp effects: Implications for asteroid dynamics. *Annual Review of Earth and Planetary Sciences*, 34:157–191.

Bouchet, J., Mazevet, S., Morard, G., Guyot, F., and Musella, R. (2013). Ab initio equation of state of iron up to 1500 gpa. *Physical Review B*, 87(9):094102.

Bouhifd, M. and Jephcoat, A. (2011). Convergence of ni and co metal–silicate partition coefficients in the deep magma-ocean and coupled silicon–oxygen solubility in iron melts at high pressures. *Earth and Planetary Science Letters*, 307(3):341 – 348.

Bouvier, A. and Wadhwa, M. (2010). The age of the solar system redefined by the oldest pb-b age of a meteoritic inclusion. *Nature Geoscience*, 3(9):637–641.

Brückner, J., Dreibus, G., Gellert, R., Squyres, S., Wänke, H., Yen, A., and Zipfel, J. (2008). Mars exploration rovers - chemical composition by apxs. *The Martian Surface: Composition, Mineralogy, and Physical Properties*, pages 58–101.

Brennecka, G. A., Borg, L. E., and Wadhwa, M. (2013). Evidence for supernova injection into the solar nebula and the decoupling of r-process nucleosynthesis. *Proceedings of the National Academy of Sciences*, 110(43):17241–17246.

Brewer, J. M., Fischer, D. A., Valenti, J. A., and Piskunov, N. (2016). Spectral Properties of Cool Stars: Extended Abundance Analysis of 1,617 Planet-search Stars. *The Astrophysical Journal Supplement Series*, 225:32.

Bromley, B. C. and Kenyon, S. J. (2019). Ohmic Heating of Asteroids around Magnetic Stars. *The Astrophysical Journal*, 876(1):17.

Buchner, J., Georgakakis, A., Nandra, K., Hsu, L., Rangel, C., Brightman, M., Merloni, A., Salvato, M., Donley, J., and Kocevski, D. (2014). X-ray spectral modelling of the AGN obscuring region in the CDFS: Bayesian model selection and catalogue. *Astronomy and Astrophysics*, 564:A125.

Buffett, B. A. (2000). Earths core and the geodynamo. *Science*, 288(5473):2007–2012.

Campbell, I. H. and O'Neill, H. S. (2012). Evidence against a chondritic Earth. *Nature*, 483:553–558.

Carter, P. J., Leinhardt, Z. M., Elliott, T., Stewart, S. T., and Walter, M. J. (2018). Collisional stripping of planetary crusts. *Earth and Planetary Science Letters*, 484:276–286.

Carter, P. J., Leinhardt, Z. M., Elliott, T., Walter, M. J., and Stewart, S. T. (2015). Compositional Evolution during Rocky Protoplanet Accretion. *The Astrophysical Journal*, 813:72.

Chambers, J. E. (2004). Planetary accretion in the inner solar system. *Earth and Planetary Science Letters*, 223(3–4):241 – 252.

Chambers, J. E. (2009). An analytic model for the evolution of a viscous, irradiated disk. *The Astrophysical Journal*, 705(2):1206.

Chandrasekhar, S. (1935a). Stellar configurations with degenerate cores. *The Monthley Notices of the Royal Astronomical Society*, 95:226–260.

Chandrasekhar, S. (1935b). The highly collapsed configurations of a stellar mass (Second paper). *The Monthley Notices of the Royal Astronomical Society*, 95:207–225.

Chayer, P. (2013). Radiative levitation of silicon in the atmospheres of two Hyades DA white dwarfs. *Monthly Notices of the Royal Astronomical Society: Letters*, 437(1):L95–L99.

Chayer, P. and Dupuis, J. (2010). Effect of radiative levitation on calculations of accretion rates in white dwarfs. *American Institute of Physics Conference Series*, 1273:394–399.

Clenet, H., Jutzi, M., Barrat, J.-A., Asphaug, E. I., Benz, W., and Gillet, P. (2014). A deep crust-mantle boundary in the asteroid 4 Vesta. *Nature*, 511:303–306.

Connolly, J. (2005). Computation of phase equilibria by linear programming: a tool for geodynamic modeling and its application to subduction zone decarbonation. *Earth and Planetary Science Letters*, 236(1):524–541.

Coutu, S., Dufour, P., Bergeron, P., Blouin, S., Loranger, E., Allard, N. F., and Dunlap, B. H. (2019). Analysis of Helium-Rich White Dwarfs Polluted by Heavy Elements in the Gaia Era. *arXiv e-prints*, page arXiv:1907.05932.

Da Silva, R., Milone, A. d. C., and Rocha-Pinto, H. J. (2015). Homogeneous abundance analysis of fgk dwarf, subgiant, and giant stars with and without giant planets. *Astronomy and Astrophysics*, 580:A24.

Dauphas, N., Burkhardt, C., Warren, P., and Teng, F.-Z. (2014). Geochemical arguments for an Earth-like Moon-forming impactor. *Philosophical Transactions of the Royal Society of London Series A*, 372:2013.0244.

Day, J. M. D. and Moynier, F. (2014). Evaporative fractionation of volatile stable isotopes and their bearing on the origin of the Moon. *Philosophical Transactions of the Royal Society of London Series A*, 372(2024):20130259–20130259.

Deal, M., Vauclair, S., and Vauclair, G. (2012). Thermohaline instabilities induced by heavy element accretion onto white dwarfs: Consequences on the derived accretion rates.

Debes, J. H. and Sigurdsson, S. (2002). Are there unstable planetary systems around white dwarfs? *The Astrophysical Journal*, 572:556–565.

Debes, J. H., Walsh, K. J., and Stark, C. (2012). The link between planetary systems, dusty white dwarfs, and metal-polluted white dwarfs. *The Astrophysical Journal*, 747:148.

Desch, S. J., Estrada, P. R., Kalyaan, A., and Cuzzi, J. N. (2017a). Formulas for Radial Transport in Protoplanetary Disks. *The Astrophysical Journal*, 840:86.

Desch, S. J., Kalyaan, A., and Alexander, C. M. O. (2017b). The Effect of Jupiter's Formation on the Distribution of Refractory Elements and Inclusions in Meteorites. *ArXiv e-prints*.

Deutsch, A. J. (1956). The Dead Stars of Population I. *Publications of the Astronomical Society of the Pacific*, 68(403):308.

Dirac, P. A. M. and Fowler, R. H. (1926). On the theory of quantum mechanics. *Proceedings of the Royal Society of London. Series A, Containing Papers of a Mathematical and Physical Character*, 112(762):661–677.

Dorn, C., Harrison, J. H. D., Bonsor, A., and Hands, T. O. (2018). A new class of super-earths formed from high-temperature condensates: Hd219134 b, 55 cnc e, wasp-47 e. *Monthly Notices of the Royal Astronomical Society*, 484(1):712–727.

Dorn, C. and Heng, K. (2018). Secondary atmospheres on hd 219134 b and c. *The Astrophysical Journal*, 853(1):64.

Dorn, C., Khan, A., Heng, K., Connolly, J. A. D., Alibert, Y., Benz, W., and Tackley, P. (2015). Can we constrain the interior structure of rocky exoplanets from mass and radius measurements? *Astronomy and Astrophysics*, 577:A83.

Dorn, C., Venturini, J., Khan, A., Heng, K., Alibert, Y., Helled, R., Rivoldini, A., and Benz, W. (2017). A generalized bayesian inference method for constraining the interiors of super earths and sub-neptunes. *Astronomy and Astrophysics*, 597:A37.

Dreibus, G. and Wanke, H. (1985). Mars, a Volatile-Rich Planet. *Meteoritics*, 20(2):367.

Dufour, P., Fontaine, G., Liebert, J., Schmidt, G. D., and Behara, N. (2008). Hot dq white dwarfs: Something different. *The Astrophysical Journal*, 683(2):978–989.

Dufour, P., Kilic, M., Fontaine, G., Bergeron, P., Melis, C., and Bochanski, J. (2012). Detailed compositional analysis of the heavily polluted dbz white dwarf sdss j073842.56+183509.06: A window on planet formation? *The Astrophysical Journal*, 749:6.

Dziewonski, A. M. and Anderson, D. L. (1981). Preliminary reference earth model. *Physics of the Earth and Planetary Interiors*, 25(4):297 – 356.

Eddington, A. S. (1926). *The Internal Constitution of the Stars.*

Embey-Isztin, A. (2007). Basaltic volcanism on the terrestrial planets: a window to planetary interiors. *ACTA GGM DEBRECINA Geology, Geomorphology, Physical Geography Series*, Vol. 2:53–57.

Farihi, J. (2016). Circumstellar debris and pollution at white dwarf stars. *New Astronomy Reviews*, 71:9–34.

Farihi, J., Barstow, M. A., Redfield, S., Dufour, P., and Hambly, N. C. (2010a). Rocky planetesimals as the origin of metals in DZ stars. *The Monthly Notices of the Royal Astronmical Society*, 404:2123–2135.

Farihi, J., Barstow, M. A., Redfield, S., Dufour, P., and Hambly, N. C. (2010b). Rocky planetesimals as the origin of metals in dz stars. *The Monthly Notices of the Royal Astronomical Society*, 404:2123–2135.

Farihi, J., Brinkworth, C. S., Gänsicke, B. T., Marsh, T. R., Girven, J., Hoard, D. W., Klein, B., and Koester, D. (2011). Possible Signs of Water and Differentiation in a Rocky Exoplanetary Body. *The Astrophysical Journal Letters*, 728:L8.

Farihi, J., Gänsicke, B. T., and Koester, D. (2013). Evidence for water in the rocky debris of a disrupted extrasolar minor planet. *Science*, 342:218–220.

Farihi, J., Gänsicke, B. T., Steele, P. R., Girven, J., Burleigh, M. R., Breedt, E., and Koester, D. (2012). A trio of metal-rich dust and gas discs found orbiting candidate white dwarfs with k-band excess. *The Monthly Notices of the Royal Astronomical Society*, 421:1635–1643.

Farihi, J., Jura, M., and Zuckerman, B. (2009). Infrared signatures of disrupted minor planets at white dwarfs. *The Astrophysical Journal*, 694:805–819.

Farihi, J., Koester, D., Zuckerman, B., Vican, L., Gänsicke, B. T., Smith, N., Walth, G., and Breedt, E. (2016). Solar abundances of rock-forming elements, extreme oxygen and hydrogen in a young polluted white dwarf. *The Monthly Notices of the Royal Astronomical Society*, 463:3186–3192.

Farihi, J., Wyatt, M. C., Greaves, J. S., Bonsor, A., Sibthorpe, B., and Panić, O. (2014). Alma and herschel observations of the prototype dusty and polluted white dwarf g29-38. *The Monthly Notices of the Royal Astronomical Society*, 444:1821–1828.

Feltzing, S., Holmberg, J., and Hurley, J. R. (2001). The solar neighbourhood age-metallicity relation - does it exist? *Astronomy and Astrophysics*, 377(3):911–924.

Fermi, E. (1926). Sulla quantizzazione del gas perfetto monoatomico. *Rendiconti dell'Accademia Nazionale dei Lincei*, 3(6):145–149.

Feroz, F. and Hobson, M. P. (2008). Multimodal nested sampling: an efficient and robust alternative to Markov Chain Monte Carlo methods for astronomical data analyses. *The Monthly Notices of the Royal Astronomical Society*, 384(2):449–463.

Feroz, F., Hobson, M. P., and Bridges, M. (2009). MULTINEST: an efficient and robust Bayesian inference tool for cosmology and particle physics. *The Monthly Notices of the Royal Astronomical Society*, 398(4):1601–1614.

Feroz, F., Hobson, M. P., Cameron, E., and Pettitt, A. N. (2013). Importance Nested Sampling and the MultiNest Algorithm. *preprint*, page 28 (arXiv:1306.2144).

Fischer, R. A., Nakajima, Y., Campbell, A. J., Frost, D. J., Harries, D., Langenhorst, F., Miyajima, N., Pollok, K., and Rubie, D. C. (2015). High pressure metal–silicate partitioning of ni, co, v, cr, si, and o. *Geochimica et Cosmochimica Acta*, 167:177 – 194.

Fontaine, G. and Michaud, G. (1979). Diffusion time scales in white dwarfs. *The Astrophysical Journal*, 231:826–840.

Fortin-Archambault, M., Dufour, P., and Xu, S. (2020). Modeling of the Variable Circumstellar Absorption Features of WD 1145+017. *The Astrophysical Journal*, 888(1):47.

Fowler, R. H. (1926). On dense matter. *The Monthly Notices of the Royal Astronomical Society*, 87:114–122.

Gänsicke, B. T. (2011). Gaseous debris disks around white dwarfs. 1331:211–214.

Gänsicke, B. T., Koester, D., Farihi, J., Girven, J., Parsons, S. G., and Breedt, E. (2012). The chemical diversity of exo-terrestrial planetary debris around white dwarfs. *The Monthly Notices of the Royal Astronomical Society*, 424:333–347.

Gänsicke, B. T., Koester, D., Marsh, T. R., Rebassa-Mansergas, A., and Southworth, J. (2008). Sdssj084539.17+225728.0: the first dbz white dwarf with a metal-rich gaseous debris disc. *The Monthly Notices of the Royal Astronomical Society*, 391:L103–L107.

Gänsicke, B. T., Marsh, T. R., and Southworth, J. (2007). Sdssj104341.53+085558.2: a second white dwarf with a gaseous debris disc. *The Monthly Notices of the Royal Astronomical Society*, 380:L35–L39.

Gänsicke, B. T., Marsh, T. R., Southworth, J., and Rebassa-Mansergas, A. (2006). A gaseous metal disk around a white dwarf. *Science*, 314:1908–.

Gansicke, B. T., Schreiber, M. R., Toloza, O., Fusillo, N. P. G., Koester, D., and Manser, C. J. (2019). Accretion of a giant planet onto a white dwarf star. *Nature*, 576(7785):61–64.

Genova, A., Goossens, S., Mazarico, E., Lemoine, F. G., Neumann, G. A., Kuang, W., Sabaka, T. J., Hauck II, S. A., Smith, D. E., Solomon, S. C., and Zuber, M. T. (2019). Geodetic evidence that mercury has a solid inner core. *Geophysical Research Letters*, 46(7):3625–3633.

Gentile Fusillo, N. P., Tremblay, P.-E., Gänsicke, B. T., Manser, C. J., Cunningham, T., Cukanovaite, E., Hollands, M., Marsh, T., Raddi, R., Jordan, S., Toonen, S., Geier, S., Barstow, M., and Cummings, J. D. (2019). A Gaia Data Release 2 catalogue of white dwarfs and a comparison with SDSS. *Monthly Notices of the Royal Astronomical Society*, 482(4):4570–4591.

Ghosh, A., Weidenschilling, S. J., McSween, Jr., H. Y., and Rubin, A. (2006). *Meteorites and the Early Solar System II*, pages 555–566.

Gillon, M., Demory, B.-O., Van Grootel, V., Motalebi, F., Lovis, C., Cameron, A. C., Charbonneau, D., Latham, D., Molinari, E., Pepe, F. A., et al. (2017). Two massive rocky planets transiting a k-dwarf 6.5 parsecs away. *Nature Astronomy*, 1(3):0056.

Girven, J., Brinkworth, C. S., Farihi, J., Gänsicke, B. T., Hoard, D. W., Marsh, T. R., and Koester, D. (2012). Constraints on the lifetimes of disks resulting from tidally destroyed rocky planetary bodies. *The Astrophysical Journal*, 749:154.

Glavin, D. P. and Dworkin, J. P. (2009). Enrichment of the amino acid L-isovaline by aqueous alteration on CI and CM meteorite parent bodies. *Proceedings of the National Academy of Science*, 106:5487–5492.

Goldschmidt, V. M. (1937). The principles of distribution of chemical elements in minerals and rocks. the seventh hugo müller lecture, delivered before the chemical society on march 17th, 1937. *J. Chem. Soc.*, pages 655–673.

Graham, J. R., Matthews, K., Neugebauer, G., and Soifer, B. T. (1990). The infrared excess of g29-38 - a brown dwarf or dust? *The Astrophysical Journal*, 357:216–223.

Guntenburg, B. (1914). Uber Erdbebenwellen. *Nachr. Ges. Wiss. Gottingen Math. Physik*, 166(125):116.

Gurri, P., Veras, D., and Gänsicke, B. T. (2017). Mass and eccentricity constraints on the planetary debris orbiting the white dwarf WD 1145+017. *Monthly Notices of the Royal Astronomical Society*, 464(1):321–328.

Haisch, Karl E., J., Lada, E. A., and Lada, C. J. (2001). Disk Frequencies and Lifetimes in Young Clusters. *The Astrophysical Journal Letters*, 553(2):L153–L156.

Hamada, T. and Salpeter, E. E. (1961). Models for Zero-Temperature Stars. *The Astrophysical Journal*, 134:683.

Hamers, A. S. and Portegies Zwart, S. F. (2016). White dwarf pollution by planets in stellar binaries. *The Monthly Notices of the Royal Astronomical Society*, 462:L84–L87.

Harrison, J. H. D., Bonsor, A., and Madhusudhan, N. (2018). Polluted white dwarfs: constraints on the origin and geology of exoplanetary material. *The Monthly Notices of the Royal Astronomical Society*, 479:3814–3841.

Hartmann, W. K. (2014). The giant impact hypothesis: past, present (and future?). *Philosophical Transactions of the Royal Society A: Mathematical, Physical and Engineering Sciences*, 372(2024):20130249.

Herschel, W. (1785). Catalogue of double stars. by william herschel, esq. f. r. s. *Philosophical Transactions of the Royal Society of London*, 75:40–126.

Hertzsprung, E. (1915). Effective wavelengths of absolutely faint stars. *The Astrophysical Journal*, 42:111–119.

Hin, R. C., Coath, C. D., Carter, P. J., Nimmo, F., Lai, Y.-J., Pogge von Strand mann, P. A. E., Willbold, M., Leinhardt, Z. M., Walter, M. J., and Elliott, T. (2017). Magnesium isotope evidence that accretional vapour loss shapes planetary compositions. *Nature*, 549(7673):511–515.

Hinkel, N. R., Timmes, F., Young, P. A., Pagano, M. D., and Turnbull, M. C. (2014). Stellar abundances in the solar neighborhood: the hypatia catalog. *The Astronomical Journal*, 148(3):54.

Holberg, J. B. (2005). How Degenerate Stars Came to be Known as White Dwarfs. In *American Astronomical Society Meeting Abstracts*, volume 207 of *American Astronomical Society Meeting Abstracts*, page 205.01.

Hollands, M. A., Gänsicke, B. T., and Koester, D. (2018). Cool dz white dwarfs ii: compositions and evolution of old remnant planetary systems. *Monthly Notices of the Royal Astronomical Society*, 477(1):93–111.

Hollands, M. A., Koester, D., Alekseev, V., Herbert, E. L., and Gänsicke, B. T. (2017). Cool DZ white dwarfs - I. Identification and spectral analysis. *The Monthly Notices of the Royal Astronomical Society*, 467:4970–5000.

Horne, K. and Marsh, T. R. (1986). Emission line formation in accretion discs. *The Monthly Notices of the Royal Astronomical Society*, 218:761–773.

Hoyle, F. and Schwarzschild, M. (1955). On the Evolution of Type II Stars. *The Astrophysical Journal Supplement Series*, 2:1.

Hurley, J. R., Pols, O. R., and Tout, C. A. (2000). Comprehensive analytic formulae for stellar evolution as a function of mass and metallicity. *The Monthly Notices of the Royal Astronomical Society*, 315:543–569.

Hurley, J. R., Pols, O. R., and Tout, C. A. (2013). SSE: Single Star Evolution.

Ida, S. and Lin, D. N. (2004). Toward a deterministic model of planetary formation. i. a desert in the mass and semimajor axis distributions of extrasolar planets. *The Astrophysical Journal*, 604(1):388.

Jacobsen, S. B. (2005). The hf-w isotopic system and the origin of the earth and moon. *Annual Review of Earth and Planetary Sciences*, 33(1):531–570.

Jura, M. (2003). A tidally disrupted asteroid around the white dwarf g29-38. *The Astrophysical Journal Letters*, 584:L91–L94.

Jura, M. (2006). Carbon deficiency in externally polluted white dwarfs: Evidence for accretion of asteroids. *The Astrophysical Journal*, 653:613–620.

Jura, M. (2008). Pollution of single white dwarfs by accretion of many small asteroids. *The Astronomical Journal*, 135:1785–1792.

Jura, M. and Xu, S. (2010a). The survival of water within extrasolar minor planets. *The Astronomical Journal*, 140:1129–1136.

Jura, M. and Xu, S. (2010b). The Survival of Water Within Extrasolar Minor Planets. *The Astronomical Journal*, 140:1129–1136.

Jura, M., Xu, S., Klein, B., Koester, D., and Zuckerman, B. (2012). Two Extrasolar Asteroids with Low Volatile-element Mass Fractions. *The Astrophsyical Journal*, 750:69.

Jura, M. and Young, E. D. (2014). Extrasolar cosmochemistry. *Annual Review of Earth and Planetary Sciences*, 42:45–67.

Kaib, N. A. and Cowan, N. B. (2015). The feeding zones of terrestrial planets and insights into Moon formation. *Icarus*, 252:161–174.

Kama, M., Folsom, C. P., and Pinilla, P. (2015). Fingerprints of giant planets in the photospheres of Herbig stars. *Astronomy and Astrophysics*, 582:L10.

Kama, M., Shorttle, O., Jermyn, A. S., Folsom, C. P., Furuya, K., Bergin, E. A., Walsh, C., and Keller, L. (2019). Abundant Refractory Sulfur in Protoplanetary Disks. *The Astrophysical Journal*, 885(2):114.

Keil, K. (2000). Thermal alteration of asteroids: evidence from meteorites. *Planetary and Space Science*, 48(10):887–903.

Kennett, B. L. N. and Engdahl, E. R. (1991). Traveltimes for global earthquake location and phase identification. *Geophysical Journal International*, 105(2):429–465.

Kepler, S. O., Pelisoli, I., Koester, D., Ourique, G., Romero, A. D., Reindl, N., Kleinman, S. J., Eisenstein, D. J., Valois, A. D. M., and Amaral, L. A. (2016). New white dwarf and subdwarf stars in the Sloan Digital Sky Survey Data Release 12. *The Monthly Notices of the Royal Astronomical Society*, 455:3413–3423.

Kite, E. S., Manga, M., and Gaidos, E. (2009). Geodynamics and rate of volcanism on massive earth-like planets. *The Astrophysical Journal*, 700(2):1732.

Klein, B., Jura, M., Koester, D., and Zuckerman, B. (2011). Rocky extrasolar planetary compositions derived from externally polluted white dwarfs. *The Astrophysical Journal*, 741:64.

Klein, B., Jura, M., Koester, D., Zuckerman, B., and Melis, C. (2010). Chemical abundances in the externally polluted white dwarf gd 40: Evidence of a rocky extrasolar minor planet. *The Astrophysical Journal*, 709:950–962.

Koester, D. (2009). Accretion and diffusion in white dwarfs. new diffusion timescales and applications to gd 362 and g 29-38. *Astronomy and Astrophysics*, 498:517–525.

Koester, D. (2010). White dwarf spectra and atmosphere models. *Memorie della Societa Astronomica Italiana*, 81:921–931.

Koester, D. (2013). *White Dwarf Stars*, pages 559–612. Springer Netherlands, Dordrecht.

Koester, D. (2014). On thermohaline mixing in accreting white dwarfs.

Koester, D., Gänsicke, B. T., and Farihi, J. (2014). The frequency of planetary debris around young white dwarfs. *Astronomy and Astrophysics*, 566:A34.

Kreidberg, L., Koll, D. D. B., Morley, C., Hu, R., Schaefer, L., Deming, D., Stevenson, K. B., Dittmann, J., Vanderburg, A., Berardo, D., and et al. (2019). Absence of a thick atmosphere on the terrestrial exoplanet lhs 3844b. *Nature*, 573(7772):87–90.

Lammer, H., Bredehöft, J. H., Coustenis, A., Khodachenko, M. L., Kaltenegger, L., Grasset, O., Prieur, D., Raulin, F., Ehrenfreund, P., Yamauchi, M., Wahlund, J.-E., Grießmeier, J.-M., Stangl, G., Cockell, C. S., Kulikov, Y. N., Grenfell, J. L., and Rauer, H. (2009). What makes a planet habitable? *Astronomy and Astrophysics Review*, 17(2):181–249.

Lin, J., Dotter, A., Ting, Y.-S., and Asplund, M. (2018). Stellar ages and masses in the solar neighbourhood: Bayesian analysis using spectroscopy and gaia dr1 parallaxes. *Monthly Notices of the Royal Astronomical Society*, 477(3):2966–2975.

Lindblad, B. (1922). Spectrophotometric methods for determining stellar luminosity. *The Astrophysical Journal*, 55:85–118.

Lodders, K. (2003). Solar System Abundances and Condensation Temperatures of the Elements. *The Astrophysical Journal*, 591:1220–1247.

Lodders, K. (2010). *Principles and Perspectives in Cosmochemistry*, pages 379–417.

Lodders, K. and Fegley, B. (1998). *The planetary scientist's companion*, pages 124–329.

Luck, R. E. and Heiter, U. (2005). Stars within 15 parsecs: abundances for a northern sample. *The Astronomical Journal*, 129(2):1063.

Luyten, W. J. (1922). The Mean Parallax of Early-Type Stars of Determined Proper Motion and Apparent Magnitude. *Publications of the Astronomical Society of the Pacific*, 34(199):156.

MacPherson, G. J., Petaev, M., and Krot, A. N. (2004). Bulk Compositions of CAIs and Al-rich Chondrules: Implications of the Reversal of the Anorthite/Forsterite Condensation Sequence at Low Nebular Pressures. In Mackwell, S. and Stansbery, E., editors, *Lunar and Planetary Science Conference*, Lunar and Planetary Science Conference, page 1838.

Madhusudhan, N. (2019). Exoplanetary atmospheres: Key insights, challenges, and prospects. *Annual Review of Astronomy and Astrophysics*, 57(1):617–663.

Madhusudhan, N., Lee, K. K. M., and Mousis, O. (2012). A possible carbon-rich interior in super-earth 55 cancri e. *Astrophysical Journal Letters*, 759:L40.

Malamud, U. and Perets, H. B. (2016). Post-main Sequence Evolution of Icy Minor Planets: Implications for Water Retention and White Dwarf Pollution. *The Astrophysical Journal*, 832:160.

Malamud, U. and Perets, H. B. (2017). Post-main-sequence evolution of icy minor planets. II. water retention and white dwarf pollution around massive progenitor stars. *The Astrophysical Journal*, 842(1):67.

Malamud, U. and Perets, H. B. (2017). Post-main-sequence Evolution of Icy Minor Planets. III. Water Retention in Dwarf Planets and Exomoons and Implications for White Dwarf Pollution. *The Astrophysical Journal*, 849(1):8.

Malamud, U. and Perets, H. B. (2020a). Tidal disruption of planetary bodies by white dwarfs – ii. debris disc structure and ejected interstellar asteroids. *Monthly Notices of the Royal Astronomical Society*, 493(1):698–712.

Malamud, U. and Perets, H. B. (2020b). Tidal disruption of planetary bodies by white dwarfs i: a hybrid sph-analytical approach. *Monthly Notices of the Royal Astronomical Society*, 492(4):5561–5581.

Maldonado, J., Eiroa, C., Villaver, E., Montesinos, B., and Mora, A. (2015). Searching for signatures of planet formation in stars with circumstellar debris discs. *Astronomy and Astrophysics*, 579:A20.

Mamajek, E. E., Usuda, T., Tamura, M., and Ishii, M. (2009). Initial conditions of planet formation: Lifetimes of primordial disks. *AIP Conference Proceedings*.

Manser, C. J., Gänsicke, B. T., Eggl, S., Hollands, M., Izquierdo, P., Koester, D., Landstreet, J. D., Lyra, W., Marsh, T. R., Meru, F., Mustill, A. J., Rodríguez-Gil, P., Toloza, O., Veras, D., Wilson, D. J., Burleigh, M. R., Davies, M. B., Farihi, J., Gentile Fusillo, N., de Martino, D., Parsons, S. G., Quirrenbach, A., Raddi, R., Reffert, S., Del Santo, M., Schreiber, M. R., Silvotti, R., Toonen, S., Villaver, E., Wyatt, M., Xu, S., and Portegies Zwart, S. (2019). A planetesimal orbiting within the debris disc around a white dwarf star. *Science*, 364(6435):66–69.

Manser, C. J., Gänsicke, B. T., Gentile Fusillo, N. P., Ashley, R., Breedt, E., Hollands, M., Izquierdo, P., and Pelisoli, I. (2020). The frequency of gaseous debris discs around white dwarfs. *Monthly Notices of the Royal Astronomical Society*, 493(2):2127–2139.

Marboeuf, U., Thiabaud, A., Alibert, Y., Cabral, N., and Benz, W. (2014). From stellar nebula to planetesimals. *Astronomy and Astrophysics*, 570:A35.

Marcus, R. A., Stewart, S. T., Sasselov, D., and Hernquist, L. (2009). Collisional stripping and disruption of super-earths. *The Astrophysical Journal Letters*, 700:L118–L122.

Marshak, R. E. (1940). The Internal Temperature of White Dwarf Stars. *The Astrophysical Journal*, 92:321.

Mayor, M. and Queloz, D. (1995). A Jupiter-mass companion to a solar-type star. *Nature*, 378(6555):355–359.

McCoy, T. J., Corrigan, C. M., and Herd, C. D. K. (2011). Combining meteorites and missions to explore mars. *Proceedings of the National Academy of Sciences*, 108(48):19159–19164.

McDonough, W. and Sun, S. (1995). The composition of the earth. *Chemical Geology*, 120(3):223 – 253.

McDonough, W. F. (2003). Compositional Model for the Earth's Core. *Treatise on Geochemistry*, 2:547–568.

McSween, H. Y. (1987). *Meteorites and their parent planets.*

McSween Jr., H. Y., Binzel, R. P., De Sanctis, M. C., Ammannito, E., Prettyman, T. H., Beck, A. W., Reddy, V., Le Corre, L., Gaffey, M. J., McCord, T. B., Raymond, C. A., Russell, C. T., and the Dawn Science Team (2013). Dawn; the vesta–hed connection; and the geologic context for eucrites, diogenites, and howardites. *Meteoritics and Planetary Science*, 48(11):2090–2104.

Melis, C. and Dufour, P. (2017). Does a differentiated, carbonate-rich, rocky object pollute the white dwarf sdss j104341.53+085558.2? *The Astrophysical Journal*, 834(1):1.

Melis, C., Dufour, P., Farihi, J., Bochanski, J., Burgasser, A. J., Parsons, S. G., Gänsicke, B. T., Koester, D., and Swift, B. J. (2012). Gaseous material orbiting the polluted, dusty white dwarf he 1349–2305. *The Astrophysical Journal*, 751(1):L4.

Meng, X., Chen, X., and Han, Z. (2008). Initial-final mass relationship for stars of different metallicities. *Astronomy and Astrophysics*, 487(2):625–635.

Mestel, L. (1952). On the theory of white dwarf stars. I. The energy sources of white dwarfs. *The Monthly Notices of the Royal Astronomical Society*, 112:583.

Michel, P., DeMeo, F. E., and Bottke, W. F. (2015). *Asteroids IV.*

Mishenina, T., Pignatari, M., Korotin, S., Soubiran, C., Charbonnel, C., Thielemann, F.-K., Gorbaneva, T., and Basak, N. Y. (2013). Abundances of neutron-capture elements in stars of the galactic disk substructures. *Astronomy and astrophysics*, 552:A128.

Mittlefehldt, D. W. (2015). Asteroid (4) vesta: I. the howardite-eucrite-diogenite (hed) clan of meteorites. *Geochemistry*, 75(2):155 – 183.

Mocquet, A., Rosenblatt, P., Dehant, V., and Verhoeven, O. (2011). The deep interior of Venus, Mars, and the Earth: A brief review and the need for planetary surface-based measurements. *Planetary and Space Science*, 59:1048–1061.

Morbidelli, A., Lunine, J., O'Brien, D., Raymond, S., and Walsh, K. (2012). Building terrestrial planets. *Annual Review of Earth and Planetary Sciences*, 40(1):251–275.

Morgan, J. W. and Anders, E. (1980). Chemical composition of earth, venus, and mercury. *Proceedings of the National Academy of Sciences*, 77(12):6973–6977.

Moriarty, J., Madhusudhan, N., and Fischer, D. (2014). Chemistry in an evolving protoplanetary disk: Effects on terrestrial planet composition. *The Astrophysical Journal*, 787:81.

Moskovitz, N. (2009). Spectroscopic and theoretical constraints on the differentiation of planetesimals.

Moskovitz, N. and Gaidos, E. (2011). Differentiation of planetesimals and the thermal consequences of melt migration. *Meteoritics and Planetary Science*, 46(6):903–918.

Motalebi, F., Udry, S., Gillon, M., Lovis, C., Ségransan, D., Buchhave, L. A., Demory, B. O., Malavolta, L., Dressing, C. D., Sasselov, D., Rice, K., Charbonneau, D., Collier Cameron, A., Latham, D., Molinari, E., Pepe, F., Affer, L., Bonomo, A. S., Cosentino, R., Dumusque, X., Figueira, P., Fiorenzano, A. F. M., Gettel, S., Harutyunyan, A., Haywood, R. D., Johnson, J., Lopez, E., Lopez-Morales, M., Mayor, M., Micela, G., Mortier, A., Nascimbeni, V., Philips, D., Piotto, G., Pollacco, D., Queloz, D., Sozzetti, A., Vanderburg, A., and Watson, C. A. (2015). The HARPS-N Rocky Planet Search. I. HD 219134 b: A transiting rocky planet in a multi-planet system at 6.5 pc from the Sun. *Astronomy and Astrophysics*, 584:A72.

Mustill, A. J. and Villaver, E. (2012). Foretellings of ragnarök: World-engulfing asymptotic giants and the inheritance of white dwarfs. *The Astrophysical Journal*, 761:121.

Mustill, A. J., Villaver, E., Veras, D., Gänsicke, B. T., and Bonsor, A. (2018). Unstable low-mass planetary systems as drivers of white dwarf pollution. *The Monthly Notices of the Royal Astronomical Society*, 476:3939–3955.

Noack, L. and Breuer, D. (2014). Plate tectonics on rocky exoplanets: Influence of initial conditions and mantle rheology. *Planetary and Space Science*, 98:41–49.

Oldham, R. D. (1906). The constitution of the interior of the earth, as revealed by earthquakes. *Quarterly Journal of the Geological Society*, 62(1-4):456–475.

O'Neill, H. S. C. and Palme, H. (2008). Collisional erosion and the non-chondritic composition of the terrestrial planets. *Philosophical Transactions of the Royal Society of London Series A*, 366(1883):4205–4238.

Palme, H. and O'Neill, H. (2014). 3.1 - cosmochemical estimates of mantle composition. In Holland, H. D. and Turekian, K. K., editors, *Treatise on Geochemistry (Second Edition)*, pages 1 – 39. Elsevier, Oxford, second edition edition.

Palme, H. and O'Neill, H. S. C. (2003). Cosmochemical Estimates of Mantle Composition. *Treatise on Geochemistry*, 2:568.

Palme, H. and O'Neill, H. S. C. (2003). *Treatise on Geochemistry*. Elsevier.

Payne, M. J., Veras, D., Gänsicke, B. T., and Holman, M. J. (2017). The fate of exomoons in white dwarf planetary systems. *The Monthly Notices of the Royal Astronomical Society*, 464:2557–2564.

Petrovich, C. and Munoz, D. J. (2017). Planetary engulfment as a trigger for white dwarf pollution. *The Astrophysical Journal*, 834(2):116.

Pizzarello, S., Cooper, G. W., and Flynn, G. J. (2006). *Meteorites and the Early Solar System II*, pages 625–651.

Preval, S. P., Barstow, M. A., Bainbridge, M., Reindl, N., Ayres, T., Holberg, J. B., Barrow, J. D., Lee, C.-C., Webb, J. K., and Hu, J. (2019). A far-UV survey of three hot, metal-polluted white dwarf stars: WD0455-282, WD0621-376, and WD2211-495. *The Monthly Notices of the Royal Astronomical Society*, 487(3):3470–3487.

Prieto, C. A., Barklem, P. S., Lambert, D. L., and Cunha, K. (2004). A spectroscopic survey of stars in the solar neighborhood-the nearest 15 pc. *Astronomy and Astrophysics*, 420(1):183–205.

Pringle, E. A., Moynier, F., Savage, P. S., Badro, J., and Barrat, J.-A. (2014). Silicon isotopes in angrites and volatile loss in planetesimals. *Proceedings of the National Academy of Science*, 111(48):17029–17032.

Provencal, J. L., Shipman, H. L., Høg, E., and Thejll, P. (1998). Testing the White Dwarf Mass-Radius Relation with HIPPARCOS. *The Astrophysical Journal*, 494(2):759–767.

Raddi, R., Gänsicke, B. T., Koester, D., Farihi, J., Hermes, J. J., Scaringi, S., Breedt, E., and Girven, J. (2015). Likely detection of water-rich asteroid debris in a metal-polluted white dwarf. *The Monthly Notices of the Royal Astronomical Society*, 450:2083–2093.

Rafikov, R. R. (2011a). Metal accretion onto white dwarfs caused by poynting-robertson drag on their debris disks. *The Astrophysical Journal Letters*, 732:L3+.

Rafikov, R. R. (2011b). Runaway accretion of metals from compact discs of debris on to white dwarfs. *The Monthley Notices of the Royal Astronomical Society*, pages L287+.

Ramírez, I., Prieto, C. A., and Lambert, D. L. (2013). Oxygen abundances in nearby fgk stars and the galactic chemical evolution of the local disk and halo. *The Astrophysical Journal*, 764(1):78.

Rappaport, S., Sanchis-Ojeda, R., Rogers, L. A., Levine, A., and Winn, J. N. (2013). The roche limit for close-orbiting planets: Minimum density, composition constraints, and application to the 4.2-hour planet koi 1843.03. *The Astrophysical Journal Letters*.

Reach, W. T., Kuchner, M. J., von Hippel, T., Burrows, A., Mullally, F., Kilic, M., and Winget, D. E. (2005). The Dust Cloud around the White Dwarf G29-38. *The Astrophysical Journal Letters*, 635(2):L161–L164.

Rebassa-Mansergas, A., Anguiano, B., García-Berro, E., Freeman, K. C., Cojocaru, R., Manser, C. J., Pala, A. F., Gänsicke, B. T., and Liu, X.-W. (2016). The age–metallicity relation in the solar neighbourhood from a pilot sample of white dwarf–main sequence binaries. *Monthly Notices of the Royal Astronomical Society*, 463(2):1137–1143.

Rebassa-Mansergas, A., Solano, E., Xu, S., Rodrigo, C., Jiménez-Esteban, F. M., and Torres, S. (2019). Infrared-excess white dwarfs in the Gaia 100 pc sample. *Monthly Notices of the Royal Astronomical Society*, 489(3):3990–4000.

Ribas, Á., Bouy, H., and Merín, B. (2015). Protoplanetary disk lifetimes vs. stellar mass and possible implications for giant planet populations. *Astronomy and Astrophysics*, 576:A52.

Ringwood, A. E. (1986). Terrestrial origin of the Moon. *Nature*, 322(6077):323–328.

Rubin, A. E. (2005). What heated the asteroids? *Scientific American*, 292(5):80–87.

Rubincam, D. (2000). Radiative spin-up and spin-down of small asteroids.

Russell, C. T., Raymond, C. A., Coradini, A., McSween, H. Y., Zuber, M. T., Nathues, A., De Sanctis, M. C., Jaumann, R., Konopliv, A. S., Preusker, F., Asmar, S. W., Park, R. S., Gaskell, R., Keller, H. U., Mottola, S., Roatsch, T., Scully, J. E. C., Smith, D. E., Tricarico, P., Toplis, M. J., Christensen, U. R., Feldman, W. C., Lawrence, D. J., McCoy, T. J., Prettyman, T. H., Reedy, R. C., Sykes, M. E., and Titus, T. N. (2012). Dawn at vesta: Testing the protoplanetary paradigm. *Science*, 336(6082):684–686.

Sandage, A. R. and Schwarzschild, M. (1952). Inhomogeneous Stellar Models. II. Models with Exhausted Cores in Gravitational Contraction. *The Astrophysical Journal*, 116:463.

Saur, J., Grambusch, T., Duling, S., Neubauer, F., and Simon, S. (2013). Magnetic energy fluxes in sub-alfvénic planet star and moon planet interactions. *Astronomy amd Astrophysics*, 552:A119.

Schaeberle, J. M. (1896). Discovery of the companion to Procyon. *The Astronomical Journal*, 17:37–37.

Scott, E. R. D. (2013). Handbook of iron meteorites by vagn f. buchwald, 1975: Electronic edition. *Meteoritics and Planetary Science*, 48(12):2608–2608.

Scott, E. R. D. and Wasson, J. T. (1975). Classification and properties of iron meteorites. *Reviews of Geophysics and Space Physics*, 13:527–546.

Seager, S., Kuchner, M., Hier-Majumder, C. A., and Militzer, B. (2007). Mass-Radius Relationships for Solid Exoplanets. *The Astrophysical Journal*, 669:1279–1297.

Sears, D. W. G. (2005). *The Origin of Chondrules and Chondrites.*

Sellke, T., Bayarri, M. J., and Berger, J. O. (2001). Calibration of p values for testing precise null hypotheses. *The American Statistician*, 55(1):62–71.

Siebert, J., Badro, J., Antonangeli, D., and Ryerson, F. J. (2012). Metal–silicate partitioning of ni and co in a deep magma ocean. *Earth and Planetary Science Letters*, 321-322:189 – 197.

Siebert, J., Sossi, P. A., Blanchard, I., Mahan, B., Badro, J., and Moynier, F. (2018). Chondritic Mn/Na ratio and limited post-nebular volatile loss of the Earth. *Earth and Planetary Science Letters*, 485:130–139.

Siess, L. (2007). Evolution of massive AGB stars. II. model properties at non-solar metallicity and the fate of Super-AGB stars. *Astronomy and Astrophysics*, 476(2):893–909.

Siess, L., Dufour, E., and Forestini, M. (2000). An internet server for pre-main sequence tracks of low- and intermediate-mass stars. *Astronomy and Astrophysics*, 358:593–599.

Sing, D. K. (2018). Observational techniques with transiting exoplanetary atmospheres.

Sossi, P. A. and Fegley, Bruce, J. (2018). Thermodynamics of Element Volatility and its Application to Planetary Processes. *Reviews in Mineralogy and Geochemistry*, 84(1):393–459.

Stephan, A. P., Naoz, S., and Zuckerman, B. (2017). Throwing Icebergs at White Dwarfs. *The Astrophysical Journal Letters*, 844:L16.

Stepinski, T. F. (1998). New approach to diagnosing properties of protoplanetary disks. *The Astrophysical Journal*, 507(1):361.

Strangeway, R. J., Russell, C. T., Luhmann, J. G., Moore, T. E., Foster, J. C., Barabash, S. V., and Nilsson, H. (2017). Does an Intrinsic Magnetic Field Inhibit or Enhance Planetary Ionosphere Outflow and Loss? In *AGU Fall Meeting Abstracts*, volume 2017, pages P11B–2506.

Swan, A., Farihi, J., Koester, D., Holland s, M., Parsons, S., Cauley, P. W., Redfield, S., and Gänsicke, B. T. (2019). Interpretation and diversity of exoplanetary material orbiting white dwarfs. *The Monthly Notices of the Royal Astronomical Society*, 490(1):202–218.

Swan, A., Farihi, J., Koester, D., Hollands, M., Parsons, S., Cauley, P. W., Redfield, S., and Gänsicke, B. T. (2019). Interpretation and diversity of exoplanetary material orbiting white dwarfs. *Monthly Notices of the Royal Astronomical Society*, 490(1):202–218.

Tackley, P. J., Ammann, M., Brodholt, J. P., Dobson, D. P., and Valencia, D. (2013). Mantle dynamics in super-earths: Post-perovskite rheology and self-regulation of viscosity. *Icarus*, 225(1):50–61.

Thévenin, F. (1998). Chemical abundances in late-type stars. *VizieR On-line Data Catalog: III/193*.

Thomas, P. C., Parker, J. W., McFadden, L. A., Russell, C. T., Stern, S. A., Sykes, M. V., and Young, E. F. (2005). Differentiation of the asteroid Ceres as revealed by its shape. *Nature*, 437:224–226.

Treiman, A. H., Gleason, J. D., and Bogard, D. D. (2000). The snc meteorites are from mars. *Planetary and Space Science*, 48(12):1213 – 1230. Mars Exploration Program.

Turner, S. G. D. and Wyatt, M. C. (2019). Modelling the distributions of white dwarf atmospheric pollution: a low mg abundance for accreted planetesimals? *Monthly Notices of the Royal Astronomical Society*.

Tychoniec, Ł., Tobin, J. J., Karska, A., Chandler, C., Dunham, M. M., Harris, R. J., Kratter, K. M., Li, Z.-Y., Looney, L. W., Melis, C., et al. (2018). The vla nascent disk and multiplicity survey of perseus protostars (vandam). iv. free-free emission from protostars: Links to infrared properties, outflow tracers, and protostellar disk masses. *arXiv preprint arXiv:1806.02434*.

Valencia, D., O'connell, R. J., and Sasselov, D. D. (2007). Inevitability of plate tectonics on super-earths. *The Astrophysical Journal Letters*, 670(1):L45.

Valenti, J. A. and Fischer, D. A. (2005). Spectroscopic properties of cool stars (spocs). i. 1040 f, g, and k dwarfs from keck, lick, and aat planet search programs. *The Astrophysical Journal Supplement Series*, 159(1):141.

van den Bos, W. H. (1926). The orbit and the masses of 40 Eridani BC. *Bulletin of the Astronomical Institutes of the Netherlands*, 3:128.

Van Heck, H. and Tackley, P. (2011). Plate tectonics on super-earths: Equally or more likely than on earth. *Earth and Planetary Science Letters*, 310(3):252–261.

van Lieshout, R., Kral, Q., Charnoz, S., Wyatt, M. C., and Shannon, A. (2018). Exoplanet recycling in massive white-dwarf debris discs. *Monthly Notices of the Royal Astronomical Society*, 480(2):2784–2812.

van Maanen, A. (1919). Stellar parallaxes derived from photographs made with the 60-inch reflector of the Mount Wilson Observatory. *The Astronomical Journal*, 32:86–88.

Vanderbosch, Z., Hermes, J. J., Dennihy, E., Dunlap, B. H., Izquierdo, P., Tremblay, P. E., Cho, P. B., Gänsicke, B. T., Toloza, O., Bell, K. J., Montgomery, M. H., and Winget, D. E. (2020). A White Dwarf with Transiting Circumstellar Material Far outside the Roche Limit. *The Astrophysical Journal*, 897(2):171.

Vanderburg, A., Johnson, J. A., Rappaport, S., Bieryla, A., Irwin, J., Lewis, J. A., Kipping, D., Brown, W. R., Dufour, P., Ciardi, D. R., Angus, R., Schaefer, L., Latham, D. W., Charbonneau, D., Beichman, C., Eastman, J., McCrady, N., Wittenmyer, R. A., and Wright, J. T. (2015). A disintegrating minor planet transiting a white dwarf. *Nature*, 526:546–549.

Vassiliadis, E. and Wood, P. R. (1993). Evolution of low- and intermediate-mass stars to the end of the asymptotic giant branch with mass loss. *The Astrophysical Journal*, 413:641–657.

Veras, D. (2016). Post-main-sequence planetary system evolution. *Royal Society Open Science*, 3:150571.

Veras, D., Carter, P. J., Leinhardt, Z. M., and Gänsicke, B. T. (2017). Explaining the variability of WD 1145+017 with simulations of asteroid tidal disruption. *Monthly Notices of the Royal Astronomical Society*, 465(1):1008–1022.

Veras, D., Jacobson, S. A., and Gänsicke, B. T. (2014a). Post-main-sequence debris from rotation-induced yorp break-up of small bodies. *The Monthley Notices of the Royal Astronomical Society*, 445:2794–2799.

Veras, D. and Kurosawa, K. (2020). Generating metal-polluting debris in white dwarf planetary systems from small-impact crater ejecta. *The Monthley Notices of the Royal Astronomical Society*, 494(1):442–457.

Veras, D., Leinhardt, Z. M., Bonsor, A., and Gänsicke, B. T. (2014b). Formation of planetary debris discs around white dwarfs - i. tidal disruption of an extremely eccentric asteroid. *The Monthly Notices of the Royal Astronomical Society*, 445:2244–2255.

Veras, D., Leinhardt, Z. M., Eggl, S., and Gänsicke, B. T. (2015). Formation of planetary debris discs around white dwarfs - ii. shrinking extremely eccentric collisionless rings. *The Monthly Notices of the Royal Astronomical Society*, 451:3453–3459.

Veras, D., Mustill, A. J., Bonsor, A., and Wyatt, M. C. (2013). Simulations of two-planet systems through all phases of stellar evolution: implications for the instability boundary and white dwarf pollution. *The Monthly Notices of the Royal Astronomical Society*, 431:1686–1708.

Veras, D., Mustill, A. J., Gänsicke, B. T., Redfield, S., Georgakarakos, N., Bowler, A. B., and Lloyd, M. J. S. (2016). Full-lifetime simulations of multiple unequal-mass planets across all phases of stellar evolution. *The Monthly Notices of the Royal Astronomical Society*, 458:3942–3967.

Veras, D., Xu, S., and Rebassa-Mansergas, A. (2017). The critical binary star separation for a planetary system origin of white dwarf pollution. *Monthly Notices of the Royal Astronomical Society*, 473(3):2871–2880.

Visscher, C. and Fegley, B. (2013). CHEMISTRY OF IMPACT-GENERATED SILICATE MELT-VAPOR DEBRIS DISKS. *The Astrophysical Journal*, 767(1):L12.

Viswanathan, V., Rambaux, N., Fienga, A., Laskar, J., and Gastineau, M. (2019). Observational constraint on the radius and oblateness of the lunar core-mantle boundary. *Geophysical Research Letters*, 46(13):7295–7303.

Walker, J. C. G., Hays, P. B., and Kasting, J. F. (1981). A negative feedback mechanism for the long-term stabilization of earth's surface temperature. *Journal of Geophysical Research: Oceans*, 86(C10):9776–9782.

Wang, K. and Jacobsen, S. B. (2016). Potassium isotopic evidence for a high-energy giant impact origin of the moon. *Nature*, 538:487–490.

Wasson, J. T. and Kallemeyn, G. W. (1988). Compositions of chondrites. *Philosophical Transactions of the Royal Society of London. Series A, Mathematical and Physical Sciences*, 325(1587):535–544.

Weidemann, V. (1960). The Atmosphere of the White Dwarf Van Maanen 2. *The Astrophysical Journal*, 131:638.

White, W. M. and Klein, E. M. (2014). Composition of the Oceanic Crust. *Treatise on Geochemistry*, 4:457–496.

Wiik, H. (1956). The chemical composition of some stony meteorites. *Geochimica et Cosmochimica Acta*, 9(5):279 – 289.

Williams, J. G. (1994). Contribution to the Earth's Obliquity Rate, Precession, and Nutation. *The Astrophysical Journal*, 108:711.

Williams, J. P. and Cieza, L. A. (2011). Protoplanetary disks and their evolution. *Annual Review of Astronomy and Astrophysics*, 49(1):67–117.

Williamson, E. D. and Adams, L. H. (1923). Density distribution in the earth. *Journal of the Washington Academy of Sciences*, 13(19):413–428.

Wilson, D. J., Gänsicke, B. T., Koester, D., Raddi, R., Breedt, E., Southworth, J., and Parsons, S. G. (2014). Variable emission from a gaseous disc around a metal-polluted white dwarf. *The Monthly Notices of the Royal Astronmical Society*, 445:1878–1884.

Wilson, D. J., Gänsicke, B. T., Koester, D., Toloza, O., Pala, A. F., Breedt, E., and Parsons, S. G. (2015). The composition of a disrupted extrasolar planetesimal at sdss j0845+2257 (ton 345). *The Monthly Notices of the Royal Astronomical Society*, 451:3237–3248.

Wyatt, M. C., Farihi, J., Pringle, J. E., and Bonsor, A. (2014). Stochastic accretion of planetesimals on to white dwarfs: constraints on the mass distribution of accreted material from atmospheric pollution. *The Monthly Notices of the Royal Astronomical Society*, 439:3371–3391.

Xu, S., Dufour, P., Klein, B., Melis, C., Monson, N. N., Zuckerman, B., Young, E. D., and Jura, M. A. (2019). Compositions of planetary debris around dusty white dwarfs. *The Astronomical Journal*, 158(6):242.

Xu, S., Jura, M., Klein, B., Koester, D., and Zuckerman, B. (2013). Two beyond-primitive extrasolar planetesimals. *The Astrophysical Journal*, 766:132.

Xu, S., Jura, M., Koester, D., Klein, B., and Zuckerman, B. (2014). Elemental compositions of two extrasolar rocky planetesimals. *The Astrophysical Journal*, 783:79.

Xu, S., Zuckerman, B., Dufour, P., Young, E. D., Klein, B., and Jura, M. (2017). The Chemical Composition of an Extrasolar Kuiper-Belt-Object. *The Astrophysical Journal Letters*, 836:L7.

Yang, J., Goldstein, J. I., and Scott, E. R. D. (2010). Main-group pallasites: Thermal history, relationship to IIIAB irons, and origin. *Geochimica et Cosmochimica Acta*, 74(15):4471–4492.

Yoneda, S. and Grossman, L. (1995). Condensation of caomgoal2o3sio2 liquids from cosmic gases. *Geochimica et Cosmochimica Acta*, 59(16):3413 – 3444.

Yung, Y., Wong, M., and Gaidos, E. (2015). Solar system/sun, atmospheres, evolution of atmospheres | evolution of earth's atmosphere. In North, G. R., Pyle, J., and Zhang, F., editors, *Encyclopedia of Atmospheric Sciences (Second Edition)*, pages 163 – 167. Academic Press, Oxford, second edition edition.

Zeng, L., Jacobsen, S. B., Sasselov, D. D., Petaev, M. I., Vanderburg, A., Lopez-Morales, M., Perez-Mercader, J., Mattsson, T. R., Li, G., Heising, M. Z., Bonomo, A. S., Damasso, M., Berger, T. A., Cao, H., Levi, A., and Wordsworth, R. D. (2019). Growth model interpretation of planet size distribution. *Proceedings of the National Academy of Sciences*, 116(20):9723–9728.

Zhang, Y., Sekine, T., He, H., Yu, Y. X., Liu, F., and Zhang, M. (2016). Experimental constraints on light elements in the earth's outer core. In *Scientific reports*.

Zuckerman, B. and Becklin, E. E. (1987). Excess infrared radiation from a white dwarf - an orbiting brown dwarf? *Nature*, 330:138–140.

Zuckerman, B., Koester, D., Dufour, P., Melis, C., Klein, B., and Jura, M. (2011). An aluminum/calcium-rich, iron-poor, white dwarf star: Evidence for an extrasolar planetary lithosphere? *The Astrophysical Journal*, 739:101.

Zuckerman, B., Koester, D., Melis, C., Hansen, B. M., and Jura, M. (2007). The chemical composition of an extrasolar minor planet. *The Astrophysical Journal*, 671:872–877.

Zuckerman, B., Melis, C., Klein, B., Koester, D., and Jura, M. (2010). Ancient planetary systems are orbiting a large fraction of white dwarf stars. *The Astrophysical Journal*, 722:725–736.

Zuckerman, B. and Reid, I. N. (1998). Metals in cool da white dwarfs. *The Astrophysical Journal Letters*, 505(2):L143.

Appendix A

Supplementary figures and tables

This appendix contains tables which display the data for the polluted white dwarf systems analsyed in Chapter 4 and the figures displaying the individual fits for every system analsyed in Chapter 4.

Table A.1 White dwarf data from Hollands et al. (2017).

System	[Ti/He]	[Ca/He]	[Ni/He]	[Fe/He]	[Cr/He]	[Mg/He]	[Na/He]
1535+1247	-9.62 ± 0.10	-8.61 ± 0.05	-8.90 ± 0.10	-7.57 ± 0.05	-9.25 ± 0.10	-7.36 ± 0.10	-8.72 ± 0.05
1330+3029	-9.7 ± 0.10	-8.40 ± 0.06	-8.66 ± 0.10	-7.3 ± 0.06	-9.00 ± 0.10	-7.15 ± 0.10	-8.80 ± 0.06
1229+0743	-9.87 ± 0.16	-8.20 ± 0.13	—	-7.09 ± 0.13	-8.85 ± 0.16	-7.29 ± 0.16	-8.48 ± 0.13
1616+3303	-9.62 ± 0.12	-8.25 ± 0.08	—	-7.14 ± 0.08	-8.80 ± 0.12	-6.95 ± 0.12	-8.93 ± 0.08
1158+0454	-9.46 ± 0.23	-8.69 ± 0.22	—	-7.58 ± 0.22	-9.34 ± 0.23	-7.68 ± 0.23	-8.97 ± 0.22
0744+4649	-9.38 ± 0.12	-8.36 ± 0.08	—	-8.17 ± 0.08	-9.69 ± 0.12	-7.99 ± 0.12	-9.26 ± 0.08
1040+2407	-9.27 ± 0.13	-8.2 ± 0.1	—	-7.59 ± 0.1	-9.35 ± 0.13	-7.29 ± 0.13	-8.88 ± 0.1
0807+4930	-9.06 ± 0.33	-8.39 ± 0.31	—	-7.28 ± 0.31	-9.34 ± 0.33	-7.58 ± 0.33	-9.27 ± 0.31
1014+2827	-9.05 ± 0.35	-7.68 ± 0.34	—	-6.47 ± 0.34	-8.43 ± 0.35	-6.47 ± 0.35	-7.86 ± 0.34
1234+5208	-8.87 ± 0.13	-7.4 ± 0.09	—	-6.39 ± 0.09	-7.95 ± 0.13	-6 ± 0.13	-7.9 ± 0.09
1430-0151	-8.8 ± 0.18	-7.55 ± 0.16	—	-6.99 ± 0.16	-8.5 ± 0.18	-6.54 ± 0.18	-8.13 ± 0.16
0901+0752	-8.79 ± 0.14	-7.12 ± 0.11	—	-6.21 ± 0.11	-8.07 ± 0.14	-6.21 ± 0.14	-7.7 ± 0.11
0916+2540	-8.75 ± 0.12	-7.48 ± 0.08	—	-7.09 ± 0.08	-8.9 ± 0.12	-6.83 ± 0.12	-9.32 ± 0.08
1132+3323	-8.7 ± 0.29	-8.23 ± 0.28	—	-7.32 ± 0.28	-8.88 ± 0.29	-6.82 ± 0.29	-8.71 ± 0.28
1351+2645	-8.61 ± 0.19	-8.04 ± 0.17	—	-7.53 ± 0.17	-9.19 ± 0.19	-8.33 ± 0.19	-9.72 ± 0.17
1024+1014	-8.52 ± 0.29	-7.5 ± 0.28	—	-6.64 ± 0.28	-8.4 ± 0.29	-6.54 ± 0.29	-8.63 ± 0.28
0806+4058	—	-8.49 ± 0.08	-9 ± 0.12	-7.49 ± 0.08	-9.11 ± 0.12	-7.38 ± 0.12	-8.33 ± 0.08
0116+2050	-9.74 ± 0.12	-8.81 ± 0.09	-8.76 ± 0.12	-7.6 ± 0.09	—	-7.65 ± 0.12	-9.29 ± 0.09
1043+3516	-10.54 ± 0.15	-8.88 ± 0.12	-8.55 ± 0.15	-7.2 ± 0.12	-8.92 ± 0.15	-8 ± 0.15	—
0741+3146	-10.06 ± 0.18	-9.55 ± 0.16	-9.09 ± 0.18	-7.5 ± 0.16	-9.6 ± 0.18	-8.94 ± 0.18	—
0150+1354	—	-7.75 ± 0.17	—	-7.24 ± 0.17	-10.1 ± 0.19	-6.54 ± 0.19	-8.03 ± 0.17
0512-0505	—	-8.99 ± 0.06	—	-7.79 ± 0.06	-10.09 ± 0.1	-8.05 ± 0.1	-9.65 ± 0.06
0852+3402	—	-9 ± 0.2	—	-7.79 ± 0.2	-9.75 ± 0.22	-8.39 ± 0.22	-9.58 ± 0.2
1524+4049	—	-8.9 ± 0.12	—	-7.79 ± 0.12	-9.65 ± 0.15	-7.69 ± 0.15	-9.18 ± 0.12
1336+3547	—	-8.5 ± 0.07	—	-7.39 ± 0.07	-9.4 ± 0.11	-7.1 ± 0.11	-9 ± 0.07
1321-0237	—	-8.48 ± 0.27	—	-7.47 ± 0.27	-9.33 ± 0.29	-7.47 ± 0.29	-8.36 ± 0.27
0937+5228	–	-8.4 ± 0.09	—	-7.5 ± 0.09	-9.25 ± 0.13	-7.09 ± 0.13	-8.98 ± 0.09
0758+1013	-8.65 ± 0.33	—	-7.34 ± 0.33	-9.2 ± 0.34	-7.54 ± 0.34	-8.73 ± 0.33	
1411+3410	—	-8.4 ± 0.25	—	-7.39 ± 0.25	-9.15 ± 0.26	-7.24 ± 0.26	-9.28 ± 0.25
0929+4247	—	-8.46 ± 0.16	—	-7.15 ± 0.16	-9.01 ± 0.18	-6.85 ± 0.18	-8.64 ± 0.16
0736+4118	—	-8.5 ± 0.12	—	-7.69 ± 0.12	-8.95 ± 0.15	-7.69 ± 0.15	-9.68 ± 0.12
1220+0929	—	-8.38 ± 0.15	—	-7.37 ± 0.15	-8.93 ± 0.17	-7.07 ± 0.17	-8.46 ± 0.15
2230+1905	—	-8.45 ± 0.28	—	-7.24 ± 0.28	-8.9 ± 0.29	-7.14 ± 0.29	-8.73 ± 0.28
1649+2238	—	-8.62 ± 0.18	—	-7.21 ± 0.18	-8.83 ± 0.2	-6.89 ± 0.2	-8.29 ± 0.18
1549+1906	—	-8.48 ± 0.28	—	-7.22 ± 0.28	-8.78 ± 0.3	-7.17 ± 0.3	-9.11 ± 0.28
0939+5019	–	-8.25 ± 0.2	—	-7.14 ± 0.2	-8.7 ± 0.22	-7.04 ± 0.22	-9.23 ± 0.2
1038-0036	-9.6 ± 0.1	-7.85 ± 0.06	—	-7.4 ± 0.06	—	-6.8 ± 0.1	-8.6 ± 0.06
1542+4650	—	-8.15 ± 0.23	—	-7.04 ± 0.23	-8.7 ± 0.25	-6.94 ± 0.25	-8.18 ± 0.23
1546+3009	—	-8.4 ± 0.12	—	-7.19 ± 0.12	-8.65 ± 0.15	-7.19 ± 0.15	-8.78 ± 0.12
0252+0054	—	-8.35 ± 0.16	—	-7.14 ± 0.16	—	-7.24 ± 0.19	-7.83 ± 0.16
1445+0913	—	-7.98 ± 0.23	—	-6.77 ± 0.23	-8.58 ± 0.24	-6.77 ± 0.24	-7.81 ± 0.23
0939+4136	—	-8.3 ± 0.19	—	-6.79 ± 0.19	-8.55 ± 0.2	-7.09 ± 0.2	-8.58 ± 0.19
0047+1628	—	-7.68 ± 0.18	—	-6.47 ± 0.18	-8.53 ± 0.2	-6.77 ± 0.2	-8.66 ± 0.18
1102+2827	—	-7.75 ± 0.38	—	-6.44 ± 0.38	-8.3 ± 0.39	-6.24 ± 0.39	-7.73 ± 0.38
0956+5912	—	-7.15 ± 0.09	—	-6.14 ± 0.09	-7.5 ± 0.12	-5.3 ± 0.12	-6.6 ± 0.09
1038+0432	—	-7.5 ± 0.16	—	-6.99 ± 0.16	-8.7 ± 0.18	-6.84 ± 0.18	-9.13 ± 0.16
0906+1141	-8.62 ± 0.26	-7.9 ± 0.25	—	-6.94 ± 0.25	—	-6.64 ± 0.26	-8.43 ± 0.25
0823+0546	-9.9 ± 0.11	-9.34 ± 0.06	-8.59 ± 0.11	-7.36 ± 0.06	—	-8.51 ± 0.11	—
1345+1153	-9.07 ± 0.23	-8.1 ± 0.21	—	-6.89 ± 0.21	-8.7 ± 0.23	-7.49 ± 0.23	—
0913+4127	-9.04 ± 0.33	-8.52 ± 0.31	—	-7.16 ± 0.31	-9.42 ± 0.33	-7.86 ± 0.33	—
0816+2330	-8.65 ± 0.26	-7.48 ± 0.25	–	-6.37 ± 0.25	-7.68 ± 0.26	-6.27 ± 0.26	—
1144+1218	—	-9.33 ± 0.11	-10.13 ± 0.14	-8.37 ± 0.11	-10.22 ± 0.14	-8.13 ± 0.14	—
1636+1619	—	-9.5 ± 0.21	—	-8.79 ± 0.21	—	-8.29 ± 0.23	-10.18 ± 0.21
1518+0506	—	-9.65 ± 0.13	—	-8.74 ± 0.13	—	-8.64 ± 0.15	-10.03 ± 0.13
1147+5429	—	-9.17 ± 0.4	—	-8.06 ± 0.4	—	-8.16 ± 0.41	-9.85 ± 0.4
1257-0310	—	-8.52 ± 0.24	—	-7.31 ± 0.24	—	-7.26 ± 0.25	—
0925+3130	—	-9 ± 0.1	—	-7.99 ± 0.1	—	-7.79 ± 0.13	-9.68 ± 0.1
0019+2209	—	-9.34 ± 0.16	—	-8.58 ± 0.16	—	-8.53 ± 0.18	-9.42 ± 0.16
0108-0537	—	-8.79 ± 0.14	—	-8.08 ± 0.14	—	-8.18 ± 0.16	-9.27 ± 0.14
0744+4408	—	-8.75 ± 0.23	—	-7.54 ± 0.23	—	-7.64 ± 0.25	-9.23 ± 0.23
1329+1301	—	-8.55 ± 0.14	—	-7.44 ± 0.14	—	-7.34 ± 0.17	-9.23 ± 0.14
2123+0016	—	-10.01 ± 0.17	—	-8.5 ± 0.17	—	-8.5 ± 0.19	-9.19 ± 0.17
2157+1206	—	-9 ± 0.1	—	-8.09 ± 0.1	—	-7.79 ± 0.13	-9.18 ± 0.1
1103+4144	—	-9.3 ± 0.11	—	-8.04 ± 0.11	—	-7.94 ± 0.14	-9.13 ± 0.11
1032+1338	—	-9.33 ± 0.28	—	-8.02 ± 0.28	—	-7.82 ± 0.3	-9.01 ± 0.28
1405+1549	—	-8.25 ± 0.1	—	-7.14 ± 0.1	—	-7.14 ± 0.14	-8.93 ± 0.1
1554+1735	—	-8.6 ± 0.07	—	-7.64 ± 0.07	—	-7.54 ± 0.11	-8.9 ± 0.07
1238+2149	—	-9.11 ± 0.22	—	-8 ± 0.22	—	-8.1 ± 0.24	-8.89 ± 0.22
2235-0056	—	-8.67 ± 0.2	—	-7.26 ± 0.2	—	-7.66 ± 0.22	-8.85 ± 0.2
0208-0542	—	-8.54 ± 0.38	—	-7.33 ± 0.38	—	-7.53 ± 0.39	-8.82 ± 0.38

Table A.2 White dwarf data from Hollands et al. (2017).

System	[Ti/He]	[Ca/He]	[Ni/He]	[Fe/He]	[Cr/He]	[Mg/He]	[Na/He]
0004+0819	—	-8.72 ± 0.42	—	-7.51 ± 0.42	—	-7.51 ± 0.43	-8.8 ± 0.42
1112+0700	—	-8.53 ± 0.15	—	-7.37 ± 0.15	—	-7.12 ± 0.17	-8.76 ± 0.15
1205+3536	—	-8.74 ± 0.16	—	-7.63 ± 0.16	—	-7.43 ± 0.18	-8.72 ± 0.16
1314+3748	—	-8.48 ± 0.34	—	-7.52 ± 0.34	—	-7.42 ± 0.35	-8.71 ± 0.34
0143+0113	—	-8.5 ± 0.08	—	-7.3 ± 0.08	—	-7.1 ± 0.12	-8.68 ± 0.08
1245+0822	—	-8.1 ± 0.19	—	-7.59 ± 0.19	—	-7.34 ± 0.21	-8.68 ± 0.19
2333+1058	—	-8.79 ± 0.31	—	-7.38 ± 0.31	—	-7.28 ± 0.32	-8.67 ± 0.31
1211+2326	—	-8.59 ± 0.23	—	-7.28 ± 0.23	—	-7.28 ± 0.25	-8.57 ± 0.23
1134+1542	—	-8.46 ± 0.24	—	-7.35 ± 0.24	—	-7.25 ± 0.25	-8.44 ± 0.24
2352+3344	—	-8.26 ± 0.2	—	-7.05 ± 0.2	—	-6.85 ± 0.22	-8.34 ± 0.2
1144+3720	—	-8.17 ± 0.17	—	-7.16 ± 0.17	—	-6.96 ± 0.19	-8.25 ± 0.17
0843+5614	—	-8.65 ± 0.16	—	-7.74 ± 0.16	—	-7.44 ± 0.18	-8.23 ± 0.16
0144+1920	—	-8.5 ± 0.18	—	-7.39 ± 0.18	—	-7.34 ± 0.2	-8.18 ± 0.18
1017+2419	—	-8.07 ± 0.14	—	-6.96 ± 0.14	—	-6.86 ± 0.16	-8.15 ± 0.14
1356+0236	—	-7.52 ± 0.15	—	-6.41 ± 0.15	—	-6.21 ± 0.17	-8 ± 0.15
1320+0204	—	-8.28 ± 0.28	—	-7.17 ± 0.28	—	-7.37 ± 0.29	-7.96 ± 0.28
0252-0401	—	-8.57 ± 0.15	—	-7.46 ± 0.15	-8.62 ± 0.17	-6.96 ± 0.17	-8.25 ± 0.15
2319+3018	—	-8.53 ± 0.18	—	-7.37 ± 0.18	—	-7.42 ± 0.2	-7.71 ± 0.18
1340+2702	—	-6.98 ± 0.22	—	-6.27 ± 0.22	—	-5.73 ± 0.23	-7.41 ± 0.22
0052+1846	—	-9.04 ± 0.32	—	-7.53 ± 0.32	-9.59 ± 0.33	-7.83 ± 0.33	—
0117+0021	—	-8.8 ± 0.08	—	-7.6 ± 0.08	-9.48 ± 0.12	-7.5 ± 0.12	—
1055+3725	—	-8.24 ± 0.14	—	-7.83 ± 0.14	-9.19 ± 0.16	-8.23 ± 0.16	—
0114+3505	—	-8.51 ± 0.21	—	-7.2 ± 0.21	-9.06 ± 0.23	-7.3 ± 0.23	—
0933+6334	—	-8.28 ± 0.38	—	-6.77 ± 0.38	-8.83 ± 0.39	-7.17 ± 0.39	—
1347+1415	—	-8.5 ± 0.11	—	-7.29 ± 0.11	-8.75 ± 0.14	-7.19 ± 0.14	—
1627+4646	—	-8.88 ± 0.2	—	-7.62 ± 0.2	-8.73 ± 0.22	-8.07 ± 0.22	—
0806+3055	—	-7.77 ± 0.23	—	7.16 ± 0.23	-8.47 ± 0.25	-7.01 ± 0.25	—
0046+2717	—	-7.65 ± 0.24	—	-6.84 ± 0.24	-7.8 ± 0.26	-6.19 ± 0.26	—
1626+3303	-9.04 ± 0.27	-8.87 ± 0.25	—	-7.61 ± 0.25	—	-7.41 ± 0.27	—
1308+0957	—	-8.03 ± 0.26	—	-6.62 ± 0.26	—	-7.52 ± 0.27	—
1033+1809	—	-8.55 ± 0.25	—	-8.04 ± 0.25	—	-8.84 ± 0.26	—
2109-0039	—	-8.78 ± 0.25	—	-7.67 ± 0.25	—	-8.42 ± 0.27	—
1158+5942	—	-8.98 ± 0.18	—	-8.02 ± 0.18	—	-8.72 ± 0.2	—
1005+2244	—	-8.96 ± 0.32	—	-7.4 ± 0.32	—	-8.1 ± 0.34	—
1006+1752	—	-9.45 ± 0.21	—	-8.34 ± 0.21	—	-8.94 ± 0.23	—
1259+3112	—	-9.65 ± 0.26	—	-8.14 ± 0.26	—	-8.74 ± 0.27	—
1308+0258	—	-9.07 ± 0.22	—	-7.66 ± 0.22	—	-8.16 ± 0.24	—
1019+2045	—	-9.36 ± 0.26	—	-8.25 ± 0.26	—	-8.65 ± 0.27	—
2231+0906	—	-9.85 ± 0.09	—	-8.84 ± 0.09	—	-9.24 ± 0.13	—
0126+2534	—	-9.95 ± 0.15	—	-8.64 ± 0.15	—	-8.94 ± 0.17	—
1610+4006	—	-8.47 ± 0.27	—	-7.11 ± 0.27	—	-7.46 ± 0.28	—
2340+0817	—	-9 ± 0.14	—	-7.69 ± 0.14	—	-7.99 ± 0.17	—
1218+0023	—	-9.61 ± 0.1	—	-8.9 ± 0.1	—	-9.2 ± 0.13	—
0002+3209	—	-9.05 ± 0.18	—	-7.84 ± 0.18	—	-8.14 ± 0.2	—
1259+4729	—	-8.8 ± 0.29	—	-7.99 ± 0.29	—	-8.29 ± 0.31	—
1534+1242	—	-8.29 ± 0.37	—	-7.48 ± 0.37	—	-7.78 ± 0.38	—
1150+4928	—	-8.76 ± 0.14	—	-7.65 ± 0.14	—	-7.95 ± 0.16	—
0908+5136	—	-9.35 ± 0.1	—	-8.24 ± 0.1	—	-8.5 ± 0.13	—
0148-0112	—	-8.82 ± 0.2	—	-7.31 ± 0.2	—	-7.56 ± 0.21	—
2238-0113	—	-8.89 ± 0.25	—	-7.78 ± 0.25	—	-7.73 ± 0.26	—
0158-0942	—	-9.52 ± 0.18	—	-8.41 ± 0.18	—	-8.61 ± 0.2	—
0830-0319	—	-9.1 ± 0.11	—	-8.29 ± 0.11	—	-8.49 ± 0.14	—
1230+3143	—	-9.12 ± 0.16	—	-8.21 ± 0.16	—	-8.41 ± 0.18	—
1350+1058	—	-10.06 ± 0.2	—	-8.75 ± 0.2	—	-8.85 ± 0.22	—
1041+3432	—	-8.2 ± 0.19	—	-7.29 ± 0.19	—	-7.49 ± 0.21	—
1046+1329	—	-9.6 ± 0.28	—	-8.29 ± 0.28	—	-8.39 ± 0.29	—
0913+2627	—	-9.75 ± 0.21	—	-8.64 ± 0.21	—	-8.74 ± 0.23	—
1342+1813	—	-9.19 ± 0.26	—	-8.58 ± 0.26	$-$	-8.68 ± 0.28	—
1102+0214	—	-9.75 ± 0.14	—	-8.74 ± 0.1	—	-8.84 ± 0.13	—
1405+2542	—	-9.5 ± 0.2	—	-8.39 ± 0.2	—	-8.49 ± 0.22	—
2110+0512	—	-9.21 ± 0.29	—	-8 ± 0.29	—	-8.1 ± 0.3	—
0044+0418	—	-9.82 ± 0.08	—	-8.71 ± 0.08	—	-8.81 ± 0.12	—
1017+3447	—	-9.34 ± 0.19	—	-8.33 ± 0.19	—	-8.43 ± 0.21	—
0013+1109	$-$	-9.11 ± 0.35	—	-8.1 ± 0.35	—	-8.2 ± 0.36	—
1545+5236	—	-9.19 ± 0.13	—	-8.18 ± 0.13	—	-8.28 ± 0.16	—
2328+0830	—	-8.8 ± 0.36	—	-7.59 ± 0.36	—	-7.69 ± 0.37	—
2330+2805	—	-8.84 ± 0.2	—	-7.63 ± 0.2	—	-7.73 ± 0.22	—
2352+1922	—	-8.34 ± 0.32	—	-7.03 ± 0.32	—	-7.13 ± 0.33	—
0818+1247	—	-8.58 ± 0.25	—	-7.77 ± 0.25	—	-7.87 ± 0.27	—
1319+3641	—	-8.6 ± 0.16	—	-7.49 ± 0.16	—	-7.59 ± 0.19	—

Table A.3 White dwarf data from Hollands et al. (2017).

System	[Ti/He]	[Ca/He]	[Ni/He]	[Fe/He]	[Cr/He]	[Mg/He]	[Na/He]
1502+3744	—	-10 ± 0.12	—	-8.99 ± 0.12	—	-8.99 ± 0.15	—
0135+1302	—	-9.5 ± 0.11	—	-8.69 ± 0.11	—	-8.7 ± 0.14	—
1429+3841	—	-9.73 ± 0.28	—	-8.72 ± 0.28	—	-8.72 ± 0.29	—
0842+1536	—	-9.47 ± 0.22	—	-8.46 ± 0.22	—	-8.46 ± 0.24	—
0800+2242	—	-9.75 ± 0.27	—	-8.69 ± 0.27	—	-8.69 ± 0.28	—
1158+4712	—	-8.06 ± 0.18	—	-6.85 ± 0.18	—	-6.9 ± 0.2	—
0744+2701	—	-7.68 ± 0.17	—	-6.87 ± 0.17	—	-6.92 ± 0.19	—
1158+5448	—	-8.82 ± 0.34	—	-7.61 ± 0.34	—	-7.61 ± 0.35	—
1448+1047	—	-8.85 ± 0.09	—	-7.8 ± 0.09	—	-7.77 ± 0.13	—
1024+4531	—	-8.92 ± 0.17	—	-8.11 ± 0.17	—	-8.06 ± 0.19	—
0739+3112	—	-9.5 ± 0.4	—	-8.39 ± 0.4	—	-8.29 ± 0.41	—
1641+1856	—	-10.3 ± 0.11	—	-9.59 ± 0.11	—	-9.49 ± 0.14	—
0056+2453	—	-9.62 ± 0.36	—	-8.71 ± 0.36	—	-8.61 ± 0.37	—
0908+4119	—	-8.73 ± 0.29	—	-7.12 ± 0.29	—	-7.07 ± 0.3	—
1257+3238	—	-9.02 ± 0.42	—	-7.61 ± 0.42	—	-7.81 ± 0.43	-9.7 ± 0.42
0924+4301	—	-9.75 ± 0.26	—	-8.54 ± 0.26	—	-8.44 ± 0.27	—
2238+0213	—	-8.56 ± 0.23	—	-7.3 ± 0.23	—	-7.55 ± 0.25	—
1401+3659	—	-9.8 ± 0.11	—	-8.94 ± 0.11	—	-8.84 ± 0.14	—
1543+2024	—	-8.09 ± 0.36	—	-7.38 ± 0.36	—	-7.33 ± 0.37	—
0144+0305	—	-8.37 ± 0.31	—	-7.26 ± 0.31	—	-7.21 ± 0.32	—
1019+3535	—	-8.75 ± 0.3	—	-7.74 ± 0.3	—	-7.64 ± 0.31	—
1604+1830	—	-9.48 ± 0.12	—	-8.57 ± 0.12	—	-8.47 ± 0.15	—
2357+2348	—	-9.07 ± 0.25	—	-7.76 ± 0.25	—	-7.66 ± 0.27	—
1443+5833	—	-8.56 ± 0.31	—	-7.25 ± 0.31	—	-7.15 ± 0.32	—
1612+3534	—	-8.54 ± 0.38	—	-7.53 ± 0.38	—	-7.43 ± 0.39	—
1224+2838	—	-10 ± 0.13	—	-8.89 ± 0.13	—	-8.69 ± 0.16	—
0842+1406	—	-8.16 ± 0.08	—	-7.3 ± 0.08	—	-7.2 ± 0.12	—
1157+6138	—	-9.15 ± 0.37	—	-7.64 ± 0.37	—	-7.44 ± 0.38	—
1428+4403	—	-8.98 ± 0.06	—	-8.4 ± 0.06	—	-8.2 ± 0.11	—
1058+3143	—	-9.02 ± 0.09	—	-8.01 ± 0.09	—	-7.81 ± 0.13	—
1226+2936	—	-10.04 ± 0.33	—	-8.93 ± 0.33	—	-8.63 ± 0.34	—
1254+3551	—	-8.96 ± 0.21	—	-7.75 ± 0.21	—	-7.55 ± 0.22	—
1152+5101	—	-10.08 ± 0.3	—	-8.97 ± 0.3	—	-8.67 ± 0.31	—
0010-0430	—	-8.38 ± 0.15	—	-7.12 ± 0.15	—	-6.92 ± 0.17	—
1537+3608	—	-9.5 ± 0.3	—	-8.49 ± 0.3	—	-8.19 ± 0.32	—
1624+3310	—	-8.64 ± 0.31	—	-7.53 ± 0.31	—	-7.28 ± 0.32	—
1549+2633	—	-9.66 ± 0.18	—	-8.25 ± 0.18	—	-7.95 ± 0.2	—
1443+3014	—	-8.16 ± 0.28	—	-7.15 ± 0.28	—	-6.9 ± 0.29	—
1105+0228	—	-9.1 ± 0.28	—	-8.14 ± 0.28	—	-7.84 ± 0.3	—
1339+2643	—	-9.13 ± 0.07	—	-8.6 ± 0.07	—	-8.3 ± 0.11	—
0721+3928	—	-8.9 ± 0.15	—	-8.09 ± 0.15	—	-7.79 ± 0.17	—
0006+0520	—	-9 ± 0.16	—	-8.39 ± 0.16	—	-8.09 ± 0.18	—
0851+1543	—	-8.5 ± 0.09	—	-8.2 ± 0.09	—	-7.89 ± 0.12	—
1500+2315	—	-8.4 ± 0.42	—	-7.19 ± 0.42	—	-6.89 ± 0.43	—
0234-0510	—	-8.27 ± 0.31	—	-7.21 ± 0.31	—	-6.91 ± 0.32	—
1149+0519	—	-8.16 ± 0.12	—	-7.6 ± 0.12	—	-7.3 ± 0.15	—
1421+1843	—	-7.35 ± 0.18	—	-6.19 ± 0.18	—	-5.89 ± 0.2	—
0838+2322	—	-9.8 ± 0.09	—	-9.3 ± 0.09	—	-8.89 ± 0.12	—
2340+0124	—	-8.5 ± 0.1	—	-7.9 ± 0.1	—	-7.54 ± 0.13	—
2343-0010	—	-9.23 ± 0.31	—	-8.22 ± 0.31	—	-7.82 ± 0.33	—
0948+3008	—	-9.15 ± 0.14	—	-8.44 ± 0.14	—	-8.04 ± 0.17	—
1303+4055	—	-9.02 ± 0.12	—	-8.11 ± 0.12	—	-7.71 ± 0.15	—
0053+3115	—	-8.87 ± 0.33	—	-8.66 ± 0.33	—	-8.26 ± 0.34	—
1706+2541	—	-9.4 ± 0.25	—	-8.89 ± 0.25	—	-8.49 ± 0.26	—
1217+1157	—	-8.93 ± 0.14	—	-7.92 ± 0.14	—	-7.52 ± 0.17	—
1540+5352	—	-8.58 ± 0.35	—	-7.47 ± 0.35	—	-7.07 ± 0.36	—
2225+2338	—	-8.81 ± 0.12	—	-7.8 ± 0.12	—	-7.4 ± 0.15	—
1316+1918	—	-9.9 ± 0.23	—	-8.99 ± 0.23	—	-8.49 ± 0.25	—
0946+2024	—	-8.07 ± 0.34	—	-7.06 ± 0.34	—	-6.66 ± 0.35	—
1404+3620	—	-9.2 ± 0.08	—	-8.5 ± 0.08	—	-7.9 ± 0.12	—
0201+2015	—	-8.96 ± 0.14	—	-8.25 ± 0.14	—	-7.65 ± 0.17	—
0744+1640	—	-10.24 ± 0.24	—	-9.33 ± 0.24	—	-8.63 ± 0.26	—
1507+4034	—	-8.18 ± 0.3	—	-7.17 ± 0.3	—	-6.57 ± 0.31	—
1356+2416	—	-9.2 ± 0.13	—	-8.54 ± 0.13	—	-7.84 ± 0.15	—
0447+1124	—	-8.77 ± 0.19	—	-8.06 ± 0.19	—	-7.26 ± 0.21	—
2304+2415	—	-9.54 ± 0.13	—	-8.93 ± 0.13	—	-7.98 ± 0.15	—
0902+1004	—	-8.25 ± 0.22	—	-8.19 ± 0.22	—	-7.29 ± 0.24	—
1158+1845	—	-7.75 ± 0.15	—	-6.84 ± 0.15	—	-5.74 ± 0.17	—

Table A.4 White dwarf data from Hollands et al. (2017).

System	q	S/N	t_{Ti}	t_{Ca}	t_{Ni}	t_{Fe}	t_{Cr}	t_{Mg}	t_{Na}
1535+1247	-5.54	57.94	5.99	6.03	6.07	6.03	6.01	6.49	6.44
1330+3029	-5.51	41.29	6.00	6.04	6.08	6.05	6.02	6.49	6.44
1229+0743	-5.53	10.63	5.98	6.02	6.06	6.03	6.00	6.46	6.41
1616+3303	-5.46	19.16	6.02	6.06	6.11	6.07	6.05	6.50	6.46
1158+0454	-5.62	6.05	5.95	6.01	6.03	5.99	5.97	6.47	6.42
0744+4649	-5.72	21.98	5.87	5.92	5.95	5.92	5.89	6.39	6.34
1040+2407	-5.62	14.26	5.92	5.96	6	5.97	5.95	6.41	6.36
0807+4930	-5.7	4.12	5.89	5.93	5.96	5.93	5.91	6.4	6.35
1014+2827	-5.59	3.85	5.92	6.36	6.01	5.97	5.95	6.39	6.34
1234+5208	-5.37	16.57	6.05	6.08	6.14	6.1	6.08	6.49	6.45
1430-0151	-5.64	8.27	5.89	5.92	5.97	5.94	5.91	6.35	6.31
0901+0752	-5.51	13.18	5.95	5.98	6.04	6	5.98	6.4	6.35
0916+2540	-5.82	21.06	5.77	5.81	5.85	5.82	5.8	6.25	6.21
1132+3323	-5.5	4.72	6	6.03	6.08	6.04	6.02	6.48	6.43
1351+2645	-5.59	7.7	5.93	5.97	6.01	5.98	5.96	6.41	6.37
1024+1014	-5.61	4.62	5.91	5.94	5.99	6.36	5.93	6.37	6.32
0806+4058	-5.34	21.08	6.11	6.14	6.19	6.15	6.13	6.58	6.53
0116+2050	-5.42	18.53	6.07	6.11	6.15	6.12	6.09	6.57	6.52
1043+3516	-5.3	11.82	6.14	6.18	6.22	6.19	6.17	6.63	6.58
0741+3146	-5.4	8.54	6.11	6.31	6.19	6.15	6.13	6.65	6.59
0150+1354	-5.56	8.03	5.94	5.97	6.02	5.99	5.97	6.41	6.36
0512-0505	-5.51	45	6.02	6.11	6.1	6.07	6.04	6.54	6.49
0852+3402	-5.51	6.43	6.03	6.11	6.1	6.07	6.05	6.54	6.49
1524+4049	-5.47	11.27	6.05	6.09	6.12	6.09	6.07	6.55	6.5
1336+3547	-5.38	28.44	6.08	6.12	6.17	6.13	6.11	6.56	6.52
1321-0237	-5.6	4.76	5.95	6.39	6.03	5.99	5.97	6.45	6.4
0937+5228	-5.39	16.23	6.07	6.11	6.15	6.12	6.09	6.55	6.5
0758+1013	-5.59	3.92	5.96	6.01	6.04	6.01	5.99	6.48	6.43
1411+3410	-5.64	5.32	5.92	6.36	6	5.97	5.94	6.43	6.38
0929+4247	-5.4	8.39	6.07	6.11	6.15	6.12	6.09	6.55	6.5
0736+4118	-5.68	11.75	5.9	5.95	5.98	5.95	5.92	6.42	6.37
1220+0929	-5.39	9.38	6.07	6.11	6.16	6.12	6.1	6.55	6.5
2230+1905	-5.61	4.61	5.94	5.99	6.02	5.99	5.96	6.45	6.4
1649+2238	-5.62	7.18	5.94	6.39	6.02	5.95	5.97	6.46	6.41
1549+1906	-5.41	4.56	6.06	6.1	6.14	6.11	6.08	6.54	6.5
0939+5019	-5.56	6.65	5.96	6	6.04	6.01	5.99	6.45	6.4
1038-0036	-5.28	51.05	5.93	5.97	6.02	5.98	5.96	6.39	6.35
1542+4650	-5.56	5.66	5.96	6	6.04	6.01	5.98	6.44	6.39
1546+3009	-5.39	12.08	6.07	6.11	6.15	6.12	6.09	6.55	6.5
0252+0054	-5.23	8.17	6.13	6.17	6.21	6.18	6.16	6.6	6.56
1445+0913	-5.46	5.82	6.01	6.05	6.09	6.06	6.04	6.48	6.43
0939+4136	-5.48	7.14	6.02	6.05	6.1	6.06	6.04	6.5	6.45
0047+1628	-5.51	7.56	5.97	6.01	6.06	6.02	6	6.43	6.39
1102+2827	-5.54	3.41	5.95	5.99	6.04	6	5.98	6.42	6.37

Table A.5 White dwarf data from Hollands et al. (2017).

System	q	S/N	t_{Ti}	t_{Ca}	t_{Ni}	t_{Fe}	t_{Cr}	t_{Mg}	t_{Na}
0956+5912	-5.3	17.71	6.08	6.11	6.18	6.14	6.11	6.51	6.47
1038+0432	-5.56	8.28	6.12	6.15	6.21	6.17	6.14	6.57	6.52
0906+1141	-5.41	5.24	6.04	6.08	6.13	6.09	6.07	6.51	6.46
0823+0546	-5.37	35	6.12	6.26	6.2	6.16	6.14	6.64	6.59
1345+1153	-5.58	6.2	5.95	5.98	6.03	5.99	5.97	6.43	6.38
0913+4127	-5.56	4.12	5.97	6.02	6.05	6.02	6	6.47	6.42
0816+2330	-5.33	5.3	6.07	6.1	6.16	6.13	6.1	6.52	6.47
1144+1218	-5.47	12.97	6.07	6.24	6.14	6.11	6.09	6.6	6.55
1636+1619	-5.56	6.31	6.05	6.32	6.1	6.07	6.05	6.61	6.56
1518+0506	-5.47	10.89	6.09	6.34	6.16	6.13	6.11	6.64	6.59
1147+5429	-5.52	3.21	6.03	6.18	6.11	6.07	6.05	6.57	6.51
1257-0310	-5.45	5.55	6	6.13	6.07	6.04	6.02	6.53	6.48
0925+3130	-5.47	14.5	6.05	6.11	6.13	6.09	6.07	6.56	6.51
0019+2209	-5.38	8.57	6.12	6.25	6.19	6.16	6.14	6.63	6.58
0108-0537	-5.46	9.81	6.04	6.09	6.12	6.09	6.06	6.54	6.49
0744+4408	-5.39	5.58	6.08	6.12	6.16	6.13	6.11	6.57	6.53
1329+1301	-5.33	9.61	6.11	6.15	6.2	6.16	6.14	6.59	6.54
2123+0016	-5.38	8.02	6.18	6.46	6.22	6.19	6.17	6.71	6.65
2157+1206	-5.41	14.89	6.08	6.13	6.16	6.13	6.11	6.59	6.54
1103+4144	-5.41	12.77	6.1	6.24	6.18	6.14	6.12	6.62	6.57
1032+1338	-5.46	4.59	6.07	6.24	6.15	6.11	6.09	6.6	6.55
1405+1549	-5.3	13.94	6.12	6.15	6.2	6.17	6.14	6.58	6.54
1554+1735	-5.36	30.09	6.1	6.14	6.18	6.15	6.12	6.58	6.53
1238+2149	-5.51	5.96	6.03	6.16	6.11	6.07	6.05	6.56	6.51
2235-0056	-5.41	6.52	6.07	6.11	6.15	6.12	6.09	6.56	6.51
0208-0542	-5.55	3.39	5.98	6.02	6.06	6.02	6	6.48	6.43
0004+0819	-5.51	3.07	6.01	6.05	6.09	6.05	6.03	6.51	6.46
1112+0700	-5.2	9.12	6.19	6.22	6.27	6.24	6.21	6.65	6.6
1205+3536	-5.46	8.59	6.04	6.08	6.12	6.09	6.07	6.54	6.49
1314+3748	-5.53	3.81	5.99	6.03	6.07	6.03	6.01	6.48	6.43
0143+0113	-5.36	21.16	6.09	6.13	6.18	6.14	6.12	6.57	6.53
1245+0822	-5.5	7.07	6	6.03	6.08	6.04	6.02	6.47	6.43
2333+1058	-5.42	4.16	6.07	6.11	6.15	6.12	6.09	6.57	6.52
1211+2326	-5.4	5.64	6.07	6.11	6.16	6.12	6.1	6.56	6.51
1134+1542	-5.37	5.49	6.09	6.12	6.17	6.14	6.11	6.57	6.52
2352+3344	-5.29	6.66	6.13	6.16	6.21	6.18	6.15	6.59	6.55
1144+3720	-5.26	8.01	6.14	6.17	6.23	6.19	6.17	6.6	6.55
0843+5614	-5.36	8.22	6.1	6.14	6.18	6.15	6.12	6.59	6.54
0144+1920	-5.4	7.24	6.07	6.11	6.15	6.12	6.09	6.55	6.5
1017+2419	-5.32	10.14	6.1	6.13	6.19	6.15	6.13	6.56	6.52
1356+0236	-5.27	9.29	6.11	6.14	6.2	6.17	6.14	6.55	6.5
1320+0204	-5.33	4.65	6.1	6.14	6.19	6.15	6.13	6.57	6.53
0252-0401	-5.3	9.34	6.16	6.19	6.25	6.21	6.19	6.62	6.58
2319+3018	-5.27	7.43	6.15	6.18	6.23	6.2	6.17	6.62	6.57

Table A.6 White dwarf data from Hollands et al. (2017).

System	q	S/N	t_{Ti}	t_{Ca}	t_{Ni}	t_{Fe}	t_{Cr}	t_{Mg}	t_{Na}
1340+2702	-5.43	6.05	6	6.03	6.09	6.06	6.03	6.44	6.39
0052+1846	-5.49	4	6.04	6.13	6.12	6.08	6.06	6.56	6.51
0117+0021	-5.3	20.22	6.14	6.18	6.22	6.19	6.17	6.63	6.58
1055+3725	-5.65	9.84	5.91	5.95	5.99	6.36	5.93	6.41	6.36
0114+3505	-5.43	6.29	6.05	6.09	6.13	6.1	6.08	6.54	6.49
0933+6334	-5.48	3.41	6.01	6.05	6.09	6.06	6.03	6.49	6.44
1347+1415	-5.35	12.88	6.1	6.14	6.18	6.15	6.12	6.58	6.53
1627+4646	-5.36	6.51	6.11	6.15	6.19	6.15	6.13	6.6	6.55
0806+3055	-5.43	5.61	6.03	6.06	6.11	6.08	6.05	6.49	6.44
0046+2717	-5.32	5.37	6.09	6.11	6.17	6.14	6.11	6.54	6.49
1626+3303	-5.4	5.14	6.09	6.13	6.17	6.13	6.11	6.58	6.53
1308+0957	-5.23	5	6.15	6.18	6.24	6.21	6.18	6.61	6.56
1033+1809	-5.49	5.31	6.02	6.06	6.1	6.06	6.04	6.51	6.46
2109-0039	-5.46	5.19	6.04	6.09	6.12	6.09	6.07	6.54	6.49
1158+5942	-5.43	7.27	6.07	6.12	6.15	6.11	6.09	6.57	6.52
1005+2244	-5.36	3.99	6.11	6.15	6.19	6.15	6.13	6.61	6.56
1006+1752	-5.4	6.32	6.11	6.28	6.18	6.15	6.13	6.64	6.58
1259+3112	-5.35	5.06	6.15	6.34	6.22	6.19	6.17	6.67	6.62
1308+0258	-5.41	5.99	6.08	6.15	6.16	6.13	6.11	6.59	6.54
1019+2045	-5.48	5.03	6.06	6.25	6.14	6.1	6.08	6.6	6.55
2231+0906	-5.31	16.22	6.18	6.39	6.25	6.22	6.2	6.71	6.65
0126+2534	-5.37	9.34	6.17	6.44	6.22	6.19	6.17	6.7	6.65
1610+4006	-5.39	4.81	6.08	6.11	6.16	6.12	6.1	6.56	6.51
2340+0817	-5.51	9.7	6.02	6.11	6.1	6.07	6.04	6.54	6.49
1218+0023	-5.32	15.78	6.16	6.34	6.24	6.21	6.18	6.68	6.63
0002+3209	-5.34	7.43	6.13	6.18	6.21	6.17	6.15	6.62	6.57
1259+4729	-5.41	4.42	6.08	6.12	6.16	6.12	6.1	6.57	6.52
1534+1242	-5.58	3.48	5.95	5.99	6.03	6	5.97	6.44	6.39
1150+4928	-5.23	9.78	6.18	6.22	6.26	6.23	6.21	6.66	6.61
0908+5136	-5.34	15.56	6.14	6.26	6.22	6.18	6.16	6.65	6.6
0148-0112	-5.29	6.73	6.15	6.19	6.23	6.19	6.17	6.63	6.58
2238-0113	-5.28	5.25	6.13	6.17	6.22	6.18	6.16	6.61	6.56
0158-0942	-5.35	7.51	6.14	6.32	6.21	6.18	6.16	6.66	6.61
0830-0319	-5.33	13.62	6.13	6.19	6.21	6.18	6.15	6.63	6.58
1230+3143	-5.31	8.59	6.15	6.2	6.23	6.19	6.17	6.64	6.59
1350+1058	-5.38	6.43	6.19	6.48	6.22	6.19	6.17	6.71	6.66
1041+3432	-5.25	6.98	6.14	6.18	6.23	6.2	6.17	6.61	6.56
1046+1329	-5.45	4.64	6.09	6.32	6.16	6.13	6.11	6.64	6.59
0913+2627	-5.42	6.2	6.12	6.37	6.19	6.16	6.14	6.67	6.61
1342+1813	-5.52	4.95	6.03	6.19	6.11	6.07	6.05	6.57	6.51
1102+0214	-5.35	14.96	6.15	6.37	6.23	6.19	6.17	6.69	6.63
1405+2542	-5.37	6.51	6.13	6.31	6.21	6.17	6.15	6.65	6.6

Table A.7 White dwarf data from Hollands et al. (2017).

System	q	S/N	t_{Ti}	t_{Ca}	t_{Ni}	t_{Fe}	t_{Cr}	t_{Mg}	t_{Na}
2110+0512	-5.45	4.54	6.07	6.2	6.15	6.11	6.09	6.59	6.54
0044+0418	-5.3	21.69	6.18	6.39	6.26	6.23	6.2	6.71	6.66
1017+3447	-5.35	6.81	6.13	6.26	6.21	6.18	6.16	6.65	6.59
0013+1109	-5.44	3.66	6.07	6.16	6.15	6.11	6.09	6.58	6.53
1545+5236	-5.43	10.34	6.08	6.19	6.16	6.13	6.1	6.6	6.55
2328+0830	-5.5	3.58	6.02	6.07	6.1	6.06	6.04	6.52	6.47
2330+2805	-5.32	6.46	6.13	6.17	6.21	6.18	6.15	6.62	6.57
2352+1922	-5.5	4.07	6	6.04	6.08	6.05	6.02	6.49	6.44
0818+1247	-5.32	5.17	6.12	6.15	6.2	6.17	6.14	6.6	6.55
1319+3641	-5.22	8.18	6.18	6.21	6.26	6.23	6.2	6.65	6.6
1502+3744	-5.36	11.76	6.18	6.45	6.24	6.2	6.18	6.71	6.66
0135+1302	-5.38	12.99	6.12	6.3	6.2	6.16	6.14	6.65	6.6
1429+3841	-5.31	4.64	6.17	6.37	6.25	6.21	6.19	6.7	6.64
0842+1536	-5.32	5.88	6.15	6.3	6.23	6.2	6.17	6.67	6.61
0800+2242	-5.27	4.84	6.19	6.38	6.27	6.24	6.21	6.71	6.66
1158+4712	-5.25	7.44	6.14	6.17	6.23	6.19	6.17	6.6	6.55
0744+2701	-5.28	7.92	6.11	6.14	6.2	6.16	6.14	6.56	6.51
1158+5448	-5.4	3.79	6.08	6.12	6.16	6.13	6.1	6.58	6.53
1448+1047	-5.34	15.86	6.12	6.16	6.2	6.16	6.14	6.61	6.56
1024+4531	-5.45	7.82	6.06	6.1	6.14	6.1	6.08	6.56	6.51
0739+3112	-5.48	3.21	6.07	6.29	6.14	6.11	6.09	6.62	6.56
1641+1856	-5.27	13.02	6.24	6.52	6.29	6.26	6.24	6.76	6.71
0056+2453	-5.41	3.55	6.11	6.33	6.19	6.15	6.13	6.65	6.6
0908+4119	-5.33	4.46	6.12	6.16	6.2	6.17	6.15	6.61	6.56
1257+3238	-5.56	3.07	6.04	6.08	6.12	6.09	6.06	6.53	6.48
0924+4301	-5.32	5.03	6.17	6.37	6.24	6.21	6.19	6.7	6.64
2238+0213	-5.29	5.62	6.15	6.19	6.23	6.2	6.18	6.64	6.59
1401+3657	-5.31	12.68	6.18	6.38	6.25	6.22	6.2	6.7	6.65
1543+2024	-5.5	3.57	5.99	6.03	6.07	6.04	6.01	6.47	6.42
0144+0305	-5.33	4.2	6.11	6.14	6.19	6.16	6.13	6.58	6.53
1019+3535	-5.51	4.37	6.02	6.06	6.09	6.06	6.04	6.52	6.47
1604+1830	-5.28	11.92	6.18	6.31	6.25	6.22	6.2	6.68	6.63
2357+2348	-5.41	5.13	6.08	6.15	6.16	6.13	6.11	6.59	6.54
1443+5833	-5.28	4.22	6.14	6.18	6.23	6.19	6.17	6.62	6.57
1612+3534	-5.34	3.43	6.11	6.14	6.19	6.15	6.13	6.58	6.54
1224+2838	-5.38	10.61	6.18	6.46	6.22	6.19	6.17	6.71	6.65
0842+1406	-5.32	18.74	6.11	6.14	6.19	6.16	6.13	6.57	6.53
1157+6138	-5.3	3.46	6.15	6.21	6.23	6.2	6.17	6.65	6.6
1428+4403	-5.31	35.3	6.14	6.18	6.22	6.18	6.16	6.63	6.58
1058+3143	-5.26	16.57	6.17	6.21	6.25	6.22	6.2	6.66	6.61
1226+2936	-5.44	3.93	6.18	6.49	6.19	6.16	6.14	6.7	6.64
1254+3551	-5.31	6.34	6.14	6.18	6.22	6.19	6.16	6.63	6.58

Table A.8 White dwarf data from Hollands et al. (2017).

System	q	S/N	t_{Ti}	t_{Ca}	t_{Ni}	t_{Fe}	t_{Cr}	t_{Mg}	t_{Na}
1152+5101	-5.4	4.29	6.19	6.49	6.22	6.18	6.16	6.71	6.65
0010-0430	-5.32	9.11	6.11	6.15	6.19	6.16	6.13	6.58	6.53
1537+3608	-5.42	4.26	6.11	6.3	6.18	6.15	6.12	6.64	6.58
1624+3310	-5.29	4.15	6.14	6.17	6.22	6.18	6.16	6.61	6.57
1549+2633	-5.28	7.37	6.19	6.35	6.26	6.23	6.21	6.7	6.65
1443+3014	-5.38	4.68	6.07	6.1	6.15	6.12	6.09	6.54	6.49
1105+0228	-5.46	4.6	6.06	6.15	6.14	6.11	6.08	6.58	6.53
1339+2643	-5.35	26.46	6.12	6.18	6.2	6.17	6.15	6.63	6.58
0721+3928	-5.39	9.02	6.09	6.13	6.17	6.14	6.12	6.59	6.54
0006+0520	-5.27	8.41	6.16	6.2	6.25	6.21	6.19	6.65	6.6
0851+1543	-5.45	17.56	6.04	6.08	6.12	6.09	6.06	6.53	6.48
1500+2315	-5.41	3.04	6.06	6.1	6.14	6.11	6.08	6.54	6.49
0234-0510	-5.32	4.14	6.11	6.14	6.19	6.16	6.13	6.58	6.53
1149+0519	-5.29	11.18	6.12	6.15	6.21	6.17	6.15	6.58	6.54
1421+1843	-5.43	7.27	6.01	6.04	6.1	6.06	6.04	6.46	6.41
0838+2322	-5.35	17.46	6.16	6.38	6.23	6.19	6.17	6.69	6.64
2340+0124	-5.47	14.5	6.03	6.07	6.11	6.07	6.05	6.52	6.47
2343-0010	-5.41	4.13	6.09	6.21	6.17	6.14	6.12	6.61	6.56
0948+3008	-5.4	9.63	6.09	6.18	6.17	6.14	6.11	6.6	6.55
1303+4055	-5.39	11.43	6.1	6.15	6.18	6.14	6.12	6.6	6.55
0053+3115	-5.41	3.95	6.08	6.12	6.16	6.12	6.1	6.58	6.53
1706+2541	-5.25	5.28	6.19	5.93	6.27	6.23	6.21	6.69	6.64
1217+1157	-5.35	9.43	6.11	6.16	6.19	6.16	6.14	6.61	6.56
1540+5352	-5.38	3.71	6.08	6.12	6.16	6.13	6.11	6.57	6.52
2225+2338	-5.26	11.41	6.16	6.2	6.25	6.21	6.19	6.64	6.59
1316+1918	-5.38	5.68	6.16	6.42	6.22	6.18	6.16	6.7	6.64
0946+2024	-5.27	3.85	6.13	6.16	6.21	6.18	6.15	6.59	6.54
1404+3620	-5.41	21.62	6.09	6.2	6.17	6.13	6.11	6.61	6.55
0201+2015	-5.4	9.55	6.09	6.13	6.17	6.13	6.11	6.59	6.54
0744+1640	-5.38	5.34	6.23	6.55	6.23	6.19	6.18	6.73	6.67
1507+4034	-5.31	4.34	6.11	6.15	6.2	6.16	6.14	6.58	6.53
1356+2416	-5.39	11.04	6.1	6.2	6.18	6.15	6.13	6.61	6.56
0447+1124	-5.35	6.96	6.11	6.15	6.19	6.15	6.13	6.59	6.55
2304+2415	-5.48	10.97	6.07	6.3	6.15	6.11	6.09	6.63	6.57
0902+1004	-5.29	5.88	6.13	6.16	6.21	6.18	6.15	6.59	6.55
1158+1845	-5.36	9.04	6.06	6.09	6.15	6.12	6.09	6.52	6.47
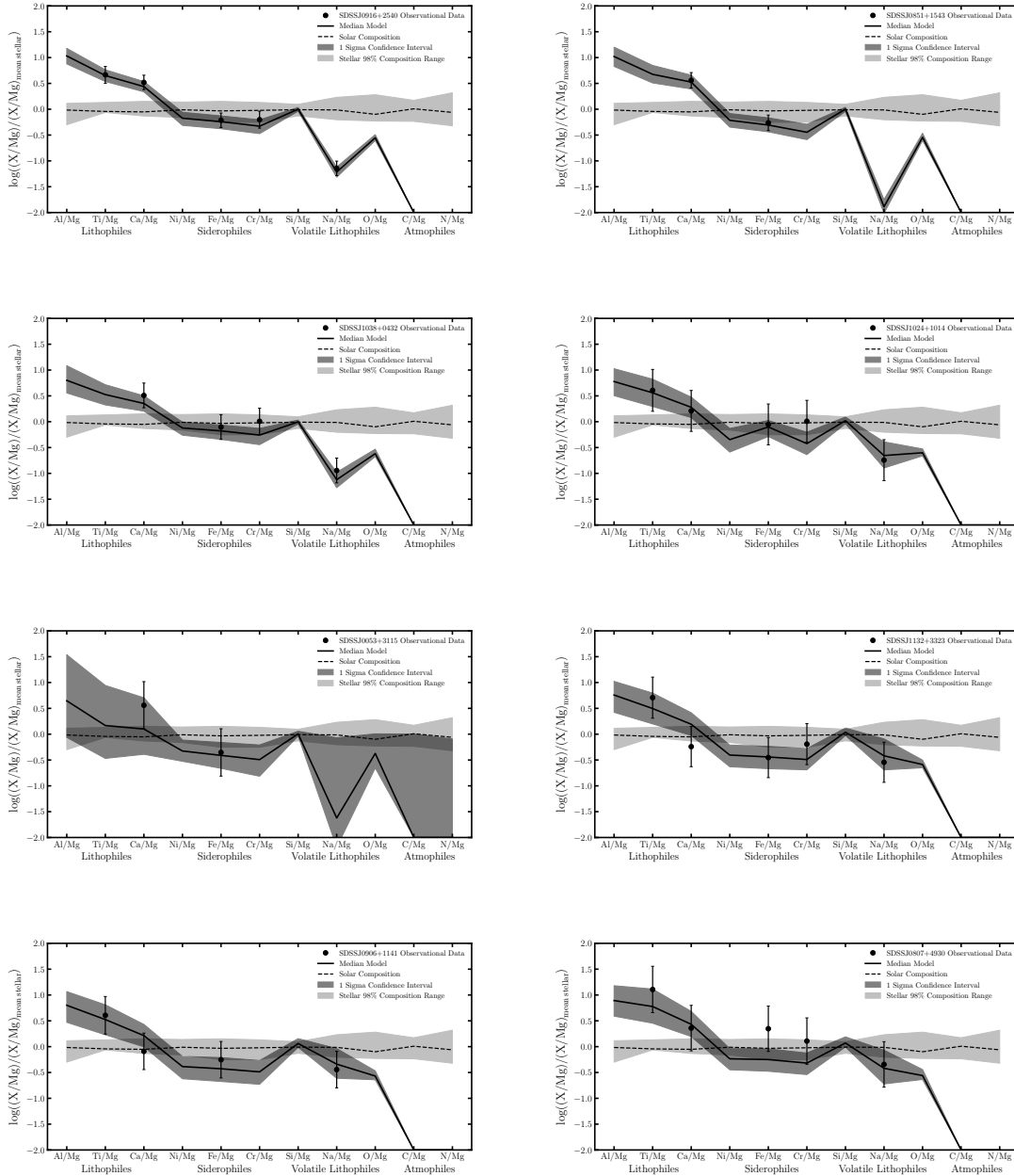
Fig. A.1 8 of the 10 white dwarf systems where the polluting material is required to be a heated such that it is depleted in the moderate-volatiles.
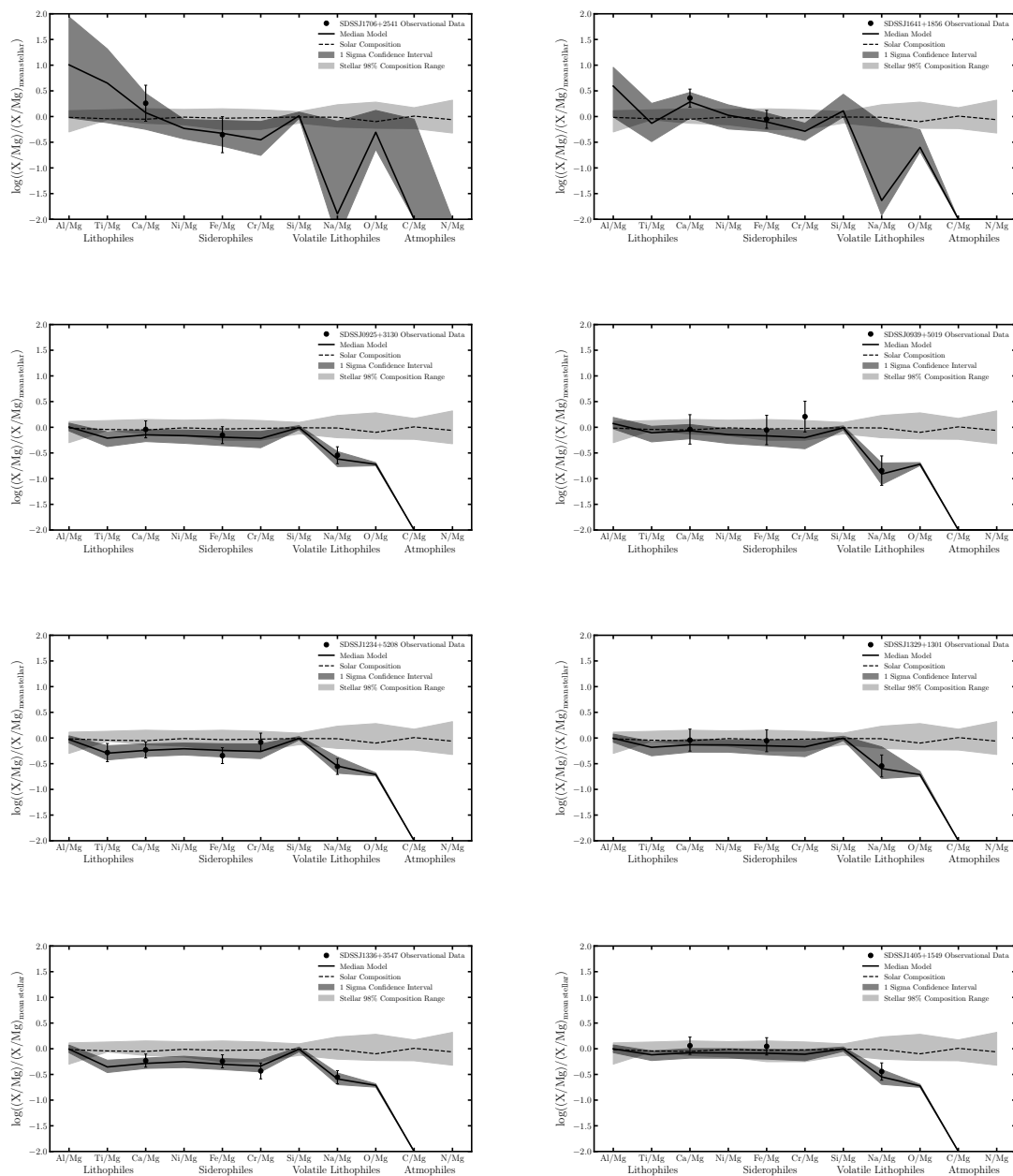
Fig. A.2 2 of the 10 white dwarf systems where the polluting material is required to be a heated such that it is depleted in the moderate-volatiles and 8 of the 10 white dwarf systems where the polluting material is required to be heated such that it is depleted in the volatiles.
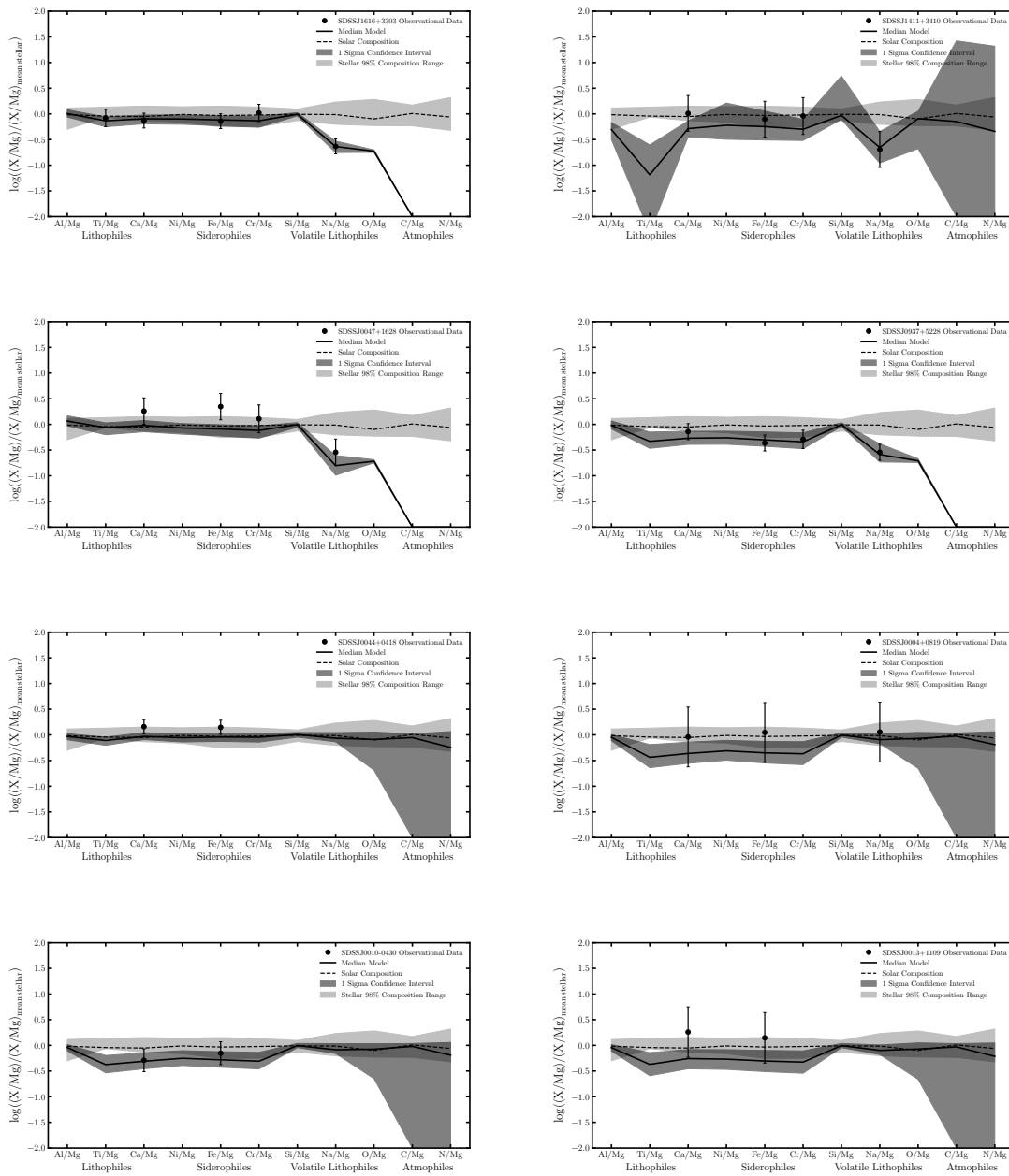
Fig. A.3 4 of the 10 white dwarf systems where the polluting material is required to be a heated such that it is depleted in the volatiles and 4 of the 135 white dwarf systems where the polluting material is consistent with the accretion of primitive material.
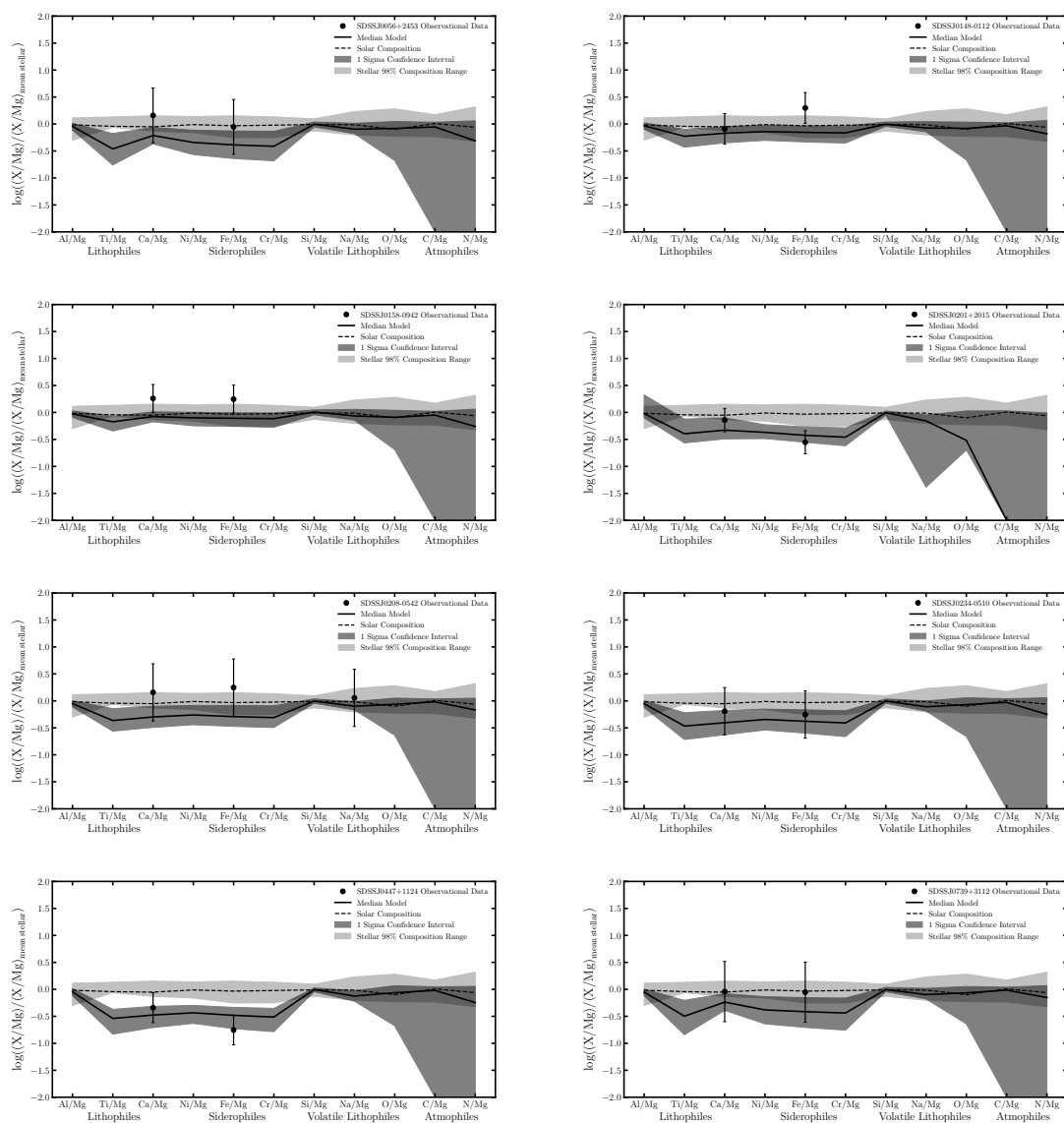
Fig. A.4 8 of the 135 white dwarf systems where the polluting material is consistent with the accretion of primitive material.
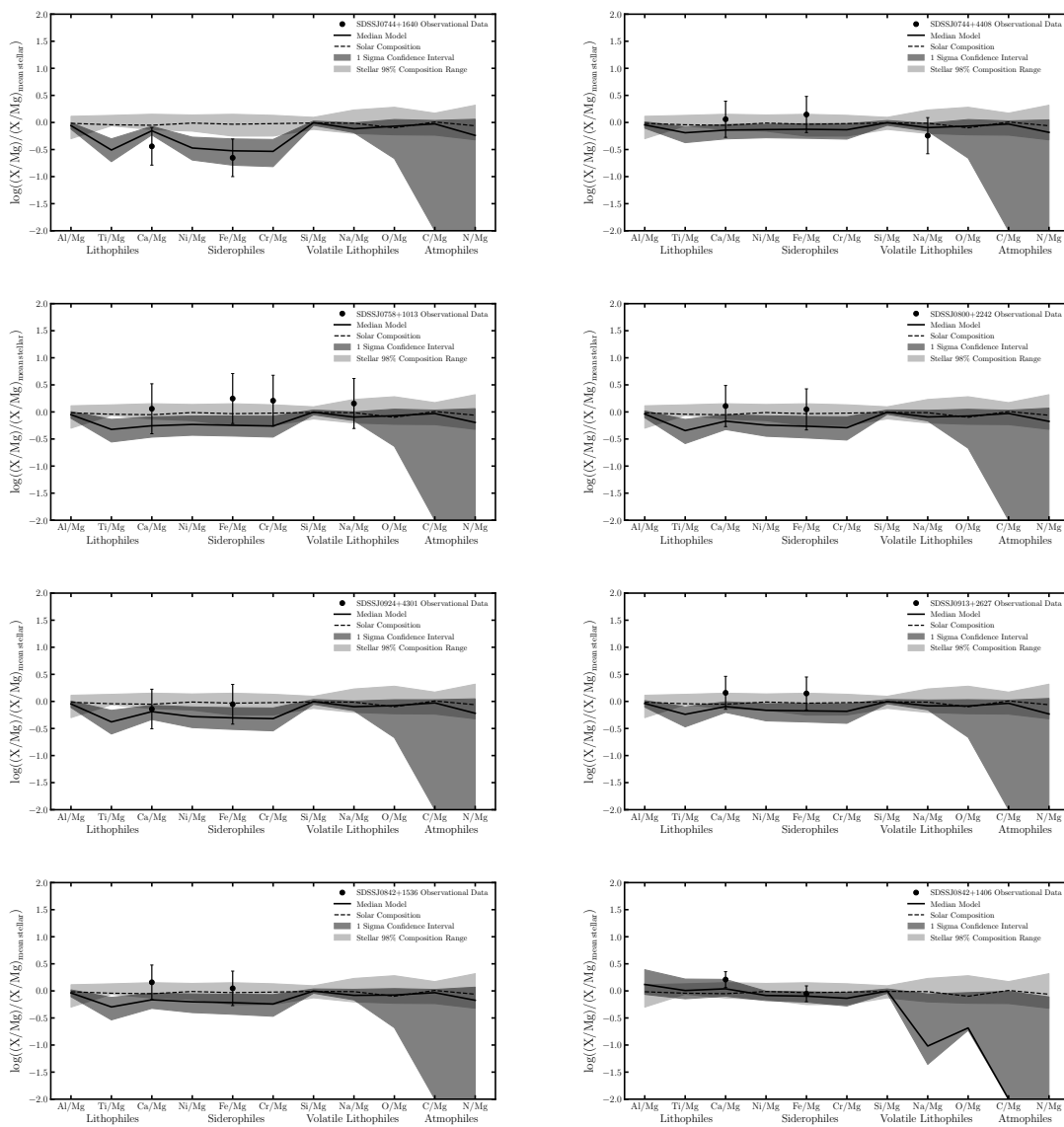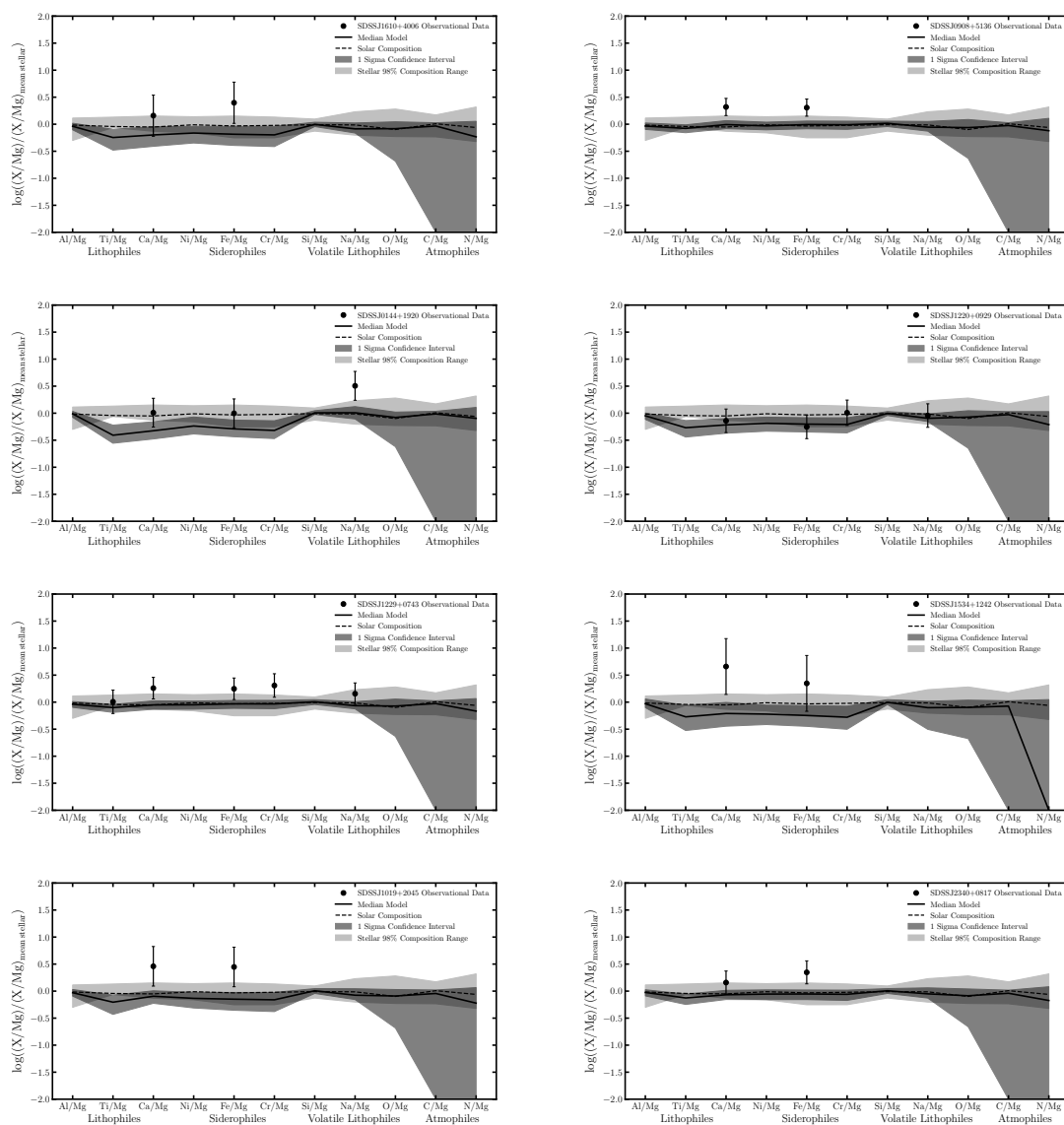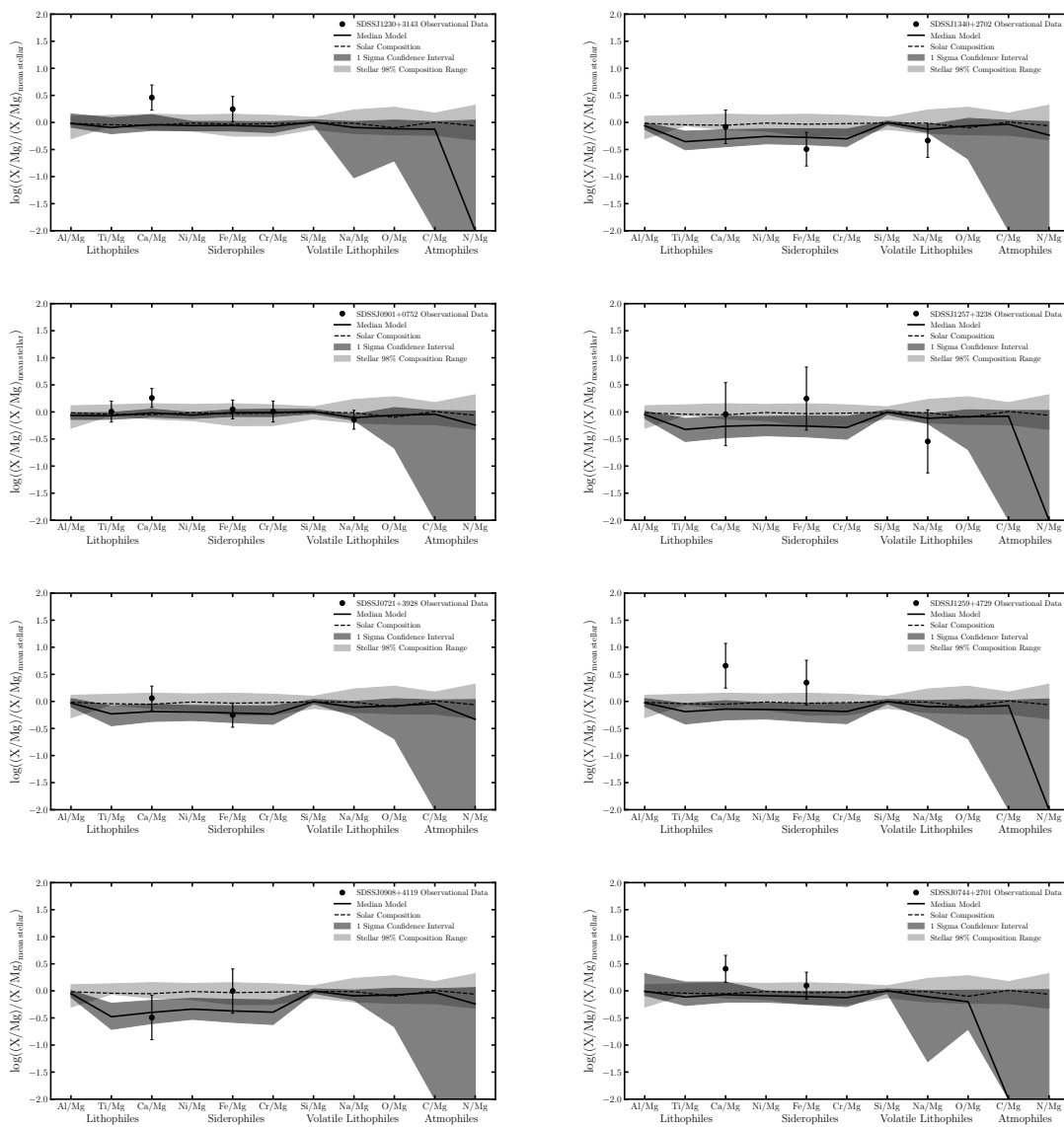
Fig. A.5 8 of the 135 white dwarf systems where the polluting material is consistent with the accretion of primitive material.
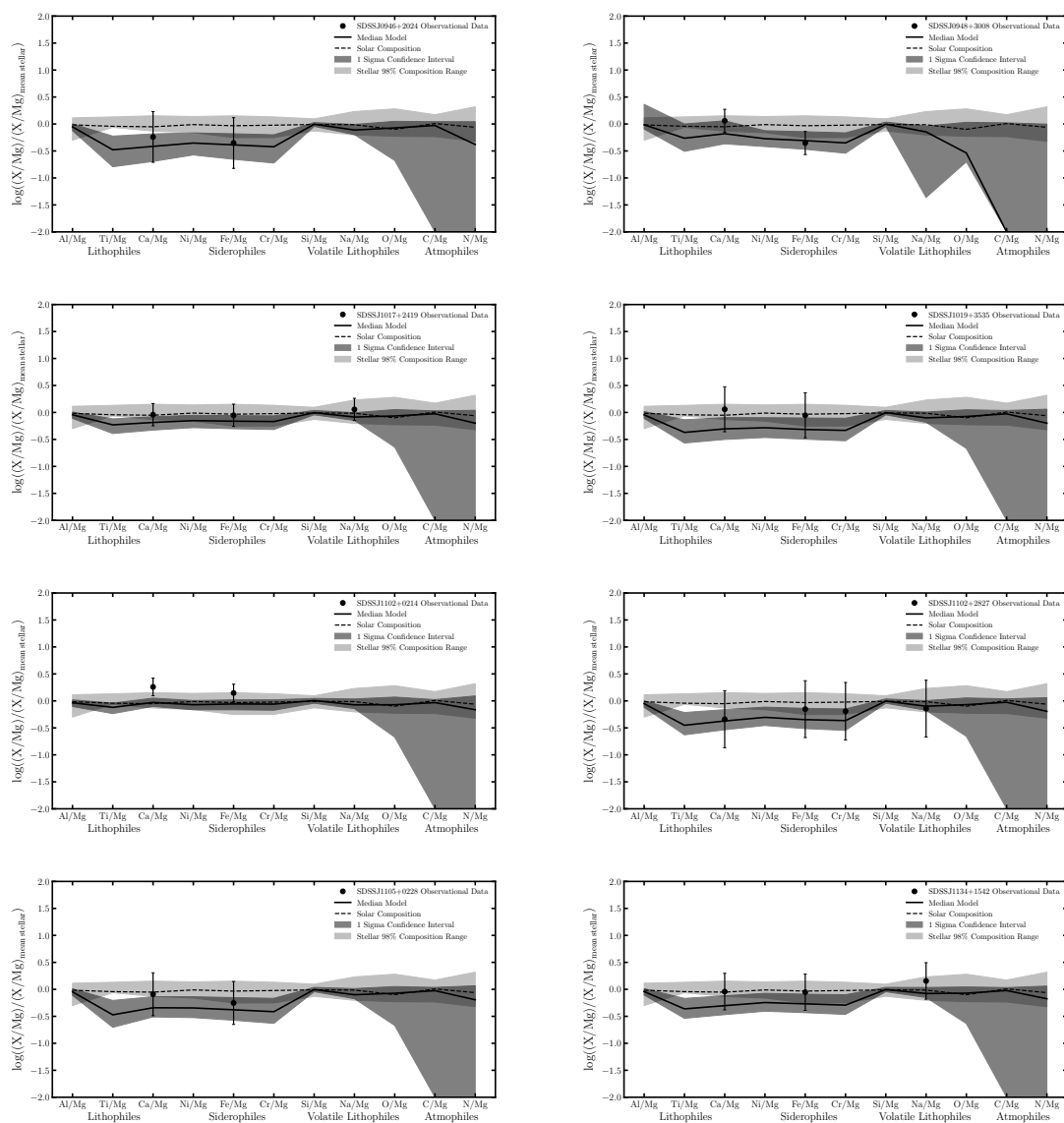
Fig. A.6 8 of the 135 white dwarf systems where the polluting material is consistent with the accretion of primitive material.
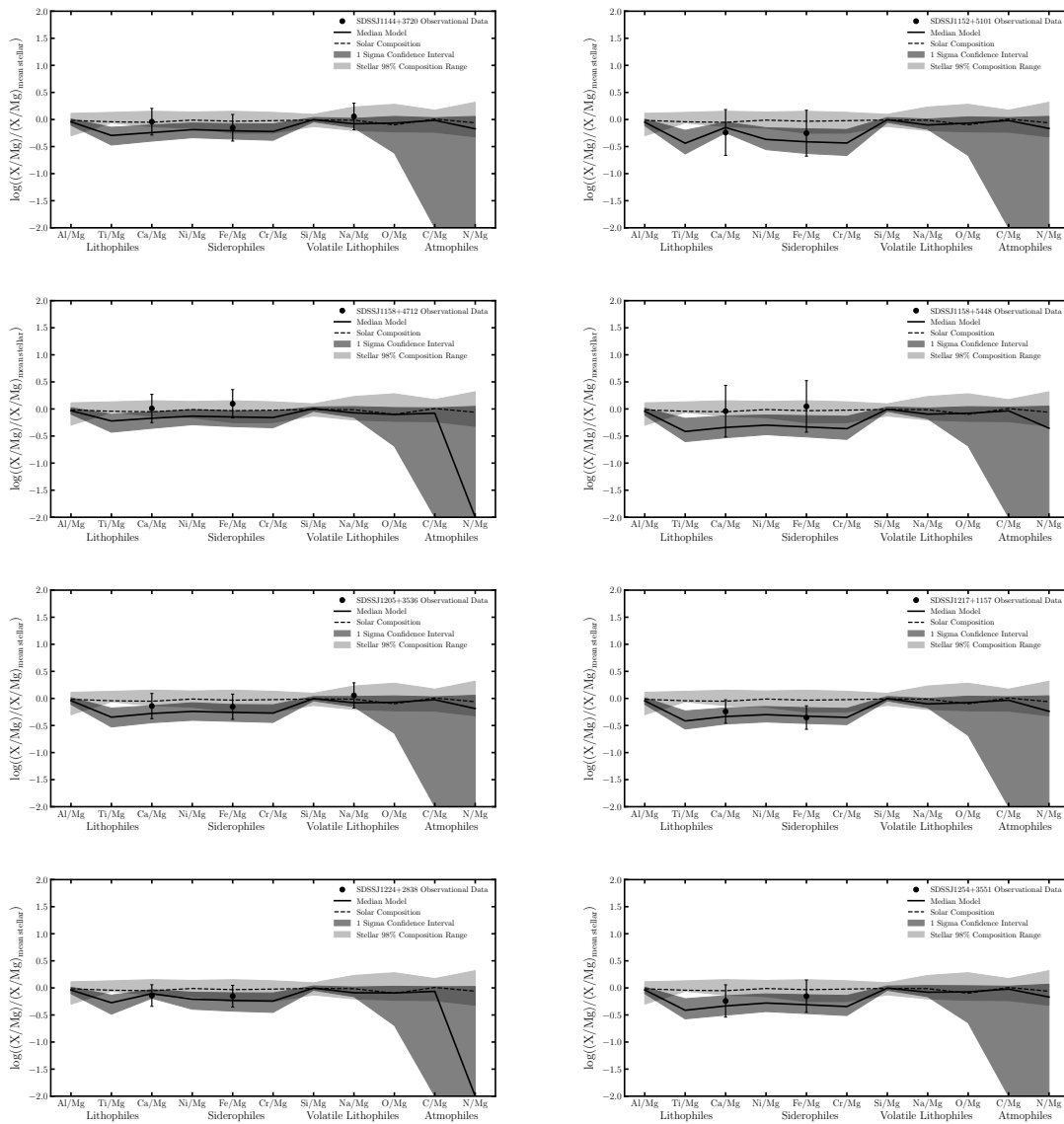
Fig. A.7 8 of the 135 white dwarf systems where the polluting material is consistent with the accretion of primitive material.
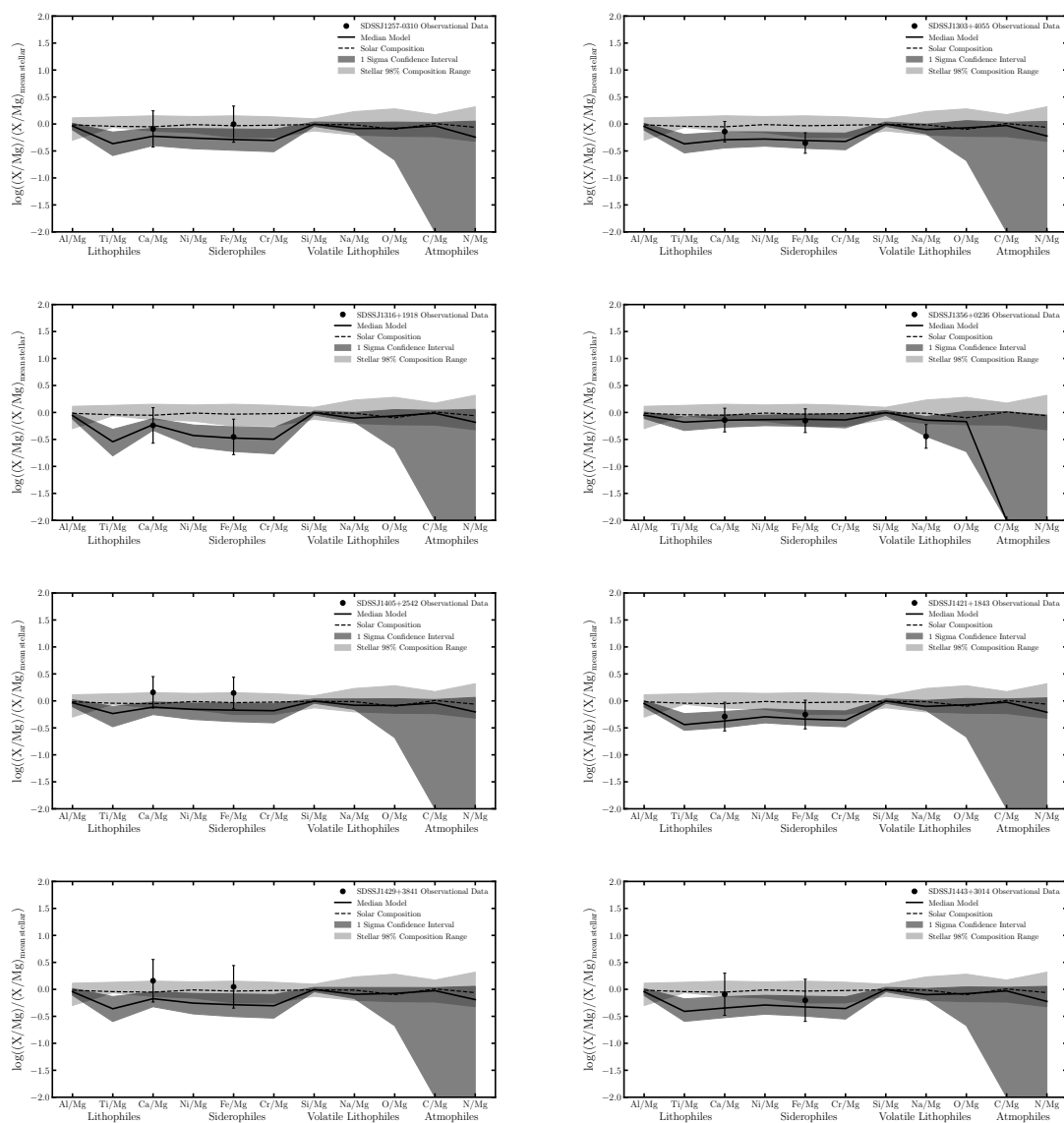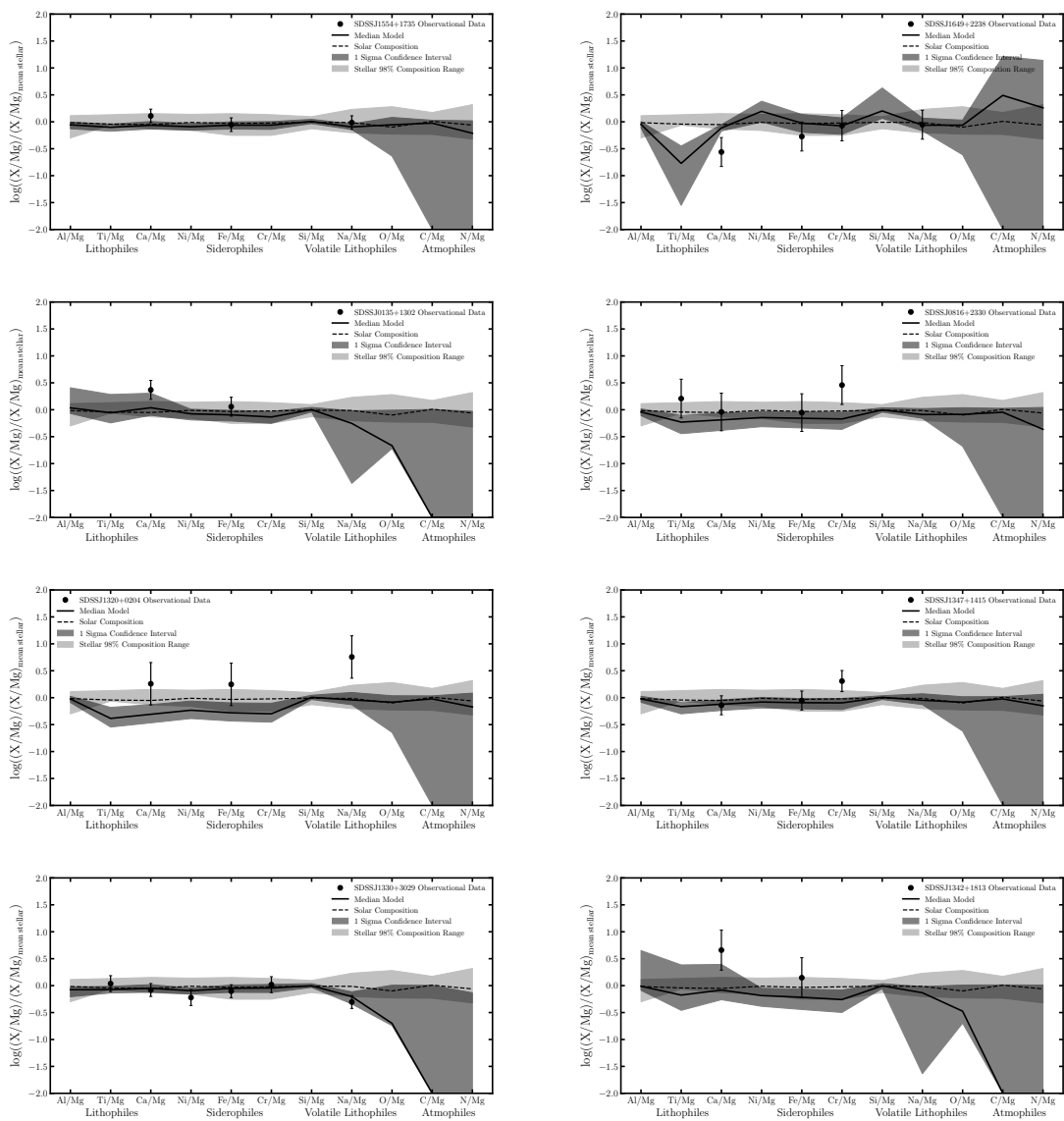
Fig. A.8 8 of the 135 white dwarf systems where the polluting material is consistent with the accretion of primitive material.
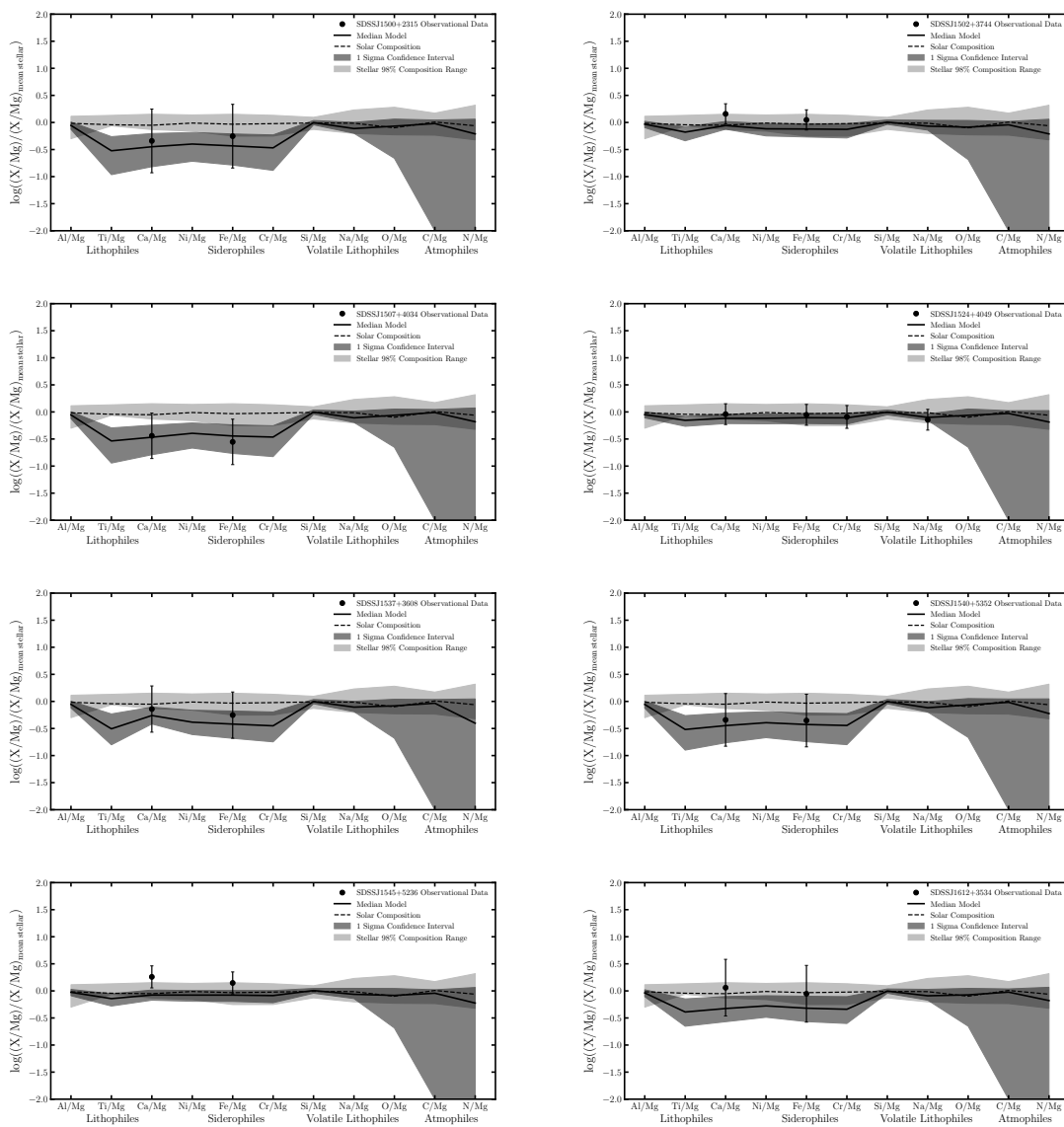
Fig. A.9 8 of the 135 white dwarf systems where the polluting material is consistent with the accretion of primitive material.
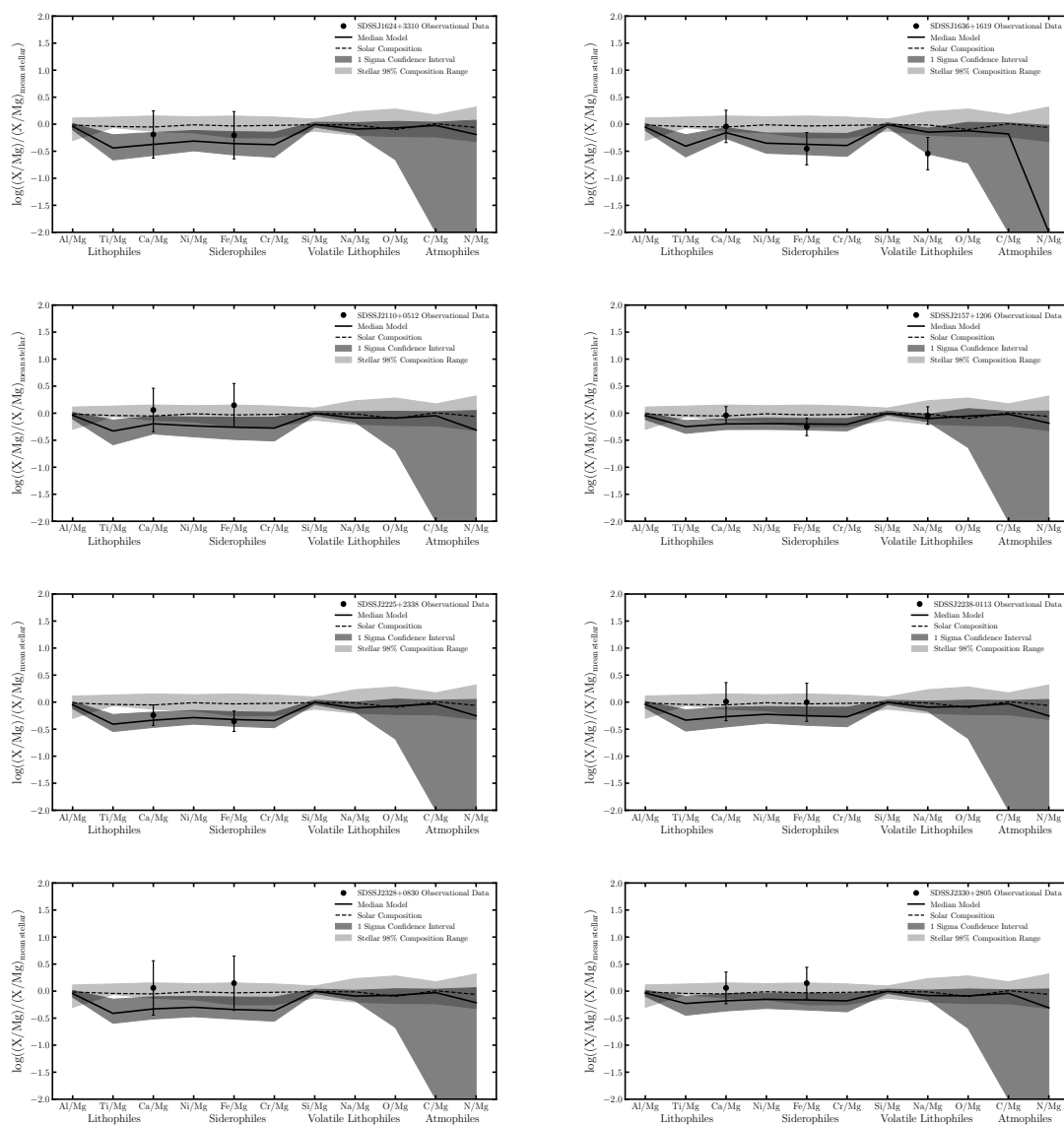
Fig. A.10 8 of the 135 white dwarf systems where the polluting material is consistent with the accretion of primitive material.
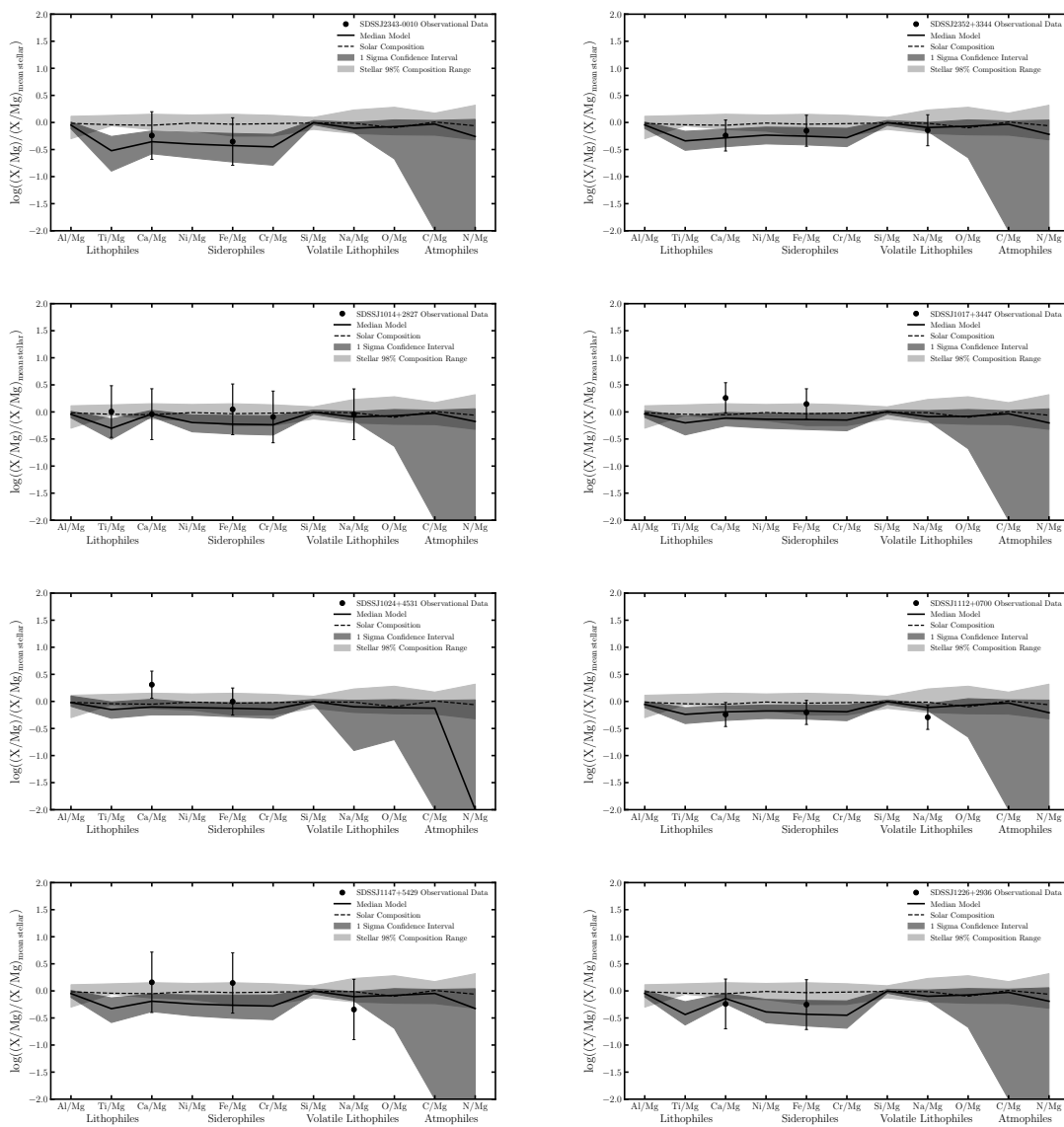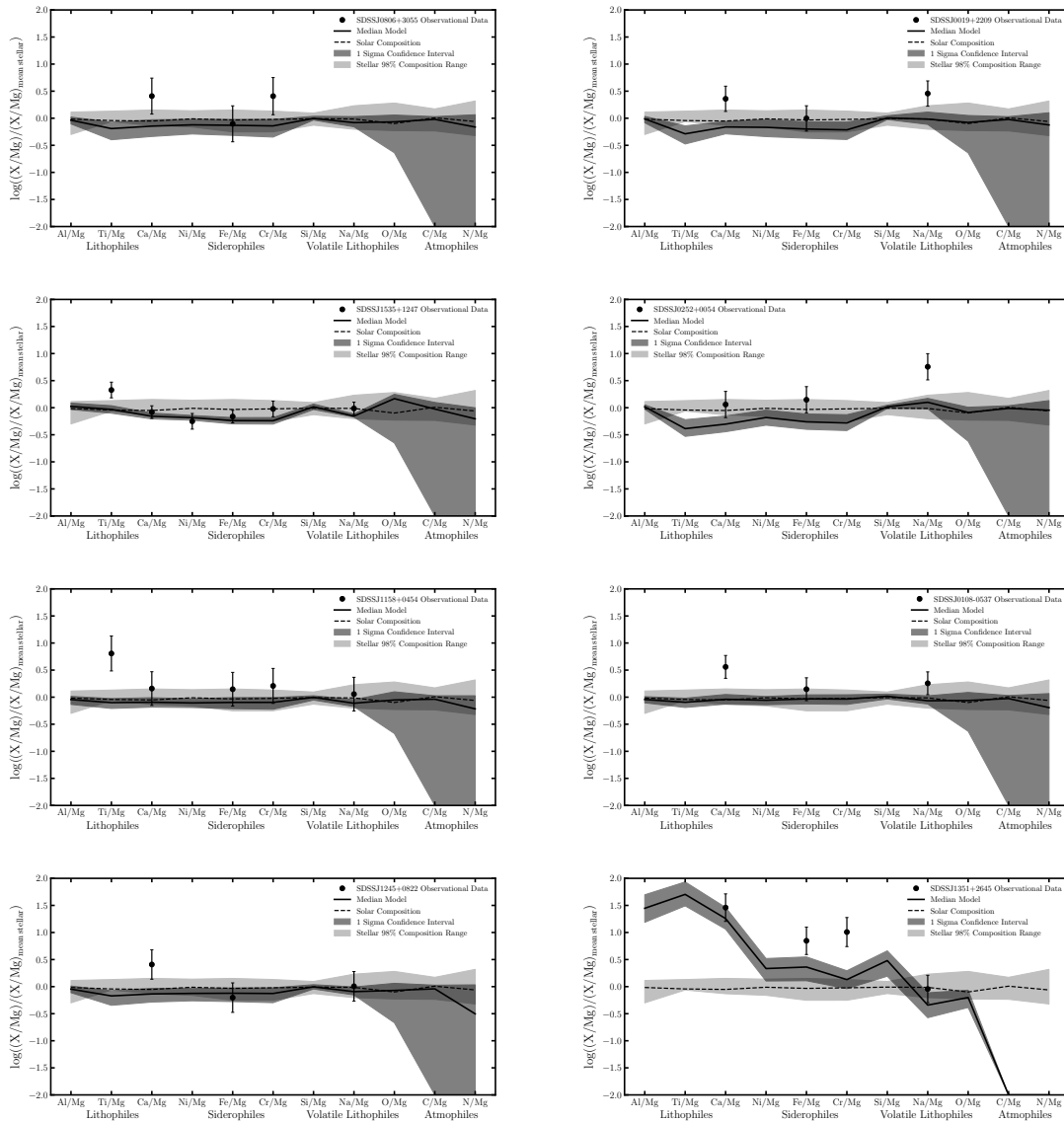
Fig. A.11 8 of the 135 white dwarf systems where the polluting material is consistent with the accretion of primitive material.
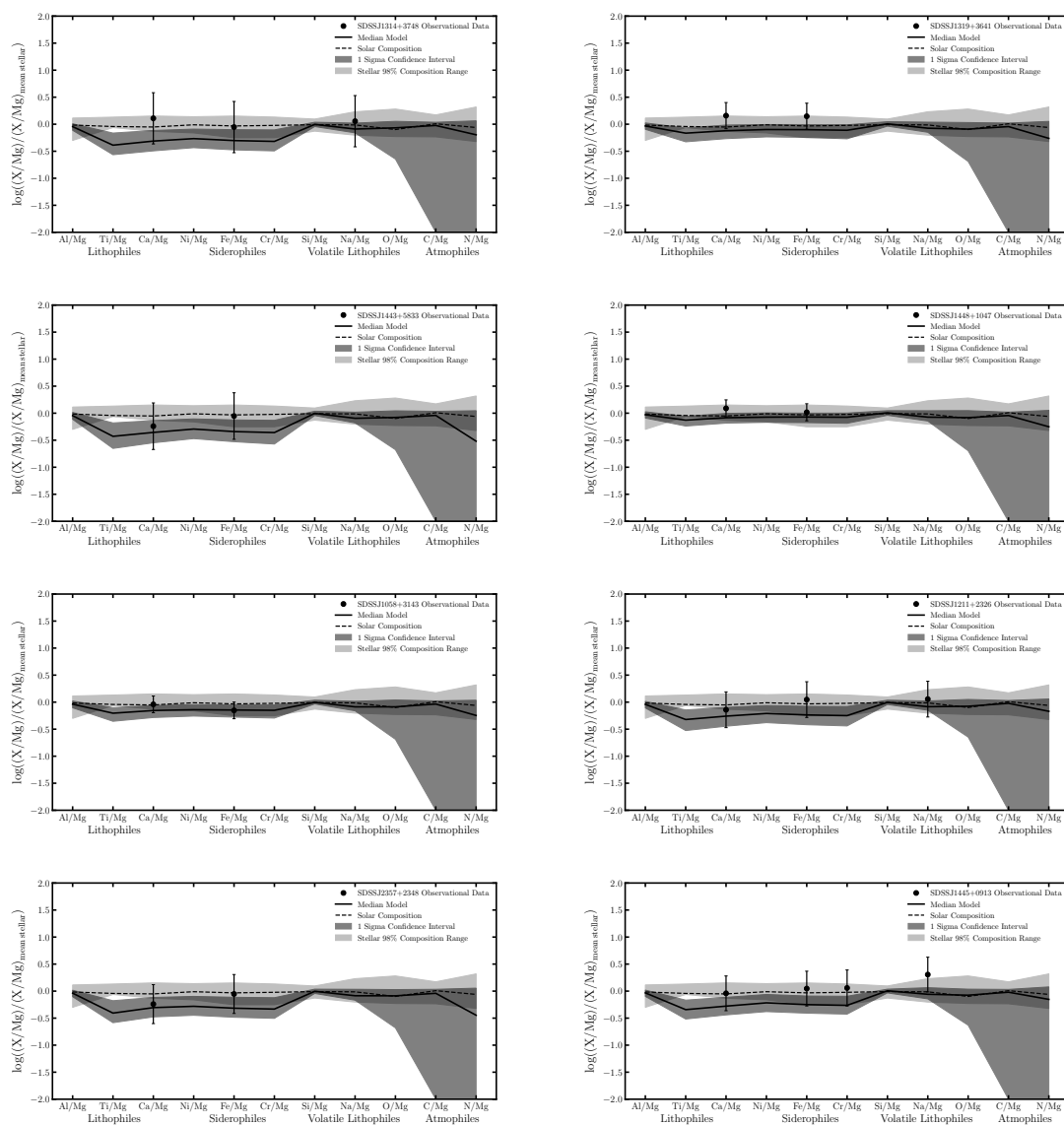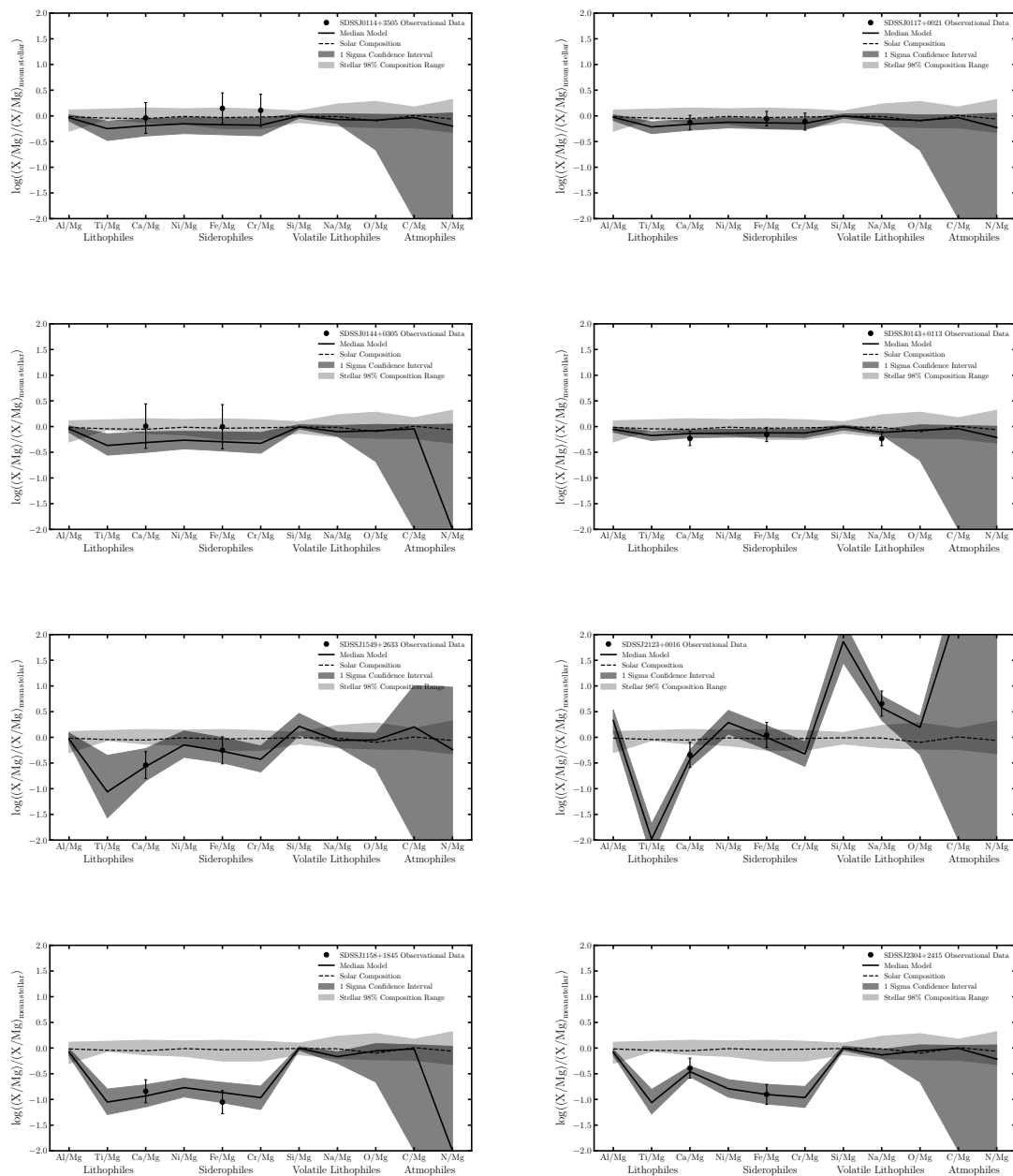
Fig. A.12 8 of the 135 white dwarf systems where the polluting material is consistent with the accretion of primitive material.
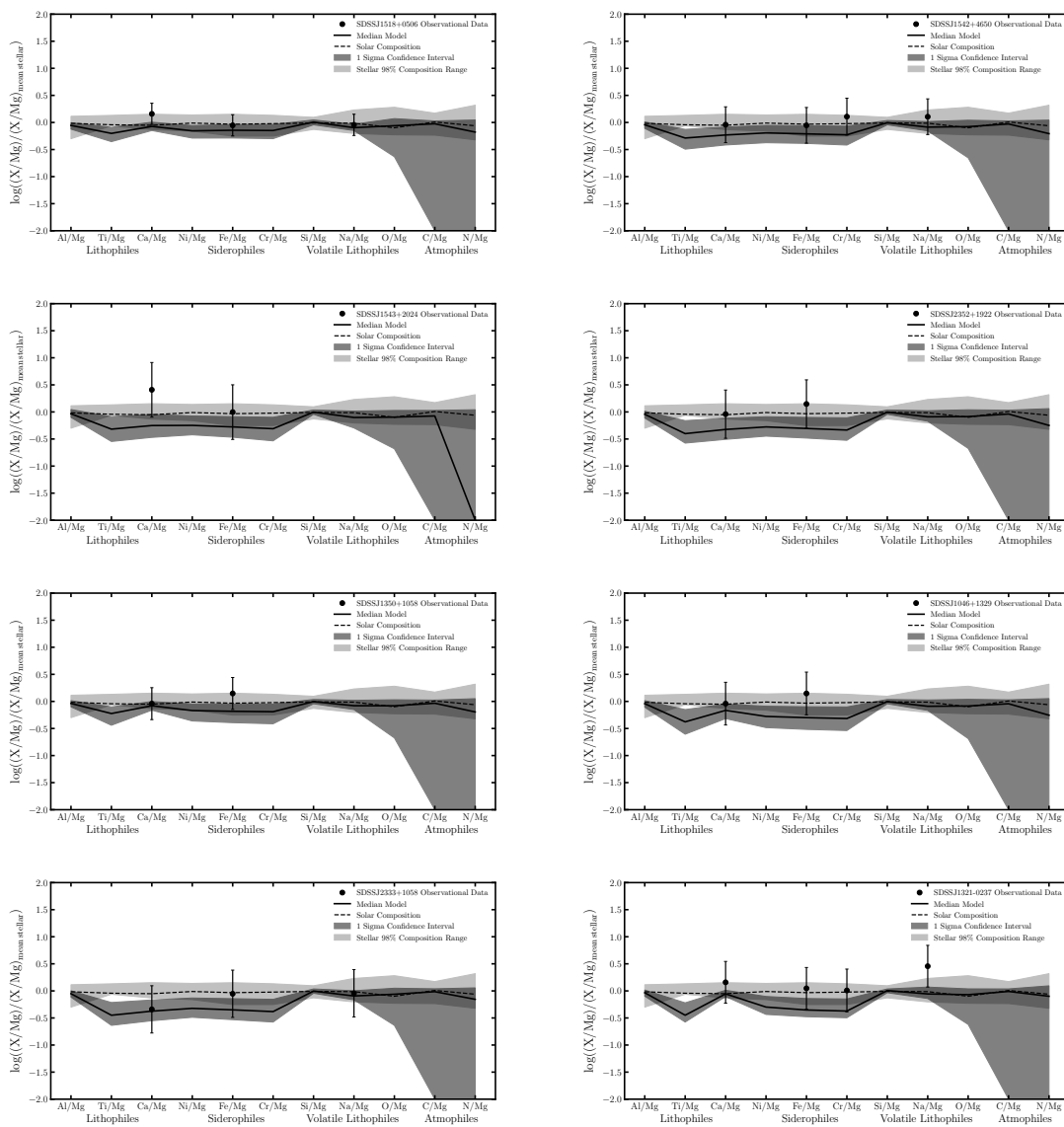
Fig. A.13 8 of the 135 white dwarf systems where the polluting material is consistent with the accretion of primitive material.
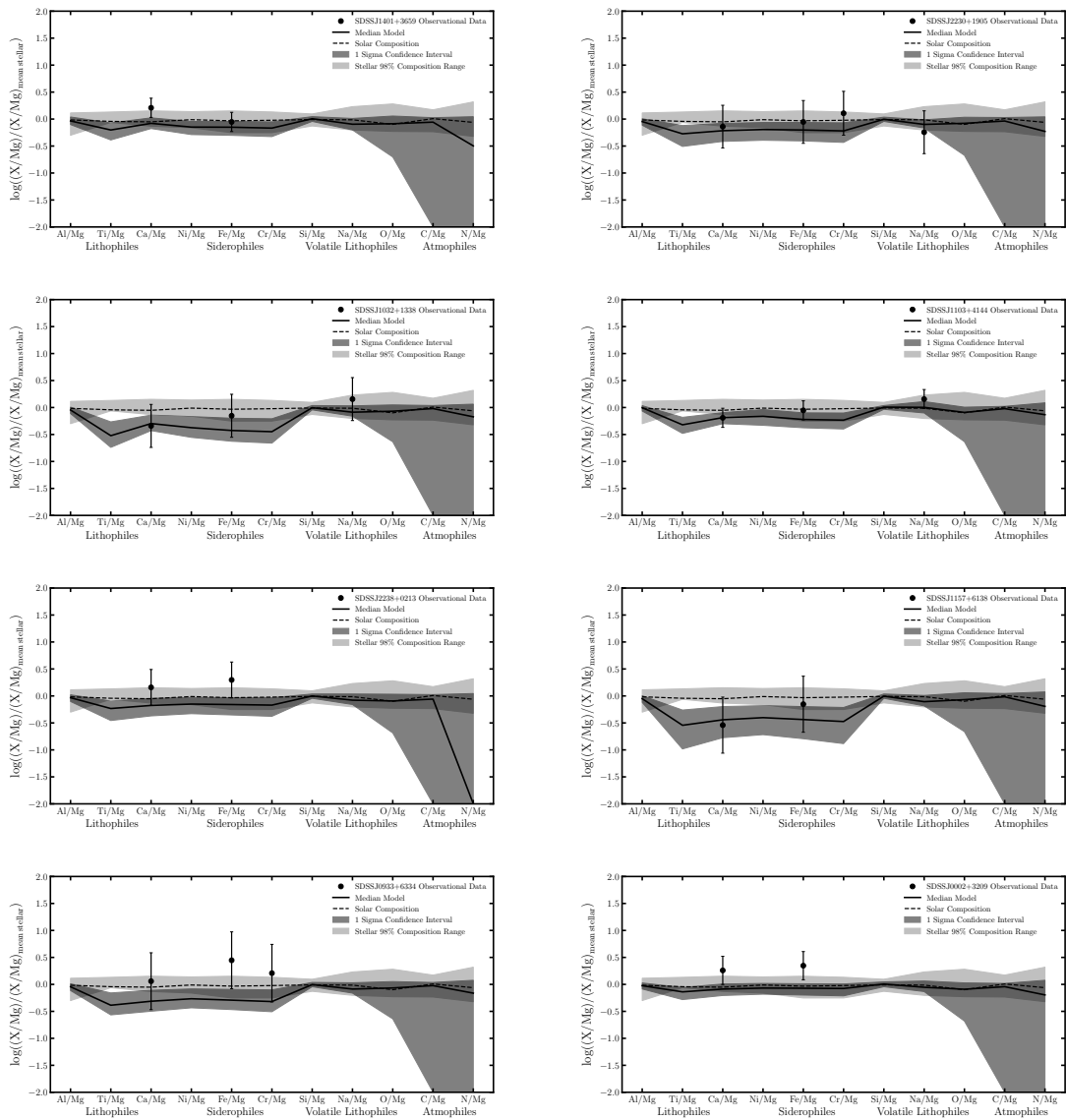
Fig. A.14 8 of the 135 white dwarf systems where the polluting material is consistent with the accretion of primitive material.
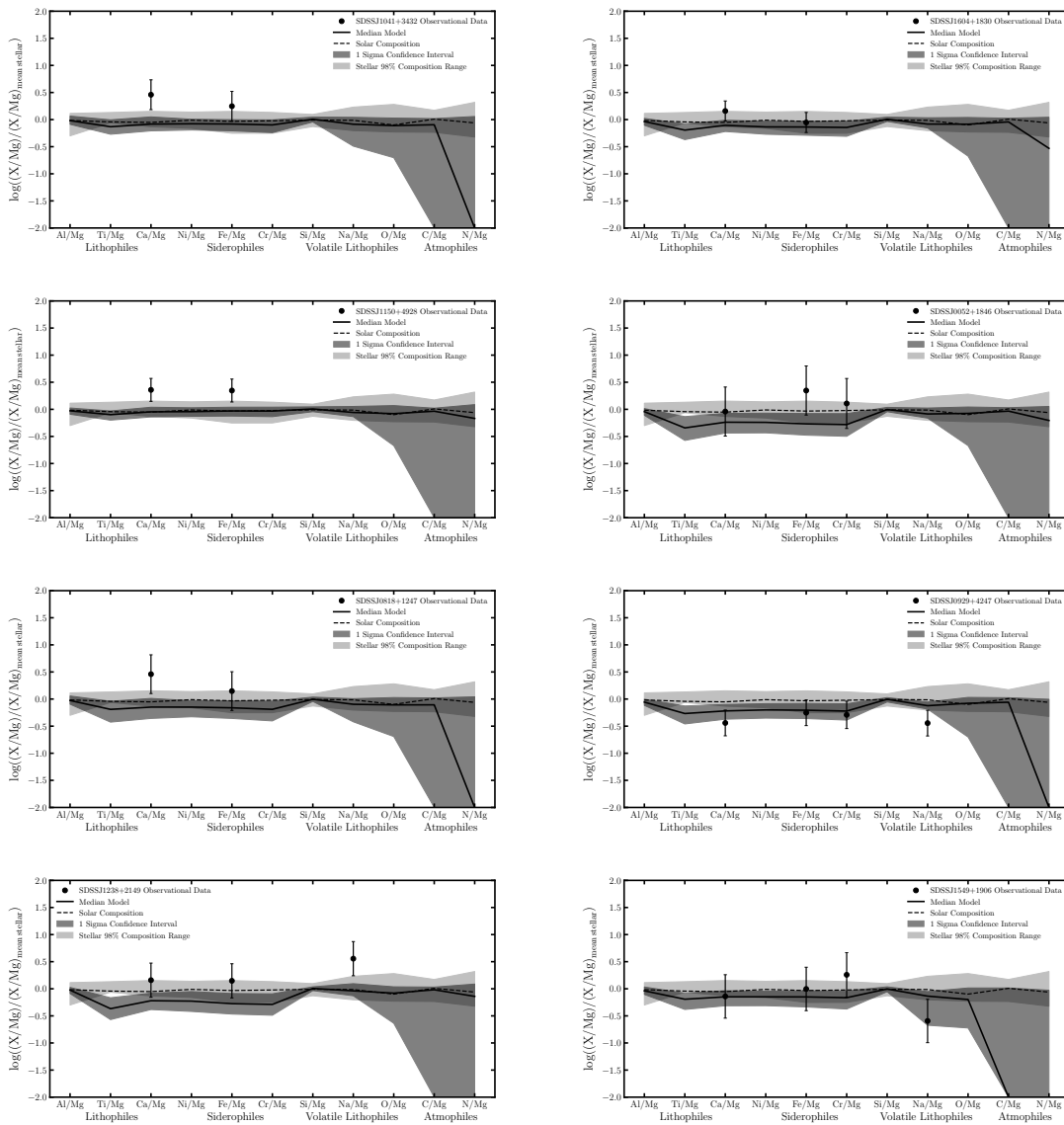
Fig. A.15 8 of the 135 white dwarf systems where the polluting material is consistent with the accretion of primitive material.

Fig. A.16 8 of the 135 white dwarf systems where the polluting material is consistent with the accretion of primitive material.

Fig. A.17 8 of the 135 white dwarf systems where the polluting material is consistent with the accretion of primitive material.

Fig. A.18 8 of the 135 white dwarf systems where the polluting material is consistent with the accretion of primitive material.

Fig. A.19 7 of the 135 white dwarf systems where the polluting material is consistent with the accretion of primitive material and the 1 system where the abundances cannot be reproduced with a χ^2 per element value of less than 1.

Fig. A.20 4 of the 135 white dwarf systems where the polluting material is consistent with the accretion of primitive material and all 4 of the systems where the material is required to have finished accreting and be in the declining phase.
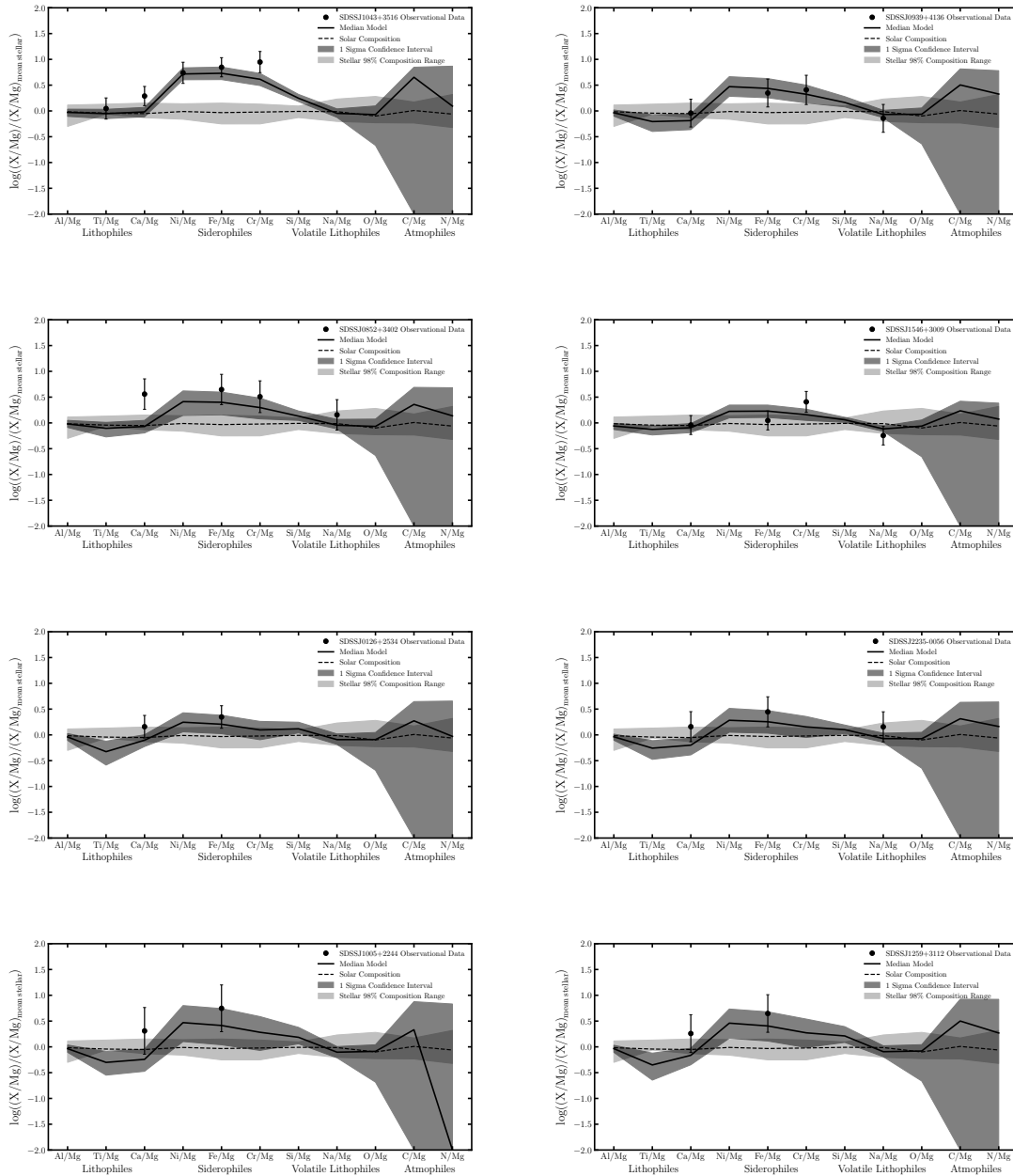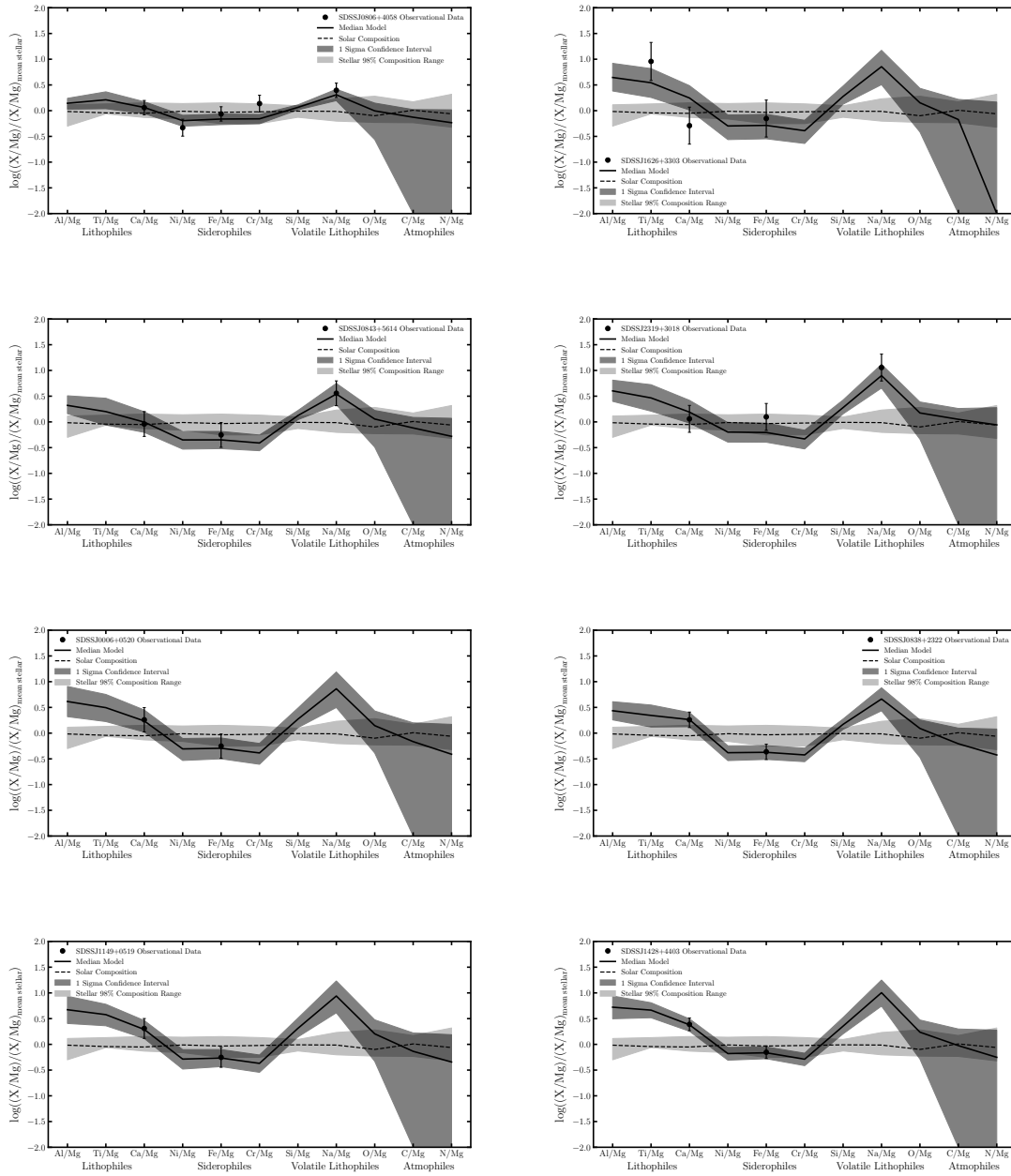
Fig. A.21 8 of the 9 white dwarf systems where the polluting material is required to be a core-rich fragment of a differentiated body.
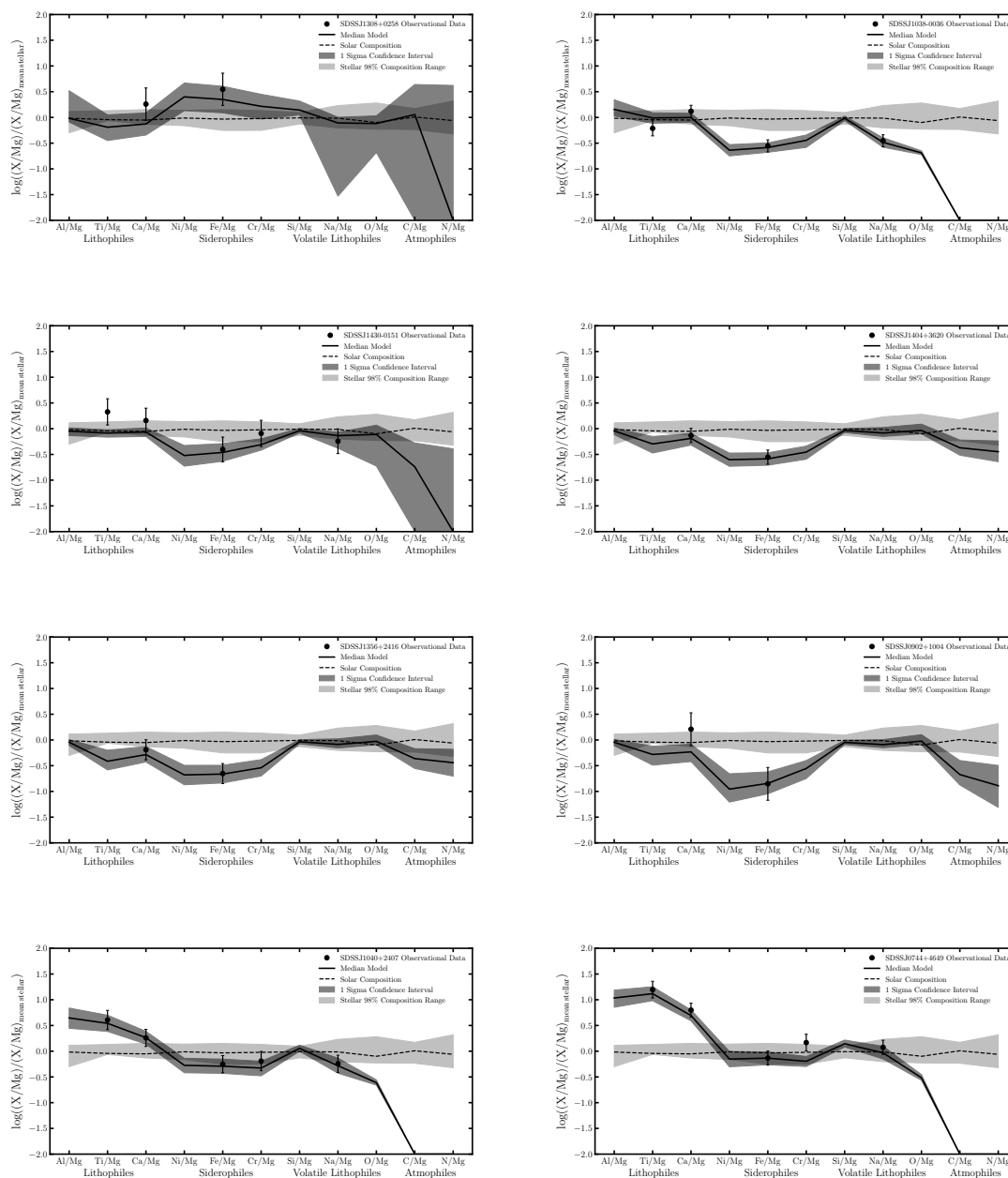
Fig. A.22 1 of the 9 white dwarf systems where the polluting material is required to be a core-rich fragment of a differentiated body, all 5 systems where the polluting material is required to be a mantle-rich fragment of a differentiated body, and 2 of the 12 white dwarf systems where the polluting material is required to be a crust-rich fragment of a differentiated body.

Fig. A.23 8 of the 12 white dwarf systems where the polluting material is required to be a crust-rich fragment of a differentiated body.
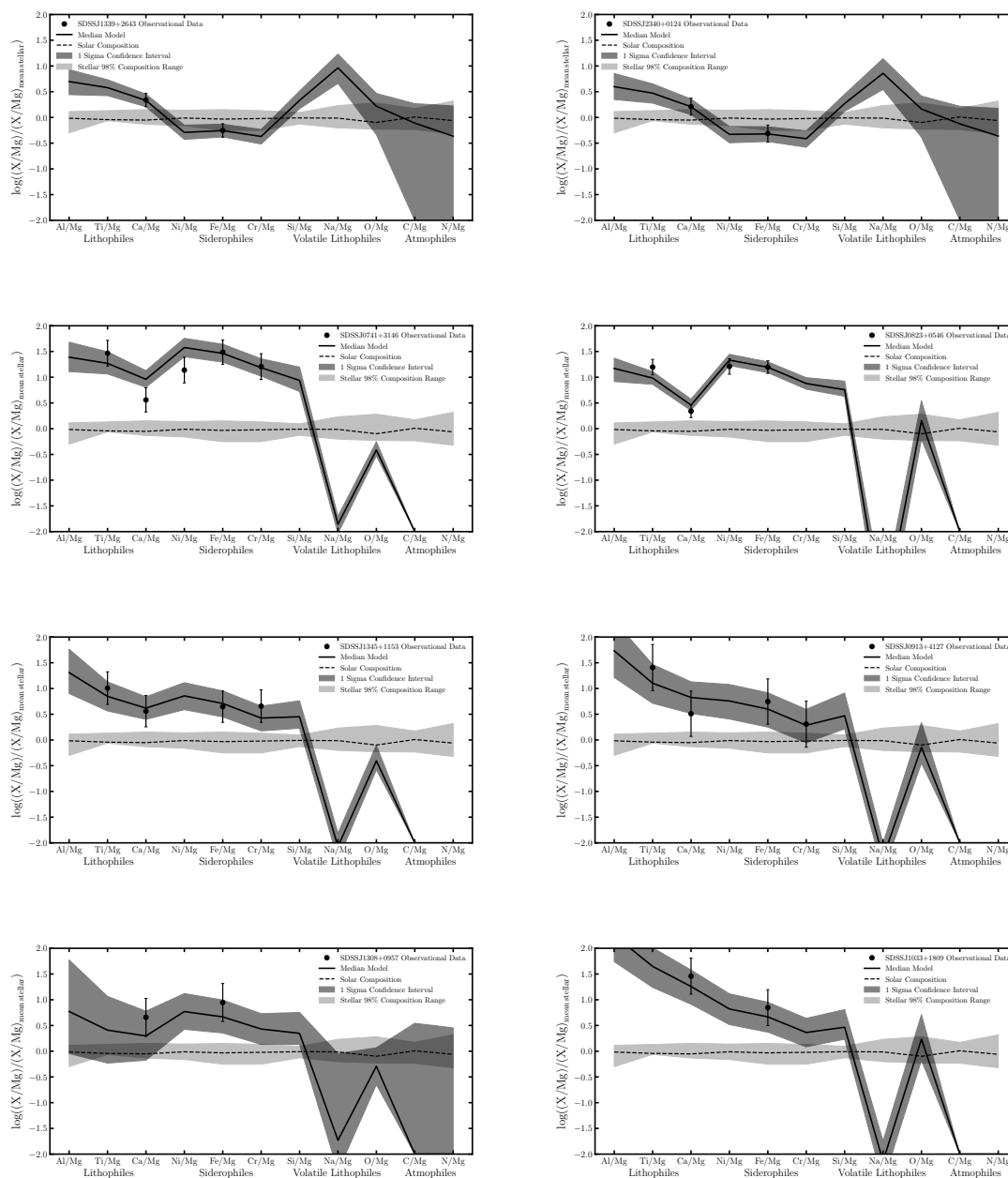
Fig. A.24 2 of the 12 white dwarf systems where the polluting material is required to be a crust-rich fragment of a differentiated body and 6 of the 13 white dwarf systems where the polluting material is required to be a core-rich fragment of a differentiated body which has undergone sufficient heating such that it is depleted in the moderate volatiles.
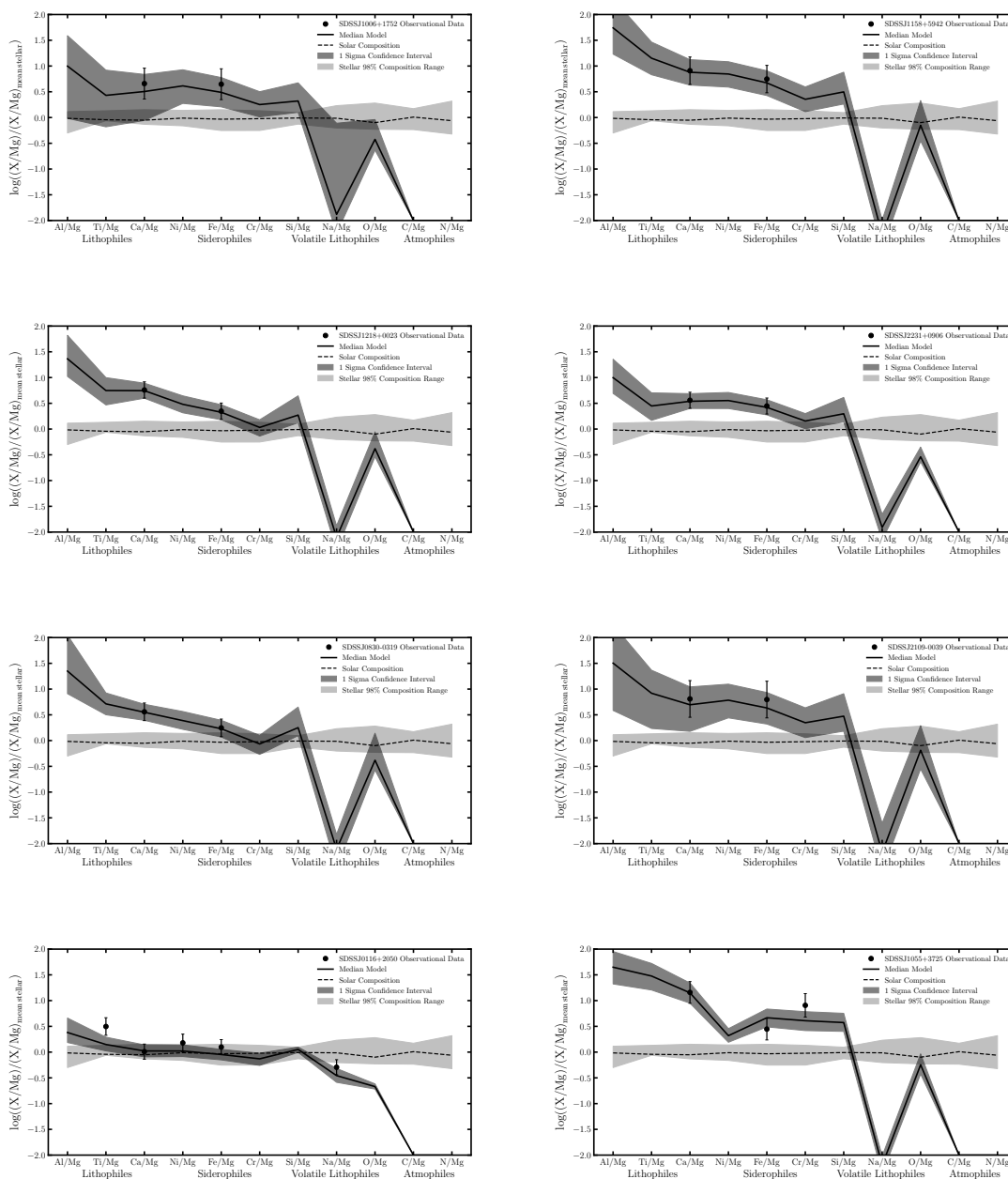
Fig. A.25 7 of the 13 white dwarf systems where the polluting material is required to be a core-rich fragment of a differentiated body which has undergone sufficient heating such that it is depleted in the moderate volatiles. The system in the bottom right panel is the one system which requires the same optimal model but needs the initial core abundances to be adjusted.
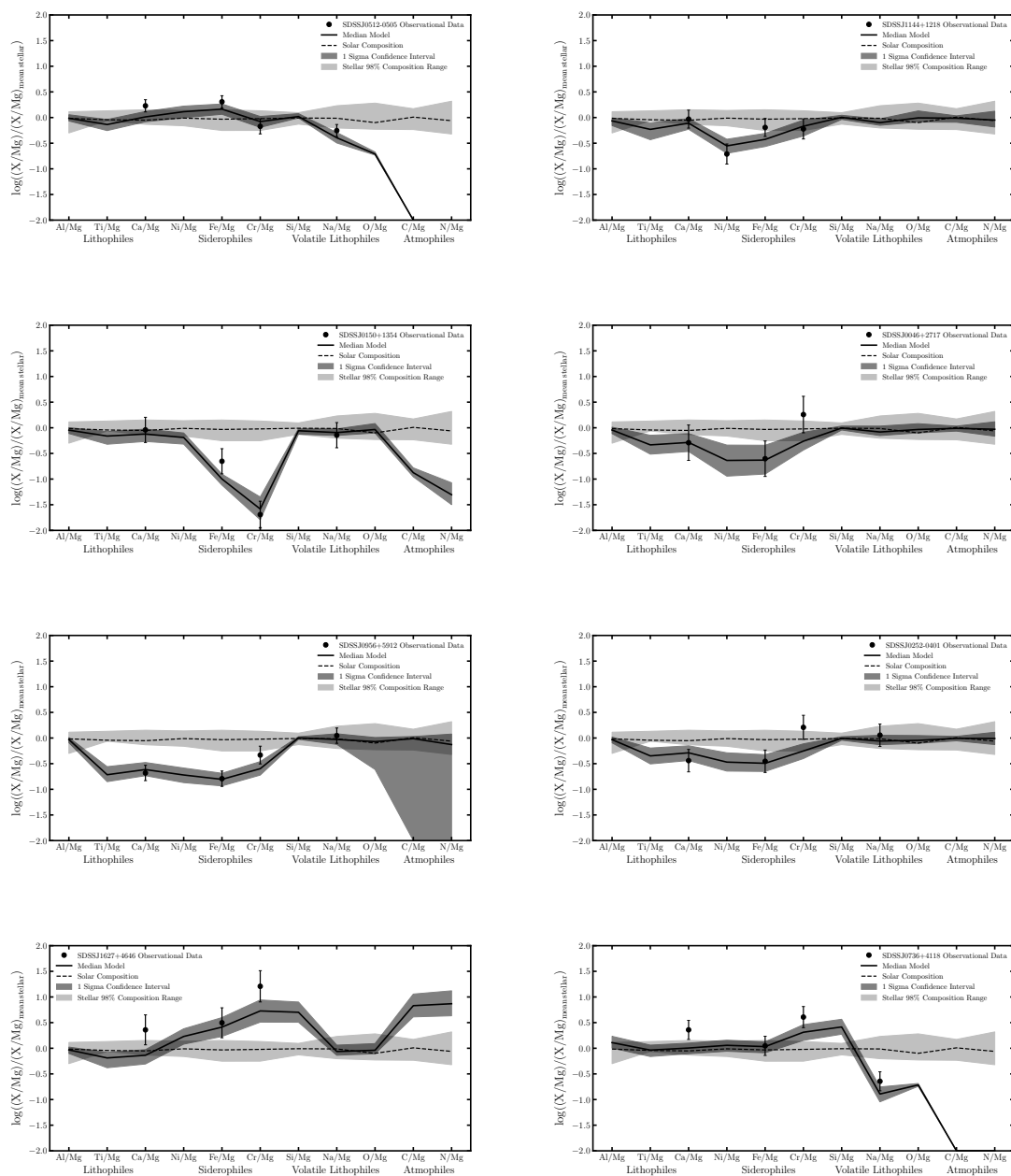
Fig. A.26 8 of the 9 white dwarf systems where the polluting material is required to be a fragment of a differentiated body which formed at non-Earth-like pressures such that the initial core abundances to be adjusted.